2007

Modeling and Simulation of a Microturbine Generator to be Coupled With a Molten Carbonate Fuel Cell for Distributed Generation

Karleine M. Justice
Wright State University

MODELING AND SIMULATION OF A MICROTURBINE GENERATOR TO BE COUPLED WITH A MOLTEN CARBONATE FUEL CELL FOR DISTRIBUTED GENERATION

A thesis submitted in partial fulfillment
of the requirements for the degree of
Master of Science in Engineering

By

KARLEINE M. JUSTICE
B.S., University of Idaho, 2003

2007
Wright State University

WRIGHT STATE UNIVERISTY

SCHOOL OF GRADUATE STUDIES

May 10, 2007

I HEREBY COMMEND THAT THE THESIS PREPARED UNDER MY SUPERVISION BY Karleine M. Justice ENTITLED Modeling and Simulation of a Microturbine Generator to be Coupled with a Molten Carbonate Fuel Cell for Distributed Generation BE ACCEPTED IN PARTIAL FULFILLMENT OF THE REQUIREMENTS FOR THE DEGREE OF Master of Science in Engineering.

Committee on
Final Examination

J. Mitch Wolff, Ph.D.
Thesis Director

J. Mitch Wolff, Ph.D.

George P.G. Huang, P.E., Ph.D.
Department Chair

P. Ruby Mawasha, P.E., Ph.D.

Haibo Dong, Ph.D.

Jeffrey Dalton, Ph.D.

Joseph F. Thomas, Jr., Ph.D.
Dean, School of Graduate Studies

ABSTRACT

Justice, Karleine M. M.S.Egr., Department of Mechanical and Materials Engineering, Wright State University, 2007. Modeling and Simulation of a Microturbine Generator to be Coupled with a Molten Carbonate Fuel Cell for Distributed Generation.

Distributed generation is desired when the individual energy requirements ranging from 25-75 kW of office buildings, restaurants, hospitals and apartments can not be met by the current electric utility grid. Microturbine generators as stand alone power generation systems have been designed to meet these requirements. For power requirements up to 50 MW, hybrid fuel cell systems offer higher efficiency and lower levels of pollutant emissions with more advanced fuel energy savings than non-hybrid systems. The objective of this project is to develop a simulation of a microturbine generator as a stand alone power generation system to validate a microturbine generator as part of a hybrid power generation system designed to produce 250 kW of usable power in MATLAB/Simulink®. The stand alone power generation system will be modeled using a 1-Dimensional approach. The hybrid power generation system is modeled as three major sub-systems; a hybrid microturbine generator, a molten carbonate fuel cell with catalytic oxidizer, and a shell-and-tube heat exchanger. The hybrid power generation system will be analyzed by two different models; a 0-Dimensional hybrid model where all the components are 0-Dimensional and a 0-Dimensional model with 1-Dimensional zooming for the hybrid microturbine generator. The analysis of the stand alone system is used for

validation of the hybrid system at the operating design point of the microturbine generator. A control system was placed on the hybrid microturbine generator power generation system and an analysis was completed on the temperature response of the 0-Dimensionl hybrid system as the microturbine generator power was ramped from 0-30 kW over six different time intervals. A second controller was placed on the fuel cell power generation system to further analyze the hybrid system's controllability. The three MATLAB/Simulink® models developed provide an initial design methodology for modeling and simulation of a hybrid power generation system.

TABLE OF CONTENTS

LIST OF FIGURES

Figure Page

LIST OF TABLES

ACKNOWLEDGEMENTS

I would like to sincerely thank my thesis advisor Dr. Mitch Wolff for getting me involved with this project and letting me charge forward with an open mind. The funding for this project was provided by the Department of Energy and special thanks to Dr. Shripad Revenkar from the Nuclear Engineering Department at Purdue University.

This project is a combination of the hard work of not only myself but Brian Wolf from Purdue University and Carlos Gutierrez at Wright State University. Without them this joint effort would not be possible.

To my thesis committee Dr. Ruby Mawasha who has been there from the beginning and Dr. Haibo Dong who willingly jumped on board. Thank you for your time and patience.

To my husband, his family and my family, who stood beside me and supported my decision to achieve an advanced degree, thank you for your support and just remember to nod and smile.

Finally, to AVETEC for allowing me to work on my thesis and to all of the people at AVETEC who tolerated all the days and nights of reading my thesis, you know who you are; you have my sincerest gratitude for what you do. Last but not least to the Chief Technology Officer at AVETEC, Dr. Jeff Dalton, my mentor and my friend, thank you for being there as I muscled on to completion.

NOMENCLATURE

Microturbine Generator

C_p – specific heat at constant pressure, *Btu/lbm-R (kJ/kg-K)*

C_v – specific heat at constant volume, *Btu/lbm-R (kJ/kg-K)*

HHV – higher heating value of natural gas, *Btu/lbm (MJ/kg)*

LHV – lower heating value of natural gas, *Btu/lbm (MJ/kg)*

M – Mach number

M_0 – upstream Mach number

N – shaft speed, *rpm*

N_{des} – design shaft speed, *rpm*

$N_{\%}$ – percent operating speed of the engine

P – power, *Btu/hr (W)*

P_{ref} – reference pressure, *psia (kPa)*

P_s – static pressure, *psia (kPa)*

P_t – total pressure, *psia (kPa)*

$\dot{Q}_{in}$ – heat added to the system, *Btu/hr (W)*

R – gas constant, *Btu/lbm-R (kJ/kg-K)*

T_{ref} – reference temperature, *R (K)*

T_s – static temperature, *R (K)*

T_t – total temperature, *R (K)*

U_t – rotor tip speed, *ft/s (m/s)*

$\forall$ – plenum volume, *ft³ (m³)*

V – absolute velocity, *ft/s (m/s)*

V_R – relative velocity, *ft/s (m/s)*

a – speed of sound, *ft/s (m/s)*

b – width of diffuser section, *ft (m)*

d_r – diameter of rotor, *ft (m)*

d_h – diameter of hub, *ft (m)*

d_t – diameter of tip, *ft (m)*

e – polytropic efficiency

f – fuel/air ratio

f_{stoich} – stoichiometric fuel/air ratio

h – enthalpy, *Btu/lbm (kJ/kg)*

$\dot{m}_{oc}$ – corrected mass flow rate of compressor, *lbm/s (kg/s)*

$\dot{m}_o$ – mass flow rate of compressor, *lbm/s (kg/s)*

$\dot{m}_f$ – mass flow rate of fuel, *lbm/s (kg/s)*

$\dot{m}_t$ – mass flow rate of turbine, *lbm/s (kg/s)*

n – number of compressor rotor vanes

r_r – radius of rotor, *ft (m)*

r_h – radius at hub of inducer, *ft (m)*

r_t - radius at tip of inducer, *ft (m)*

u – axial component of velocity, *ft/s (m/s)*

v – tangential (swirl) component of velocity, *ft/s (m/s)*

w – radial component of velocity, *ft/s (m/s)*

Subscripts

c – compressor

cc – combustion chamber

d – diffuser

m – mechanical power

net – net power produced

t – turbine

th – thermal power

0,1, 2, 3 ...– stage or station locations

Heat Exchangers – Primary Surface and Shell-and-Tube

A_i – inner surface area of cold flow geometry, *ft^2 (m^2)*

A_o – outer surface area of cold flow geometry, *ft^2 (m^2)*

A_{Sm} – flow area at middle of central baffle compartment, *ft^2 (m^2)*

A_{Sw} – flow area through baffle window, *ft^2 (m^2)*

A_x – cross-sectional area of single flow channel geometry, *ft^2 (m^2)*

A_{xtot} – total cross sectional area of entire recuperator core, *ft^2 (m^2)*

C_c – cold flow heat capacity rate, *Btu/hr-R (W/K)*

C_h – hot flow heat capacity rate, *Btu/hr-R (W/K)*

C_p – specific heat at constant pressure, *Btu/lbm-R (kJ/kg-K)*

C^* - heat capacity rate ratio

D_h – hydraulic diameter, *ft (m)*

D_i – inner diameter of single tube, *ft (m)*

D_o – outer diameter of single tube, *ft (m)*

D_s – shell diameter, *ft (m)*

$\dot{E}_{in}$ – energy into a control volume, *Btu/hr (W)*

$\dot{E}_{out}$ – energy out of a control volume, *Btu/hr (W)*

$\dot{E}_{st}$ – energy stored within a control volume, *Btu/hr (W)*

G_s – mass velocity of fluid in shell-side, *lbm/s-ft^2 (kg/s-m^2)*

G_t – mass velocity of fluid in tube-side, *lbm/s-ft^2 (kg/s-m^2)*

L_{hx} – length of heat exchanger, *ft (m)*

L_b – distance between baffles, *ft (m)*

N_a – anode molar flow, *mol/s*

N_c – cathode molar flow, *mol/s*

N_{ox} – oxidizer molar flow, *mol/s*

N_b – number of baffles

N_c – number of tube rows crossed during one cross flow

N_{cw} – number of tube rows crossed in each baffle window

N_t – number of tubes

NFC – total number of cold flow channels

NS – number of heat exchanger sections – 1 section is equivalent to one tube bundle pass

NTU – number of transfer units

Nu – Nusselt number

P – wetted perimeter, *in (mm)*

$P_{c,in}$ – inside wetted perimeter of cold flow geometry, *in (mm)*

$P_{c,out}$ – outside wetted perimeter of cold flow geometry, *in (mm)*

P_{hot} – inside wetted perimeter of hot flow geometry, *in (mm)*

ΔP – pressure drop on hot or cold side of recuperator, *psia (kPa)*

ΔP_{bi} – pressure drop of an ideal tube bank in one baffle compartment of the central baffle spacing, *psia (kPa)*

ΔP_c – pressure drop in the entire interior cross-flow section, *psia (kPa)*

ΔP_e – combined pressure drop for entrance and exit sections, *psia (kPa)*

ΔP_s – pressure drop on shell-side, *psia (kPa)*

ΔP_t – pressure drop on tube-side, *psia (kPa)*

ΔP_w – pressure drop for entire window in the arrangement, *psia (kPa)*

ΔP_{wi} – pressure drop of an ideal tube bank in one baffle window section, *psia (kPa)*

Pr – Prandtl number

$\dot{Q}$ – heat transfer rate, *Btu/hr (W)*

$\dot{Q}_{\max}$ – maximum possible heat transfer rate, *Btu/hr (W)*

Re – Reynolds number

R_{fi} – fouling resistance of air, *hr-ft^2-R/Btu (m^2-K/W)*

R_{fo} – fouling resistance of natural gas flue gas or oxidizer exhaust, *hr-ft^2-R/Btu (m^2-K/W)*

R_b – correlation factor for baffle bypass flow

R_l – correlation factor for baffle leakage effects

R_s – correlation factor for entrance and exit sections

R_w – material wall resistance, *hr-ft^2-R/Btu (m^2-K/W)*

$T_{c,avg}$ – average temperature of cold flow, *R (K)*

T_{ci} – temperature of cold flow into, *R (K)*

T_{co} – temperature of cold flow out of, *R (K)*

$T_{h,avg}$ – average temperature of hot flow, *R (K)*

T_{hi} – temperature of hot flow into, *R (K)*

T_{ho} – temperature of hot flow out of, *R (K)*

$\dot{U}$ – internal energy stored in a control volume, *Btu/hr (W)*

U_o – overall heat transfer coefficient, *Btu/hr-ft^2-R (W/m^2-K)*

$\forall$ – volume, *ft^3 (m^3)*

X_a – anode mass fractions

X_c – cathode mass fractions

X_{ox} – oxidizer mass fractions

b – base of cell geometry, *in (mm)*

ff – Darcy friction factor

h – height of cell geometry, *in (mm)*

h_i – convective heat transfer coefficient of inner fluid, *Btu/hr-ft^2-R (W/m^2-K)*

h_o – convective heat transfer coefficient of outer fluid, *Btu/hr-ft^2-R (W/m^2-K)*

k – thermal conductivity, *Btu/hr-ft-R (W/m-K)*

m – mass of the fluid, *lbm (kg)*

$\dot{m}_s$ – mass flow rate of fluid on shell-side, *lbm/s (kg/s)*

$\dot{m}_t$ – mass flow rate of fluid on tube-side, *lbm/s (kg/s)*

t_{ss} – thickness of Type 347 stainless steel, *in (mm)*

t_b – baffle thickness, *ft (m)*

u_m – mean velocity of the fluid, *ft/s (m/s)*

Molten Carbonate Fuel Cell (SI Units Only)

E_o – standard potential, *(V)*

F – Faraday's constant, *(C/mol)*

I – cell current density, *(A/cm^2)*

$M_{ox}C_{pox}$ – oxidizer solid mass-specific heat product, *(J/K)*

M_sC_{ps} – stack solid mass-specific heat product, *(J/K)*

N_i – total molar flow of gas species *i*, *(mol/s)*

P_{dc} – stack DC power, *(W)*

R – Universal gas constant, *(J/mol-K)*

R_i – total production rate of species *i (from all reactions)*, *(mol/s)*

T_s – fuel cell stack solid average temperature, *(K)*

$\forall$ – compartment volume, *(m^3)*

V_{cell} – cell voltage, *(V)*

V_o – equilibrium potential, *(V)*

h_i – partial molar enthalpies of species *i, (J/mol)*

n_i – number of moles of species *i*

x_i – mol fraction of species *i*

z – cell ohmic impedance, *(Ω-cm)*

Superscript

air – air flow into oxidizer

gas – anode off-gas into oxidizer

in – flow in

out – flow out

s - stack

Subscript

a – anode

c – cathode

ox – oxidizer, oxidizer exhaust

tot – total

Greek

α – absolute flow angle, ° *(degrees)*

β_h – relative flow angle at inducer hub, ° *(degrees)*

β_t – relative flow angle at inducer tip, ° *(degrees)*

γ – compressor specific heat ratio

δ – normalized pressure

ε – heat exchanger effectiveness

ε_{avg} – heat exchanger effectiveness averaged over operating design line

η – isentropic efficiency

η_{act} – activation polarization, *(V)*

η_{conc} – concentration polarization, *(V)*

η_{th} – thermal efficiency

θ – normalized temperature

κ – turbine specific heat ratio

μ – viscosity, *lbm/ft-hr (kg/m-s)*

$1/\pi$ – expansion ratio

π – total pressure ratio

σ – slip factor

τ – total temperature ratio

τ_C – compressor torque, *ft-lbf (N-m)*

τ_T – turbine torque, *ft-lbf (N-m)*

τ_{LOAD} – load applied to shaft, *ft-lbf (N-m)*

τ_{LOSS} – bearing loss, *ft-lbf (N-m)*

φ – equivalence ratio

ω – angular velocity, *(rad/s)*

ξ – total number of gas species

CHAPTER 1: INTRODUCTION

The introduction of distributed generation for electrical power is the result of changing market forces, energy security issues and advancement in energy technology. A few of the driving forces behind distributed generation are the ever increasing need for reliable digital systems with quality power, the overburdening of the transmission and distribution grid of the nation, and energy security with efficient and productive use of domestic resources. Environmental concerns also play a big role in distributed generation. Near zero emissions and ultra-high efficiency help to compel today's electric production market towards distributed generation.

Distributed generation (DG) is the use of small electric power generators whether located on the utility system, at the site of the utility costumer or at an isolated site not connected to the power grid. The application of these DG systems is to provide lower voltage when needed to the distribution parts of an electric utility grid. Most types of distributed generators use the traditional power generation systems, i.e., diesel, combustion turbine, combined cycle turbine, or other various types of turbomachinery. These traditional systems give on average between 20 to 30 percent plant efficiency. This efficiency is determined by the amount of energy in the fuel that is converted to useful electric power. The plant efficiency can be increased by 50 percent for small hybrid systems suitable for distributed generation [1].

The use of small power plants in the distribution network allows for the relief of congested distribution networks and avoids transmission losses and costs. A need for small power generation is seen in remote areas and areas where emergency and uninterrupted power is critical. The most economical solution available is to generate power through small gas turbine systems, categorized as microturbines (3-200 kW) and miniturbines (200-500 kW) [26]. Microturbines enable small energy consumers to generate their own electricity from a secured power supply even at peak load periods.

Microturbines have been design to meet the energy requirements ranging from 25-75 kW of office buildings, restaurants, hospitals and apartments. Cogeneration systems (i.e., combined heat and power) for a single household would require the microturbine to give 3 kW of power output [27]. Microturbines must compete directly with reciprocating engines and the continuous improvements of small diesel engines. Nonetheless, microturbines have over-ruling benefits in terms of low emissions, multi-fuel capability, compact size, and low maintenance cost. Gaining a low unit price cost of the gas turbine unit together with low emissions should be of highest priorities for gas turbine manufactures [28, 29].

Hybrid fuel cell designs under development and consideration include a high temperature fuel cell with a gas turbine generator, a fuel cell with a reciprocating or more commonly referred to piston engine, and designs that incorporate different fuel cell technologies. Fuel cell hybrid systems that incorporate gas turbine technology that can generate power on the scale of 10 kW to 50 MW are envisioned to participate in the new market for distributed generation [3]. Figure 1.1 represents the hybrid power generation system that will be modified and is the focus of this paper.

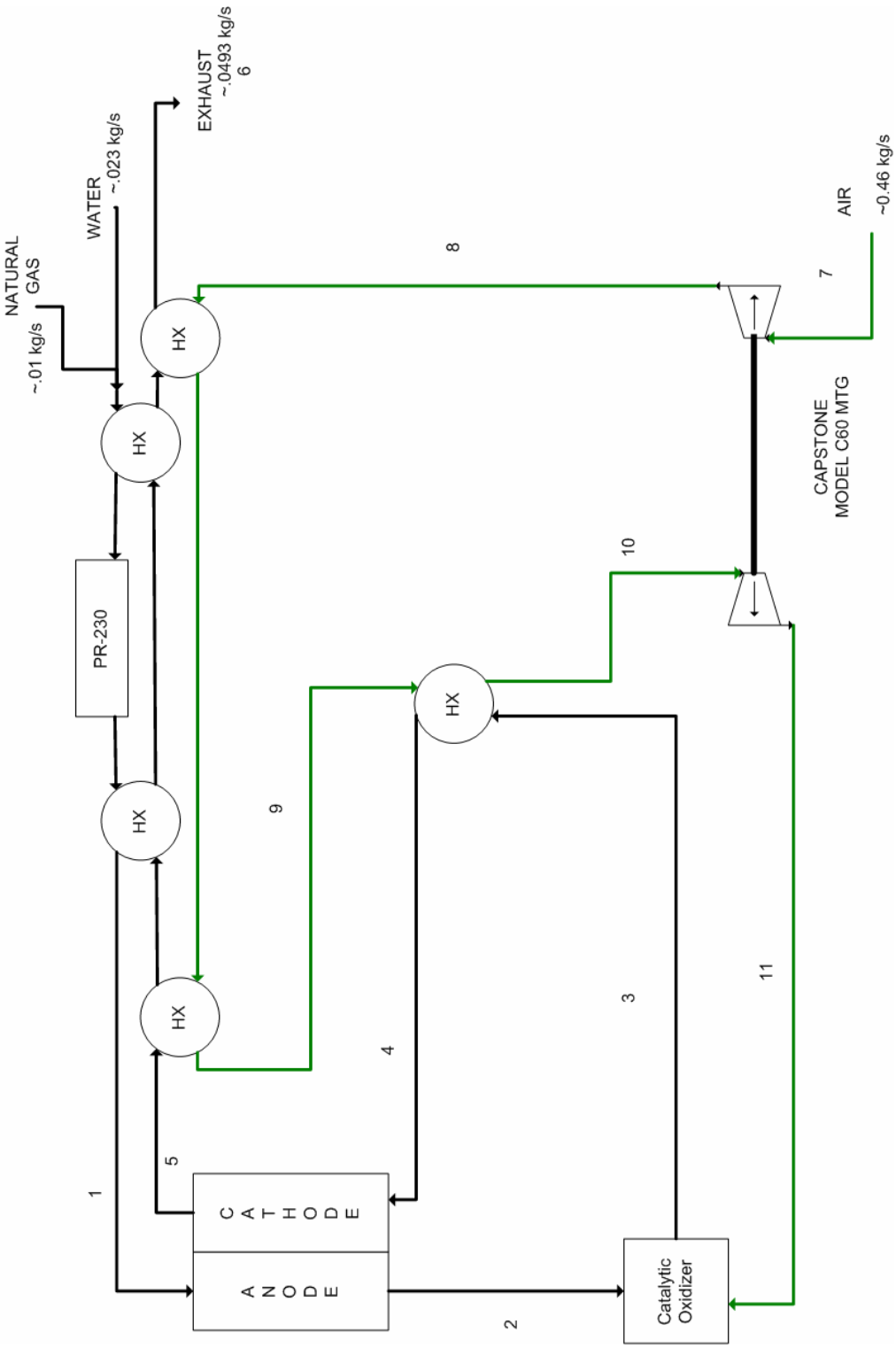

Figure 1.1: Fuel Cell/Microturbine Generator Hybrid for Distributed Generation

CHAPTER 2: LITERATURE REVIEW

2.1 Background and Existing Modeling Efforts

Fuel cells are classified primarily by the type of electrolyte they have. The type of electrolyte determines the chemical reactions that take place in the cell, the catalysts required, the temperature range in which the cell operates, and the fuel required. These characteristics affect the applications for which the fuel cells are most suitable. There are several types of fuel cells currently under development, each with its own advantages, limitations and potential applications [4]. This chapter will describe three different types of fuel cells and fuel cell hybrid systems; the proton exchange membrane (PEM) fuel cell, the molten carbonate fuel cell (MCFC), and the solid oxide fuel cell (SOFC). The emphasis will be placed on hybridization of the MCFC and SOFC, since these two are more apt to be modeled with a heat engine, such as a microturbine generator (MTG).

The background and modeling of a microturbine generator as it is applied to a hybrid system will be described in the hybrid power generation section, Section 2.2, and the MTG will be described in Section 2.3 as a stand alone power generation system. Since recuperation plays such a large role in the efficiency of a MTG, this chapter has a section dedicated explicitly to the background and design of a primary surface recuperator.

2.2 Hybrid Power Generation Systems

Hybrid fuel cell designs under development and consideration include a high temperature fuel cell with a gas turbine generator, a fuel cell with a reciprocating or more commonly referred to as a piston engine, and designs that incorporate different fuel cell technologies. It is very important to properly match and integrate the fuel cell with the gas turbine portions of the cycle. A complete shut down of the turbine can be damaging to the fuel cell and other system components [5]. Hybrid systems have proven to generate high efficiency with essential low levels of pollutant emissions at greater fuel energy savings than non-hybrid systems. Fuel cell hybrid systems that incorporate gas turbine technology in the form of microturbines that generate power on the scale of 10 kW to 50 MW are envisioned to participate in the new market for distributed generation [3, 6, 7, 8].

The National Fuel Cell Research Center (NFCRC) was established in 1998 to accelerate the evolution of fuel cells and fuel cell systems. The Center assists the market in understanding this unique power system and the opportunities for both central and distributed power generation. With the ability for high fuel-to-electrical efficiency, hybrid systems pose a shift for the future of power generation for a variety of applications. The fuel cells most attractive for hybridization are the Molten Carbonate Fuel Cell (MCFC) and the Solid Oxide Fuel Cell (SOFC) due to the high operating and discharge temperatures. Hybrid power systems that combine a gas turbine with the high temperature fuel cell (HTFC) has been extensively analyzed by U.S. Department of Energy, industry such as Fuel Cell Energy, Inc., National Energy Technology Laboratory (NETL), and the NFCRC over the last 5 years. As of 2004, Fuel Cell Energy, Inc. in

Danbury, CT has been operating a 250kW MCFC/MTG sub-MW hybrid system in cooperation with Capstone Turbine Corporation for over 4,500 hours in successful duration [7, 9, 10].

A fuel cell generates electricity directly through electrochemical reactions. Generating electricity in this matter is more efficient than a heat engine (gas turbine) because losses due to mechanical or rotating machinery are not an issue. The most efficient heat engine cycle allowed by physical laws is the Carnot cycle. When the second law of thermodynamics states that not all the supplied heat in a heat engine can be used to do work, the Carnot efficiency sets the limiting value on the fraction of the heat which can be used. A fuel cell is not limited to the Carnot efficiency constraints so the fuel cell will most likely be the core of a high-efficiency hybrid power cycle [7]. A fuel cell derives its power from the heat of electrochemical reactions occurring within. Therefore, the limit of efficiency for direct energy conversion is the ratio of available Gibb's free energy to the total heat of electrochemical reaction. The fuel cell model is developed on the basis of thermodynamics of the applicable reforming and electrochemical reactions and the associate reaction kinetics [8].

Fuel cells operate at high efficiencies regardless of size and load. The high temperature waste heat can be transformed into electricity. The gas turbine in the hybrid system can be arranged in such a way that the thermal energy from the waste heat can be extracted to drive the compressor which in turn supplies the pressurized air to the fuel cell. Any additional enthalpy is expanded through the turbine and additional electricity is produced by a shaft connected to a generator. In this manner, efficiencies can reach upwards of 80 percent of the lower heating value (*LHV*) of the fuel used by the fuel cell,

natural gas. With the extremely low NO_x admissions from the fuel cell, the hybrid system will also be very environmentally aware [7, 9, 11].

2.2.1 Proton Exchange Membrane (PEM) Fuel Cell Hybrid Power Generation

Proton exchange membrane (PEM) fuel cells deliver high power density and offer the advantages of low weight and volume. PEM fuel cells use a solid polymer as an electrolyte and porous carbon electrodes containing a platinum catalyst. These fuel cells need only hydrogen, the oxygen from air, and water to operate and do not require any corrosive fluids. Typically, they are fueled by pure hydrogen from storage tanks or onboard reformers. The chemical reactions can be seen in Figure 2.1.

PEM fuel cells operate at very low temperatures (when compared to MCFC or SOFC), around 353°K (635°R). Low temperature operation allows for quick start up and results in less wear on system components giving better durability. Requiring a noble metal catalyst (platinum) to separate the hydrogen's electrons and protons adds to the cost of the fuel cell. The platinum catalyst is exceptionally sensitive to carbon monoxide (CO) poisoning. This increases cost by requiring an additional reactor to reduce CO in the fuel if the hydrogen is derived from an alcohol or hydrocarbon fuel (CH_4). PEM fuel cells are primarily for transportation application and some stationary applications. A significant barrier to using these fuel cells in vehicles is hydrogen storage [4].

Auxiliary power units (APUs) on military and commercial aircraft may be replaced by a fuel cell system. Barchewitz et al [12] modeled a fuel cell system comprised of a compressor-turbine unit, a kerosene reformer, and a proton exchange

membrane fuel cell PEM-FC. With the increase in electric power demand a move toward more electric or all electric aircraft is feasible.

Hussain et al [13] claim that PEM fuel cells have the potential to replace conventional internal combustion engines in transportation applications. A thermodynamic analysis of a PEM fuel cell power system for a light-duty fuel cell vehicle was done using the exergy method of analyzing energy systems. The exergy method integrates the first and second law of thermodynamics and reference environmental conditions. Exergy is defined as the maximum amount of work which can be obtained from a system or a flow of matter when it is brought reversibly to equilibrium with the reference environment.

Jagaduri et al [14] developed a MATLAB/Simulink® model to simulate a combined hybrid PEM fuel cell microturbine distributed generation plant. The purpose of the modeling was to address a grid connected fuel cell where the fuel cell controls the voltage magnitude and the reactive power compensation. The bulk of the load following is provided by the microturbine. The transient behavior of the distributed generation model reacted to the expectations of the authors.

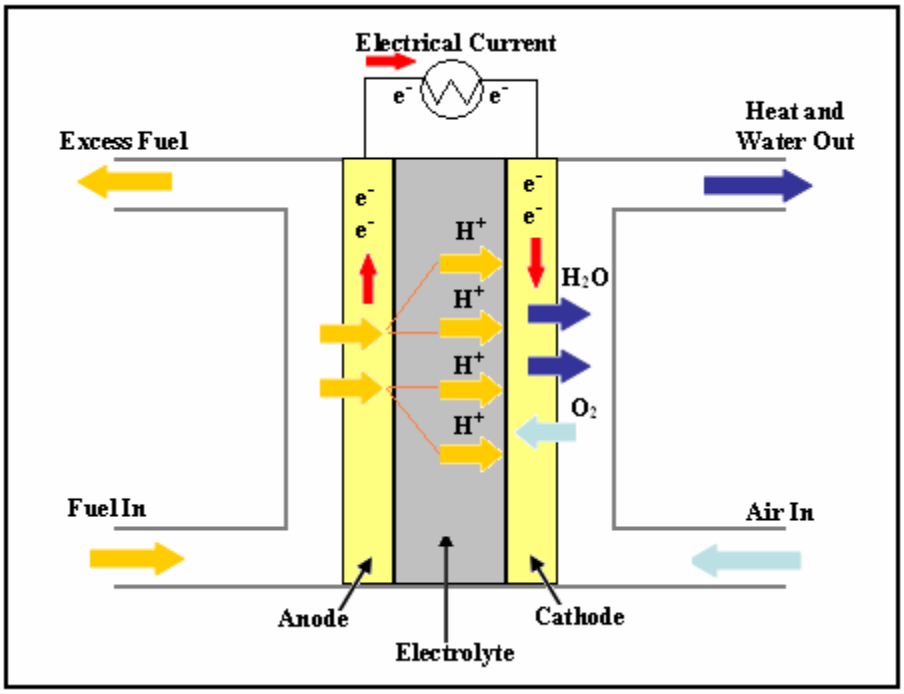

Figure 2.1: Proton Exchange Membrane (PEM) Fuel Cell Reactions

2.2.2. Molten Carbonate Fuel Cell (MCFC) Hybrid Power Generation

Molten carbonate fuel cells (MCFC) are currently being developed for natural gas (CH_4) and coal based power plants. The power plants include electrical utility, industrial, and military applications. The MCFC, seen in Figure 2.2, is a high temperature fuel cell that uses an electrolyte composed of a molten carbonate salt mixture suspended in porous chemically inert ceramic lithium aluminum oxide ($LiAlO_2$) matrix. Since these fuel cells operate at very high temperatures, roughly 923°K (1661°R), non-precious metals can be used for the catalysts at the anode and cathode, thus cost of the fuel cell is reduced.

Molten carbonate fuel cells can reach efficiencies approaching 60 percent [15], and when the waste heat is captured and reused, overall fuel efficiencies can reach as high as 85 percent. An external reformer, used to convert more energy dense fuels to hydrogen, is not required for a MCFC. With the high operating temperatures, fuels are converted to hydrogen within the fuel cell itself, this process is known as internal reforming. The carbon monoxide poisoning mentioned in Section 2.2.1, does not affect the MCFC. Carbon oxides (CO and CO_2) can be used as fuel for the MCFC. The primary disadvantage of current MCFC technology is durability. The high temperatures and corrosive electrolyte accelerate component breakdown and corrosion, this decreases cell life [4].

A Direct FuelCell/Turbine® (DFC/T®) power plant for generation of clean power at very high efficiency has been developed by FuelCell Energy, Inc. The DFC/T® is an internally reformed molten carbonate fuel cell. The system is based on an indirectly heated gas turbine to supplement fuel cell generated power. The DFC/T® concept extends the high efficiency of the fuel cell by utilizing the fuel cell's byproduct heat in a

Brayton cycle. A 250kW fuel cell stack is integrated with the Capstone C60 (60kW) MTG. Tests were conducted with the power plant connected to the utility grid and providing real time grid connected operational experience. A power plant flowsheet and model were prepared using Chemcad simulation software by Ghezel-Ayagh et al [9, 10 16]. The dynamic modeling was done in MATLAB/Simulink®, with the primary focus on the fuel cell. The model of the fuel cell stack is based on a lumped-parameter assumption, for each the anode and cathode, with interchange of mass (ions) through the electrolyte matrix separating the two sides. The direct fuel cell stack model is completed by supplementing the process states with a model for average fuel cell voltage, determined from the Nernst equation.

The dynamic simulation capabilities developed at National Fuel Cell Research Center (NFCRC) and National Energy Technology Laboratory (NETL) are useful for determining design requirements, analyzing dynamic response, and developing control strategies for MCFC/MTG hybrid systems. The NETL model used C++ in combination with ProTRAX software package. NFCRC used MATLAB/Simlink® software package. Identical assumptions were made to formulate the governing equations for the fuel cell models; includes discretized solution of the Nernst equation, all major electrochemical losses (polarizations), mass conservation, energy conservation and heat transfer processes. Slightly different compressor and turbine performance maps were used. The MCFC models are constructed to simulate the fundamental operation of a MCFC similar to that currently manufactured by FuelCell Energy, Inc. The hybrid models described in [5] by Roberts et al, have similar features and the configuration of FuelCell Energy, Inc. DFC/T® sub-MW system.

There are two distinct features that make SOFC and MCFC differ from one another when it comes to positioning and integrating them in the gas turbine based system. The first is the operating temperature – 1073-1273°K (1931-2291°R) for the SOFC and 873-923°K (1571-1661°R) for the MCFC. The other is the requirement of carbon dioxide (CO_2). CO_2 in the anode stream adversely affects the performance of a SOFC; but it is a requirement for the MCFC. A SOFC is almost constantly placed upstream of the microturbine while the MCFC is integrated downstream of the microturbine. For a system with the combustion chamber still present is the microturbine model, the MCFC is integrated such that the exhaust gas from the microturbine is used to feed the MCFC along with the anode exhaust [8].

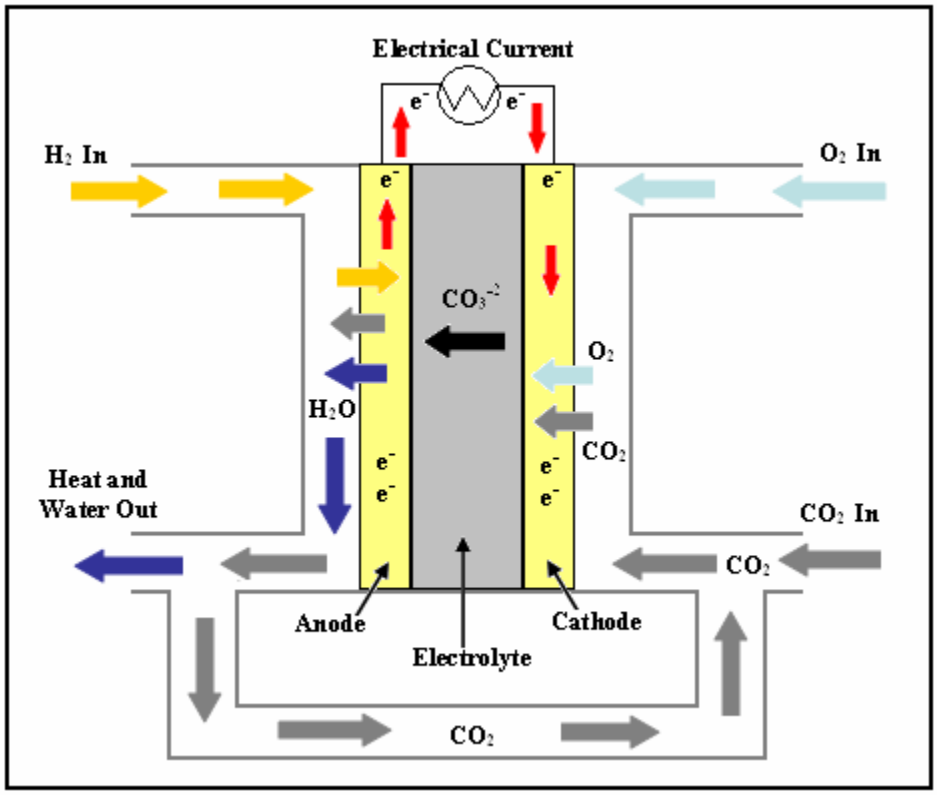

Figure 2.2: Molten Carbonate Fuel Cell (MCFC) Reactions

2.2.3 Solid Oxide Fuel Cell (SOFC) Hybrid Power Generation

Solid oxide fuel cells (SOFC), seen in Figure 2.3, use a hard, non-porous ceramic compound as the electrolyte. Since the electrolyte is a solid, construction of the SOFC does not have to be in the plate-like configuration typical of other fuel cell types. It is expected that SOFC efficiency at converting fuel to electricity is between 50-60 percent. In co-generation or combined heat and power (CHP) applications where the waste heat is captured and utilized, the overall system fuel use efficiencies can reach 80-85 percent. The solid oxide fuel cell operates at extremely high temperatures, 1273°K (2290°R). The high operating temperature removes the need for precious-metal catalysts, thus reducing the cost of the fuel cell. Internal reforming is also seen with the SOFC, enabling a variety of fuels to be used and reducing the cost of having to add a reformer to the system. The SOFC is the most sulfur-resistant type of fuel cell and it does not suffer from carbon monoxide poisoning. This allows the SOFC to use fuel made from coal.

High temperature operation has disadvantages in the form of slow startup and the requirement of significant thermal shielding to retain heat and protect personnel. The high temperatures of the SOFC may be acceptable for utility purposes, but not for transportation and small portable applications. Durability of materials is also of high concern. The development of low-cost materials with high durability at SOFC operating temperatures is the key technical challenge facing this technology [4].

As of 2004, the first hybrid demonstration of a pressurized SOFC/MTG is being conducted at the NFCRC. The initiative lead by Southern California Edison is a 220kW unit that used a Siemens Westinghouse SOFC and an Ingersoll-Rand Energy Systems MTG. This system has over 2,000 hours of operation and attained the world record in

fuel-to-electricity conversion efficiency. The unit is natural gas fired and controlled through two dissipaters. AC is used for the turbine output and DC for the fuel cell output [7].

Modeling and simulation is performed at the Pacific Northwest National Laboratory (PNNL) located in Richland, Washington on SOFC cells, stacks, and systems as means for stationary power systems (distributed generation and centralized power plants), automotive power systems, and military power systems. Modeling activity includes thermal-fluid modeling tools (CFD based) and thermodynamic and electrochemistry analysis using MATLAB/Simulink® [17].

Auxiliary power units (APUs) are devices that can provide all or part of the non-propulsion power of a vehicle. The SOFC technology is most favorable due to characteristics such as the ability to use a variety of hydrocarbon fuels with a simpler reforming process and no need for any water management system. The SOFC is predicted to be the first fuel cell to penetrate the transportation industry, for heavy-duty trucks and luxury vehicles. The SOFC APU would replace the need for drivers to idle their engines to produce power for climate-control devices, and sleeper compartment accessories. Baratto et al [18] has simulated the entire fuel cell system in ASPEN PLUS™ simulation software and the results where compared to experimental data whenever available and other models published in the literature showing good agreement.

SOFC-MTG hybrid power plants are a very attractive near term option, achieving efficiencies of over 60% with small power outputs (200-400kW). Since the operating temperature of a SOFC stack is similar to the turbine inlet temperatures of the latest

generation microturbine generator around 1170°K (2106°R), the combustion chamber can be replaced by the SOFC stack.

The SOFC-MTG power plant performance was evaluated by means of the ASPEN PLUS™ simulation software by Cocco et al [19]. The ASPEN model library, consisting of many standard components used by energy conversion systems, has been integrated with a dedicated fuel cell model. The model simulates fuel cell performance by solving mass and energy balances for given values of the main operating parameters. The results of using ASPEN PLUS™ simulation software demonstrate that methanol is a viable fuel for SOFC hybrid plants especially when reformed externally.

Costamagna et al [20] modeled the design and off-design performance of a SOFC-MTG hybrid. The SOFC clean effluent replaced the combustor in this model and was written in the MATLAB® language. This model demonstrated the feasibility of achieving efficiency of 60 percent at design point and always over 50 percent at part load conditions.

A SOFC system was modeled dynamically to provide data for the specification of equipment and control philosophy of an experimental test facility. The balance of plant (BOP) of a SOFC carries out a number of service functions for the fuel cell stack. The BOP alters the fuel and air supply to the fuel cell stack in response to changes in the electrical load while maintaining the inlet and outlet temperature constraints of the system, nominally set to 1123°K (2020°R) and 1323°K (2380°R), respectfully. The dynamic modeling for this system was done by Dicks et al [21] and an in-house code was used. The in-house code usage and modeling provided data for specification of equipment and control philosophy for and experimental test facility.

Successful commercial application of SOFC technologies will require selection of appropriate operating conditions. By varying operating conditions, a wide range of power and efficiency may be derived from a SOFC system. Based on isothermal closed form parametric performance modeling, natural gas performance maps were created. The functional form of the model and the boundaries of the operating envelope provide useful insight into SOFC operating characteristics and simple means of selecting conditions for natural gas operation. The operating temperature of the SOFC system was not considered an independent variable by Hartvigsen et al [22]. It is assumed that to minimize resistance, the stack is operated at the highest temperature consistent with stack life and system balance of plant constraints.

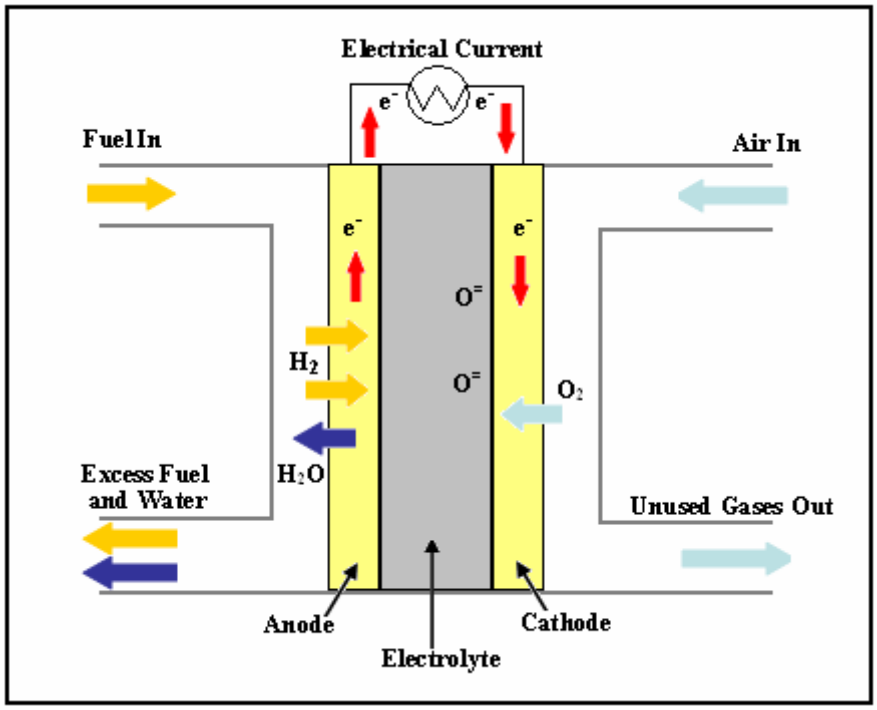

Figure 2.3: Solid Oxide Fuel Cell (SOFC) Reactions

2.3 Microturbine Generator (MTG) Stand Alone Power Generation

The microturbine generator has a single-stage centrifugal compressor, low emission annular combustor that operates on natural gas, single-stage radial inflow turbine, a recuperator used to pre-heat the air into the combustor for increased efficiency thus resulting in the air returning to the surroundings to experience additional cooling, and a single shaft design running on a thin film of pressurized air inside the bearings. These very small, high-speed, gas turbine engines are of radial design and can be compared more easily to low-cost turbochargers than to the more complex axial designs seen in larger industrial gas turbines or aircraft gas turbine engines. The MTG operates at a more conservative temperature eradicating the need for high-cost materials. This elimination of the need for high-cost materials coupled with simplicity of microturbine generator design leads to low costs for production and the desire to do so in volume [6].

Distributed generation in the form of microturbine generators offers an attractive strategy for meeting future demands for reliable, cost effective electrical energy. However, the widespread commercialization of the microturbine generator may be limited due to recently adopted regulations that require the emissions of criteria pollutants such as nitrogen oxides (NO_x) and carbon monoxide (CO) to be on par with advanced central power station's emissions. Capstone® Model C60 microturbine generator is one of the most widely used commercial microturbines [23].

FuelCell Energy, Inc. has created mathematical models and computer simulations of the Capstone® Model 330 (30kW) MTG in 2003 and Model C60 (60kW) MTG by 2005. The Capstone® Model 330 has a rated power of 30kW and *LHV* efficiency of 14%±2% at ISO Conditions operating on natural gas. In [16], Ghezel-Ayagh et al

performed the computer simulation on the MTG section of the DFC/T® hybrid using ChemCad process simulation software.

For modeling of the Capstone® Model C60, Ghezel-Ayagh et al [9] used 0-Dimensional correlations on the manufacturer's performance curves of the microturbine to determine any unknown parameters. The compressor and turbine exhaust temperature was correlated to the inlet temperature, pressure ratio, and efficiency. The compressor and turbine are mechanically linked via a common shaft and thermodynamic cycle analysis is compared to known manufacturer performance.

Kim et al [24] transiently modeled a single spool turbojet engine using MATLAB/Simulink® and compared the model to an existing transient FORTRAN code. The Simulink model is of modular construction to represent the components, i.e. compressor, turbine, combustor, etc. with the controls being fuel flow, altitude and Mach number. The compressor performance map is represented by a 2-D array in a look-up table. This has been modified from the existing FORTRAN code for improved transient behavior. The inputs for the look-up table are the R- or β-line, and corrected engine speed. The tables give corrected mass flow rate, efficiency, and pressure ratio. Typical isentropic equations give compressor power, exit pressure and temperature. The objective of this paper was to check fuel flow control for fuel cut-off and starting fuel schedule. The comparison between the two models was inconclusive since the FORTRAN model had a limited initial rotation speed range.

Al-Hamdan et al [25] also created a transient model in MATLAB/Simulink®. Component matching was done by the way of superimposing the turbine performance map on the compressor map while meeting the component matching conditions of

compressor and turbine shaft speed, continuity and energy balances. The performance maps were also placed into 2-D arrays represented as look-up tables with the same input and table values seen in [24]. The model was created to satisfy the matching conditions analytically between the various gas turbine components to produce an equilibrium running line and to verify that the engine is operating in a region of adequate compressor and turbine efficiency.

2.3.1 MTG Primary Surface Recuperator Modeling

Compact heat exchangers are commonly used in the automotive, aerospace, gas turbine, and cryogenics industries as well as in power generation, air conditioning, refrigeration, process industries and some heat recovery and process applications. More recently newer applications of compact heat exchangers have been used in fuel cell and microturbine systems. The compact heat exchanger is most common of the primary surface type. The thermal efficiency for microturbines is about 20 percent without a recuperator and to achieve thermal and electrical efficiency of 30 percent (a 50 percent increase), exhaust heat recovery with a recuperator is mandatory. To achieve thermal efficiency of 30 percent, the recuperator effectiveness must be 85 percent or higher. Effectiveness values of 90 percent and higher are usually considered for today's standards [26, 28, 29, 30].

There is the desire to increase the overall thermal efficiency of the microturbine cycle and this can be accomplished by integrating a heat exchanger in to the overall power generation system. There are two common locations for the primary surface recuperators used in conjuncture with microturbines; the recuperator can either be an

annular wrap-around recuperator that is around the microturbine's rotating machinery, Figure 2.4, or the recuperator is installed behind, above or alongside the microturbine's rotating machinery giving the option for the recuperator to be bypassed. With the annular wrap-around recuperator, the recuperator is closely coupled with the microturbine; this is common with Capstone® microturbines [31, 2]. The advantages of an annular wrap-around recuperator are quality aerodynamic gas flow paths that result in low or non-existent pressure loses, a lower acoustic signature, built in rotor burst shield, and the elimination of the need for external duct work and thermal expansion devises [31]. The core of the heat exchanger is modeled as a primary surface recuperator (PSR) with a gas-to-gas counter-flow arrangement where the hot turbine exhaust gas passes by the cooler compressed air leaving the compressor. The cooler stream recovers (recuperates) heat from the hotter stream. This recovery is done in an indirect method since the contact between the hot and cold fluids is done via a heat transfer surface such as a wall or plate [32].

The requirements for a gas-to-gas recuperator are compact size and weight (small hydraulic diameter), high effectiveness ($\varepsilon \geq 85\%$), minimal pressure drops ($\Delta P < 5\%$), and high reliability with low maintenance cost and long operational life [26, 28, 29, 30, 33, 34]. Additional factors are a primary surface characterized by a single sheet between two fluids, minimal number of moving parts, near 100 percent utilization of the material, welded construction to maintain leak-tight seal on the side edges, an automated, high-volume manufacturing process, a core fabricated in an annular or box type construction, and ease of installation, removal, and replacement of the core [26, 34].

To achieve the requirement of compact size and weight, there are no secondary surface fin efficiency effects. Secondary fins may add weight and cost to the recuperator core without any visible increase in overall heat exchanger effectiveness. The core is made of a very thin (0.1mm) material that assists in keeping the core volume and weight to a minimum. High effectiveness is essential, but to further increase the effectiveness would require dramatic growth of the heat transfer surface, and this would lead to forced growth of the recuperator core [33]. Growth in the recuperator core increases the cost of the recuperator. Efforts are being made to design of compact and low cost heat exchangers, able to minimize pressure drops and maximize effectiveness [30]. To minimize the cost of the recuperator core without any loss to performance, the primary surface heat exchanger without brazing, i.e., soldering using high temperature alloys to join high temperature metals is desired.

The PSR core is created from Type 347 stainless steel; this material is used because it meets requirements for low cost, excellent oxidation resistance needed due to the presence of water from the combustion process in the exhaust gas, and relatively high heat tolerances. The temperature limit for primary surface recuperator core created from Type 347 stainless steel is 750ºC (1845°R) with typical operating temperatures at or below 650 ºC (1661°R) [33]. The maximum use temperature of the steel is 816ºC (1963.8°R) [35].

High turbine inlet temperature and high effectiveness of the recuperator are the two parameters that will allow for a possibility of microturbine efficiency increase. Both these parameters impact the recuperator design. With an increase in turbine inlet temperature, the recuperator hot exhaust gas inlet temperature will increase, causing a

necessity for high cost super alloys. Designing a surface area that is able to absorb the required amount of heat and also be able to handle the thermal shock due to temperature gradient is a major challenge especially given the size restrictions of a microturbine.

A primary surface design reduces heat exchange stress by maintaining a constant surface area. Traditional compact recuperators have one of the following four types of heat transfer surfaces: plate-fine type, cross-corrugated (CC), corrugated-undulated (CU) or cross-wavy (CW) [30]. A constant surface area is created by alternating layers of thin metal sheets, Type 347 stainless steel 0.1mm in thickness, fin folded into a corrugated pattern forming narrow passages and giving the required surface area. The Laboratory of Chemical Process and Plant Design in Thessaloniki, Greece have analyzed compact heat exchanger passages using low Reynolds number CFD methodology [36]. Sheet A and Sheet B in Figure 2.5 are welded together along the perimeter to form an air cell. This is pressure checked before each air cell is welded together with spacers along the perimeter to form the annular recuperator core. The sides are sealed to form the flow passages and spacer bars are inserted to assist with stability of the air cells. The PSR core used by Solar Turbines, Caterpiller and Capstone® contains 169 individual air cells [2, 26, 36, 37, 38, 39, 40].

The creation of the PSR is described by McDonald [41]. Fabrication of primary surface recuperator begins with a single part, a spool of thin foil, i.e., AISI 347 stainless steel. This stock is stamped and fin-folded in a to and fro manner to produce the matrix that is then externally welded to form an air-tight flow path. The compressed air and exhaust gas streams enter and leave from opposite sides of the core; this gives a counterflow arrangement in the core of the heat exchanger. The ends are welded shut and

the fluids flow through the top and the bottom of the matrix. The corrugated form extends the full length of the unit. Cross corrugation of the two foils over the full length allows for many primary surface contact points that support the structure and prevents surface nesting during operation. The formed herringbone corrugation or cross corrugation has a sine curve form to it and also provides the counter flow of the fluids. When the foil is stamped and folded it is then compressed and forced into an annular core. This annular design causes an involute structure. The fin folding and counter flow pattern can be seen in Figures 2.6 and 2.7 respectfully.

Sizing of a heat exchanger is dependent on the flow arrangement, the materials and the physical type of heat exchanger to meet requirements on the heat transfer rate and pressure drops. When flow, material and physical type are selected, the remaining problem is to determine physical size, i.e., length, width, height and surface areas on both the hot and cold flow sides of the heat exchanger. For microturbine applications, the cross sectional area of the flow channels, i.e. the hydraulic diameter must be small. A hydraulic diameter less than 1mm leads to very compact technology. Compactness or surface compactness is defined as the ratio of heat transfer surface area to enclosed volume (m^2/m^3 or ft^2/ft^3). A compact heat exchanger is defined by having a core with compactness of 700 m^2/m^3 (~213 ft^2/ft^3) or higher [32]. It is common to have hydraulic diameters ranging from 0.6-2mm with even larger values (5mm) for industrial applications [29, 33, 34].

The hydraulic diameter is a design variable that has the greatest impact on the recuperator core volume. A small hydraulic diameter gives a small volume, but too small will lead to fouling and shape distortion under mechanical and thermal stresses. The

length of the flow channels should be a low as possible. Values between 75 and 150 mm (approximately 3 to 4 inches) are practical for today's industry standards [30].

Reynolds numbers are very low through the air flow channels, roughly $400 < Re < 2000$. The hydraulic diameter is given by $D_h = 4A_x/P$ where A_x is the cross sectional area and P is the wetted perimeter. Depending on the Reynolds number, three flow regimes exist: laminar ($Re \leq 2300$), transitional ($2300 \leq Re \leq 10000$) or turbulent ($Re \geq 10000$). At low Reynolds numbers, wavy geometries provide little advantage over straight channels, but maximum advantage at transitional Reynolds numbers. For wavy ducts, the transition to turbulent occurs at $Re \approx 1200$.

A higher volume flow rate is seen on the exhaust (hot) side which leads to a higher pressure drop. This is balanced by having a larger hydraulic diameter which will decrease the velocity on the exhaust side. To reduce the volume of the recuperator core, allow for a larger total pressure drop over the heat transfer core or decrease the size of the core passages. The cross wavy (CW) and especially the cross-corrugated (CC) surfaces have shown superior performance over others given a small volume and weight. The CC surface, see Figure 2.8, is well documented in literature and easier to manufacture with the small passage dimensions that are essential to the small size and weight required for a primary surface recuperator [29].

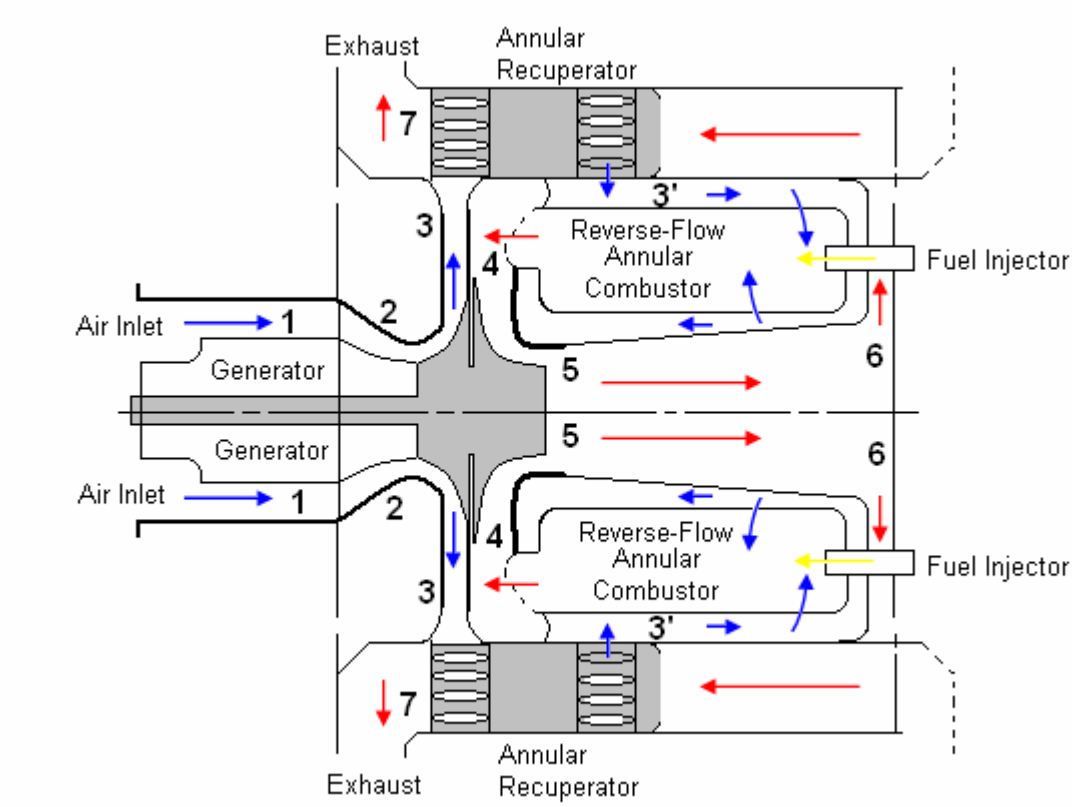

Figure 2.4: Schematic of Microturbine Generator

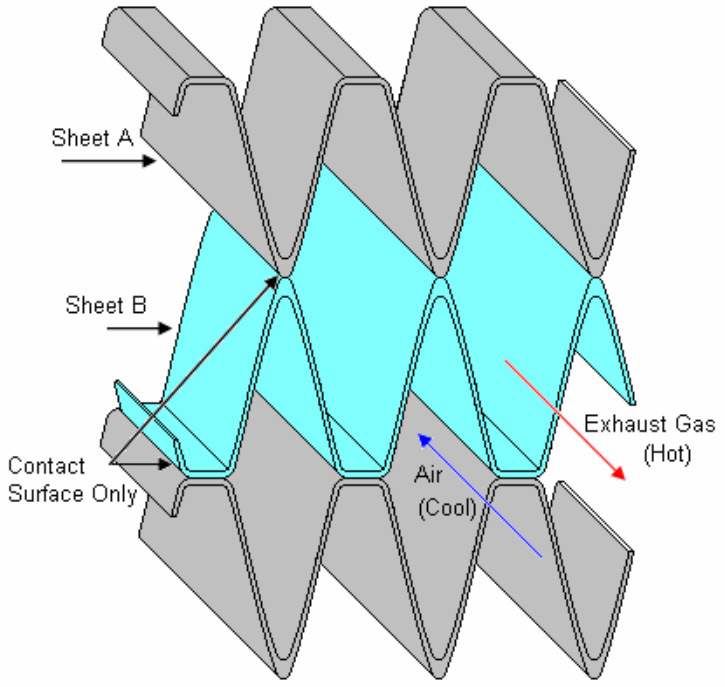

Figure 2.5: Typical Primary Surface Recuperator Air Cell Construction

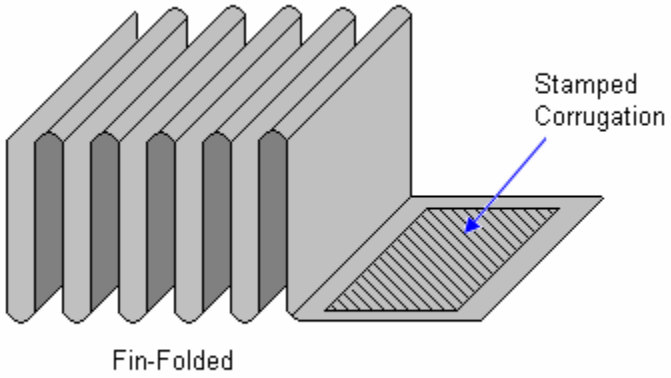

Figure 2.6: Stamped and Fin-Folded Type 347 Stainless Steel

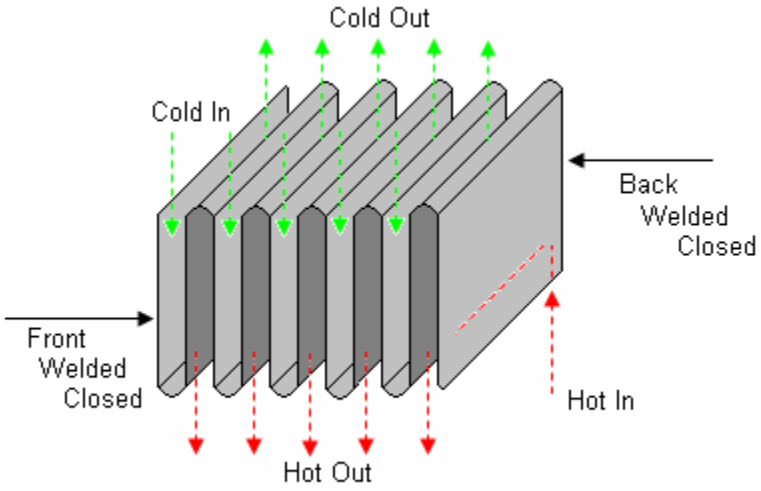

Figure 2.7: Flow Path for Counter Flow Air and Exhaust Gas

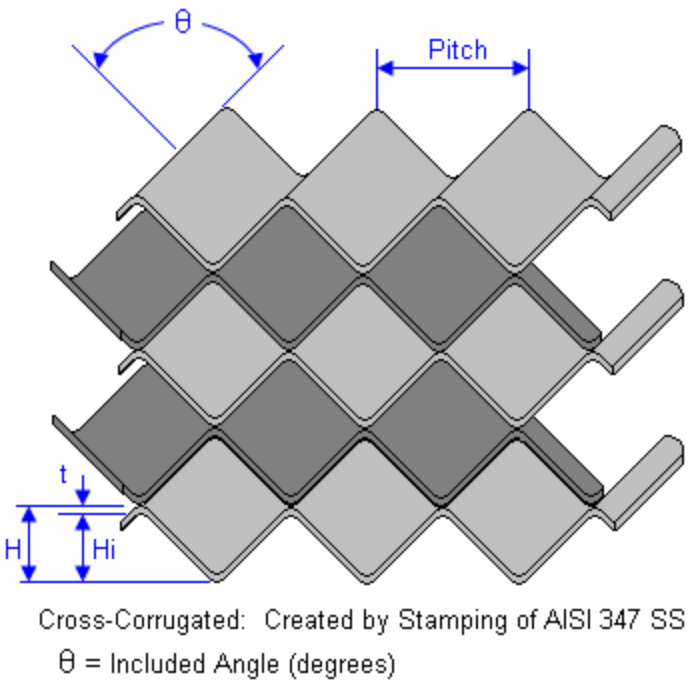

Figure 2.8: Cross-Corrugated Heat Transfer Surface

CHAPTER 3: MTG DESCRIPTION AND LOCATION DESIGNATIONS

This chapter focuses on the trends behind the locations and labeling of the microturbine generator in the 1-Dimensional stand alone model and the hybrid-microturbine generator in the 0-Dimensional hybrid and 1-Dimensional zooming hybrid generation models developed in the MATLAB/Simulink® environment. The sizing of the recuperator core is described in Section 3.5 of this chapter.

3.1 Brayton Cycle

Microturbine generators are still considered gas turbine engines and are designed based on the Brayton cycle. Figures 3.1a is an illustration of a simple gas turbine with air entering at Stage 2, natural gas as the fuel into the combustor, and the products from the combustion process leaving the turbine at Stage 5 at or near atmospheric pressure with an elevated temperature. Figure 3.1b is the Temperature-entropy or *T-s* diagram and Figure 3.1c is the Pressure-specific volume or *P-v* diagram for the simple gas turbine cycle (Brayton cycle) seen in Figure 3.1a. Compression is seen from Stage 2 – 3, combustion from Stage 3 – 4, and expansion from Stage 4 – 5. The dashed line seen from Stage 5 – 2 represents an open cycle. If the Brayton cycle was closed, then an element such as a heat exchanger would need to be present to complete the close cycle.

For the case involving the microturbine generator, it is desired to increase the efficiency of the cycle. This is done by adding regeneration in the form of a heat exchanger to the Brayton cycle. The heat exchanger used is called a recuperator; due to the cooler stream recovering (recuperating) heat from the hotter stream [32]. Figure 3.2a gives a representation of this cycle and Figure 3.2b portrays the *T-s* diagram of the Brayton cycle with regeneration. The turbine exhaust temperature is typically well above the ambient temperature of the surroundings that it is entering. With this elevated temperature, the exhaust has high potential for use that would normally be lost to the environment.

Adding the recuperator to the system allows for the high pressure air exiting the compressor to be preheated before entering the combustor. With the interaction of the two streams, energy is taken out of the hotter exhaust and placed into the compressed air entering the combustor. This allows for the amount of fuel entering the combustor to be decreased thus raising the efficiency of the system. The combustor then only has to work enough to raise the temperature of the system from Stage 3 to 3', rather then from Stage 3 to 4. Since there is less heat added to the cycle without the net work being affected by the addition of the recuperator, the overall thermal efficiency of the gas turbine cycle increases.

Analysis of the simple gas turbine cycle as an air-standard Brayton cycle would see air as the working fluid throughout the entire system and the temperature increase due to the combustion process would be replaced with a heat exchanger or other element bringing in heat from an outside source to be added to the working fluid. The hybrid power generation system uses the exhaust energy from the molten carbonate fuel cell

(MCFC) via a shell-and-tube heat exchanger to increase the temperature of the working fluid to the desired turbine inlet temperature T_{t4}. If enough heat is added, the turbine will be able to extract energy from the working fluid to produce net power. The air standard Brayton cycle is seen in Figure 3.3. The air leaving Stage 7 at an elevated temperature is given to the oxidizer to help the oxidizer convert any carbon monoxide (CO) from the fuel cell anode to carbon dioxide (CO_2), and any remaining unreacted methane (CH_4) to water. The *T-s* diagram of the air standard Brayton cycle in Figure 3.3 is similar to that seen in Figure 3.1b. The pressure loss in the microturbine inlet is a very small percentage of the atmospheric pressure, so it will be assumed $P_{t2} \approx P_{t1}$. Although the pressure loss in the diffuser is not represented in Figure 3.1b, it will be accounted for in the Matlab/Simulink® modeling of the hybrid and the stand alone power generation systems.

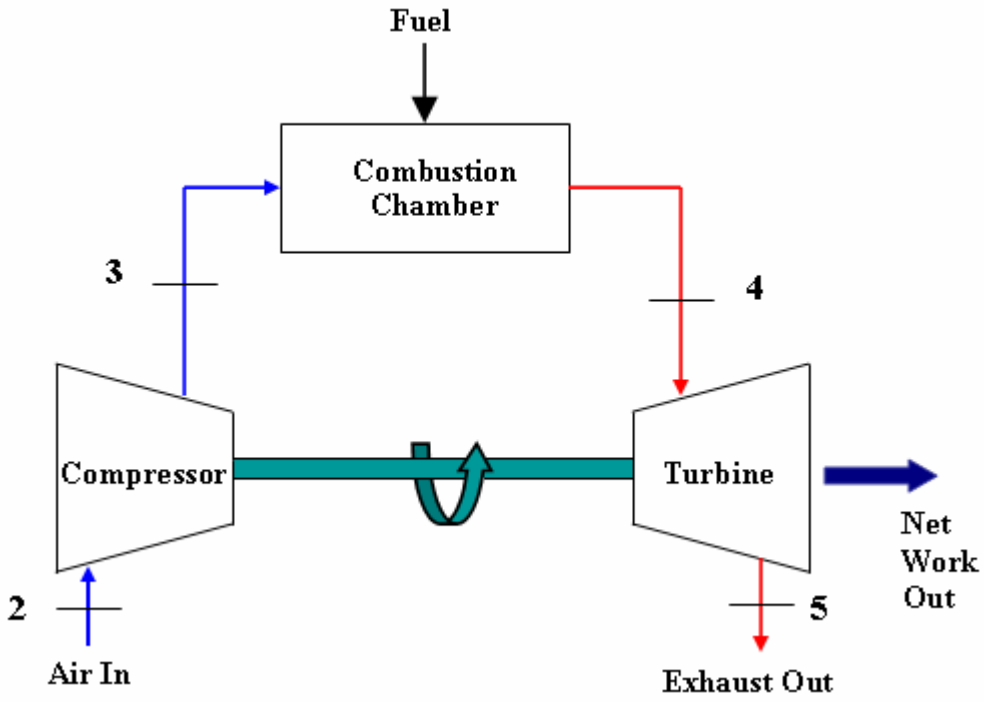

Figure 3.1a: Simple Gas Turbine Open to Atmosphere

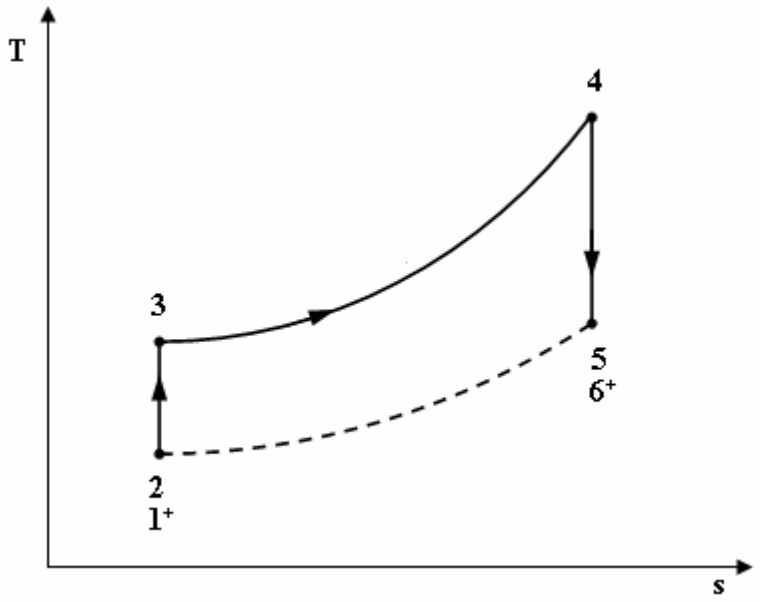

Figure 3.1b: *T-s* Diagram of Simple Gas Turbine Open to Atmosphere: [+]Stages 1 and 6 are represented in Figure 3.3, Air Standard Brayton Cycle

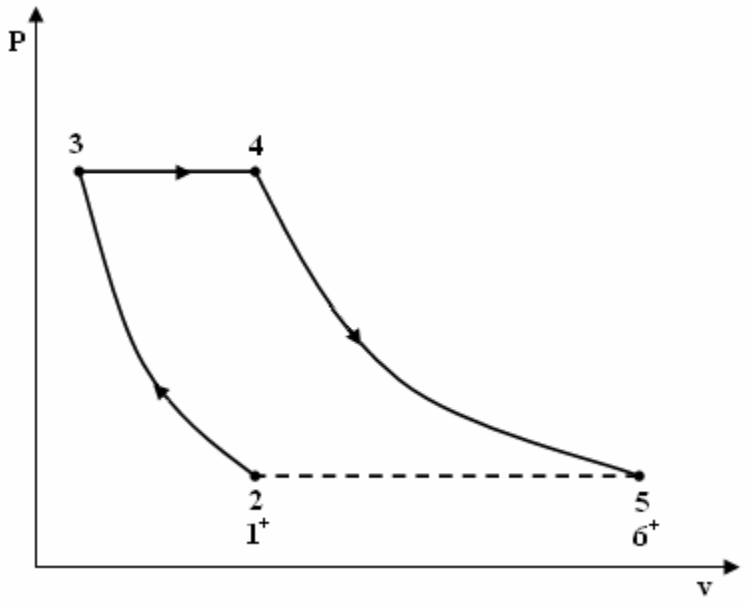

Figure 3.1c: *P-v* Diagram of Simple Gas Turbine Open to Atmosphere: [+]Stages 1 and 6 are represented in Figure 3.3, Air Standard Brayton Cycle

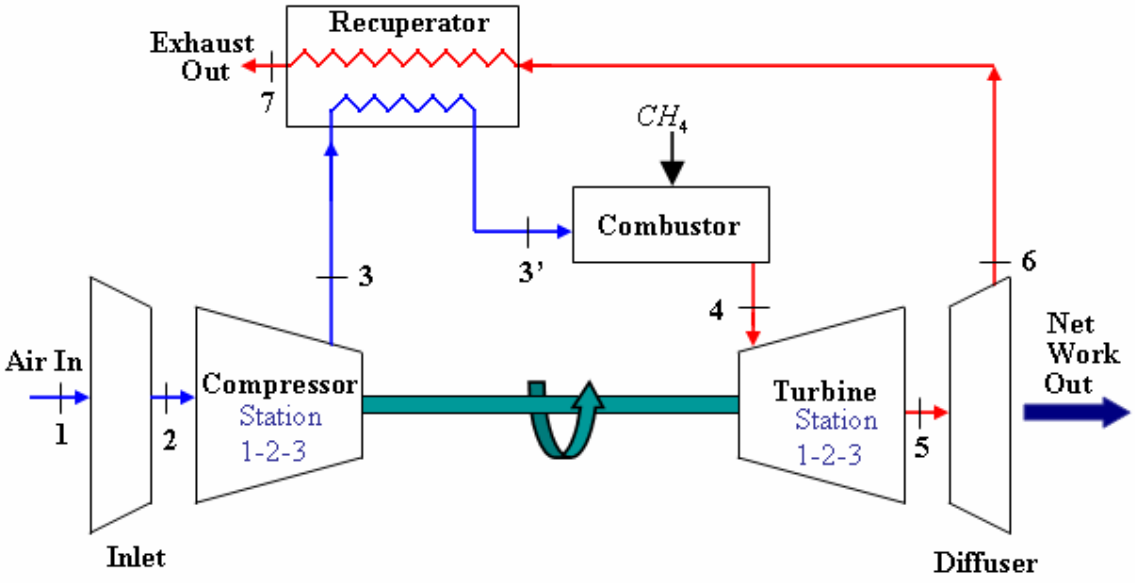

Figure 3.2a: Simple Gas Turbine Open to Atmosphere with Regeneration

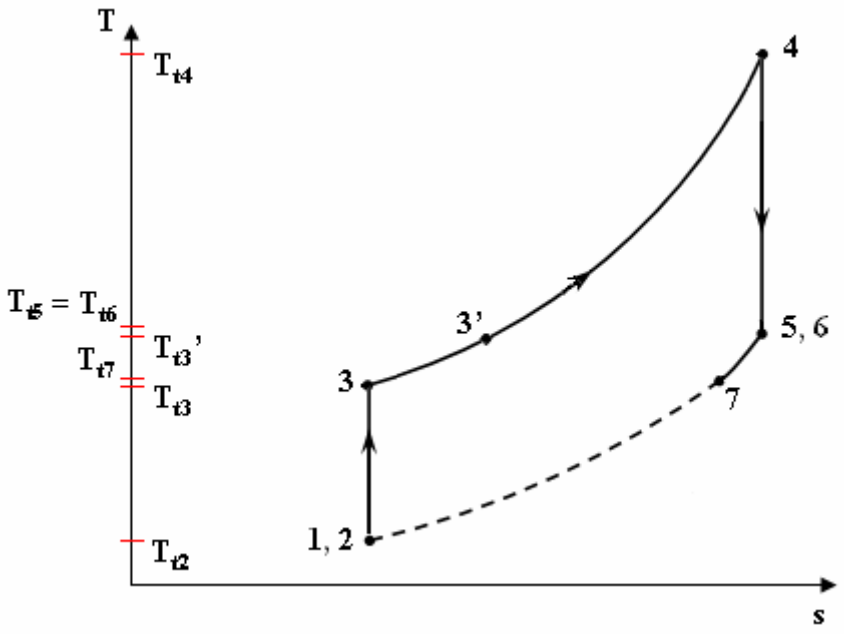

Figure 3.2b: *T-s* Diagram of Simple Gas Turbine Open to Atmosphere with Regeneration

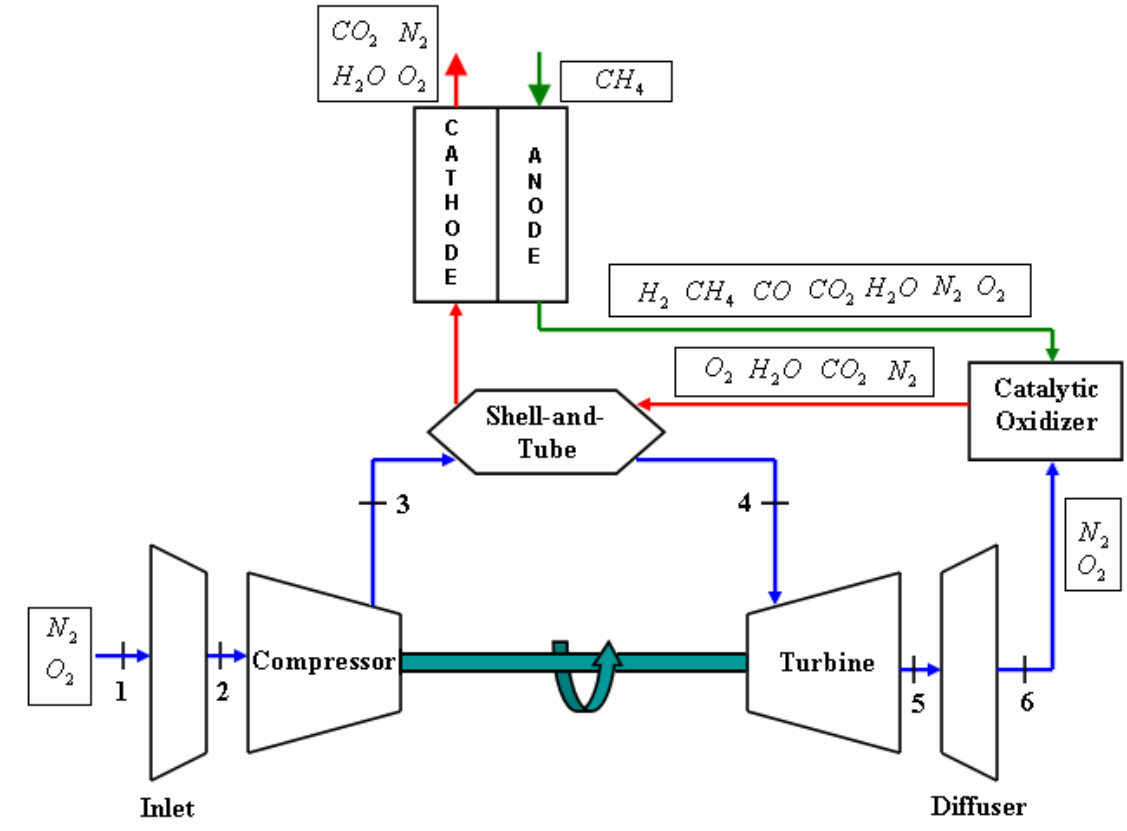

Figure 3.3: Air-Standard Brayton Cycle for Hybrid Power Generation

3.2 Centrifugal Compressor

Small engines, typically those with power output under 200kW, are more likely to have centrifugal (radial) compressors and radial turbines. A centrifugal compressor can be designed to have a much larger head or enthalpy rise per stage than is possible for axial-flow machines. This gives centrifugal compressors the advantage when the desire is to minimize the number of stages for any given purpose. For small sizes where the Reynolds number will be low and relative blade shroud clearance will be high, centrifugal compressors have advantages over multistage axial machines when is comes to cost and efficiency. For any feasible size, centrifugal or radial-flow machines cost less to manufacture than equivalent multistage axial turbomachinery. Instances where both radial and axial technologies can be effectively applied the efficiency of radial-flow machines generally will be less than that for axial machines.

For relatively small radial-flow machines, including compressors or turbines, more work per stage, i.e., a larger head rise or larger pressure ratio can be seen than for an equally small size axial-flow stage. This can be contributed to the "centrifugal effect" or the radial pressure gradient caused by the mass of the fluid that is rotated by the impeller. Temperature rise and therefore enthalpy rise is determined by the result of the torque given by the impeller to accelerate the fluid [42]. In other words, the amount of work it takes to move a given mass of fluid is determined from the torque of the compressor and the shaft speed of the compressor, where the shaft speed is determined from the compressor's rotor tip speed.

Most centrifugal compressors have mixed flow, where the flow enters in the axial direction and exits radially. The relative flow angle at the tip, β_{1t}, has a high absolute velocity and a swirl angle of 60 – 70 degrees from the radial direction. Although the pressure rise is primarily due to the centrifugal effects, high kinetic energy can be seen leaving the rotor which can only be recovered by diffusion. Diffusion takes place in the stator blades or a vaneless diffuser or volute [43]. The rotor vanes can be designed with backward-curved, radial-flow, or forward-curved exit angles, Figure 3.4. The forward-curved blades yield the highest increase in pressure but give the highest absolute velocity at the rotor exit and are seldom used [44].

For stress-related reasons, centrifugal compressors with relatively high pressure ratios (around 4:1 and higher) tend to have rotor blades that are radial. The cross-sectional view of a centrifugal compressor with radial rotor vanes is represented in Figure 3.5. The flow enters the compressor through the annulus between r_{1t} and r_{1h} at Station 1 then through to the inducer section of the rotor. The purpose of the inducer is to keep the flow in the axial direction before the rotor begins its large radius change from r_{1h} to r_{2r} [45]. Fluid leaves the rotor at Station 2 through a cylindrical area of radius r_{2r} and width b. Flow passes through the diffuser, where it is slowed then enters the collector scroll at Station 3. The diffuser entrance angle must be approximately the same angle as the absolute flow direction, α_2. The rotor tip velocity is limited to 2000 to 2200 ft/s (610 to 670 m/s) due to material stresses [44].

The velocity diagrams, representing the entrance and exit of the rotor section, are shown in Figure 3.6. Inlet flow is assumed axial and of uniform flow u_1. The relative flow angle of the flow increase from hub to tip, β_{1h} to β_{1t} giving the twist of the inlet to

the inducer section of the rotor. The flow leaves the rotor with a radial component of velocity w_2 that is approximately equal to u_1. A tangential or swirl velocity is seen exiting the rotor v_2 that is roughly 90 percent of the absolute rotor tip velocity U_{2t}. The absolute velocity exiting the diffuser, V_3 (not shown) is nominally 300 ft/s (90 m/s) [46].

The total temperature and pressure entering the compressor is giving the notation T_{t2} and P_{t2} respectfully. This corresponds with the Stage numbering seen in Figure 3.2a. The 1-Dimensional mean-line analysis is done within the compressor from Station 1 to Station 3. The properties at Station 1 of the compressor are identical to the properties at Stage 2. Properties at Station 3 of the compressor are identical to Stage 3. The calculations done at Stage 2 and 3 are considered core calculations and are critical to analyzing the Brayton cycle. The mean-line calculations are critical to 1-D analysis of the centrifugal compressor.

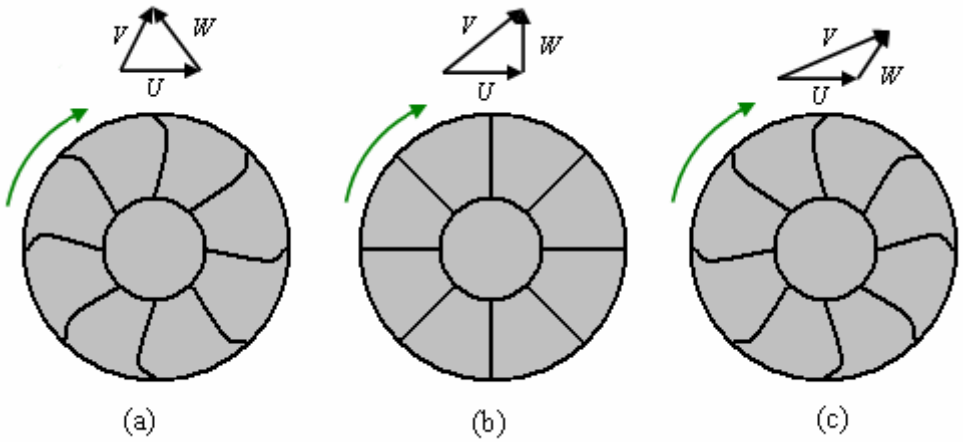

Figure 3.4: Rotor Blade Exit Angles, (a) Backward-curved, (b) Radial-flow, (c) Forward-curved

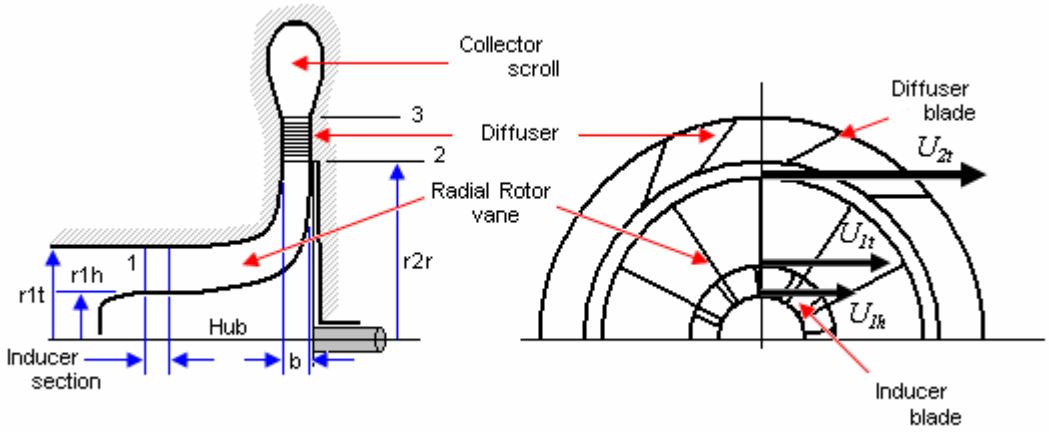

Figure 3.5: Centrifugal Compressor with Station Numbering

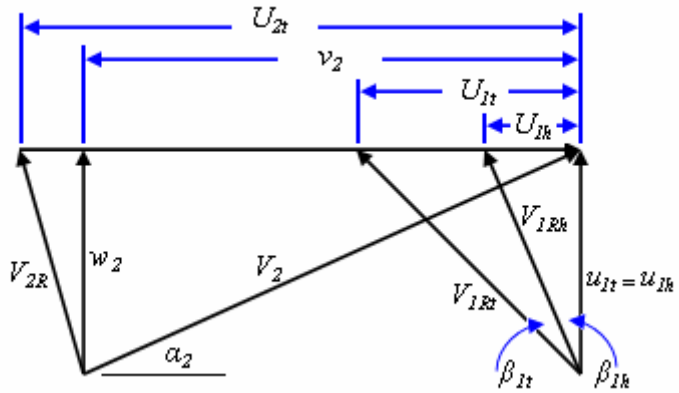

Figure 3.6: Velocity Diagram for Centrifugal Compressor with Radial Rotor Vanes

3.3 Radial Inflow Turbine

The hot gas expansion turbine is the power producing component of the microturbine generator. As the hot gas is *allowed* to expand rapidly through the blades of the turbine, work is extracted from this process. The goal of designing a turbine is to control the rate at which this expansion occurs. This is done by controlling the cross-section of the turbine casing, the turbine wheel diameter and vane angles. The hot gas needs to be slowed, cooled and expanded at an optimal rate to allow for as much energy as possible to be drawn out of the gas as it passes from one blade to another. Of the power extracted from the expansion process, approximately one-third is used to drive the generator to produce electricity; the remaining amount is used to drive the compressor [1].

In comparison to radial flow compressors and fans, radial-flow turbines produce lower head or enthalpy drops per stage at efficiencies that are higher than what is possible for axial-flow turbines operating at the same peripheral speeds and rotor diameter. This is seen primarily in turbomachinery of smaller sizes. Radial-flow turbines are seen essentially in applications where the lower cost of manufacturing small single-stage radial turbines is the prevailing factor; such as is seen for fuel cell hybrid systems.

The blades of a hot gas expansion turbine are nearly always radial at the periphery to minimize the blade bending stress. Figure 3.7 is of a radial inflow turbine and station numbering is shown. The flow through the stators of the radial inflow turbine is accelerated and the tangential velocity is increased. The rotor then decreases the tangential velocity as the flow is expanded and energy is removed producing work. The

flow that exits the rotor is predominantly axial although some tangential velocity or swirl may still be present [46].

A velocity diagram depicting the direction and magnitude of the flow entering the rotor of a radial-inflow turbine can be seen in Figure 3.8. The exit flow angle, α_2, is habitually chosen to be 70 degrees and this is given relative to the axial direction. The blade angle, β_3, can be determined from using trigonometry on the velocity diagram. The only indefinite is the direction, $\alpha_{2R,}$ of the relative flow, $V_{2R,}$ at the inlet. The relative velocity of flow entering the rotor is designed to be radial to obtain zero incidence [47], $w_2 = V_{2R}$. With this being said the tangential velocity at station 2, v_2, is then equal to the rotor tip speed U_{2t}. The rotor tip speed squared is directly proportional to the temperature drop through the radial inflow turbine and is limited to between 1148 and 1640 ft/s (360 and 500 m/s) [46].

In the stator of an axial turbine, the fluid is accelerated and the tangential velocity is increased in the direction of rotation. The rotor decreases the tangential velocity in the direction of rotation causing the flow to exert tangential force on the rotor blades. This produces a torque on the output shaft. The flow leaving the rotor is sent into the next stage of the turbine consisting of another pair of stators and rotors. Flow is expanded and accelerated through each blade row. The static pressures are dropping across both the stator and rotor and separation can then be avoided.

Comparing the magnitude of the absolute velocity V_2, Figure 3.8, with the magnitude of the absolute velocity V_2 for an axial turbine stage, Figure 3.9, it can be seen why more work per stage is achieved for a radial inflow turbine. Although the magnitudes of the velocity vectors seen in Figures 3.8 and 3.9 are not literal

representations of the velocities, it is still shown that the absolute velocity of a radial turbine is three times as large as that of the axial turbine. There is more flow through a single radial turbine compared to a single stage axial turbine of the same size. With more flow comes more torque on the shaft producing energy. This then demonstrates how more work per stage can be seen with a radial turbine than an axial turbine when compared at small sizes. In reference to "small size," the size being considered is on the scale of 3.6 inches in diameter (91.5 mm).

The total temperature and pressure entering the turbine is giving the notation T_{t4} and P_{t4} respectfully. This corresponds with the Stage numbering seen in Figure 3.2a. The 1-Dimensional mean-line analysis is done within the turbine from Station 2 to Station 3. The total properties (temperature and pressure) at Station 1 are equal to the total properties at Station 2 of the turbine. All of the properties at Station 2 are identical to the properties at Stage 4. Properties at Station 3 of the turbine are identical to Stage 5. The calculations done at Stage 4 and 5 are considered core calculations and are critical to analyzing the Brayton cycle. The analysis of the turbine's diffuser is done separately. Station 4 corresponds to Stage 6 in Figure 3.2a. The mean-line calculations are critical to 1-D analysis of the radial inflow turbine.

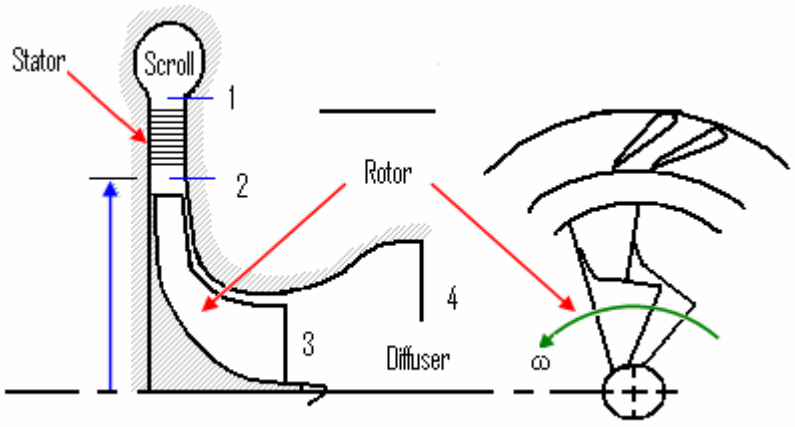

Figure 3.7: Radial Inflow Turbine with Station Numbering

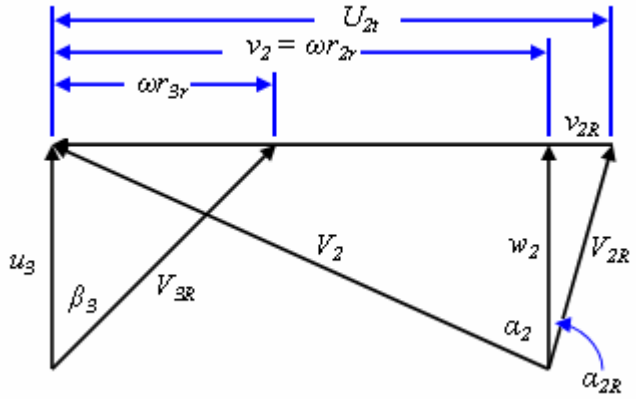

Figure 3.8: Velocity Diagram for Radial Inflow Turbine with Radial Rotor Vanes

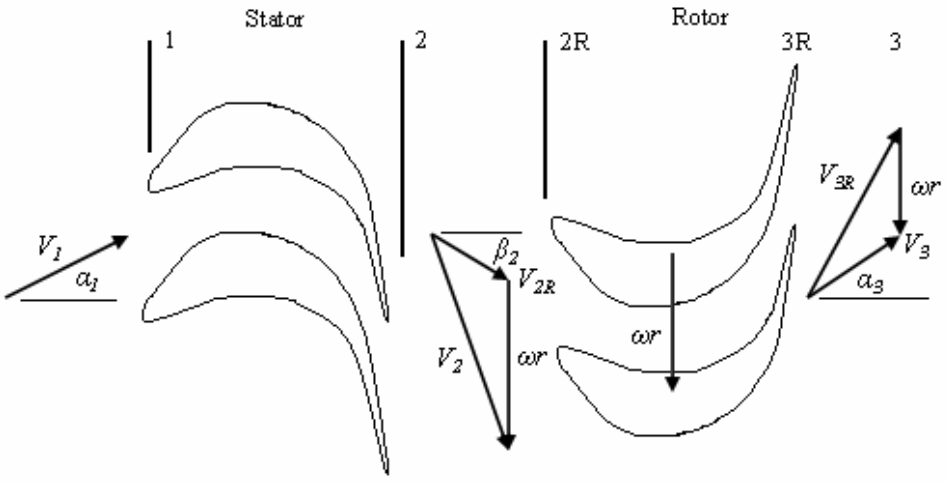

Figure 3.9: Single Stage Axial Turbine with Station Numbering

3.4 Reverse Flow Annular Combustor

Combustion is the process in which some material or fuel is burned. Whether it involves striking a match or firing a jet engine, the products of combustion are similar. Heat input to the gas turbine Brayton cycle is provided by a combustor. The combustor receives pressurized air from the compressor and delivers it at an elevated temperature to the turbine. Ideally this is done with minimal or no pressure loss. There are three major types of combustors, tubular, tubo-annular and annular. Tubular are single can designs and tend to be very large. Tubo-annular or can-annular combustors are the most common type of combustors used in gas turbines. Annular combustors are primarily used in applications where frontal area is important. Since less cooling air is need than for tubo-annular types, annular combustors are growing in importance for high-temperature applications, i.e., microturbines. Annular type combustors are used by Capstone Turbine Corporation and Solar Turbines Incorporated [48, 49].

The combustor inlet temperature depends on whether or not the engine is regenerative or nonregenerative. Nonregenerative, Figure 3.1a, inlet temperatures vary from 709 to 1419 R (394 to 788 K). Regenerative, Figure 3.2a, inlet temperatures range from 1159 to 1559 R (644 to 866 K). Combustor outlet temperatures range from 1919 to 2769 R (1066 to 1538 K) for small engines. Combustor pressures for a full-load operation vary from 45 psia for small engines to as much as 370 psia for complex engines [48].

The annular combustor is of reverse flow design and uses natural gas as the fuel. The natural gas is modeled as primarily methane (CH_4). The chemical energy present in

the combustion reactants is transferred to the gas stream during the combustion process. The chemical reaction equation for the combustion process is

$$CH_4 + 2O_2 + 7.52N_2 \rightarrow CO_2 + 7.52N_2 + 2H_2O + \text{Heat} \quad (3.1)$$

From Equation 3.1, the stoichiometric fuel/air ratio is determined to be

$$f_{stoich} = \frac{1(12)+4(1)}{2(2(16))+7.52(2(14))} = 0.05828 \quad (3.2)$$

The chemical energy is measured in terms of enthalpy and is converted to mechanical work by expansion of the gas through the turbine [15].

Equation 3.1 represents the chemical reaction seen in the combustion chamber and Table 3.1 has the mass fractions of the chemical reaction. From this, it can be determined that since the mass fraction of the unreacted nitrogen (N_2) is much higher than the mass fraction of the carbon dioxide (CO_2) and the water (H_2O), then the fluid used to transport energy in the turbine can be modeled as air and the other products of the chemical reaction can be neglected.

A reverse flow combustor is desired because they are ideal for small engines. Small engines run at high shaft speeds and to prevent shaft whirling problems the compressor and turbine need to be closely coupled. The reverse flow combustor takes advantage of short shaft length, efficient utilization of available combustion volume and easy accessibility of the fuel injectors [50]. The annular combustor with compressed air and exhaust gas flow directions can be seen in Figure 2.4.

The inlet total temperature and pressure for the combustion chamber are denoted T_{t3}' and P_{t3}' respectfully. Since there is recuperation in the gas turbine Brayton cycle, the compressed air is flowing through the primary surface recuperator before entering the combustor. The total temperature and pressure exiting the combustion chamber are

denoted T_{t4} and P_{t4} respectfully. The inlet and exit locations can be seen in the Brayton cycle representation, Figure 3.2a.

Table 3.1: Combustion Chamber Mass Fractions

	mass [lbm]	Molar mass lbm/lbmol]	# moles [lbmol]	mol fraction Compressor Inlet	mol fraction Combustor Inlet	mol fraction Turbine Inlet	mass fraction Compressor Inlet	mass fraction Combustor Inlet	mass fraction Turbine Inlet
O_2	2	32.0000	0.0625	0.1888	0.1589	0.0000	0.2101	0.1901	0.0000
N_2	7.52	28.0100	0.2685	0.8112	0.6826	0.6675	0.7899	0.7148	0.7148
CH_4	1	16.0400	0.0623	0.0000	0.1585	0.0000	0.0000	0.0951	0.0000
CO_2	1	44.0100	0.0227	0.0000	0.0000	0.0565	0.0000	0.0000	0.0951
H_2O	2	18.0200	0.1110	0.0000	0.0000	0.2760	0.0000	0.0000	0.1901

		[lbmol]	[lbm]	molar mass of mixtures:
Combustor:	$CH_4 + 2O_2 + 7.52N_2$:	0.3933	10.52	26.7467 [lbm/lbmol]
Compressor:	$2O_2 + 7.52N_2$:	0.3310	9.52	28.7635 [lbm/lbmol]
Turbine:	$CO_2 + 2H_2O + 7.52N_2$:	0.4022	10.52	26.1571 [lbm/lbmol]

Complete Reaction: $CH_4 + 2O_2 + 7.52N_2 \rightarrow CO_2 + 7.52N_2 + 2H_2O + (Heat)$

3.5 Annular Wrap-Around Primary Surface Recuperator

The core of the heat exchanger will be modeled as a primary surface recuperator (PSR) after the heat exchanger core used by Capstone®, with a gas-to-gas counter-flow arrangement where the hot exhaust gas passes by the cooler compressed air leaving the compressor, Figure 3.2a. For convenience, T_{t3} and T_{t3}' the temperature of the compressed air into and exiting the recuperator core will be designated T_{ci} and T_{co}, respectfully. The temperature of the exhaust gas inlet and exit, T_{t6} and T_{t7} will be designated T_{hi} and T_{ho}, respectfully.

Sizing a heat exchanger is quite a challenge. The recuperator core used by Capstone® has 169 individual air cells. Each of these air cells is created by the fin folded 347 stainless steel. The fin folding creates air channels for the hot and cold fluids. The geometry of the flow channels, i.e., the hydraulic diameter D_h, and the depth of the recuperator core determines the number of flow channels per air cell. The actual geometry of a flow channel that is used for this paper is much simpler than what is seen in Figure 2.5. The geometry of the air (cold) flow channel and of the exhaust (hot) flow channel are represented as two isosceles trapezoids inverted one over the other, Figure 3.10. A higher volume flow rate is seen on the exhaust side which leads to a higher pressure drop. This is balanced by having a larger hydraulic diameter which will decrease the velocity on the exhaust side. The hydraulic diameter is the variable having the greatest impact on the recuperator core volume. A small hydraulic diameter will give a small recuperator volume [29].

The hydraulic diameter is determined by the following equation:

$$D_h = 4\frac{A_x}{P} \tag{3.3}$$

Where A_x is the cross-sectional area and P is the wetted perimeter of the flow channel geometry. The cross-sectional area of a trapezoid is

$$A_x = \frac{1}{2} h(b_1 + b_2) \tag{3.4}$$

Where h is the height of the trapezoid and b_1 and b_2 are the respective bases of the trapezoid. For the flow geometry seen in Figure 3.10, the cross-sectional area is twice the cross-sectional area calculated by Equation 3.4, therefore the A_x of the cold flow geometry is

$$A_x = h(b_1 + b_2) \tag{3.5}$$

The same is seen for the hot flow geometry where b_1 and b_2 are replaced by b_3 and b_4 in equation 3.5. The wetted perimeter $P_{c,in}$, of the cold flow geometry in Figure 3.10 is determined from

$$P_{c,in} = 4\sqrt{\frac{1}{4}(b_1 - b_2)^2} + 2b_2 \tag{3.6}$$

Replacing b_1 and b_2 with b_3 and b_4 in Equation 3.6 gives the wetted perimeter P_{hot}, of the hot flow geometry.

The one other wetted perimeter that needs to be calculated is the outside wetted perimeter $P_{c,out}$ of the cold flow geometry. This is done by increasing the flow geometry of the cold side by the thickness of the Type 347 stainless steel. In essence, this approach is similar to finding the outer diameter of a pipe if the inner diameter and the thickness of the material of the pipe are known.

The calculated hydraulic diameter and wetted perimeters for the cold and hot flow channels along with corresponding geometry sizes can be seen in Table 3.2.

Once the hydraulic diameter of the flow channel has been decided, the next step is to determine the length and depth of the recuperator core. To reduce the volume of the recuperator core, allow for a larger total pressure drop over the heat transfer matrix or decrease the size of the matrix passages. The cross-corrugated is well documented in literature and easier to manufacture with the small passage dimensions that are essential to the small size and weight required for a primary surface recuperator. The length and depth are determined based on the heat exchanger effectiveness, ε and the pressure drop, ΔP of the hot and cold flows. Figure 3.11 represents the pressure drop on the hot and cold side for a given recuperator core length versus depth of the recuperator core. Figure 3.12 portrays the heat exchanger effectiveness for a given recuperator core length versus depth of the recuperator core. As stated in Section 2.3.3, the effectiveness should be as high as possible ($\varepsilon \geq 85\%$), and the pressure drop should be as small as possible ($\Delta P < 5\%$). For the purpose of this paper, the effectiveness will need to be $\varepsilon \geq 75\%$, and the pressure drop on the hot side will be allowable to $\Delta P < 7\%$.

For Figure 3.11, any length and depth above the red line on the cold side ($\Delta P < 5\%$), and above the blue line on the hot side, $\Delta P < 7\%$ is eliminated. The only length and depth that will be considered in Figure 3.12 are those above the red line signifying $\varepsilon \geq 75\%$. From inspection of the data in Figures 3.11 and 3.12, there is only one possibility for the length and corresponding depth of the recuperator core that match the requirements stated above, these parameters are listed in Table 3.3.

From Table 3.3 the length of the recuperator core will be 9.8 inches (250 mm) and the depth of the recuperator core will be 12 inches (305 mm). These sizing parameters will be used to calculate the overall heat transfer coefficient based on outer surface area,

U_oA_o. The overall heat transfer coefficient will be used in conjecture with the *ε-NTU* method to determine the heat exchanger effectiveness. The *ε-NTU* method will be discussed in Section 4.1.4.

Based on the flow channel geometry, Table 3.2, and the recuperator core depth established in Table 3.3, the total number of flow channels in one air cell is calculated to be 122. For 169 air cells, the total number of air flow channels, *NFC*, in the recuperator core is 20,618 channels. The number of flow channels can be compared to the number of tubes that might be in a shell-and-tube heat exchanger with the hot flow channels being similar to the shell of a shell-and-tube heat exchanger.

The calculations done in Table 3.3 are at the design point of the microturbine generator. The 1-Dimensional model will be analyzed on the actual microturbine operating line. The heat exchanger effectiveness is averaged on the ideal operating line, running from 40-110 percent of the design speed. The effectiveness is 0.9328 to 0.7584 and this averages out to be 0.8320. The average heat exchanger effectiveness, ε_{avg} will be held constant for all calculations.

Table 3.2: Air Cell Channel Flow Geometry

	Value	Units	Value	Units
h	0.01969	in	0.5	mm
b_1	0.07874	in	2.0	mm
b_2	0.00394	in	0.1	mm
b_3	0.09843	in	2.5	mm
b_4	0.01969	in	0.5	mm
t	0.00394	in	0.1	mm
$D_{h,cold}$	0.03679	in	0.9345	mm
$D_{h,hot}$	0.04299	in	1.0920	mm
$P_{c,in}$	0.17688	in	4.3336	mm
P_{hot}	0.21540	in	5.2773	mm
$P_{c,out}$	0.17688	in	4.3336	mm

Table 3.3: Matching Design Requirements for Recuperator Core

Length	*Depth*	*ε*	*ΔP cold*	*ΔP hot*
in (mm)	in (mm)	-	%	%
7.9 (200)	**12 (305)**	**0.7744**	**0.8359**	**6.6900**

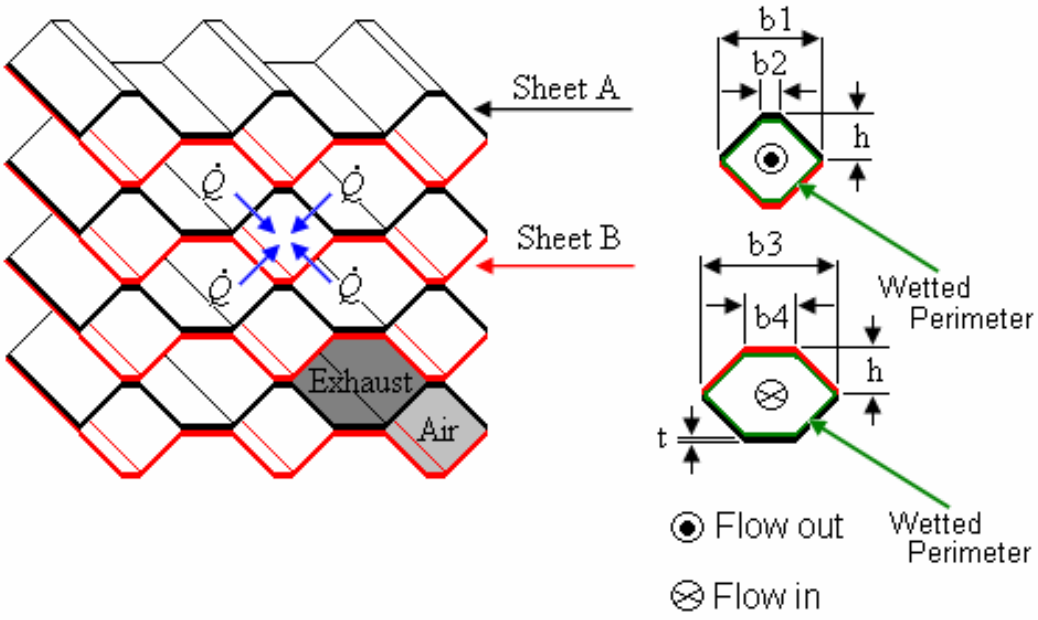

Figure 3.10: Air Cell Channel Flow Geometry

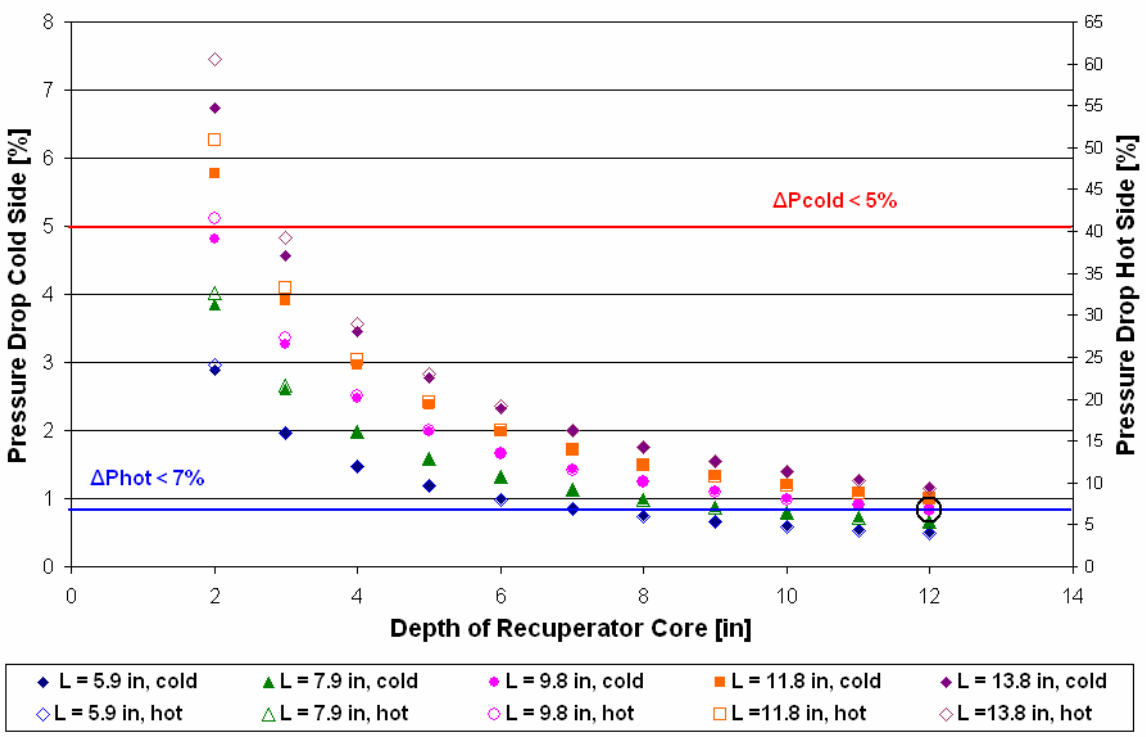

Figure 3.11: Pressure Drop on Hot and Cold Side for Given Heat Exchanger Length

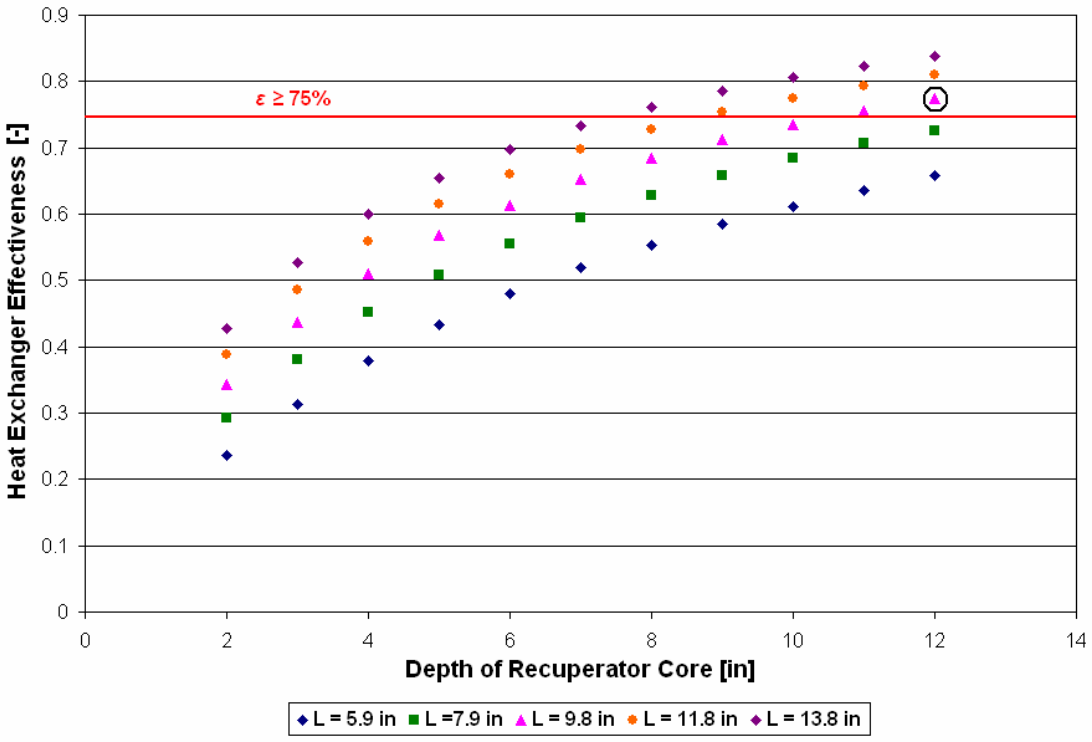

Figure 3.12: Heat Exchanger Effectiveness for Given Heat Exchanger Length

CHAPTER 4: METHODOLOGY OF STAND ALONE POWER GENERATION SYSTEM

There will be a total of three different MATLAB/Simulink® models developed, each with a separate Simulink Graphical User Interface (GUI) model and MATLAB m-file controller and variable files. The stand alone power generation system will be analyzed using 1-Dimensional approach to determine the feasibility of the mathematical model that will be applied to the 0-Dimensional and 1-Dimensional analysis of the hybrid power generation system in Chapter 5. Through 1-D analysis, the parameters produced by the 0-D approach can be validated. Further validation of the 1-D stand alone model will be accomplished through the use of Engineering Equation Solver (EES) a product of F-Chart Software. A thermodynamic cycle analysis of the stand alone system will be discussed in Chapter 6. The verification of the 0-Dimensional hybrid model will be used to justify the performance maps used for the centrifugal compressor and radial inflow turbine. The results and comparisons will be discussed in Chapter 6.

For 0-Dimensional analysis, a lumped approach is used to create each module. The centrifugal compressor and radial turbine on the microturbine generator have

multiple stations created by the geometry of the rotating machinery. These stations are simulated as a single component for the 0-D analysis. When using performance maps, the number of stages or stations being modeled in the compressor and turbine are irrelevant for the reason that performance maps are created from rig tests performed on the compressor and turbine. The 0-D approach is transient and incorporates 1st order ordinary differential equations (O.D.E). Equation 4.1 is an example of a 1st O.D.E.

$$\frac{du}{dt} + \frac{dv}{dt} = 1 + 5t \tag{4.1}$$

1-Dimensional mean-line analysis is done along a streamline through the compressor or turbine. At each of the stations, a single calculation of pressure, temperature, Mach number, velocity, etc. is made relative to the flow and this is related to the absolute flow through the component. 1-D analysis is used when zooming is required to analyze areas in the component that experience more drastic changes in properties (turbine rotor tip) without incorporating computational fluid dynamics (CFD) techniques. The 1-D approach incorporates algebraic equations for steady state calculations and 1st order partial differential equations (P.D.E) for transient behavior. The 1-D approach used for the MTG is for steady state conditions only. Equation 4.2 is an example of an algebraic expression. An algebraic expression incorporates signs and symbols that represent algebra and the expression represents one number or one quantity. Since transient modeling is not observed, a generic example of a 1-D transient 1st order P.D.E can be seen in Equation 4.3 below and is known as the 1-D transient Laplace equation.

$$\tau_c = \pi_c^{\gamma - 1 / \gamma e_c} \tag{4.2}$$

$$\frac{\partial u}{\partial t} + \frac{\partial u}{\partial x} = 0 \tag{4.3}$$

2-Dimensional analysis is used when further fidelity of a model is required and visualization of actual flow characteristics, turbulence, vortex shedding, etc., are essential to the analysis of the component behavior. This analysis incorporates computational fluid dynamics (CFD) techniques. 2-D analysis can be at steady-state conditions or demonstrate transient behavior and this is done by using a 2nd order P.D.E. An example of a 2-D steady-state 2nd order P.D.E is the Laplace equation, Equation 4.4. A 2-D transient 2nd order P.D.E. would be the Wave equation, Equation 4.5.

$$\frac{\partial^2 u}{\partial x^2} + \frac{\partial^2 u}{\partial y^2} = 0 \tag{4.4}$$

$$\frac{\partial^2 u}{\partial t^2} = c^2\left(\frac{\partial^2 u}{\partial x^2} + \frac{\partial^2 u}{\partial y^2}\right) \tag{4.5}$$

3-Dimensional analysis increases the visualization of the flow characteristics. This CFD approach incorporates higher fidelity and is much more difficult to solve. 3-D analysis can be done at steady-state but it is more commonly carried out with transient modeling. A 3rd order P.D.E is used with 3-D modeling. The Wave equation is seen as a 3rd order P.D.E in Equation 4.6.

$$\frac{\partial^3 u}{\partial t^3} = c^3\left(\frac{\partial^3 u}{\partial x^3} + \frac{\partial^3 u}{\partial y^3} + \frac{\partial^3 u}{\partial z^3}\right) \tag{4.6}$$

Figure 4.1 gives a visual representation of the 0-D, 1-D, 2-D, and 3-D modeling approaches.

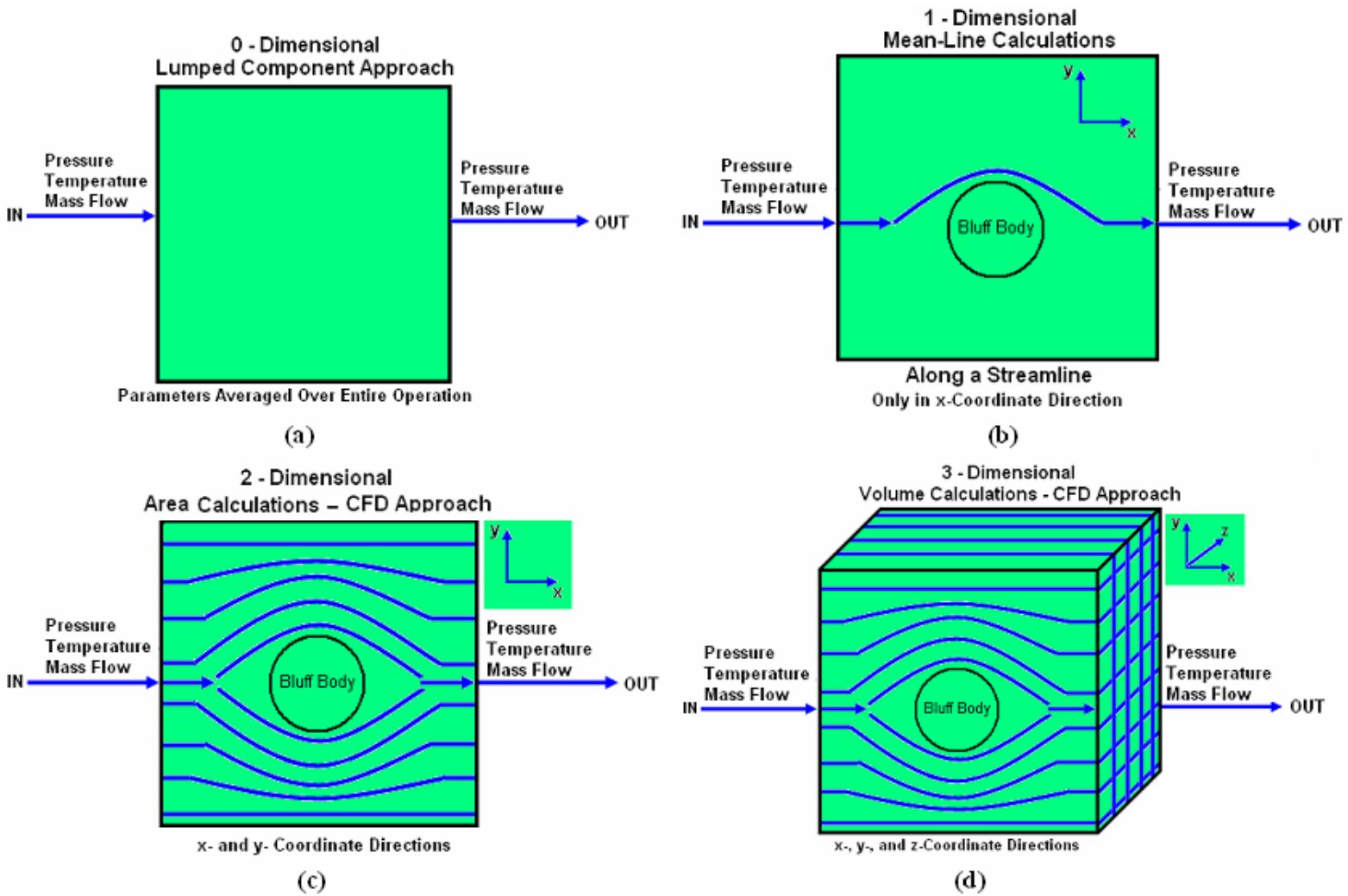

Figure 4.1: a) 0-Dimensional Flow, b) 1-Dimensional Flow, c) 2-Dimensional Flow, and d) 3-Dimensional Flow

4.1 1 – Dimensional

The 1-D simulation of the stand alone model is initiated by loading the MATLAB m-file controller. This will load the thermodynamic property tables and run additional m-files that provide individual component parameters that are required by Simulink into the MATLAB workspace and executes the Simulink Graphical User Interface (GUI). The flow diagram to execute the 1-D modeling and simulation is in Figure 4.2.

The 1-D model executes algebraically so the variables are solved linearly. The solver type employed by Simulink® uses a variable time step and is discrete with no continuous states. This negates the need for a controller to be present in the system. A desired engine speed is given as the input and the resulting compressor operating line values are determined. Each module represents the set of equations needed to solve for the performance parameters of each component. The top level Simulink model is shown in Figure 5.3 and the computer flow diagram is represented in Figure 5.4. Since the variables are determined in a linear manner, the solution path of the core variables is shown in Figure 5.5. The results of the mean-line calculations will be discussed in Chapter 6.

The mathematical modeling of the centrifugal compressor, radial inflow turbine, annular combustor and primary surface recuperator Sections 4.1.1 to 4.1.4, give the core calculations required to analyze the Brayton cycle and a brief description of the 1-D mean-line calculations. The calculations are carried out using the English unit system. All values have corresponding SI values and units. For the English unit system, the unit of force is derived from Newton's second law of motion and relates force to mass, length,

and time with constant of proportionality being $1/g_c$. This is derived in Mattingly [46]. In English units the value of g_c is given as

$$g_c = 32.17 \frac{ft \cdot lbm}{lbf \cdot s^2}$$

Several assumptions were made with the creation of the MATLAB/Simulink® model of the microturbine generator. The assumptions for each of the core components, i.e., the compressor, combustor, and turbine are a generic representation of Capstone's Model 330 and C30 microturbines [51] and the scaling of the rotor size for the compressor and the turbine was done through suggestions from literature.

For a simple constant-area-flow engine or MTG, the performance; which is the pressure ratio and the mass flow rate of the compressor, depends on the power from the turbine and the inlet conditions of the compressor. The performance varies with the inlet conditions and the power determined by throttle setting and is limited by the MTG control system. For an aircraft engine, the pilot controls the operation of the engine directly through the throttle and indirectly by changing the flight conditions. Looking at the interaction of the compressor-combustor-turbine combination; know as the *pumping characteristics* of the gas generator [46] the MTG performance can be obtained. Sea-level-static (SLS) is the normal reference condition for the values of the microturbine generator variables.

The microturbine generator 1-Dimensional mathematical model begins by determining at what throttle setting the model will run. The performance of the model is given from 40 percent of throttle to 110 percent of throttle. The design point of the MTG will be located at 100 percent of the throttle position or full throttle with a maximum throttle of 110 percent. At 100 percent of the throttle, the model will be operating at the

design shaft speed. The common method for portraying the performance characteristics, often called performance mapping is with a plot of speed lines, efficiency, pressure ratio, and corrected mass flow rate, Figure 4.6.

Since the 1-D model is run on a single operating line with no off-design capabilities, the performance characteristics of the compressor are portrayed by 1-D look-up tables in the MATLAB/Simulink® environment with either corrected mass flow, $\dot{m}_{0c}$ or pressure ratio, π_c versus the throttle position input as a percentage. The desired throttle setting is the control for the 1-D model. The operating design point parameters are displayed in Table 4.1. Due to the linear nature of the mathematical modeling and variable calculation, these values will be used to portray the microturbine generator model at steady state conditions.

Table 4.1: Design Point Parameters

	Value	Units	Value	Units
T_{t2}	550.8	°R	306	°K
P_{t2}	14.696	psia	101.3	kPa
π_c	3.5	-	3.5	-
$\dot{m}_{0c}$	1.664	lbm/s	0.7548	kg/s
P_{t5}	18.5	psia	127.6	kPa

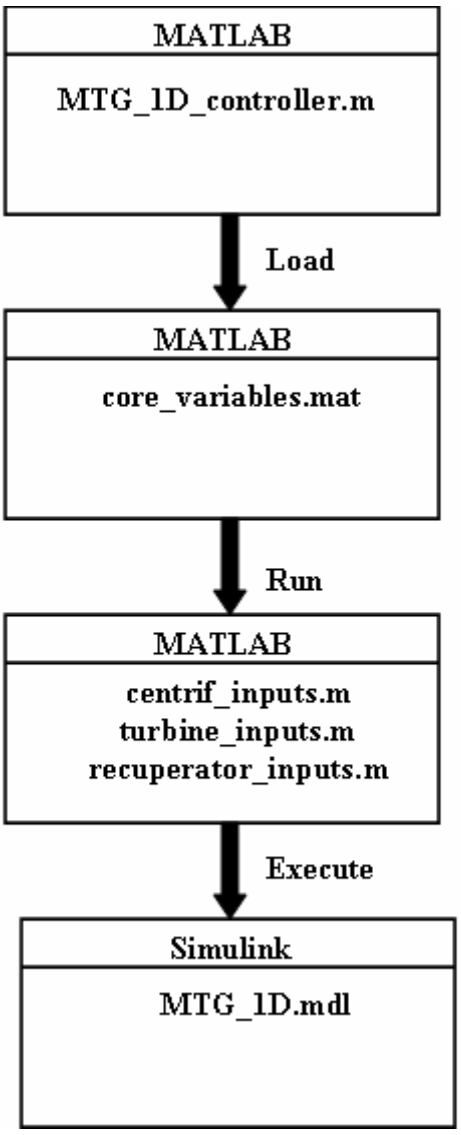

Figure 4.2: Flow Diagram to Execute 1-D Modeling and Simulation of Stand Alone Power Generation System

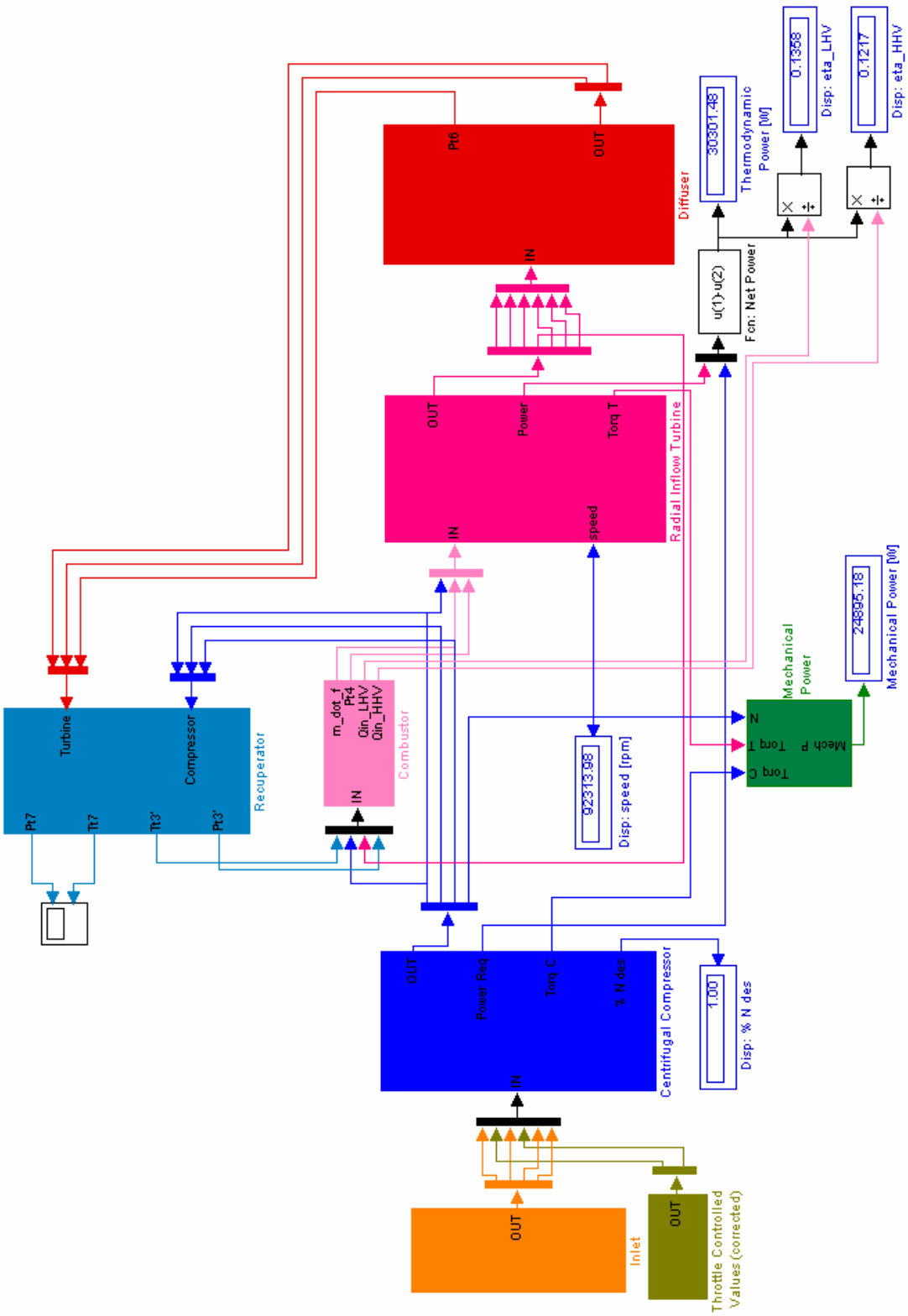

Figure 4.3: Top Level 1-D Stand Alone Power Generation Model

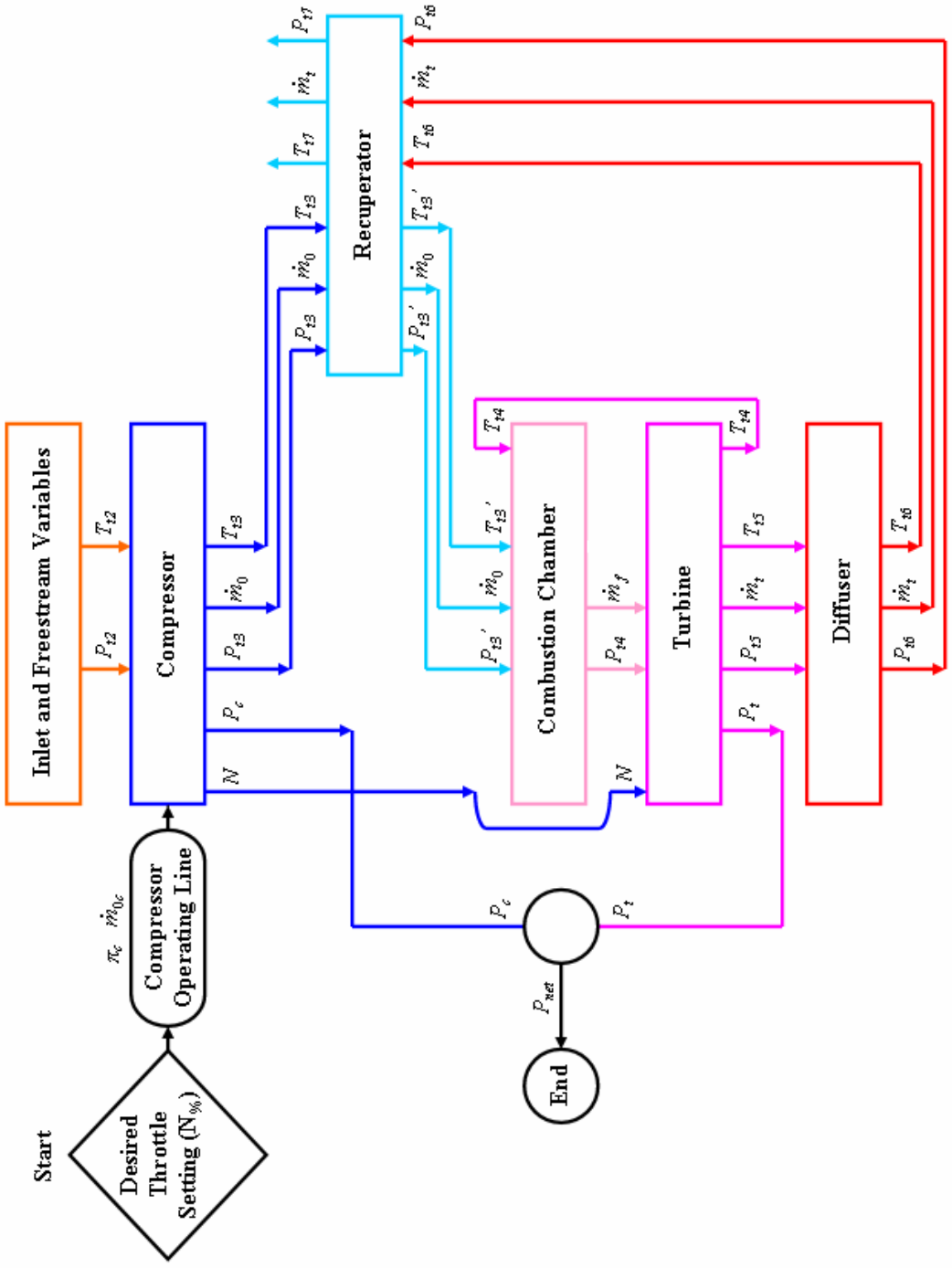

Figure 4.4: Computer Flow Diagram for Top Level 1-D Stand Alone Model

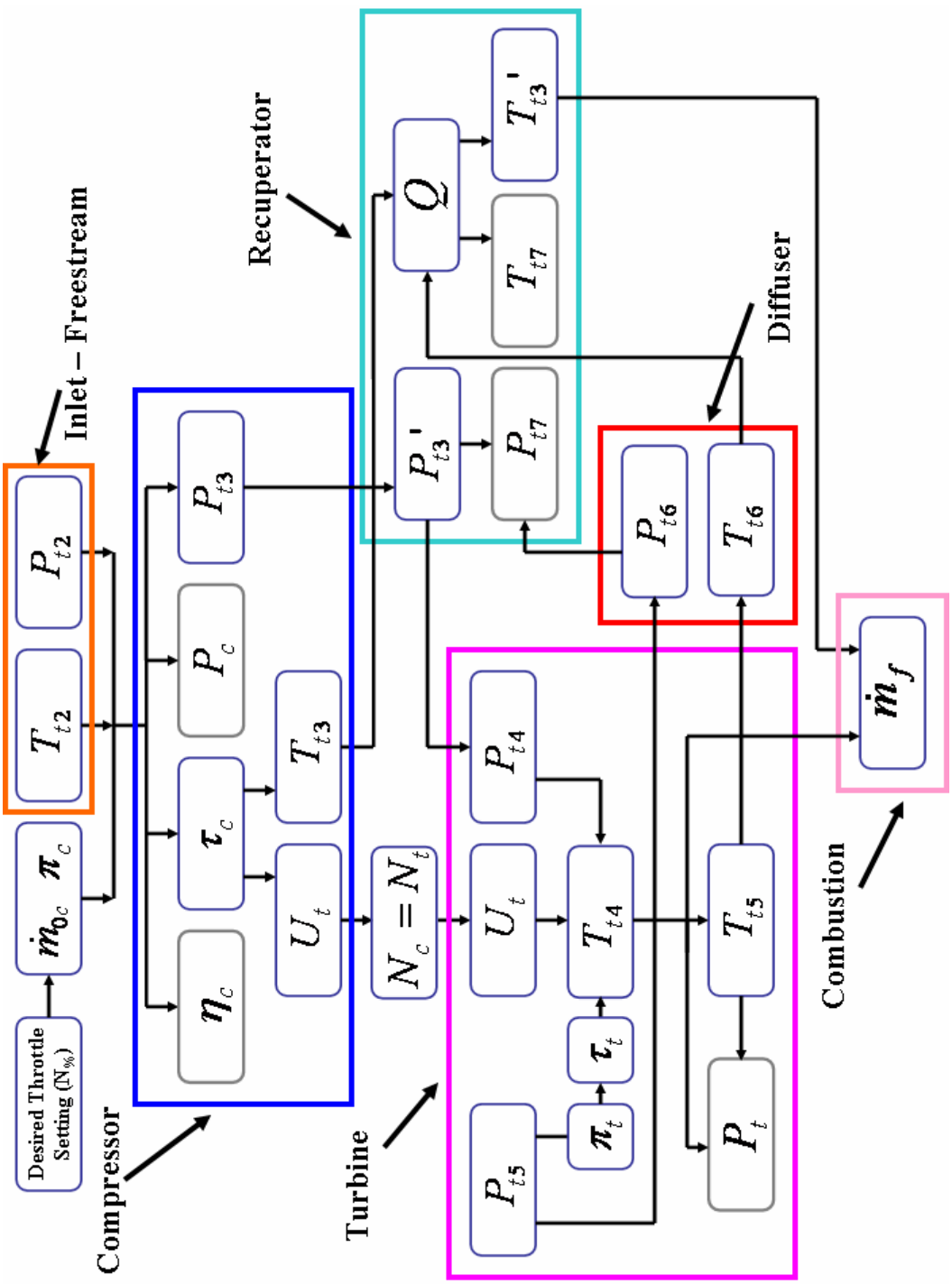

Figure 4.5: 1-D Core Variables Solution Path

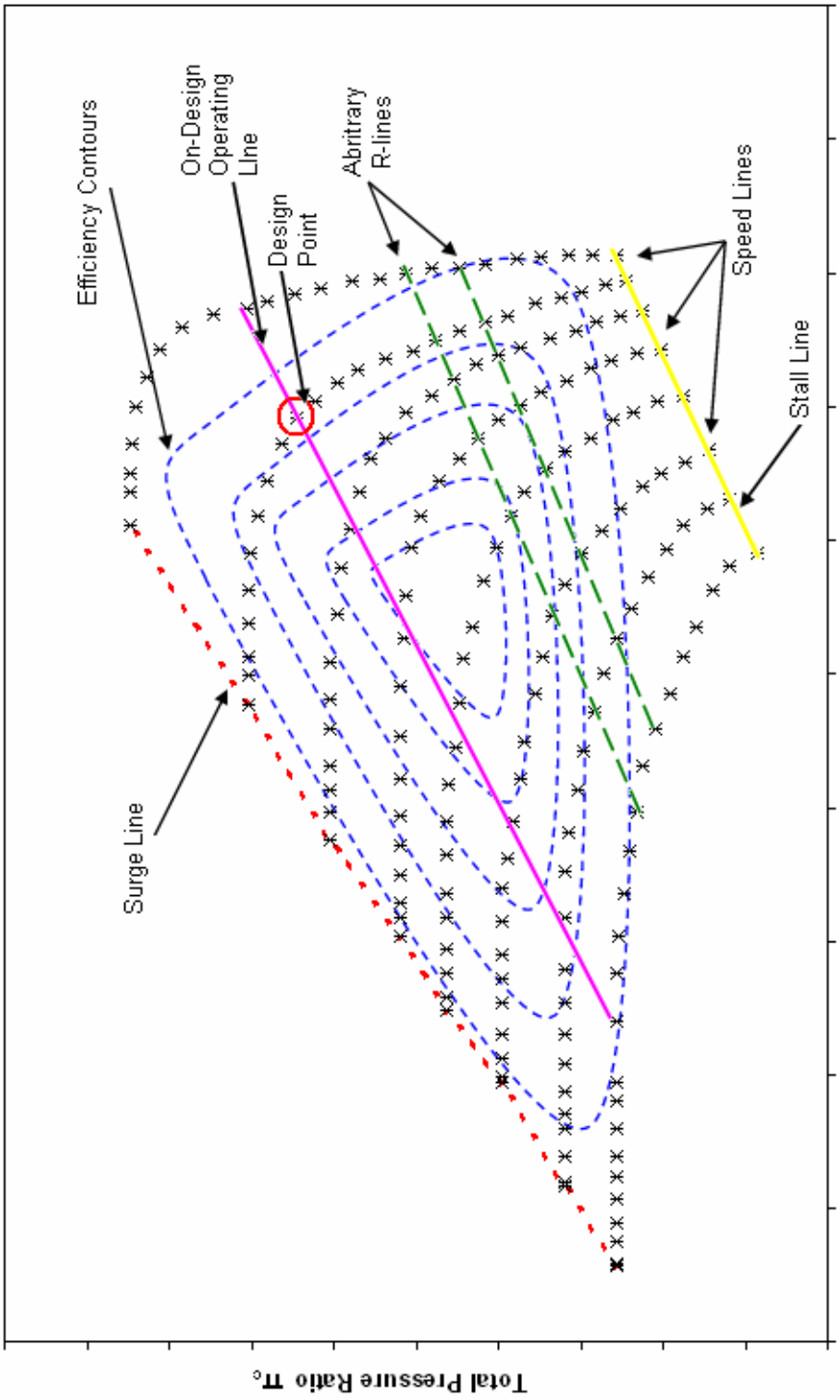

Figure 4.6: Theoretical Compressor Performance Map

4.1.1 Centrifugal Compressor

The microturbine generator inlet conditions are used to calculate the parameters at the compressor inlet, P_{t2} and T_{t2}. Using isentropic relations and the known freestream Mach number, static pressure and static temperature at the inlet, M_0, P_{s1}, and T_{s1} the total properties in the MTG inlet can be determined from,

$$\frac{T_{t1}}{T_{s1}} = 1 + \frac{\gamma - 1}{2} M_0^2 \tag{4.7}$$

and

$$\frac{P_{t1}}{P_{s1}} = \left(\frac{T_{t1}}{T_{s1}} \right)^{\gamma - 1 / \gamma} \tag{4.8}$$

Since the power generation system is stationary, the upstream Mach number is zero. The inlet is assumed adiabatic, therefore $P_{t2} \approx P_{t1}$ and $T_{t2} \approx T_{t1}$. The total pressure and temperature at the compressor inlet establish the operating properties, specific heat at constant pressure and volume and density of the flow through the compressor.

The assumptions applied to the centrifugal compressor are listed below and the values pertaining to the assumptions are listed in tabular form in Table 4.2:

- The MTG inlet is adiabatic
- The inlet static pressure and temperature are held constant, P_{s1} and T_{s1}
- The upstream Mach number M_0 is zero
- The area at the entrance to the inducer, Station 1 and entrance and exit to the compressor rotor, Station 2 and 3 are calculated at the design point and then held constant, A_1, A_2 and A_3 respectfully
- The number of rotor vanes n on the compressor is held constant

- The polytropic efficiency e_c of the compressor is held constant
- The compressor corrected mass flow rate $\dot{m}_{0c}$ is found by applying the desired throttle setting to the operating line
- The compressor total pressure ratio π_c is found by applying the desired throttle setting to the operating line

To calculate the actual mass flow rate in the compressor, $\dot{m}_0$ the total properties of pressure and temperature must be normalized (nondimensionalized) to sea-level-static (SLS) conditions in the following manner:

$$\delta = \frac{P_t}{P_{ref}} \tag{4.9}$$

$$\theta = \frac{T_t}{T_{ref}} \tag{4.10}$$

Where δ is the normalized pressure and θ is the normalized temperature. The reference pressure and temperature at SLS conditions are P_{ref} = 14.696 psia (101.3 kPa) and T_{ref} = 518.69ºR (288.2ºK) respectfully. Normalization identifies parameters that are associated with the microturbine generator's surroundings or environment and can be used to allow one set of data taken at a given set of conditions to be applied to that same set of data at other given set of conditions. These parameters are very useful since it is often unrealistic to gather experimental data for the seemingly infinite number of operating conditions that can be available, and it may not be feasible to obtain certain operating conditions in the laboratory.

Corrected mass flow rate for the compressor is defined as

$$\dot{m}_{0c} = \frac{\dot{m}_0 \sqrt{\theta_c}}{\delta_c} \tag{4.11}$$

From Equation 4.11, the actual mass flow rate through the compressor $\dot{m}_0$ is determined. With the compressor inlet pressure P_{t2} and compressor pressure ratio π_c known, the total pressure at the outlet of the compressor can be found from

$$\pi_c = \frac{P_{t3}}{P_{t2}} \tag{4.12}$$

The total temperature at the outlet of the compressor is found using an isentropic relationship between pressure and temperature ratios

$$\frac{T_{t3}}{T_{t2}} = \tau_c = \pi_c^{(\gamma-1)/\gamma e_c} \tag{4.13}$$

The polytropic efficiency e_c is assumed constant, and γ is the specific heat ratio. Once the total temperature ratio has been established, the isentropic efficiency of the compressor can be determined from

$$\eta_c = \frac{\pi_c^{\gamma-1/\gamma} - 1}{\tau_c - 1} \tag{4.14}$$

Applying the Euler equation for turbomachinery to the flow through the centrifugal compressor, the compressor rotor tip speed, U_{2t} is calculated by

$$T_{t3} - T_{t2} = \frac{\sigma U_{2t}^2}{g_c C_{pc}} \tag{4.15}$$

Where the slip factor, σ is related to the number of vanes on the rotor, n. As the number of vanes increases, the slip factor approaches 1. Selecting the number of vanes is a balance between high slip factor and reasonable friction loss. A slip factor of around 0.9 is very reasonable. The correlation between slip factor and number of vanes is

$$\sigma = 1 - \frac{2}{n} \tag{4.16}$$

The rotor tip speed U_{2t} is a tangential velocity and can be determined from the angular velocity, ω and the diameter of the rotor, d_2.

$$U_{2t} = d_2 \omega \tag{4.17}$$

Compressor shaft speed, N_c is related to the angular velocity, ω by the following

$$N_c = \omega \frac{60}{2\pi} \tag{4.18}$$

Solving for ω in Equation 4.18 and substituting into Equation 4.17 gives an equation for determining the shaft speed N_c with the tip speed U_{2t} and diameter of the rotor d_2 known.

$$U_{2t} = d_2 \frac{2\pi N_c}{60} \tag{4.19}$$

To ensure component matching, the shaft speed established in Equation 4.19 will be used to determine the turbine rotor tip speed and subsequently the turbine inlet temperature T_{t4} in Section 4.1.2. Energy rate balance is applied to the compressor parameters to determine the thermodynamic power or ideal power, Equation 4.20a, required to operate the compressor. The thermodynamic power is defined as the rate of mechanical energy input to the flowing fluid stream [65].

$$P_{c,th} = \dot{m}_0 C_{pc} \left(T_{t3} - T_{t2} \right) \tag{4.20a}$$

Where C_{pc} is the specific heat at constant pressure and is determined at the compressor inlet temperature T_{t2}. The mechanical power produced by turbomachinery, Equation 4.20b, is defined as the rate of work done on the rotor of the piece of turbomachinery [65]. This is considered the actual power required to operate the compressor and is calculated using enthalpy which is found individually at the entrance and exit temperatures of the compressor.

$$P_{c,m} = \dot{m}_0 \left(h_3 - h_2 \right) \tag{4.20b}$$

The 1-D mean-line calculations are completed station by station through the centrifugal compressor. A visual representation of this method is seen in Figure 4.7. The following parameters are calculated at each station: total and static temperature, total and static pressure, Mach number, absolute and relative velocity and all components of velocity, absolute and relative flow angles and the areas are calculated from the design point conditions. Calculations are based on trigonometry being applied to the velocity diagram in Figure 3.6, the rotor tip speed established in Equation 4.19, and isentropic relationships. Equations 4.21 through 4.24 demonstrate the application of trigonometry and isentropic relationships to the compressor stations. The compressor's stations can be reference in Figures 3.5 and 3.6 and an example of the 1-D Simulink model for Station 1 calculations is in Figure 4.8.

$$V_1 = u_1 = \sqrt{2 g_c C_{pc} T_{t1} \left(1 - \frac{1}{1 + \frac{\gamma - 1}{2} M_1^2} \right)} \tag{4.21}$$

$$v_{1Rh} = \frac{d_{1h}}{d_2} U_{2t} \tag{4.22}$$

$$V_{1Rh} = \sqrt{V_1^2 + v_{1Rh}^2} \tag{4.23}$$

$$\beta_{1h} = \tan^{-1} \frac{v_{1Rh}}{u_1} \tag{4.24}$$

In Equation 4.21, V_1 is the absolute velocity, u_1 is the axial component of absolute velocity, M_1 is the Mach number, and T_{t1} is the total temperature. For Equations 4.22 through 4.24, v_{1Rh} is the radial component of the relative velocity at the inducer hub, d_{1h} is the diameter of the inducer hub, d_2 is the diameter of the rotor, V_{1Rh} is the relative velocity at the inducer hub, and β_{1h} is the relative flow angle at the inducer hub. All 1-D

mean-line calculations listed in the above equations are located at Station 1 in the centrifugal compressor, see Figure 3.5. A similar approach is used to find the properties at Stations 2 and 3 in the compressor.

Table 4.2: Centrifugal Compressor Assumptions and Values

	Value	Units	Value	Units
P_{ref}	14.696	psia	101325	Pa
T_{ref}	518.67	ºR	288.2	ºK
P_{s0}	14.696	psia	101.3	kPa
T_{s0}	550.8	ºR	303.15	ºK
M_0	0	-	0	-
A_2	0.008273	ft^2	0.000769	m^2
A_3	0.348	ft^2	0.3233	m^2
n	18	-	18	-
e_c	0.87	-	0.87	-
d_{1h}	0.0925	ft	0.02819	m
d_{1t}	0.0185	ft	0.0056	m
d_{2r}	0.2846	ft	0.0867	m

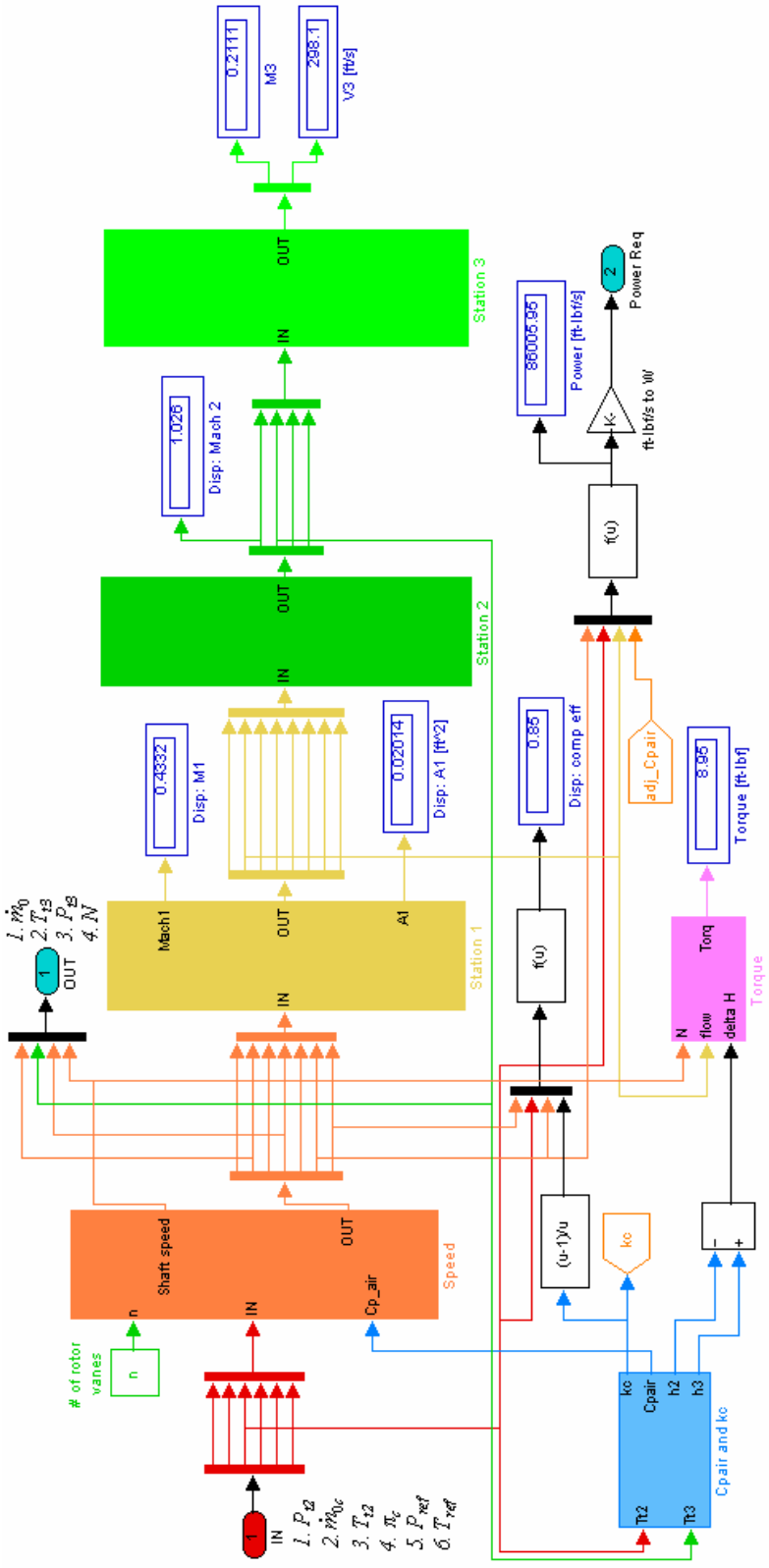

Figure 4.7: 1-D Centrifugal Compressor Model

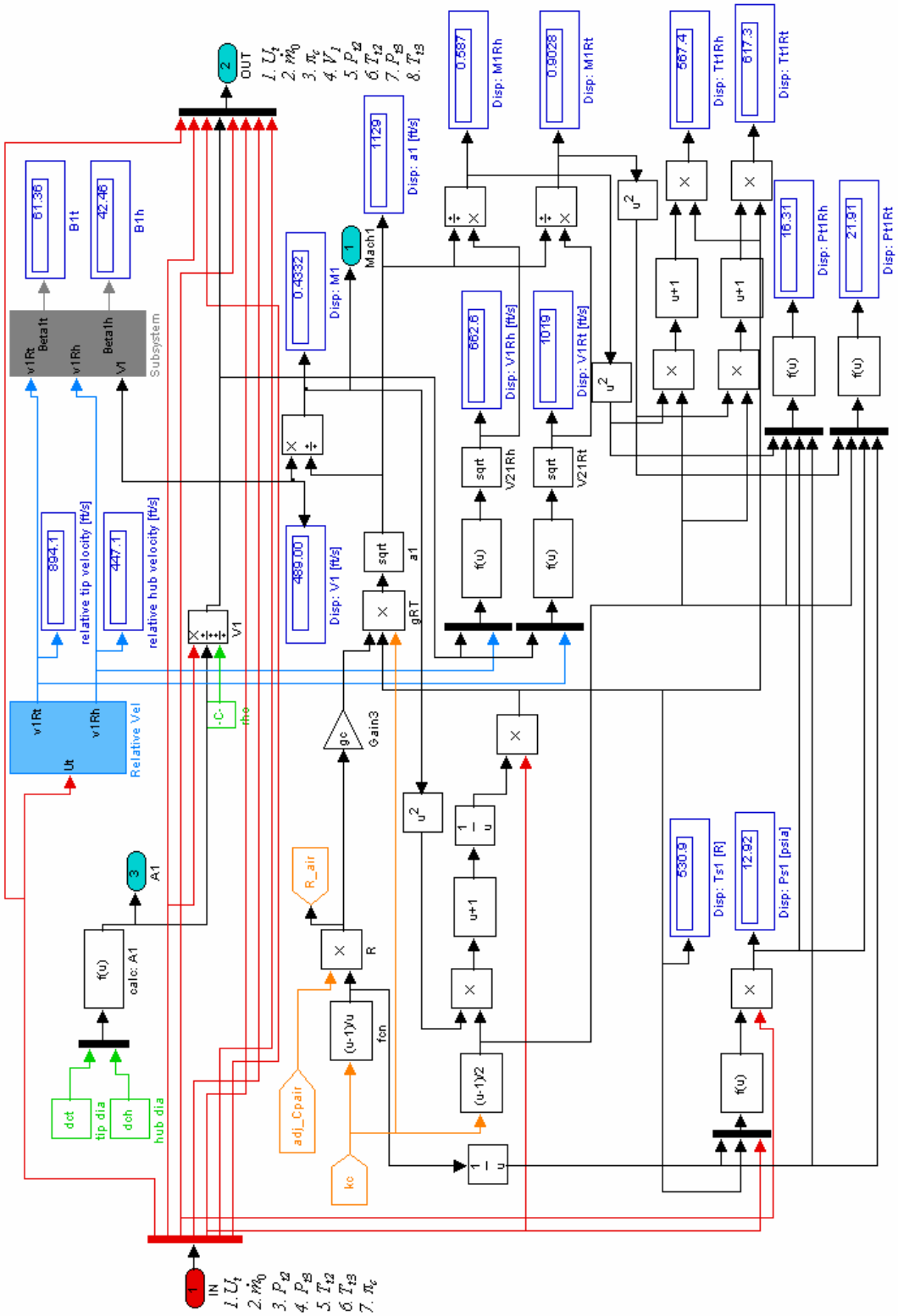

Figure 4.8: 1-D Centrifugal Compressor Station 1 Model

4.1.2 Radial Inflow Turbine

Component matching is used to begin the mathematical analysis on the single-stage radial inflow turbine. The centrifugal compressor and radial inflow turbine are mounted on a single shaft that is closely coupled; this requires that the shaft speed of the turbine be equal to the shaft speed of the compressor.

$$N_c = N_t = N \tag{4.25}$$

The additional assumptions applied to the turbine are listed below and the values pertaining to the assumptions are listed in tabular form in Table 4.3:

- The total pressure at the exit to the turbine P_{t5} is held constant
- The working fluid in the turbine is air
- The turbine isentropic efficiency, η_t is held constant
- The turbine polytropic efficiency e_t is assumed constant, from isentropic efficiency calculations
- The stator blade exit angle (absolute flow angle) α_2 is held constant
- The turbine hub/tip ratio r_h/r_t at Station 3 is held constant
- The areas entering and exiting the turbine rotor, Station 2 and 3 and exiting the turbine diffuser, Station 4 are calculated at the design point and held constant, A_2, A_3, and A_4 respectfully
- The turbine diffuser efficiency η_d is held constant
- The turbine diffuser is adiabatic

The tip speed of the turbine rotor, U_{2t} can be found from applying Equation 4.19 to the turbine

$$U_{2t} = d_{2r}\frac{2\pi N_t}{60} \tag{4.26}$$

Where d_{2r} is the diameter of the turbine rotor and U_{2t} is tip speed of the turbine rotor at Station 2. As the microturbine generator is driven along the operating line, to ensure that no violation of the conservation equations takes place, the total pressure at the exit to the turbine rotor P_{t5} is held constant. This allows for the isentropic efficiency η_t to be constant and the polytropic efficiency $e_c \approx$ constant.

The total properties at Station 1 of the turbine are equal to total properties at Station 2. The total pressure, P_{t4} corresponds to the total pressure at Station 2 and has been found through the combustion chamber mathematical modeling. Since the total pressure exiting the turbine rotor is held constant, the expansion ratio in the turbine $1/\pi_t$ is calculated by

$$1/\pi_t = P_{t4}/P_{t5} \tag{4.27}$$

Employing an isentropic relationship, the total temperature ratio in the turbine is

$$\tau_t = 1 - \eta_t\left(1 - \pi_t^{\kappa-1/\kappa}\right) \tag{4.28}$$

The isentropic efficiency η_t is held constant and κ is the specific heat ratio of the air flow in the turbine. Exploiting the Euler equation for turbomachinery, the temperature decrease in the radial inflow turbine is directly proportional to the rotor tip speed squared. A turbine inlet temperature T_{t4} can be found that will satisfy the assumption made in Equation 4.25

$$U_{2t}^2 = g_c C_{pt} T_{t4}\left(1 - \tau_t\right) \tag{4.29}$$

In Equation 4.29, C_{pt} is the specific heat at constant pressure of the air flow in the turbine taken at T_{t4}. The turbine inlet temperature is applied to the combustion chamber mathematical modeling to determine the mass flow rate of fuel required during combustion to reach the turbine inlet temperature calculated in Equation 4.29. The combustion chamber mathematical modeling is described in Section 4.1.3.

The energy rate balance is applied to the turbine flow parameters to determine the thermodynamic power produced by the turbine, Equation 4.30. The mechanical power or actual power produced by the turbine is given in Equation 4.31 and is produced through determining the actual enthalpy of the entrance and exit states of the turbine.

$$P_{t,th} = \dot{m}_t C_{pt} \left(T_{t4} - T_{t5} \right) \tag{4.30}$$

$$P_{t,m} = \dot{m}_t \left(h_4 - h_5 \right) \tag{4.31}$$

The net thermodynamic power output of the microturbine generator P_{th} is the thermodynamic power produce by the turbine $P_{t,th}$ minus the thermodynamic power required to run the compressor $P_{c,th}$. The net mechanical power or actual power produced by the microturbine generator P_m is $P_{t,m}$ minus $P_{c,m}$.

The actual power produced will be used to validate the 0-D hybrid power generation model and the 1-D zooming of the hybrid power generation model. The net thermodynamic power output will be used to determine the thermal efficiency η_{th} in the next section based on the lower heating value *LHV* and the higher heating value *HHV* of the fuel. The mass flow rate of the air in the turbine $\dot{m}_t$ is determined from conservation of mass

$$\dot{m}_t = \dot{m}_0 + \dot{m}_f \tag{4.32}$$

Where $\dot{m}_f$ is the mass flow rate of fuel required during combustion to obtain the desired turbine inlet temperature T_{t4}.

The 1-D mean-line calculations are completed station by station through the radial inflow turbine. A visual representation of this method is seen in Figure 4.9. As stated previously, the total properties at Station 1 are equal to the total properties at Station 2. The following parameters are calculated at Stations 2 and 3: total and static temperature, total and static pressure, Mach number, absolute and relative velocity and all components of velocity, absolute and relative flow angles and the areas are calculated from the design point conditions. Calculations are based on trigonometry being applied to the velocity diagram in Figure 3.8, the rotor tip speed established in Equation 4.26, and isentropic relationships. An example of the 1-D Simulink model for Station 2 calculations is in Figure 4.10.

Equations 4.33 through 4.36 demonstrate the application of trigonometry and isentropic relationships to the turbine stations. The turbine's stations can be referenced in Figures 3.7 and 3.8.

$$V_2 = \frac{U_{2t}}{\sin\alpha_2} \tag{4.33}$$

$$M_2 = \sqrt{\frac{2/(\kappa-1)}{2g_c C_{pt} T_{t2} \sin^2\alpha_2 / U_{2t}^2 - 1}} \tag{4.34}$$

$$u_3 = V_3 = w_2 = V_2 \cos\alpha_2 \tag{4.35}$$

$$M_3 = \sqrt{\frac{2/(\kappa-1)}{2g_c C_{pt} T_{t3} / V_3^2 - 1}} \tag{4.36}$$

At Station 2, Equations 4.33 and 4.34, V_2 is the absolute velocity, α_2 is the absolute flow angle, M_2 is the Mach number and T_{t2} is the total temperature where $T_{t2} = T_{t4}$. For Station 3 calculations, Equations 4.35 and 4.36, u_3 is the axial component of absolute velocity, V_3 is the absolute velocity, w_2 is the radial component of the absolute velocity at Station 2, M_3 is the Mach number, and T_{t3} is the total temperature where $T_{t3} = T_{t5}$.

The total pressure decrease seen in the turbine diffuser, Station 3 to Station 4 in Figure 3.7 and Stage 5 to Stage 6 in Figure 3.2a, is modeled by the following equation:

$$\frac{P_{t6}}{P_{t5}} = 1 - \frac{\frac{\kappa}{2} M_5^2 (1 - \eta_d)\left(1 - A_5 / A_6\right)^2}{\left[1 - \left(\frac{\kappa - 1}{2}\right) M_5^2\right]^{\kappa/\kappa - 1}} \tag{4.37}$$

All of the variables in Equation 4.37 are either held constant or calculated through the 1-D mean-line mathematical modeling. The diffuser is assumed adiabatic, therefore $T_{t5} \approx T_{t6}$ and conservation of mass gives $\dot{m}_6 = \dot{m}_5 = \dot{m}_t$.

Table 4.3: Radial Inflow Turbine Assumptions and Values

	Value	Units	Value	Units
P_{t5}	18.5	psia	127.6	kPa
η_t	0.88	-	0.88	-
α_2	70	º	70	º
d_{2r}	0.30	ft	0.0914	m
r_h/r_t	0.4	-	0.4	-
A_2	0.0113	ft^2	0.00105	m^2
A_3	0.0565	ft^2	0.00525	m^2
A_4	0.1876	ft^2	0.01743	m^2
η_d	0.9	-	0.9	-

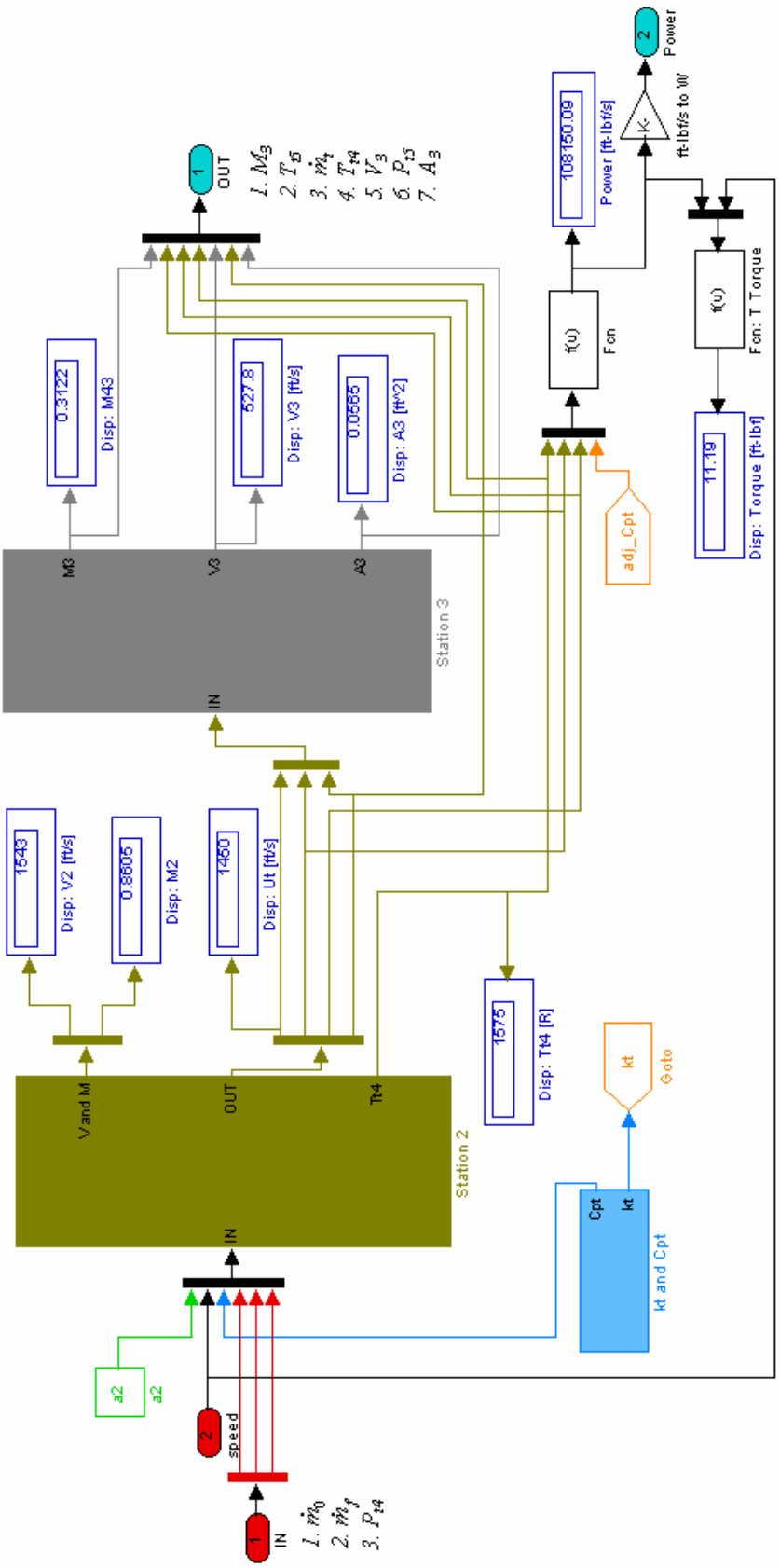

Figure 4.9: 1-D Radial Inflow Turbine Model

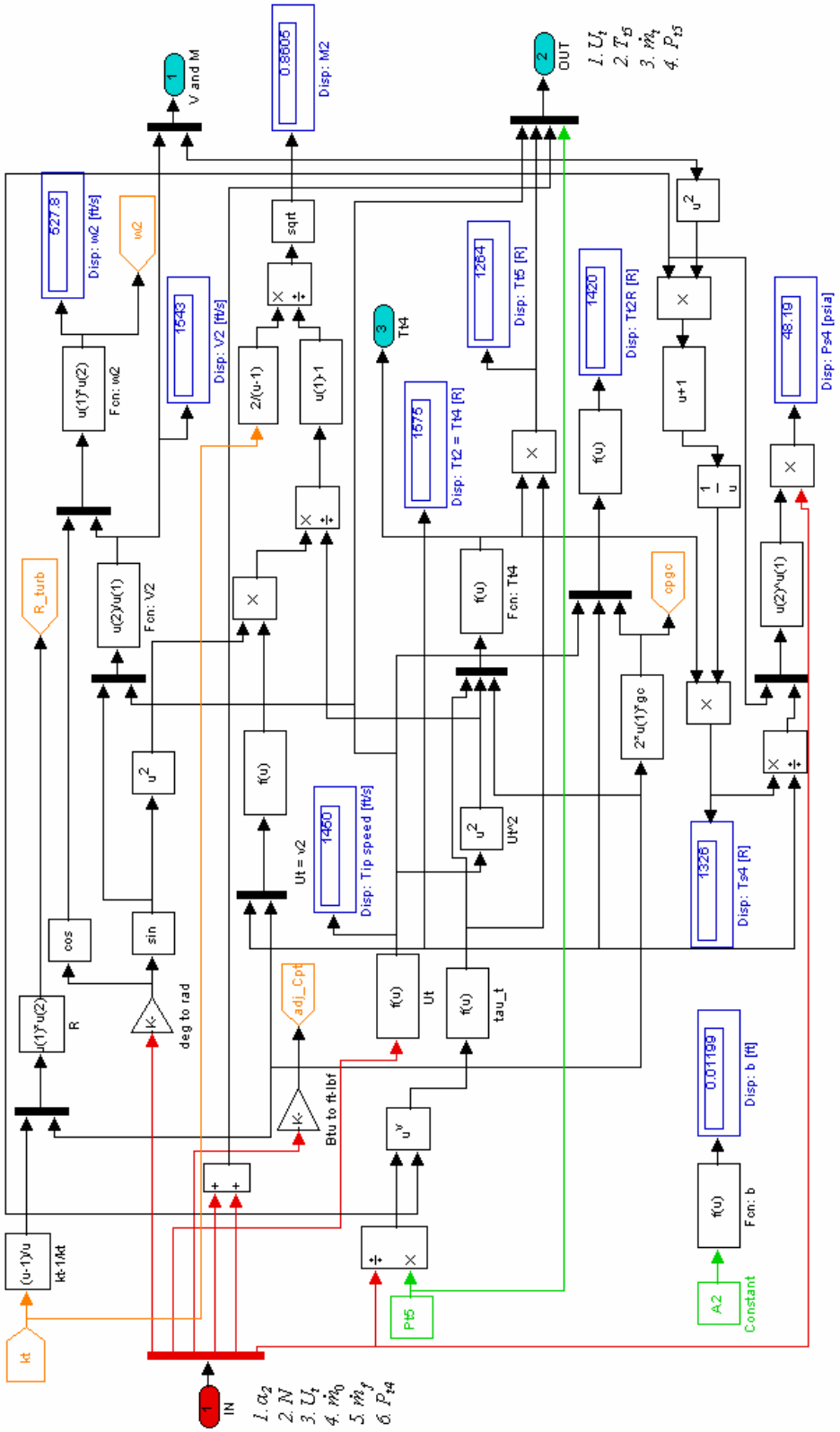

Figure 4.10: 1-D Radial Inflow Turbine Station 2 Model

4.1.3 Reverse Flow Annular Combustor

Combustor performance is measured by efficiency and the static pressure increase encountered in the combustor. The reaction in the combustion chamber is assumed to be isentropic; therefore a static pressure increase will give a resulting total pressure decrease. The combustor efficiency is a measure of the combustion completeness. The combustion completeness affects fuel consumption completely, since the heating value or lower heat value, LHV of any unburned fuel in not used to increase the turbine inlet temperature [48]. If there is less than 100 percent combustion, then total pressure loss will be present.

Combustion problems, not unlike fluid mechanics, can seldom be linearized. Analytical strategies require mathematical tools capable of dealing with non-linearities. It is a fact that simple mathematical models that incorporate a minimum of physics can be a source of physical insight superior to any other. When combustion is modeled in one dimension with simple chemistry the nonlinear nature of the conservation equations will prohibit obtaining exact solutions, but accurate estimations are possible [52].

Since combustion efficiency η_{cc} and total pressure loss represented by total pressure ratio π_{cc} are important to combustor performance, these two parameters are assumed to be of known and constant values, Table 4.4. A design parameter used is the maximum combustor exit temperature or turbine inlet temperature, T_{t4}. This design parameter is critical since the turbine blade material and configuration must be determined based on how hot the gases through the turbine will become. T_{t4} along with the combustion efficiency η_{cc}, will determine the mass flow rate of fuel needed to obtain

the desired turbine inlet temperature. Equation 4.38 is used in conjunction with equation 4.39 to find the fuel/air ratio, f and the mass flow rate of the fuel $\dot{m}_f$

$$f = \frac{\dot{m}_f}{\dot{m}_0} \tag{4.38}$$

$$\eta_{cc} = \frac{(1+f)C_{pt}T_{t4} - C_{pcc}T_{t3}'}{f \cdot LHV} \tag{4.39}$$

The equivalence ratio, φ is utilized to determine whether or not the combustor is running lean or rich. If $\varphi = 1$, then the combustor is said to be running stoichiometrically. For lean combustion (desired for low emissions) $\varphi < 1$, and for rich combustion $\varphi > 1$. The equivalence ratio is the ratio of actual fuel/air ratio to stoichiometric fuel/air ratio.

$$\varphi = \frac{f}{f_{stoich}} \tag{4.40}$$

In Equation 4.39, C_{pt} and C_{pcc} are the specific heat at constant pressure for the air in the turbine and the compressed air from the recuperator. The temperature of the compressed air out of the recuperator, T_{t3}', is higher than the compressed air directly from the compressor, T_{t3}. Therefore the specific heat, C_{pcc} is not the same as C_{pc}, defined in Section 4.1.2.

The performance of a system experiencing a power cycle can be expressed in terms of the extent to which energy is added by heat

$$\dot{Q}_{in\_LHV} = \dot{m}_f \cdot LHV \tag{4.41a}$$

$$\dot{Q}_{in\_HHV} = \dot{m}_f \cdot HHV \tag{4.41b}$$

This addition of heat is converted to a net thermodynamic power output of the microturbine generator, P_{th}. The degree of the energy conversion from heat to power is known as the thermal efficiency and can be determined from the *LHV* and from the *HHV* of the fuel. The *HHV* is considered by some to be the true energy content of the fuel [57]. The heat addition to the system will be calculated based on the *LHV* and on the *HHV* of natural gas, Equations 4.41a and 4.41b. The lower heating value thermal efficiency of the Capstone® Model 330 MTG is around 14 percent [16].

$$\eta_{th\_LHV} = \frac{P_{th}}{\dot{Q}_{in\_LHV}} \tag{4.42a}$$

$$\eta_{th\_HHV} = \frac{P_{th}}{\dot{Q}_{in\_HHV}} \tag{4.42b}$$

The lower and higher heating values of natural gas are given in Table 4.4. The pressure entering the combustion chamber P_{t3}' from the recuperator is used along with the combustion chamber total pressure ratio, held constant, to determine the total pressure entering the turbine, P_{t4}, Equation 4.43.

$$\pi_{cc} = \frac{P_{t4}}{P_{t3}'} < 1 \tag{4.43}$$

The parameters determined from the combustor calculations are the fuel mass flow rate needed to obtain the desired turbine inlet total temperature and the turbine inlet total pressure.

Table 4.4: Combustion Chamber Values

	Value	Units	Value	Units
π_{cc}	0.987	-	0.987	-
η_{cc}	0.98	-	0.98	-
f_{stoich}	0.05828	-	0.05828	-
LHV	16381	Btu/lbm	38.1	MJ/kg
HHV	18273	Btu/lbm	42.5	MJ/kg

4.1.4 Annular Wrap-Around Primary Surface Recuperator

The primary surface recuperator is modeled as a counter-flow heat exchanger with compressed air on the cold side and natural gas exhaust on the hot side. The hot side flow will be modeled as air. The Simulink model of the 1-D primary surface recuperator is represented in Figure 4.11. The heat transfer surface is a thin sheet of fin folded Type 347 stainless steel. On the cold side, mass flow rate $\dot{m}$, total pressure, and total temperature of compressed air are the input values. The same input values are seen on the exhaust (hot) side. The desired output values are the total pressure and total temperature of the compressed air and the exhaust. Parameters that are to be held constant can be seen in Table 4.5. The following equations can be applied to both the hot and cold sides of the recuperator core.

The inlet temperature is used to determine specific heat C_p, viscosity μ, density ρ, and thermal conductivity, k of the fluid. With these parameters the Prandtl number, Pr is determined from

$$\mathrm{Pr} = \frac{C_p \mu}{k} \tag{4.44}$$

The Reynolds number of a fluid is used to determined if the flow is laminar ($Re \leq 2300$), transitional ($2300 \leq Re \leq 10000$) or turbulent ($Re \geq 10000$). The Reynolds number is found from

$$\mathrm{Re} = \frac{\rho V D_h}{\mu} \tag{4.45}$$

The velocity of the fluid, V is determined from the mass flow rate, density, and the total cross sectional area of the flow geometry. The total cross sectional area of the flow A_{xtot}, both hot and cold, will be derived later in this section.

From the Reynolds number, the Darcy friction factor, *ff* as described by [36, 53] can be obtained. If the flow is laminar, $Re \leq 2300$, then

$$ff = \frac{64}{\mathrm{Re}_{Dh}} \tag{4.46}$$

For flow with Reynolds and Prandtl numbers of ($3000 < Re_{Dh} < 10^6$ and $0.5 < Pr < 2000$) the Darcy friction factor is calculated by

$$ff = \left(0.79 \ln \mathrm{Re}_{D_h} - 1.64\right)^{-2} \tag{4.47}$$

Equation 4.47 applies to internal flow with smooth surfaces [53]. The Nusselt number, *Nu* is the nondimensional convective heat transfer coefficient. This can be found based on the Reynolds number, Prandtl number and the Darcy friction factor. For laminar flow,

$$Nu = 4.36 \tag{4.48}$$

For Reynolds and Prandtl numbers of ($3000 < Re_{Dh} < 10^6$ and $0.5 < Pr < 2000$) the Nusselt number is calculated from

$$Nu_{Dh} = \frac{\left(ff/8\right)\left(\mathrm{Re}_{Dh} - 1000\right)\mathrm{Pr}}{1 + 12.7\left(ff/8\right)^{1/2}\left(\mathrm{Pr}^{2/3} - 1\right)} \tag{4.49}$$

Once the Nusselt number is known, the convective heat transfer coefficient *h*, Btu/hr-ft^2-R (W/m^2-K) can be determined from Equation 4.50.

$$Nu_{Dh} = \frac{hD_h}{k} \tag{4.50}$$

The convective heat transfer coefficient is used for determining the overall heat transfer coefficient for the recuperator core. The overall heat transfer coefficient is based on the outer heat transfer surface (hot flow side).

$$U_o A_o = \frac{1}{\frac{1}{A_i h_i} + \frac{1}{A_o h_o} + \frac{R_{fi}}{A_i} + R_w + \frac{R_{fo}}{A_o}} \tag{4.51}$$

In Equation 4.51, A_i is the total inner surface area of the air flow channel geometry and A_o is the outside surface area of the air flow channel geometry. The surface area for both inside and outside of one channel geometry is found by multiplying the wetted perimeter of one channel by the length of the recuperator core. The surface area is then multiplied by the total number of flow channels to get the total surface area. This technique is analogous with multiplying the circumference of a pipe by its length.

$$A_i = P_{c,in} L_{hx} \cdot NFC \tag{4.52}$$

$$A_o = P_{c,out} L_{hx} \cdot NFC \tag{4.53}$$

Where L_{hx} is the length of the recuperator core, $P_{c,in}$ is the wetted perimeter of the inside of the cold flow channel and NFC is the total number of flow channels. The parameters in Equations 4.52 and 4.53 are from Section 3.5. $P_{c,out}$ is the wetted perimeter of the outside of the cold flow channel. The convective heat transfer coefficients of the hot and cold flow, h_o and h_i, respectfully are found from Equation 4.50.

Applying a fouling factor or fouling resistance to each side of the heat transfer surface will help with design of an heat exchanger where fouling is anticipated. Fouling is the condition where undesirable substances may have accumulated on the heat transfer surface. The fouling resistance for compressed air, R_{fi} and natural gas exhaust, R_{fo} are given in Table 4.5. The last variable to be discussed in Equation 4.51 is the wall resistance, R_w based on the thickness of the channel material, t_{ss} and the thermal conductivity, k of the material.

$$R_w = \frac{t_{ss}}{kA_o} \tag{4.54}$$

Since the overall heat transfer coefficient has been established, the next step to mathematically modeling the recuperator core is to determine the heat capacity rate of both the hot and cold fluids. The fluid that may undergo the maximum temperature difference is the fluid with the minimum heat capacity rate. The heat capacity rates of the hot and cold fluids are denoted as C_h and C_c, respectfully. Where $C_h = \left(\dot{m}C_p\right)_{hot}$ and $C_c = \left(\dot{m}C_p\right)_{cold}$. If $C_c < C_h$, then $C_c = C_{min}$, else $C_h = C_{min}$. The number of transfer units, *NTU* is used to determine the heat exchanger effectiveness, ε.

$$NTU = \frac{U_o A_o}{C_{\min}} \tag{4.55}$$

Along with the capacity rate ratio, $C^* = \frac{C_{\min}}{C_{\max}}$, *NTU* is applied to Equation 4.56, for counterflow recuperator configurations.

$$\varepsilon = \frac{1 - \exp\left[-NTU\left(1 - C^*\right)\right]}{1 - C^* \exp\left[-NTU\left(1 - C^*\right)\right]} \tag{4.56}$$

Using the number transfer units and heat exchanger effectiveness to determine the heat transfer rate, $\dot{Q}$ is the ε-*NTU* method. The heat exchanger effectiveness calculated in Equation 4.56 is averaged for the actual operating cycle described in Section 3.5 and is held constant. The averaged heat exchanger effectiveness, ε_{avg} is used throughout the rest of the recuperator core mathematical modeling; a representation of this mathematical modeling can be seen in Figure 4.12.

The maximum possible heat transfer rate is expressed as [32]

$$\dot{Q}_{\max} = C_{\min}\left(T_{hi} - T_{ci}\right) \tag{4.57}$$

From Equation 4.57 and ε_{avg}, the heat transfer rate in the recuperator core is defined by

$$\varepsilon_{avg} = \frac{\dot{Q}}{\dot{Q}_{\max}} \tag{4.58}$$

The heat transfer rate is used in Equation 4.59 to determine the exit temperatures of the hot and cold fluids, T_{ho} and T_{co} which are the only unknowns.

$$\dot{Q} = C_h\left(T_{hi} - T_{ho}\right) \qquad \text{and} \qquad \dot{Q} = C_c\left(T_{co} - T_{ci}\right) \tag{4.59}$$

The pressure drop on both the hot and cold sides is calculated using the Darcy friction factor *ff*, the hydraulic diameter D_h, and the total cross-sectional area A_{xtot} of the respective hot and cold flow geometries. The Darcy friction factors are calculated from Equation 4.46 or 4.47, Reynolds number dependent, the hydraulic diameters are given in section 3.5, and the total cross-sectional area is given as

$$A_{xtot} = A_x NFC \tag{4.60}$$

The cross-sectional area A_x multiplied by the total number of flow channels, gives the total cross-sectional area. Equation 4.60 can be applied to the hot and cold flow channels. The pressure drop on the hot and cold side can then be calculated by

$$\Delta P = \frac{ff}{g_c}\frac{L_{hx}}{D_h}\frac{\dot{m}^2}{2\rho A_{xtot}^2} \tag{4.61}$$

Table 4.5: Recuperator Core Values

	Value	Units	Value	Units
R_{fi}	0.000999	hr-ft^2-R/Btu	0.000176	m^2-K/W
R_{fo}	0.005001	hr-ft^2-R/Btu	0.000881	m^2-K/W
ε_{avg}	0.8320	-	0.8320	-
$A_{xtot,c}$	0.233	ft^2	0.021647	m^2
$A_{xtot,h}$	0.3329	ft^2	0.030928	m^2
NFC	20618	-	20618	-

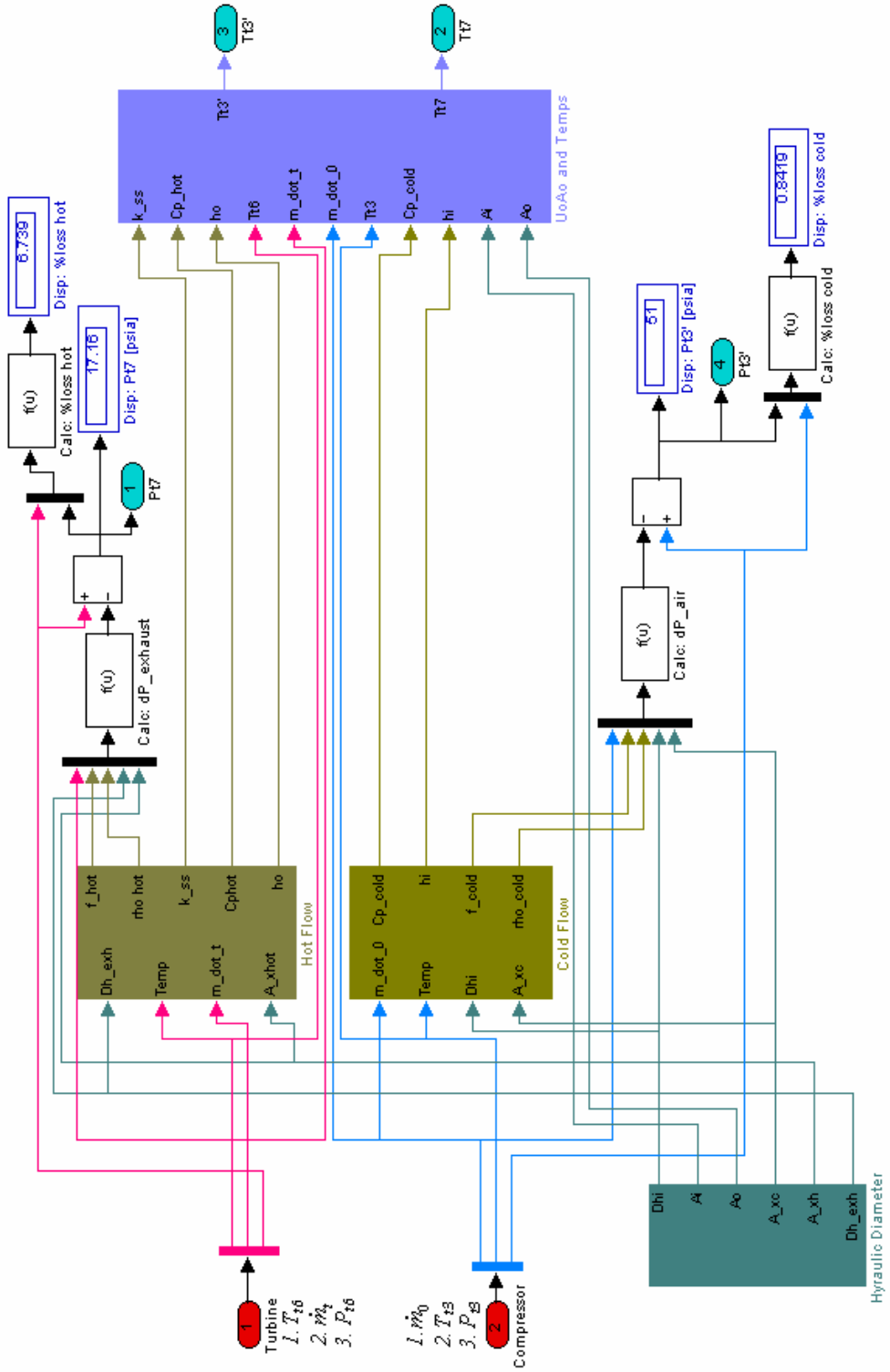

Figure 4.11: 1-D Primary Surface Recuperator Model

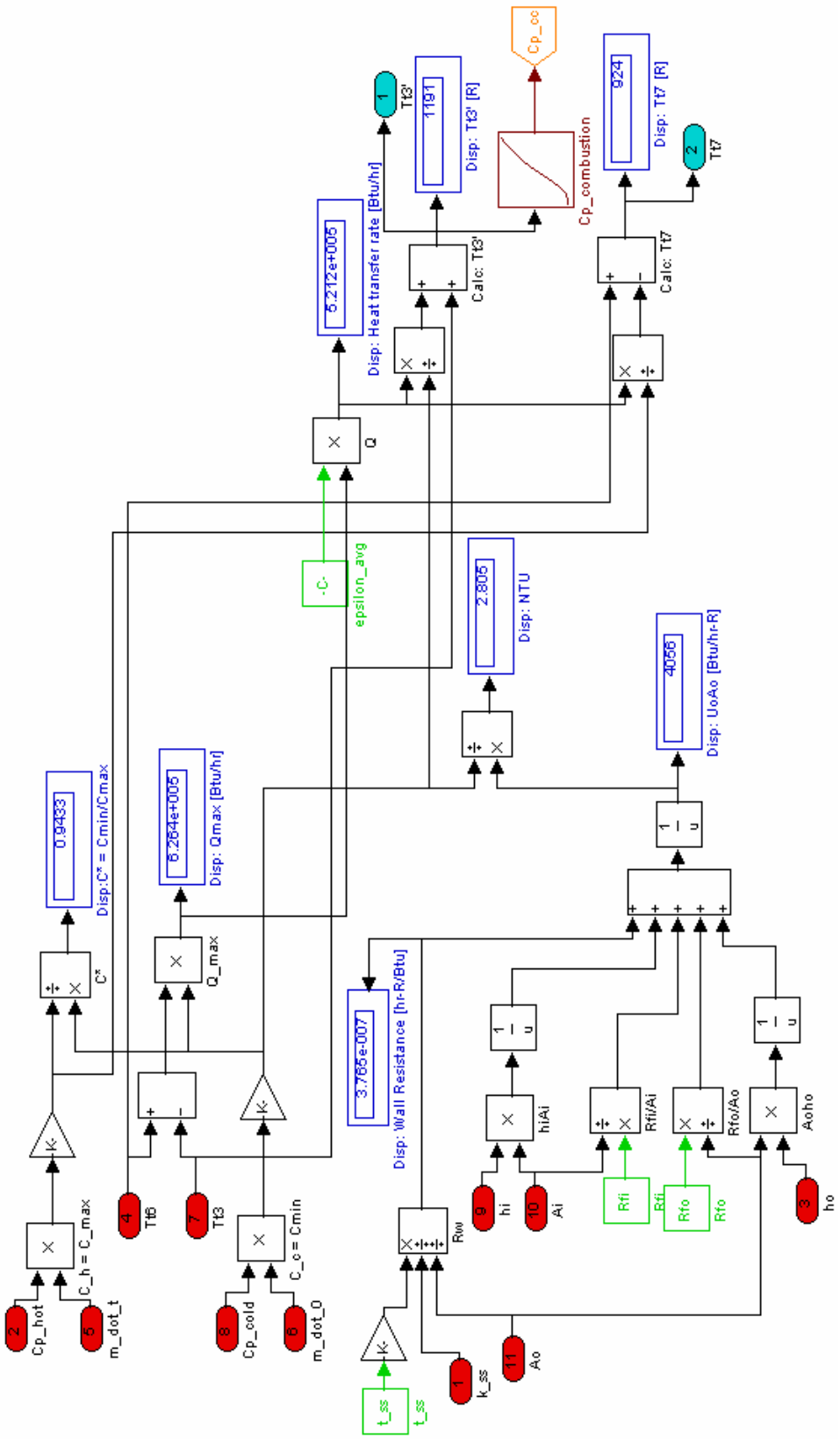

Figure 4.12: 1-D Primary Surface Recuperator T_{co} and T_{ho} Calculation Model

CHAPTER 5: METHODOLOGY OF HYBRID POWER GENERATION SYSTEM

There will be two MATLAB/Simulink® models discussed in this chapter; a 0-Dimensional analysis where all the components will be 0-Dimensional, and a 0-Dimensional model with 1-Dimensional zooming on the hybrid microturbine generator. Both of these models use the Simulink® variable time-step solver *ode23s* (stiff/Mod. Rosenbrock). The first model has the 0-Dimensional mathematical modeling of the hybrid microturbine generator (MTG) given in Section 5.1.1. The molten carbonate fuel cell (MCFC) model will be discussed in Section 5.1.2. The shell-and-tube heat exchanger will be mathematically modeled in Section 5.1.3. Section 5.1.2 and 5.1.3 are not the primary concern of this thesis but are included to provide closure for the mathematical modeling of the hybrid power generation system.

For the second model discussed, beginning with Section 5.2, the hybrid MTG main components, centrifugal compressor and radial inflow turbine, will be modeled with the 1-Dimensional approach while the remaining components of the hybrid power generation system will stay 0-Dimensional. This method is called zooming and is used when higher fidelity computations are desired for certain components in a system. The 1-D zooming of the MTG components will be mathematically modeled in Sections 5.2.1 and 5.2.2 and the method is analogous to the 1-D modeling of the compressor and turbine of the stand alone model simulation described in Sections 4.1.1 and 4.1.2, respectfully.

5.1 0 – Dimensional

The 0-D simulation is started by loading the MATLAB m-file controller. There are three components to the hybrid power system, the microturbine generator (MTG), the shell-and-tube heat exchanger and the molten carbonate fuel cell (MCFC). With the implementation of m-file controller file, the thermodynamic properties and individual component parameters of the MTG, the gas properties and sizing parameters of the heat exchanger, and the variables for the MCFC and the oxidizer are all loaded into the MATLAB workspace. Once all of the required information has been entered into the MATLAB workspace, the Simulink Graphical User Interface (GUI) is opened and the hybrid model is displayed.

The hybrid model operates with two different basis; the MTG and heat exchanger are on mass basis and the MCFC is mol basis. Also present in the model are two different unit systems. The MTG uses English units while the heat exchanger and MCFC use SI units. To compensate for the differences, a subsystem is employed to convert from one unit system to the other. The flow from the compressor into the shell of the shell-and-tube heat exchanger is converted from English to SI and then back again before it enters the turbine. The flow from the MTG diffuser is converted from English mass basis to SI mol basis before it enters the oxidizer subsystem. The flow from the oxidizer, tube-side flow, is converted from molar flow to mass flow in an internal subsystem located in the shell-and-tube heat exchanger model. This flow is converted back to molar flow before it enters the cathode on the MCFC.

The top level computer flow diagram to execute the 0-D modeling of the hybrid power system is in Figure 5.1. The top level Simulink model of the hybrid power system

can be seen in Figure 5.2 and the corresponding variable flow diagram is in Figure 5.3. The computational flow of the three main structures of the hybrid model; the MTG, the MCFC and shell-and-tube heat exchanger will be analyzed in Sections 5.1.1, 5.1.2 and 5.1.3, respectfully.

The hybrid Simulink model provides a modular environment with a GUI that allows for ease of operation and manipulation of a PID controller attached to the MTG subsystem. The proportional-integral-derivative (PID) controller is a feedback loop used to manipulate the power output of the microturbine generator. The controller takes an output value from the model and compares it with the model's desired output value. The difference or error is then used to adjust an input value in order to reach the desired output value. The PID controller adjusts the input value based on the rate of change of the error giving more accurate and stable control. The input that is fed to the Simulink model from the PID controller is the torque load applied to the shaft of the microturbine generator τ_{LOAD}. A model of the PID controller is shown in Figure 5.4. A controller has not been implemented for the MCFC portion of the model. The fuel flow to the anode of the MCFC is seen to be constant.

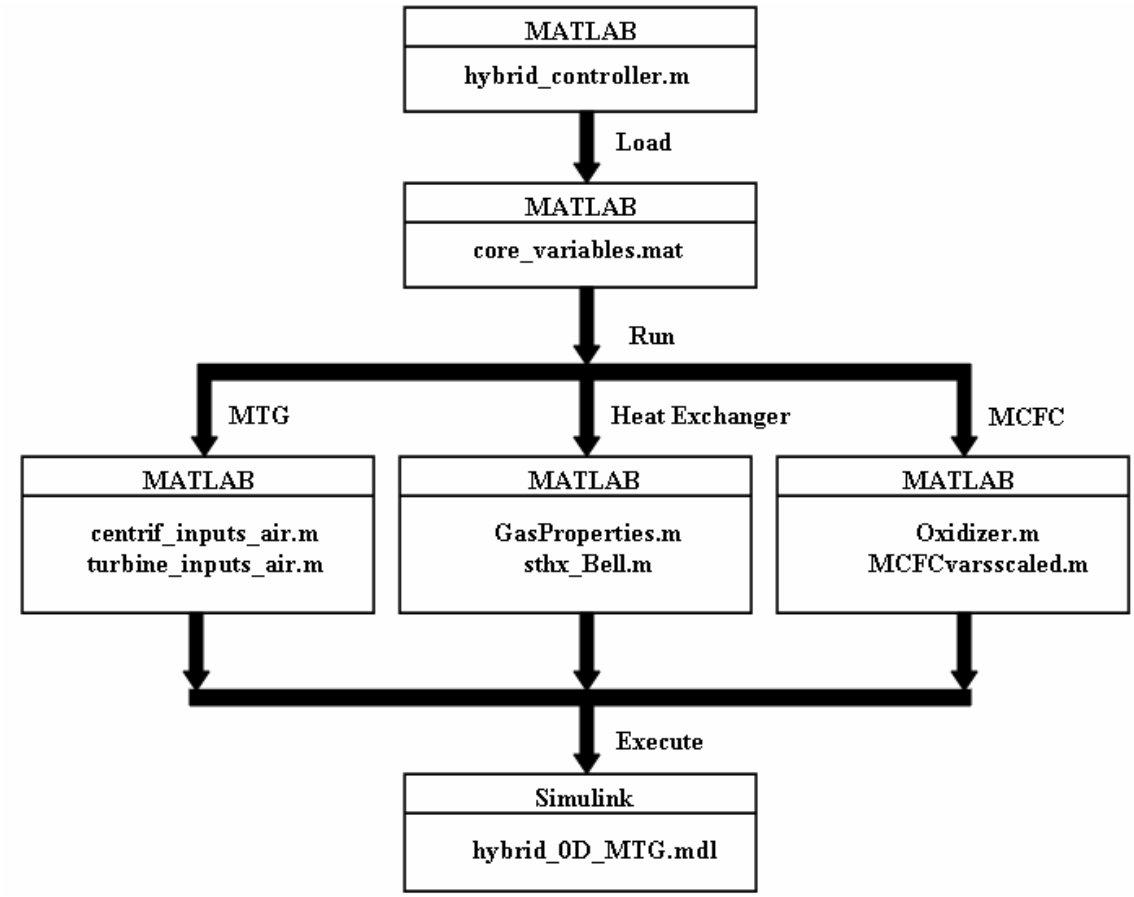

Figure 5.1: Computer Flow Diagram to Execute 0-D Modeling and Simulation of Hybrid Power Generation System

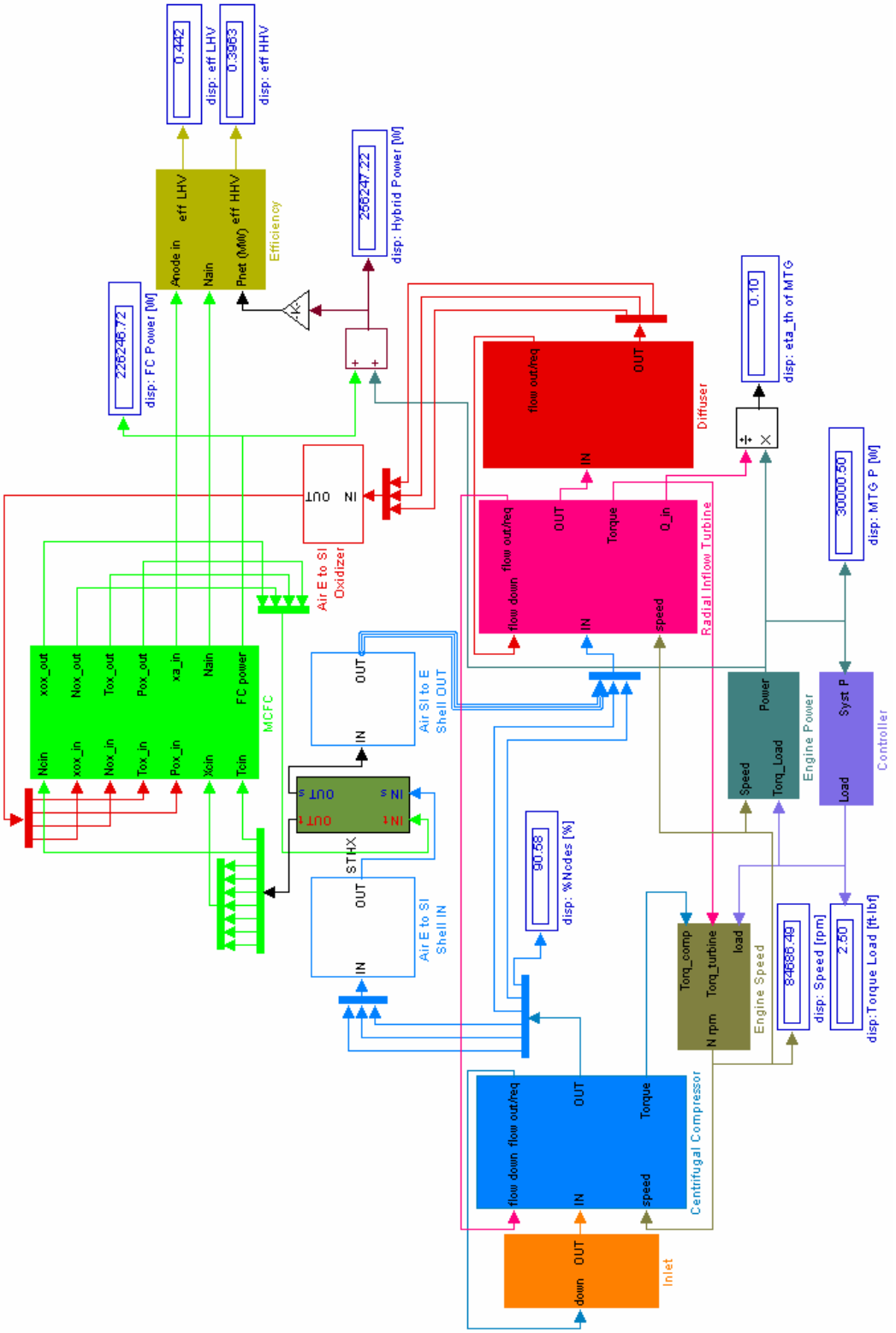

Figure 5.2: Top Level 0-D Hybrid Power Generation Model

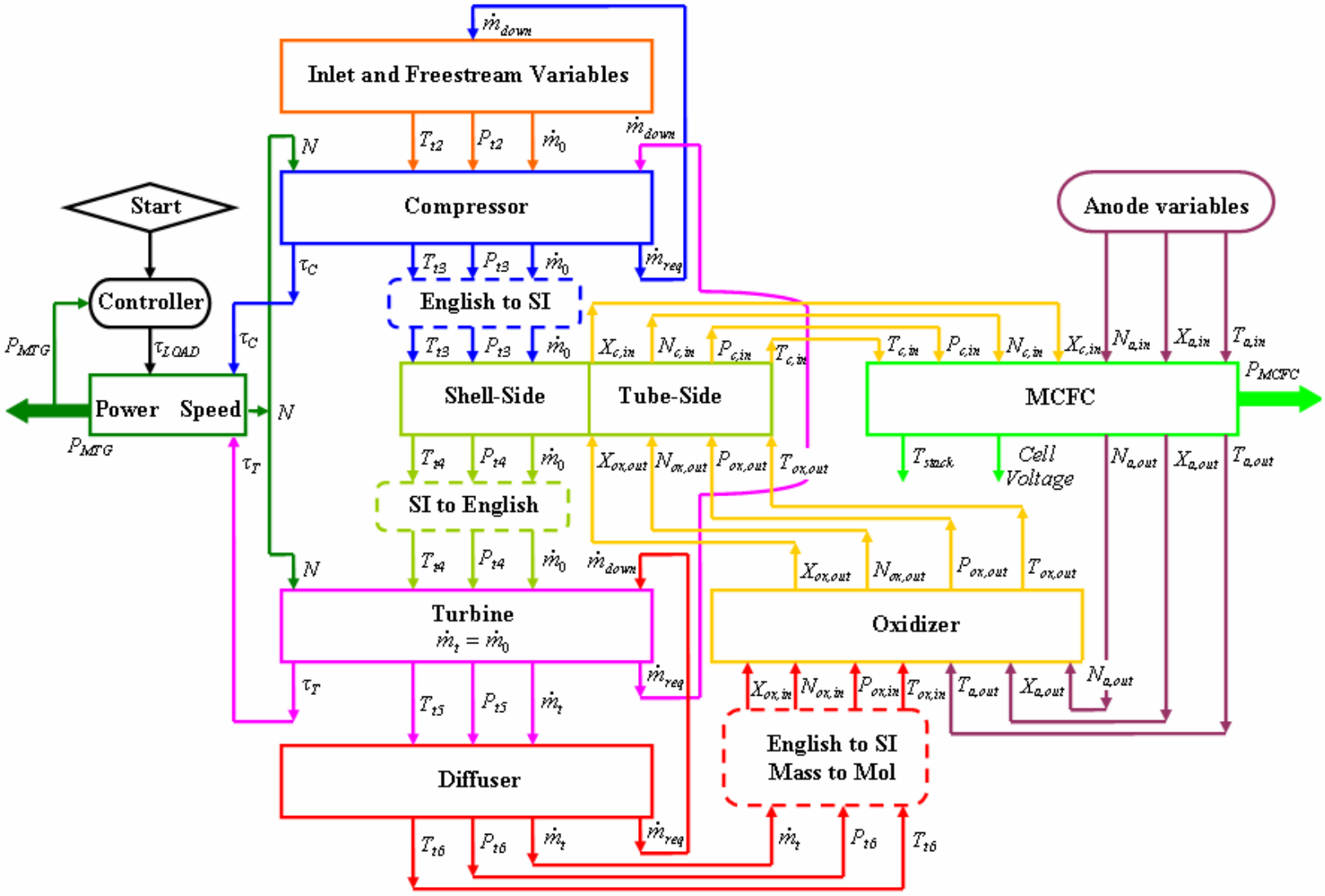

Figure 5.3: Variable Flow Diagram for Top Level 0-D Hybrid Model

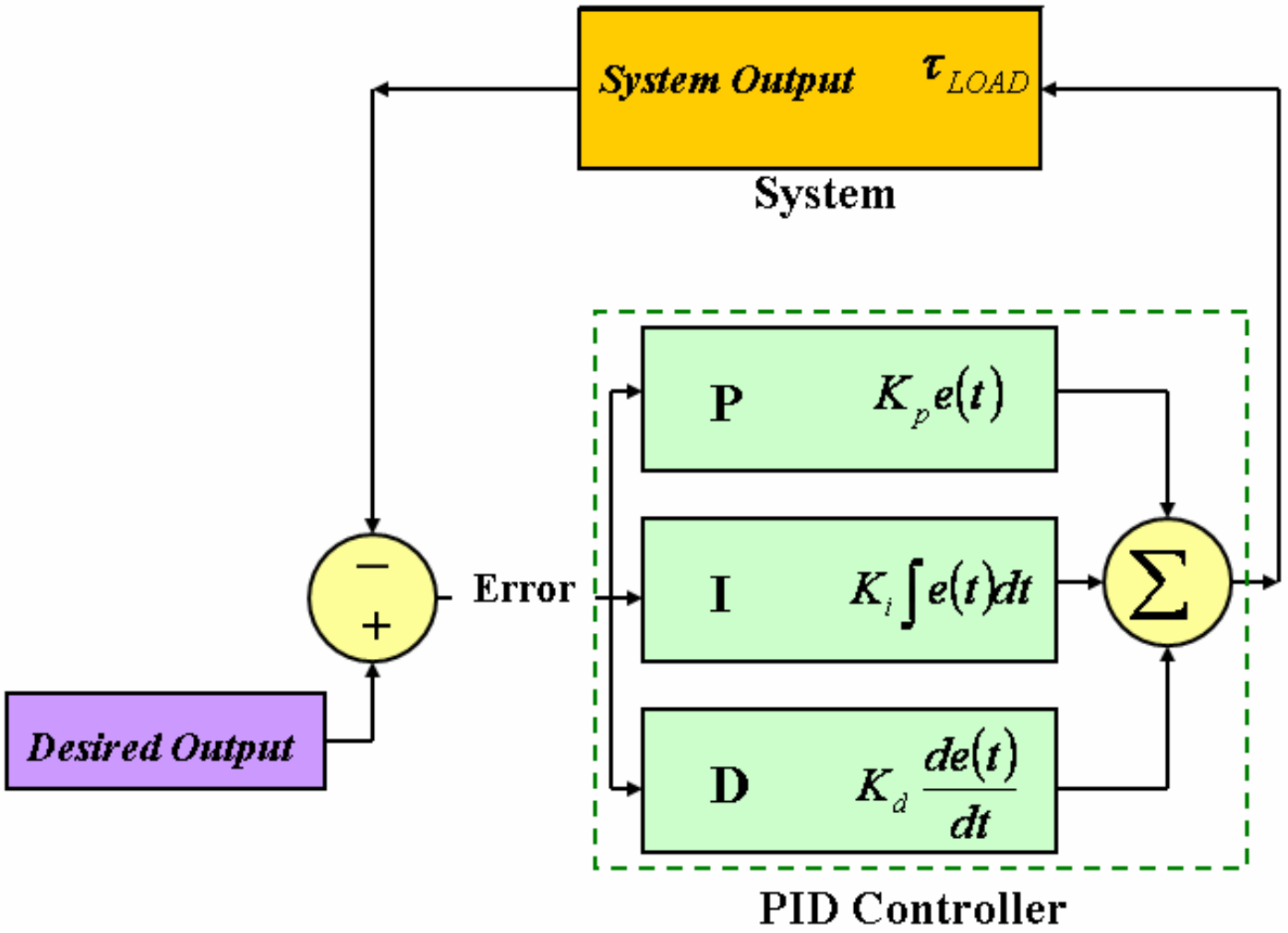

Figure 5.4: PID Controller for 0-D Hybrid Power Generation Model

5.1.1 Microturbine Generator (MTG)

5.1.1.1 Centrifugal Compressor

The 0-D centrifugal compressor is modeled using performance maps and isentropic relationships. The compressor inlet total pressure and temperature P_{t2} and T_{t2} are determined from the isentropic and adiabatic flow in the MTG inlet. To determine the total pressure and temperature exiting the compressor P_{t3} and T_{t3}, the compressor total pressure ratio π_c must be determined. The total pressure ratio along with the corrected mass flow rate $\dot{m}_{0c}$, and the isentropic efficiency η_c are seen in the compressor performance map portrayed in Figure 4.6. These three parameters are represented by 2-D arrays where the input values are the *R-line* as the row index input values and $N_{\%}$ as the column index input values. Using interpolation-extrapolation of the 2-D look-up tables representing the 2-D arrays in the MATLAB/Simulink® environment, the total pressure ratio π_c, corrected mass flow rate $\dot{m}_{0c}$ and isentropic efficiency η_c can be determined. A representation of the 2-D arrays is presented in Figures 5.5, 5.6, and 5.7. The tabular and plotted data can be seen in Appendix C.

The compressor *R-line* is determined through an algebraic constraint that is applied to an algebraic loop within the compressor module. This algebraic constraint incorporates the mass flow determined from the compressor maps $\dot{m}_0$, the compressor exit pressure P_{t3} determined from compressor mapping and from the volume dynamics applied to the compressor plenum volume The corresponding exit temperature T_{t3} is found after applying isentropic relationships to the pressure. A means of comparing the variables obtained from the compressor mapping to the variables provided through volume dynamics was establish. The mass flow rate, temperatures, and pressures

associated with the performance mapping and volume dynamics are compared by using a variation on the corrected mass flow equation, i.e.:

$$\left(\dot{m} \frac{\sqrt{T_{t3} / T_{t2}}}{P_{t3} / P_{t2}} \right)_{map} \tag{5.1}$$

$$\left(\dot{m} \frac{\sqrt{T_{t3} / T_{t2}}}{P_{t3} / P_{t2}} \right)_{voldyn} \tag{5.2}$$

Where $\dot{m}$ is the actual mass flow rate produced by the compressor performance mapping and is the same value in Equations 5.1 and 5.2. The difference between Equations 5.1 and 5.2 is sent to the algebraic constraint as *f(z)*. An algebraic loop created with this constraint can be seen in Figure 5.8. The *R-line* is the *z* that gives *f(z) = 0.* The algebraic constraint block in the Simulink environment is used to determine the *R-line* that allows for the compressor mapping technique to be feasible. In order for the *R-line* to converge, the difference between Equations 5.1 and 5.2 must be zero.

From the total pressure ratio and isentropic efficiency, the total temperature ratio, τ_c is found thus giving the total temperature exiting the compressor T_{t3}.

$$\tau_c = \frac{\left(\pi_c^{\gamma-1/\gamma} - 1 \right)}{\eta_c} + 1 \tag{5.3}$$

The polytropic efficiency is not directly used to calculate total pressure ratio and only the isentropic efficiency must be determined. To ensure that the 0-D simulation is correct

and has not been falsified, polytropic efficiency can be found from equation 5.4 and e_c must be less than one, $e_c < 1$ and should fundamentally be constant.

$$\tau_c = \pi_c^{\gamma-1/\gamma e_c} \tag{5.4}$$

The thermodynamic properties of enthalpy h, specific heat at constant pressure C_{pc}, and specific heat ratio γ are determined at the entrance and exit to the compressor based on the temperatures determined from the MTG inlet, T_{t2} and the relationship seen in Equation 5.3, T_{t3}. The torque that the centrifugal compressor applies to the microturbine generator τ_C is calculated in Equation 5.5 and this will be used to help with calculating the net mechanical power produced by the MTG.

$$\tau_C = \frac{60\dot{m}_0(h_3 - h_2)}{2\pi N} \tag{5.5}$$

The corrected mass flow rate in the compressor is determined from the 2-D array portrayed in Figure 5.5. The actual mass flow rate $\dot{m}_0$ is determined from the corrected mass flow rate equation

$$\dot{m}_{0c} = \frac{\dot{m}_0\sqrt{\theta_c}}{\delta_c} \tag{5.6}$$

This mass flow rate will be provided as the downstream flow for the inlet and represents the amount or value that is required from the upstream flow. The isentropic efficiency and total pressure ratio are determined by the 2-D array such that the total temperature exiting the compressor T_{t3} can be used to determine the total pressure exiting the compressor P_{t3} via the volume dynamics equation.

Volume dynamics, also known as the pressure derivative, represents the pressure variation due to the differential mass flow rate applied to a control volume on the

compressor. This control volume has been seen as a plenum volume by Roberts [54] and applied to the volume seen between the compressor and the turbine. For the MTG, the plenum volume will be within the control volume placed around the 0-Dimensional compressor mathematical modeling space. The differential pressure calculation is given in Equation 5.7.

$$\frac{dP_{t3}}{dt} = \frac{\gamma R T_{t3}}{\forall_c}\left(\dot{m}_{up} - \dot{m}_{down}\right) \tag{5.7}$$

The mass flow rate of fluid upstream of the compressor, from the inlet for the hybrid power generation systems is noted by $\dot{m}_{up}$. The mass flow rate of fluid downstream of the compressor, from the turbine in the hybrid power generation system is noted by $\dot{m}_{down}$. The shell-and-tube heat exchanger is downstream from the compressor, but since continuity is conserved, the downstream flow from the turbine is allowable. The plenum volume $\forall_c$ is a constant, and the value is determined from literature and has been optimized based on the results of the simulation.

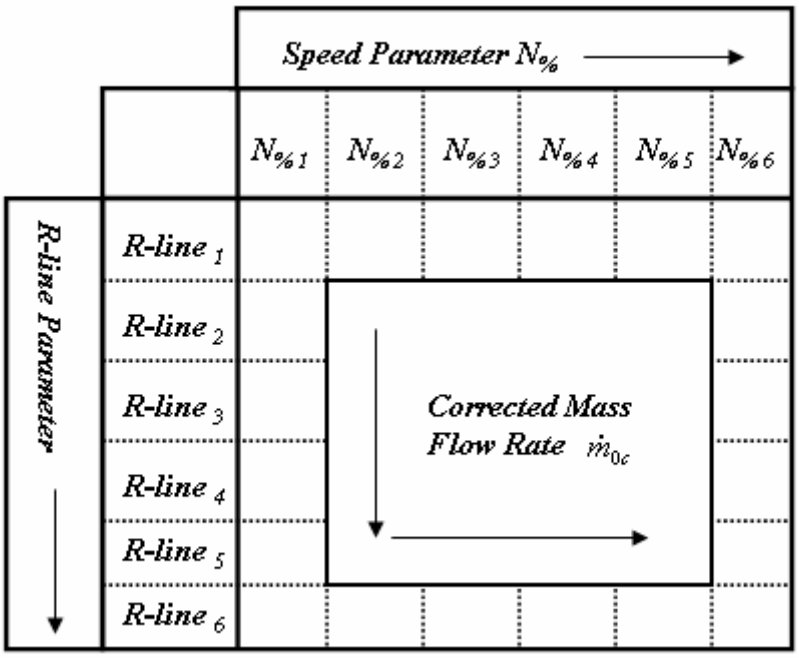

Figure 5.5: Compressor 2-D Array: Corrected Mass Flow Rate vs. Speed Parameter

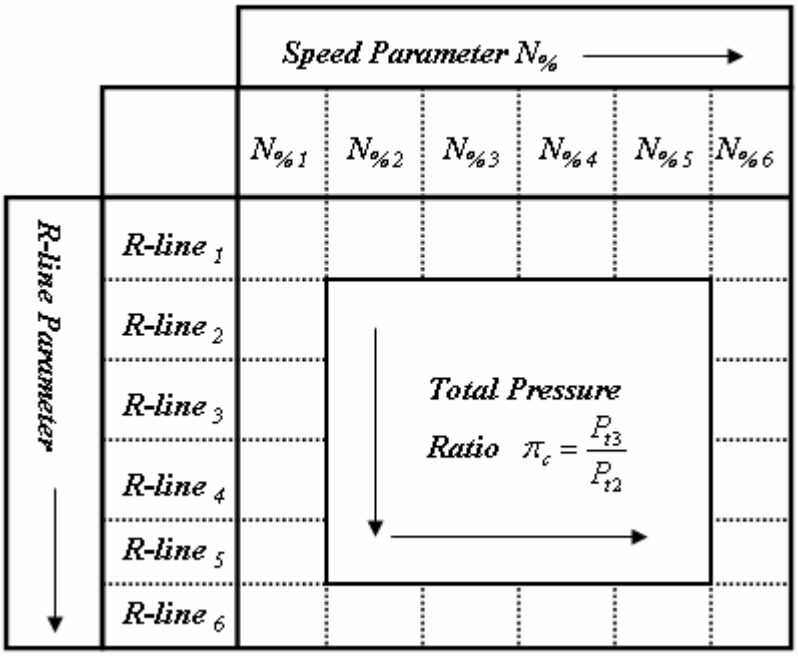

Figure 5.6: Compressor 2-D Array: Total Pressure Ratio vs. Speed Parameter

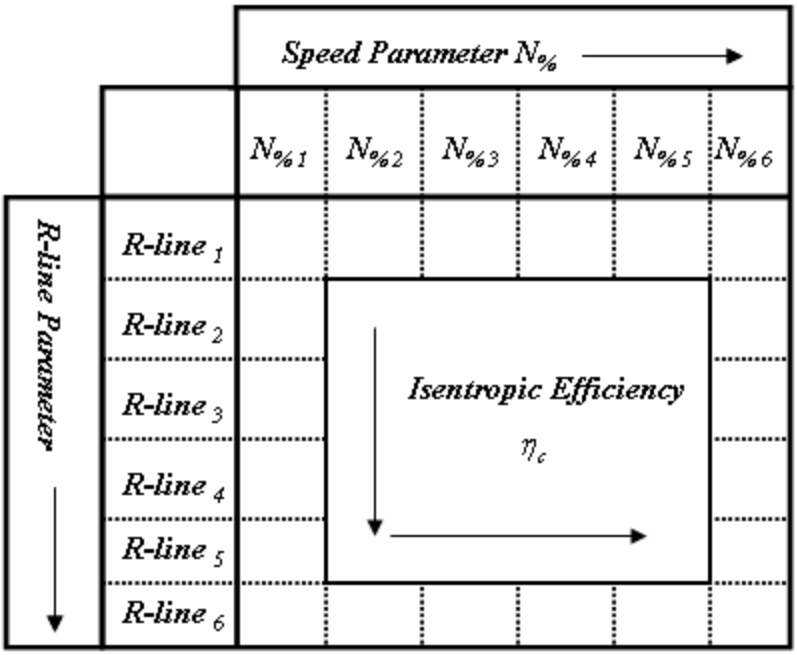

Figure 5.7: Compressor 2-D Array: Isentropic Efficiency vs. Speed Parameter

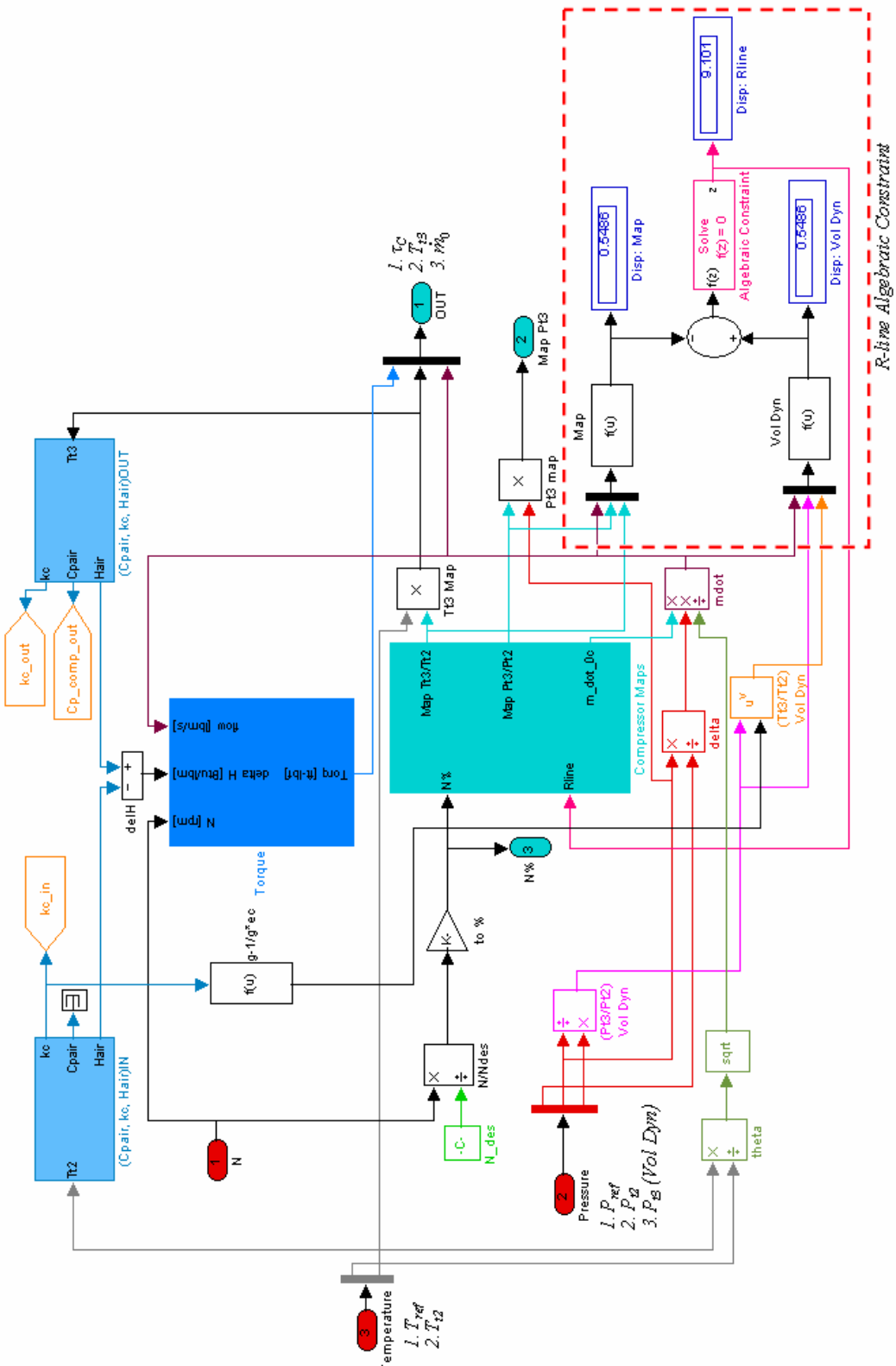

Figure 5.8: Compressor *R-line* Algebraic Constraint

5.1.1.2 Radial Inflow Turbine

Much like the centrifugal compressor, the radial inflow turbine is modeled using performance mapping and isentropic relationships. For the hybrid power generation system, P_{t4} and T_{t4} are determined from the 0-Dimensional mathematical modeling on the shell-and-tube heat exchanger described in Section 5.1.3. Performance mapping of the turbine incorporates the corrected mass flow rate $\dot{m}_{tc}$ only. The isentropic efficiency of the turbine η_t is still assumed constant and the expansion ratio $1/\pi_t$ of the turbine is determined from P_{t4} from the shell-and-tube heat exchanger and P_{t5} which is determined from applying volume dynamics or the pressure derivative to the plenum volume of the 0-Dimensional turbine mathematical modeling space. Since the 0-D calculations express a change in pressure based on the differential mass flow rate, P_{t5} cannot be held constant as with the 1-D case. The expansion ratio is not constant since it is dependent on the rotational speed of the microturbine generator which varies with the load applied on the shaft of the microturbine generator.

The 2-D array representing the corrected mass flow rate of the turbine $\dot{m}_{tc}$ with the expansion ratio as the row index input values and $N_{\%}$ as the column index input values is seen in Figure 5.9. The tabular and plotted data can be seen in Appendix D. Interpolation-extrapolation is used on the 2-D look-up table representing the 2-D array in the MATLAB/Simulink® environment. The total temperature ratio τ_t can be determined from Equation 5.8. This will be used to calculate the total temperature exiting the turbine T_{t5}. The specific heat ratio of the air in the turbine is represented by κ.

$$\tau_t = 1 - \eta_t \left(1 - \left(1/\pi_t \right)^{1-\kappa/\kappa} \right) \tag{5.8}$$

The torque applied to the microturbine generator by the turbine τ_T is calculated from the power provided by the turbine, $P = \dot{m}_t \Delta h$ and the rotational speed of the shaft *N*. The turbine torque is calculated from Equation 5.9 and this torque will be used along with the compressor torque to calculate the net mechanical power produce by the MTG.

$$\tau_T = \frac{60\dot{m}_t \left(h_4 - h_5\right)}{2\pi N} \tag{5.9}$$

The actual mass flow rate in the turbine $\dot{m}_t$ can be determined from the equation representing the corrected mass flow rate in the turbine

$$\dot{m}_{tc} = \frac{\dot{m}_t \sqrt{\theta_t}}{\delta_t} \tag{5.10}$$

Where δ_t is the normalized pressure ratio in the turbine and θ_t is normalized temperature ratio in the turbine. This mass flow rate will be provided as the downstream flow for the compressor in the hybrid power system and represents the amount or value that is required from the upstream flow.

The volume dynamics is represented in the same fashion as seen with the compressor. The control volume is place around the turbine 0-D mathematical modeling space and is represented by the following equation:

$$\frac{dP_{t5}}{dt} = \frac{\kappa R T_{t5}}{\forall_t} \left(\dot{m}_{up} - \dot{m}_{down}\right) \tag{5.11}$$

The plenum volume of the turbine is constant and determined from literature and optimization based on simulation results. The mass flow rate of fluid upstream of the turbine, from the shell-and-tube heat exchanger for the hybrid power system is distinguished by $\dot{m}_{up}$. The mass flow rate of fluid downstream of the turbine, flow from the diffuser in the hybrid power system is given $\dot{m}_{down}$.

The final step to mathematically modeling the 0-D compressor and turbine is to calculate the rotational speed of the shaft and the power output of the microturbine generator. A turbine shaft is mathematically modeled to mechanically connect the compressor and turbine components and determine the speed and net power relationships of a microturbine. The general approach is to sum the torques seen in the system where a positive torque balance will increase the rotational speed and a negative torque balance will decrease the rotational speed [54].

$$\Delta\tau = \tau_t - \tau_C - \tau_{LOAD} - \tau_{LOSS} \tag{5.12}$$

The torque on the turbine is τ_T, τ_C is the torque on the compressor, τ_{LOAD} is the load on the shaft (generator load used to determine power) and τ_{LOSS} is the bearing loss. The bearing loss is to be neglected since the shaft runs on air bearings with no friction [6], therefore $\tau_{LOSS} \approx 0$ in Equation 5.12 and is neglected. Equilibrium or convergence of the torques will establish that steady-state operation has been reached. The shaft balance equation in differential form is represented by Equation 5.13.

$$\frac{d\omega}{dt} = \frac{1}{J}\left(\tau_T - \tau_C - \tau_{LOAD}\right) \tag{5.13}$$

Where J is the combined compressor and turbine moment of inertia and ω is the angular velocity of the shaft. The combined moment of inertia is calculated by superposition of the compressor and turbine moment of inertia

$$J = J_c + J_t \tag{5.14}$$

Where $J_c = \frac{1}{2} m_c r_c^2$ and $J_t = \frac{1}{2} m_t r_t^2$. The radius of the compressor and turbine are given r_c and r_t, respectfully. The masses of the compressor and turbine m_c and m_t are roughly based on a 3.4 inch diameter compressor made out of aluminum and a 3.6 inch diameter turbine made of steel. These values can be seen in Table 5.1. The values of the plenum volume for both compressor and turbine will also be represented in Table 5.1. All other mentioned constants are the same as seen in the 1-D analysis, Sections 4.1.1 and 4.1.2. The relationship between the angular velocity ω and shaft rotational speed N is established as

$$\omega = N \frac{2\pi}{60} \tag{5.15}$$

Substituting Equation 5.15 into Equation 5.13 yields the shaft balance equation in terms of shaft rotational speed N.

$$\frac{dN}{dt} = \frac{60}{2\pi J} \left(\tau_T - \tau_C - \tau_{LOAD} \right) \tag{5.16}$$

The mechanical power produced by turbomachinery is defined as the rate of work done on the rotor of the piece of turbomachinery [56]. The net mechanical power output of the microturbine generator is calculated from the torque load applied to the generator τ_{LOAD} and the angular velocity ω. The relationship between angular velocity and rotational speed N is utilized and the net mechanical power is calculated from Equation 5.17.

$$P_m = \tau_{LOAD} \omega = \tau_{LOAD} \frac{2\pi N}{60} \tag{5.17}$$

Table 5.1: Compressor and Turbine Values as Applied to the 0-Dimensional Analysis

	Value	Units	Value	Units
m_c	2.27070	lbm	1.02998	kg
m_t	6.08470	lbm	2.76000	kg
J_c	0.02299	lbm-ft^2	0.00097	kg-m^2
J_t	0.06850	lbm-ft^2	0.00289	kg-m^2
J	0.09144	lbm-ft^2	0.00385	kg-m^2
r_c	0.14230	ft	0.04337	m
r_t	0.15000	ft	0.04572	m
$\forall_c$	0.00500	ft^3	0.00014	m^3
$\forall_t$	0.01185	ft^3	0.00034	m^3

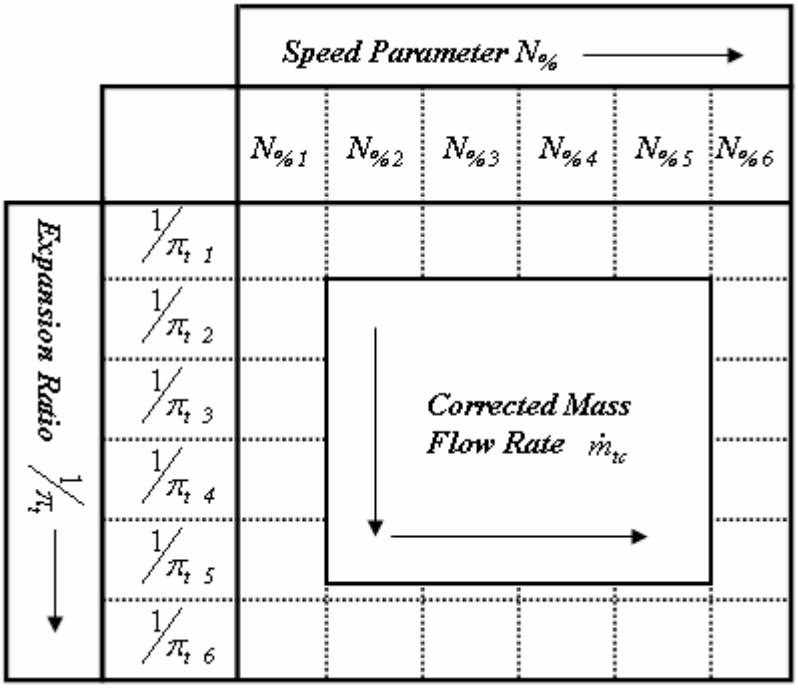

Figure 5.9: Turbine 2-D Array: Corrected Mass Flow Rate vs. Speed Parameter

5.1.2 Molten Carbonate Fuel Cell (MCFC)

Molten carbonate fuel cells (MCFC) that operate at high temperatures are an excellent source of clean and reliable power. These energy plants use fossil fuel in an efficient and affordable manner to produce electricity. The high temperature allows for the MCFC to operation on a more abundant array of fuels, such as natural gas, gasified coal and biomass derivatives than lower temperature fuel cells and this is done without the use of an external reformer. The high temperature operation also allows for cogeneration applications that take advantage of the waste heat generated from the fuel cell reactions.

The MCFC model is fed a mixture of water and natural gas. Before the natural gas can enter the fuel cell it must be processed. The natural gas may contain additives that are harmful to the fuel cell's performance. Sulfur compounds (H_2S), halides (HCl), and nitrogen compounds (NO_x) are undesirable in any concentration in the fuel cell operations. The water is preheated by the cathode off-gas through a series of heat exchangers and then fed to the fuel cell with the natural gas at a 2:1 steam to carbon ratio. This is done to prevent carbon deposits.

The MCFC model developed for this hybrid system incorporates internal reforming of the natural gas. Once the natural gas/steam mixture is inside the fuel cell model, the mixture is reformed to hydrogen through direct internal reforming (DIR) and indirect internal reforming (IIR), Figure 5.10. The combination of DIR and IIR gives a more efficient use of the useful waste heat to drive the reformation reactions. The IIR occurs through the use of a nickel based catalyst placed between every 10 cells of the stack [59]. DIR occurs via the water-gas shift reaction that occurs at the high operating

temperatures of the MCFC. The reformation reaction is seen in Equation 5.18 and the water-gas shift (WGS) reaction is given in Equation 5.19.

$$CH_4 + H_2O \rightarrow CO + 3H_2 \tag{5.18}$$

$$CO + H_2O \rightarrow CO_2 + H_2 \tag{5.19}$$

As described by Lukas and Lee [58] there are two additional electrochemical reactions of note taking place within the molten carbonate fuel cell. The hydrogen produced by the IIR reaction is introduced to the porous anode. An oxidant comprised of a mixture of oxygen and carbon dioxide is introduced at the porous cathode electrode. At the cathode, the O_2 and CO_2 in the oxidant stream react with electrons to form carbonate ions, this is seen in Equation 5.20.

$$\frac{1}{2}O_2 + CO_2 + 2e^- \rightarrow CO_3^= \quad Cathode \tag{5.20}$$

The carbonate ions migrate to the anode through the molten salt electrolyte. The hydrogen reacts with the carbonate ions to produce water and carbon dioxide, Equation 5.21.

$$H_2 + CO_3^= \rightarrow H_2O + CO_2 + 2e^- \quad Anode \tag{5.21}$$

The anode and cathode reactions are combined to get the overall chemical reaction of the fuel cell. The carbon dioxide present on both sides of the chemical reaction in Equation 5.22 does not cancel as is normally seen in chemical equation balancing. This is because the CO_2 on the anode side is generated when the anode gas is oxidized.

$$H_{2(anode)} + \frac{1}{2}O_{2(cathode)} + CO_{2(cathode)} \rightarrow H_2O + CO_{2(anode)} + HEAT + POWER \tag{5.22}$$

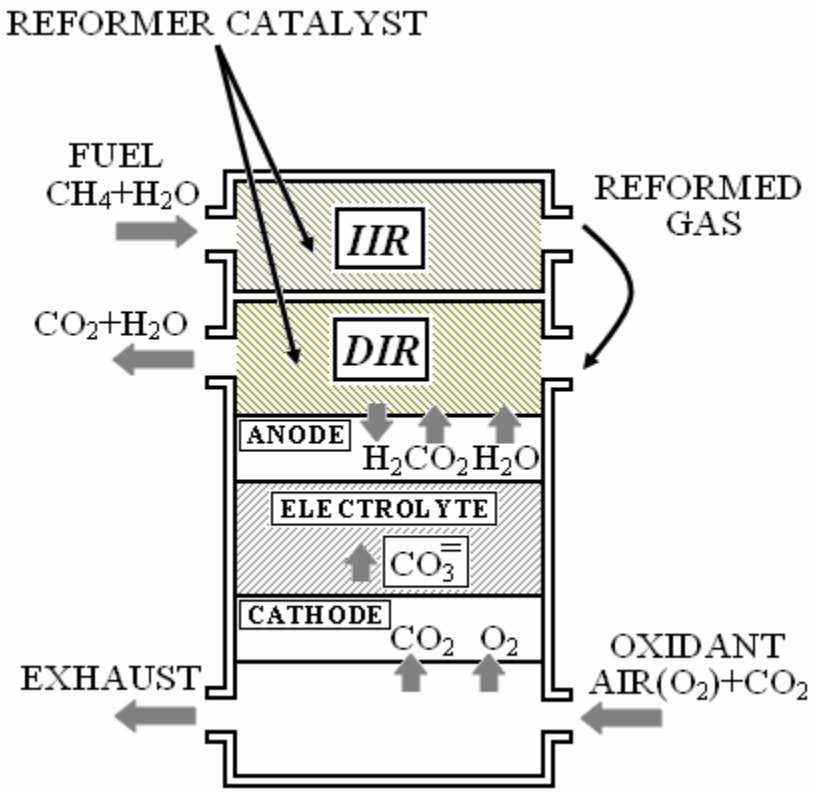

Figure 5.10: MCFC with Structure for Indirect and Direct Internal Reforming

5.1.2.1 Anode and Cathode Ideal Gas Equations

A complete derivation of all the equations modeling in the MCFC section of the 0-D hybrid power generation model is not given in this thesis. The parameters associated with the conservation equations, power and voltage will be addressed. The following assumptions derived from Lukas and Lee [58] have been applied to the 0-Dimensional modeling of the MCFC in the hybrid power generation model:

- The model uses lumped-parameter dynamics (0-Dimensional analysis) with no concern for geometry
- All gas mixtures are ideal gas mixtures
- The thermodynamic properties of the system follow the ideal gas law
- Exit stream is at fuel cell stack temperature
- Accumulation of gas phase enthalpy is negligible compared to that of solid components

The principal obstacle to creating the mathematical model of the fuel cell is the reaction rate of the reformation reaction, Equation 5.18. The reformation reaction is the most complicated reaction. The water-gas shift reaction is assumed to be an equilibrium reaction and anode and cathode reactions are electrochemical reactions. Since this is the case, if the current density is known, then the reaction rate can be determined.

The ideal gas equation

$$P\forall = nRT \tag{5.23}$$

is used to determine the gas component mole balances for each gas species, *i*, within the anode and cathode. For Equation 5.23, if $C = \frac{P}{RT}$ then $\forall C = n$. Integrating *n* for each gas species gives

$$\forall \frac{\partial C_i}{\partial t} = \frac{\partial n_i}{\partial t} = N_i^{in} - N_i^{out} + R_i \tag{5.24}$$

Where n is the number of moles in a mixture, N_i is the molar flow rate into and out of the system and R_i represents the total rate of production of species i. For a set of μ independent reactions, the rate of production can be written as

$$R_i = \sum_{i=1}^{\mu} v_{ij} r_j \tag{5.25}$$

For Equation 5.25, v_{ij} are the stoichiometric coefficients of species i in reaction j, and r_j is the rate of reaction of j. For the fuel cell stack model, there are for reactions rates, r_1, r_2, r_3, and r_4, these are anodic, water-gas shift, reforming and cathodic reactions. The anodic and cathodic reaction rates are equal ($r_1 = r_4$) and proportional to the stack current. The water-gas shift reaction is assumed to be in equilibrium and equilibrium constraints imply that r_2 can be eliminated when calculating gas component mole balances.

To complete the derivation for determining the gas component mole balances, it is shown that $N_i = x_i N_{tot}$ where x_i are the mole fractions of species i. This leads to the following

$$\forall C_{tot} \frac{\partial x_i}{\partial t} = N_{tot}^{in} x_i - \left(N_{tot}^{in} + \sum_{i=1}^{\xi} R_i \right) x_o + R_i \tag{5.26}$$

When Equation 5.26 is applied to the anode and cathode, respectfully and $C = \frac{P}{RT}$ is substituted back in, the anode gas component mole balances become

$$\frac{P_a \forall_a}{RT_s} \frac{dx_{i,a}}{dt} = N_a^{in} \left(x_{i,a}^{in} - x_{i,a}^{out} \right) - \sum_{i=1}^{\xi} R_{i,a} x_{i,a}^{out} + R_{i,a} \tag{5.27}$$

The gas component mole balances for the cathode are:

$$\frac{P_c \forall_c}{RT_s}\frac{dx_{i,c}}{dt} = N_c^{in}\left(x_{i,c}^{in} - x_{i,c}^{out}\right) - \sum_{i=1}^{\xi} R_{i,c}x_{i,c}^{out} + R_{i,c} \tag{5.28}$$

All of the variables in Equations 5.27 and 5.28 are for the anode or cathode, respectfully. On the left hand side of Equations 5.27 and 5.28, P, $\forall$, R, T_s and x_i are pressure, volume, gas constant, stack temperature, and mole fractions of species i, respectfully. On the right hand side of Equations 5.27 and 5.28, N, x_i, ξ, and R_i are total molar flow, mole fractions of species i, total number of species and total production rate of species i from all reactions.

5.1.2.2 Conservation of Energy and Nernst Equation

The first law of thermodynamics is applied to the MCFC stack model in the following form

$$\frac{\partial E}{\partial T} = \dot{Q} - \dot{W} \tag{5.29}$$

Where each of the three terms in Equation 5.29 is described by the following:

$$\frac{\partial E}{\partial T} = M_s C_{ps}\frac{\partial T_s}{\partial t} + \forall \sum_{i=1}^{\xi}\frac{\partial h_i C_i}{\partial t} \tag{5.30}$$

$$\dot{Q} = \sum\left(h_i^{in} N_i^{in} - h_i^s N_i^{out}\right) - Q_{conv} \tag{5.31}$$

$$\dot{W} = P_{dc} \tag{5.32}$$

Where M_sC_{ps} is the stack solid mass-specific heat, h_i are the partial molar enthalpies and P_{dc} is the direct current power produced the fuel cell stack. In Equation 5.30, the second term on the right-hand-side (RHS) is defined as

$$\forall \sum_{i=1}^{\xi} \frac{\partial h_i C_i}{\partial t} = \forall C_{tot} \sum_{i=1}^{\xi} \frac{\partial h_i^s}{\partial t} + \forall \frac{\partial C_{tot}}{\partial t} \sum_{i=1}^{\xi} h_i^s \tag{5.33}$$

Substituting a modified version of Equation 5.24 in for the term $\forall \frac{\partial C_{tot}}{\partial t}$ in Equation 5.33, Equation 5.30 becomes

$$\frac{\partial E}{\partial T} = M_s C_{ps} \frac{\partial T_s}{\partial t} + \forall C_{tot} \sum_{i=1}^{\xi} \frac{\partial h_i^s}{\partial t} + N^{in} \sum_{i=1}^{\xi} h_i^s - N^{out} \sum_{i=1}^{\xi} h_i^s + \sum_{i=1}^{\xi} R_i h_i^s \tag{5.34}$$

Combining Equations 5.31, 5.32 and 5.34 yields a single energy conservation equation for solving the fuel cell stack temperature. All of the terms have been categorized for anodic or cathodic reactions and can be seen in Equation 5.35. With Equations 5.27, 5.28 and 5.35 the reaction rates and fuel cell stack temperature can be determined. The pressure in the anode and cathode of the MCFC is not calculated in this hybrid power generation model.

$$M_s C_{ps} \frac{dT_s}{dt} = N_a^{in} \left[\sum_{i=1}^{\xi} x_{i,a}^{in} \left(h_{i,a}^{in} - h_i^s \right) \right] - \sum_{i=1}^{\xi} h_i^s R_{i,a} +$$

$$N_c^{in} \left[\sum_{i=1}^{\xi} x_{i,c}^{in} \left(h_{i,c}^{in} - h_i^s \right) \right] - \sum_{i=1}^{\xi} h_i^s R_{i,c} - Q_{conv} - P_{dc} \tag{5.35}$$

Lukas and Lee [59] express the cell voltage under load current I as

$$V_{cell} = V_o - \eta_{act} - \eta_{conc} - Iz \tag{5.36}$$

Where V_o is the equilibrium potential, η_{act} is the activation polarization, η_{conc} is the concentration polarization and z is the cell ohmic impedance. The activation polarization is caused by electrode kinetics while the concentration polarization is cased by concentration gradients in the electrode. The polarization losses in this hybrid model are known from empirical observation and the cell voltage, ultimately found from the Nernst equation will account of the ohmic and polarization losses. The equilibrium potential is

described by the Nernst equation, Equation 5.37; with this and the empirically determined polarization losses, the cell voltage in Equation 5.36 can be determined.

$$V_o = E_o + \frac{RT}{2F} \cdot \ln \frac{P_{H_2,a} P_{O_2,c}^{1/2} P_{CO_2,c}}{P_{H_2O,a} P_{CO_2,a}} \tag{5.37}$$

5.1.2.3 Catalytic oxidizer

The anode off-gas which is commonly composed of unused fuel (CH_4), carbon dioxide, and water is taken to a catalytic oxidizer where it is oxidized with the air from the turbine diffuser; this can be referenced in Figure 3.3. Utilizing this technique creates more valuable heat energy and prepares the gases for the cathode reactions. Once all of the gasses have been oxidized, they are fed through the shell-and-tube heat exchanger where the excess heat is used to elevate the temperature of the compressed air before it enters the turbine stage of the microturbine generator. The oxidized gases then complete the cycle by entering the cathode where they undergo electrochemical reactions.

The chemical reactions that take place within the catalytic oxidizer are

$$\begin{aligned} H_2 + \frac{1}{2} O_2 &\rightarrow H_2O \\ CO + \frac{1}{2} O_2 &\rightarrow CO_2 \\ CH_4 + 2O_2 &\rightarrow CO_2 + 2H_2O \end{aligned} \tag{5.38}$$

The reactions in Equation 5.38 are considered to be complete and spontaneous with the Minimum Theoretical Air (MTA) required to support oxidation and is assumed to be always available. Given this information the reaction rates are written by inspection and used to determine the mole balance equations similar to Equations 5.27 and 5.28. The mole balance equations are taken from Lukas and Lee [59] and are listed as follows:

$$\frac{dx_{CO_2,ox}}{dt} = \alpha_1\left[\alpha_2 x_{CO_2,ox} + N_{ox}^{gas}\left(x_{CO_2,ox}^{gas} + x_{CO,ox}^{gas} + x_{CH_4,ox}^{gas}\right)\right]$$
$$\frac{dx_{H_2O,ox}}{dt} = \alpha_1\left[\alpha_2 x_{H_wO,ox} + N_{ox}^{gas}\left(x_{H_2O,ox}^{gas} + x_{H_2,ox}^{gas} + 2x_{CH_4,ox}^{gas}\right)\right] \quad (5.39)$$
$$\frac{dx_{N_2,ox}}{dt} = \alpha_1\left[\alpha_2 x_{N_2,ox} + N_{ox}^{air} x_{N_2,air}\right]$$
$$x_{O_2,ox} = 1 - \left[x_{CO_2,ox} + x_{H_wO,ox} + x_{N_2,ox}\right]$$

Where α_1 and α_2 are defined as

$$\alpha_1 = \frac{RT_{ox}}{V_{ox}P_{ox}}$$
$$\alpha_2 = 0.5N_{ox}^{gas}\left(x_{H_2,ox}^{gas} + x_{CO,ox}^{gas}\right) - N_{ox}^{gas} - N_{ox}^{air} \quad (5.40)$$

For Equations 5.39 and 5.40 x is the mol fraction of CO_2, H_2, N_2, and O_2, respectfully. The total molar flow for each of the compounds is defined by N where N_{ox}^{gas} is the anode off-gas and N_{ox}^{air} is the diffuser air.

An energy conservation equation to determine the oxidizer temperature is given in Equation 5.41 and is developed in a similar fashion to the fuel cell stack temperature equation. The oxidizer pressure is not calculated in this model. The pressure exiting the catalytic oxidizer is assumed to be 98 percent of the pressure entering the oxidizer from the radial inflow turbine diffuser.

$$\frac{dT_{ox}}{dt} = \frac{N_{ox}^{gas}\left(h_{i,ox}^{gas} \cdot x_{i,ox}^{gas}\right) + N_{ox}^{air}\left(h_{i,air} \cdot x_{i,air}\right) - N_{ox}\left(h_{i,ox} \cdot x_{i,ox}\right)}{M_{ox}C_{pox}} \quad (5.41)$$

In Equation 5.41, $N_{ox}^{gas}, N_{ox}^{air}$ and N_{ox} are the total molar flows of the anode off-gas, air, and the oxidizer exhaust, respectfully. $h_{i,ox}^{gas}$, $h_{i,air}$ and $h_{i,ox}$ are the molar enthalpy of the anode off-gas, air and oxidizer exhaust for each species i. Similarly x_i is the respective compositions of the anode off-gas, air and the oxidizer exhaust. The

MATLAB/Simulink® 0-D model of the MCFC is represented in Figures 5.11 and 5.12. The total molar flow rates at anode and cathode, fuel cell stack temperature and fuel cell voltage can be seen.

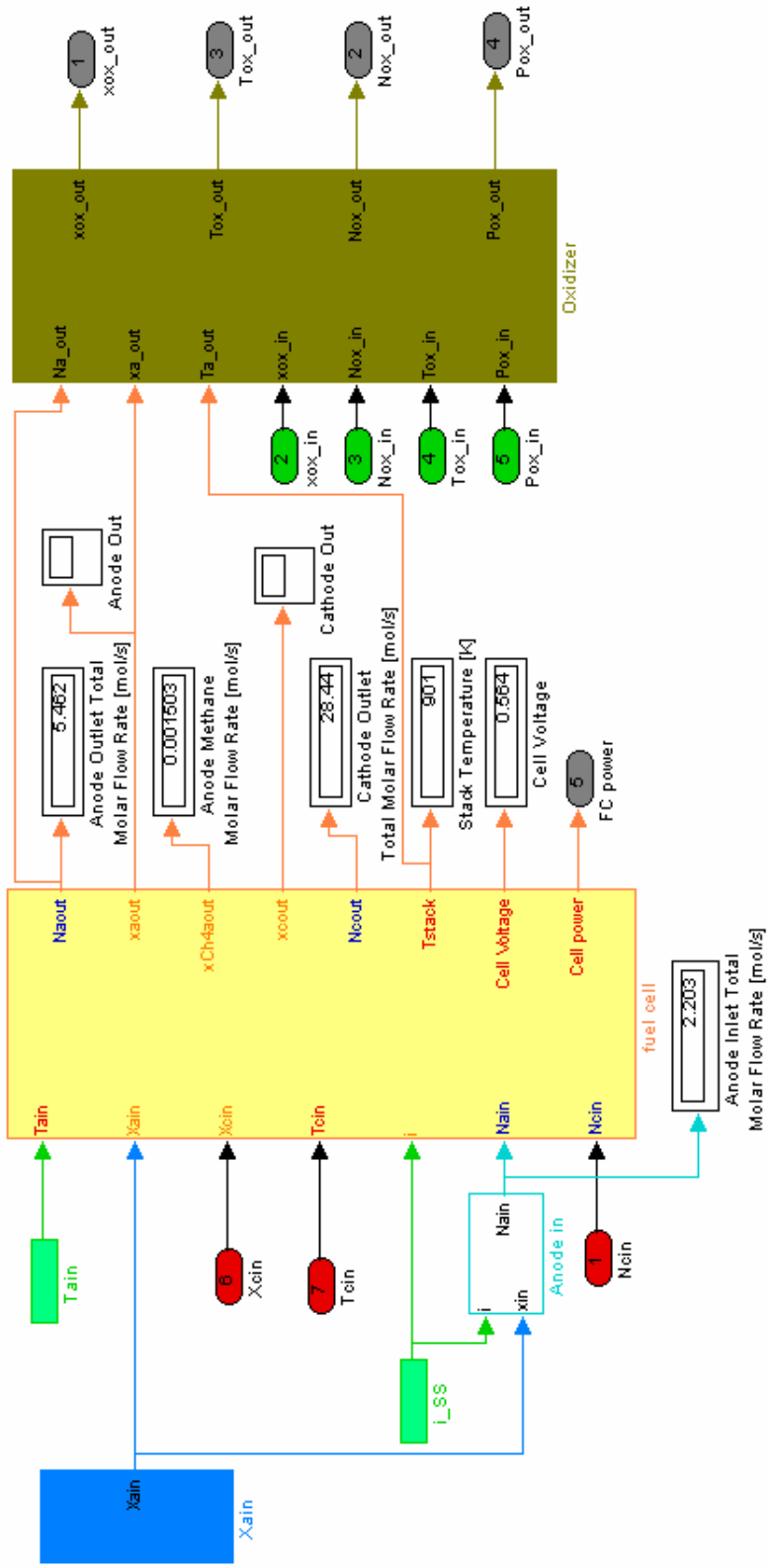

Figure 5.11: Top Level 0-D Molten Carbonate Fuel Cell Model

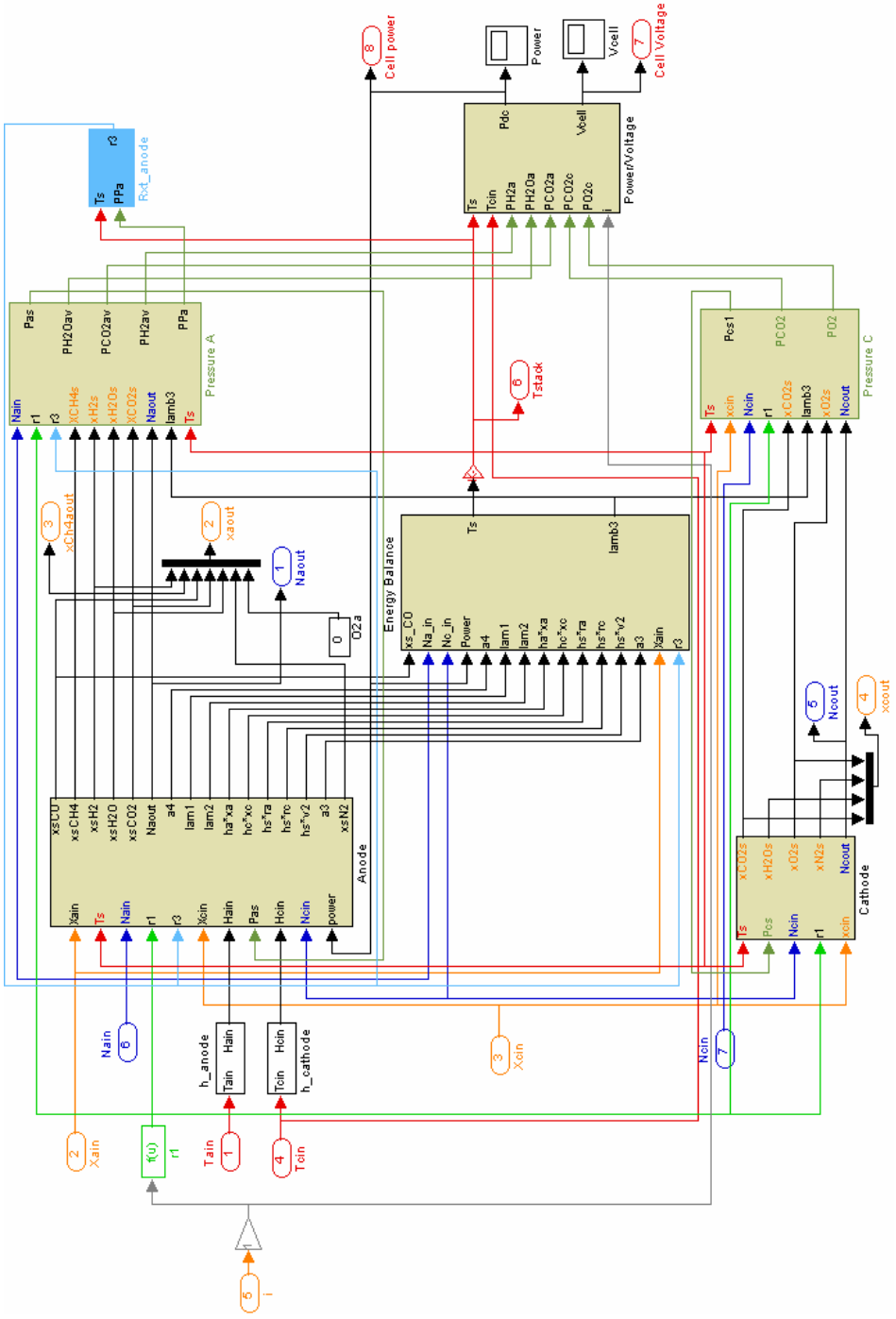

Figure 5.12: Anode and Cathode Model

5.1.3 Shell-and-Tube Heat Exchanger

Shell-and-tube heat exchangers are the most versatile type of heat exchanger. They provide large ratios of heat transfer area to volume and weight. Shell-and-tube heat exchangers are built of round tubes mounted in a cylindrical shell with the tubes running parallel to the shell, Figure 5.13. Fluid from the oxidizer flows in the tubes, while the other fluid, the compressed air from the microturbine generator, flows across and along the axis of the heat exchanger. The major components of this type of heat exchanger are the tubes, with tube bundle type of square pitch, shell, front- and rear-end head, baffles and tube sheets [32]. The shell-and-tube heat exchanger described in the following sections was sized based on results from CHEMCAD a product of Chemstations, Inc. The shell-and-tube heat exchanger has 305 tubes of length 0.5578 ft (1.83 m). There are three baffles with 0.1067 ft (0.35 m) between the baffles. The geometric parameters and constant values can be seen in Table 5.2.

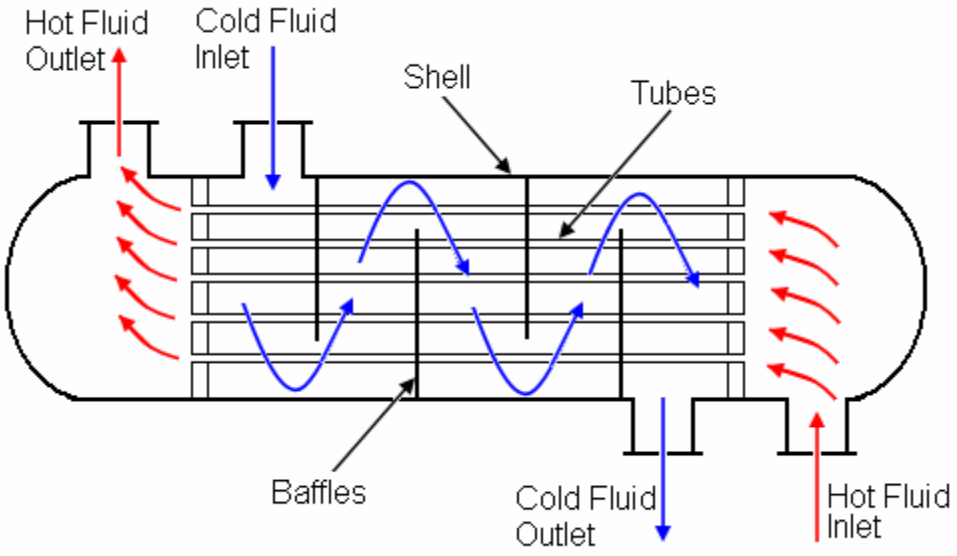

Figure 5.13: Shell-and-Tube Heat Exchanger

5.1.3.1 1st Law of Thermodynamics

The overall heat transfer coefficient of the shell-and-tube heat exchanger is determined in the same manner as for the primary surface recuperator, Section 4.1.4. This method will be described briefly below. For heat exchanger purposes, the overall heat transfer coefficient is typically based on the outer area. For known hot side (tube-side) and cold side (shell-side) heat transfer coefficients, fouling resistances (described in Section 4.2.4), and proper geometric parameters, the overall heat transfer coefficient of the shell-and-tube heat exchanger is distinguish by Equation 5.42.

$$U_o A_o = \frac{1}{\frac{1}{A_i h_i} + \frac{1}{A_o h_o} + \frac{R_{fi}}{A_i} + R_w + \frac{R_{fo}}{A_o}} \tag{5.42}$$

Where U_o is the overall heat transfer coefficient based on the outer area, A_o is the surface area of the outside of the tube, h_o is the heat transfer coefficient of the fluid in the shell, and R_{fo} is the fouling for the compressed air. The heat transfer is through the tube material from the hot flow in the tubes to the cold flow in the shell. R_w is the material wall resistance of the tubes, A_i is the surface area of the inside of the tube, h_i is the heat transfer coefficient of the fluid in the tubes, and R_{fi} is the fouling of the exhaust flow from the oxidizer.

0-Dimensional analysis of the shell-and-tube heat exchanger incorporates an average of the hot flow temperatures and a separate average of the cold flow temperatures. This averaging can be seen as transient behavior and integration is not occurring over a length scale but over a time scale. The average is taken of the hot and cold flows, respectfully and utilized to calculate the heat transfer rate, $\dot{Q}$.

$$T_{h,avg} = \frac{T_{ho} + T_{hi}}{2} \tag{5.43}$$

$$T_{c,avg} = \frac{T_{co} + T_{ci}}{2} \tag{5.44}$$

T_{hi} and T_{ho} represent the flow into and out of the hot side (tube-side) of the heat exchanger and T_{ci} and T_{co} represent the flow into and out of the cold side (shell-side) of the heat exchanger. The centrifugal compressor from the microturbine generator provides the compressed air flow, T_{ci} for the shell-side of the heat exchanger. This flow is heated and fed to the radial inflow turbine section where the flow is expanded and energy is extracted for additional power generation. The flow out of the oxidizer is sent through the tubes of the heat exchanger. This flow is cooled before it goes to the cathode of the molten carbonate fuel cell (MCFC). The heat transfer rate for the shell-and-tube heat exchanger is characterized by

$$\dot{Q} = U_o A_o \left(T_{h,avg} - T_{c,avg}\right) \tag{5.45}$$

The first law of thermodynamics [53] is given by Equation 5.46,

$$\dot{E}_{in} - \dot{E}_{out} - \dot{Q} = \dot{E}_{st} \tag{5.46}$$

It is used to determine the unknown temperatures exiting both the hot and cold sides of the shell-and-tube heat exchanger. The energy into the control volume of the system is defined as

$$\dot{E}_{in} = \dot{m} C_p T_{in} \tag{5.47}$$

The energy exiting the control volume of the system is identified by

$$\dot{E}_{out} = \dot{m} C_p T_{out} \tag{5.48}$$

The rate of change of energy stored in the control volume

$$\dot{E}_{st} = \frac{dE_{st}}{dt} \tag{5.49}$$

is equal to the rate of change of internal energy stored in the control volume

$$\frac{dE_{st}}{dt} = \frac{dU}{dt} \tag{5.50}$$

Where

$$\dot{U} = (\rho \forall) C_v T \tag{5.51}$$

The quantity $(\rho \forall)$ is the density (lbm/ft^3 or kg/m^3) multiplied by the volume (ft^3 or m^3), this yields mass m and C_v is the specific heat at constant volume of the fluid in the heat exchanger. This value is dependent on the type of gas or liquid present in the system. Replacing the terms in Equation 5.46 by Equations 5.47 through Equations 5.51 yields the following

$$\dot{m} C_p T_{in} - \dot{m} C_p T_{out} - \dot{Q} = \frac{d}{dt}(m C_v T_{out}) \tag{5.52}$$

Applying Equation 5.52 to the cold and hot sides of the heat exchanger, the flow out of the hot and cold sides, T_{ho} and T_{co}, respectfully can be determined from Equations 5.53 and 5.54.

$$HotSide: mC_v \frac{dT_{ho}}{dt} = \left(\dot{m} C_p\right)_h \left(T_{hi} - T_{ho}\right) + \dot{Q} \tag{5.53}$$

$$ColdSide: mC_v \frac{dT_{co}}{dt} = \left(\dot{m} C_p\right)_c \left(T_{ci} - T_{co}\right) - \dot{Q} \tag{5.54}$$

The quantities $\left(\dot{m} C_p\right)_h$ and $\left(\dot{m} C_p\right)_c$ are the heat capacity rates of the hot and cold sides, respectfully. The Simulink model of the 0-D shell-and-tube heat exchanger heat transfer, energy, and pressure drop calculations is represented in Figure 5.14.

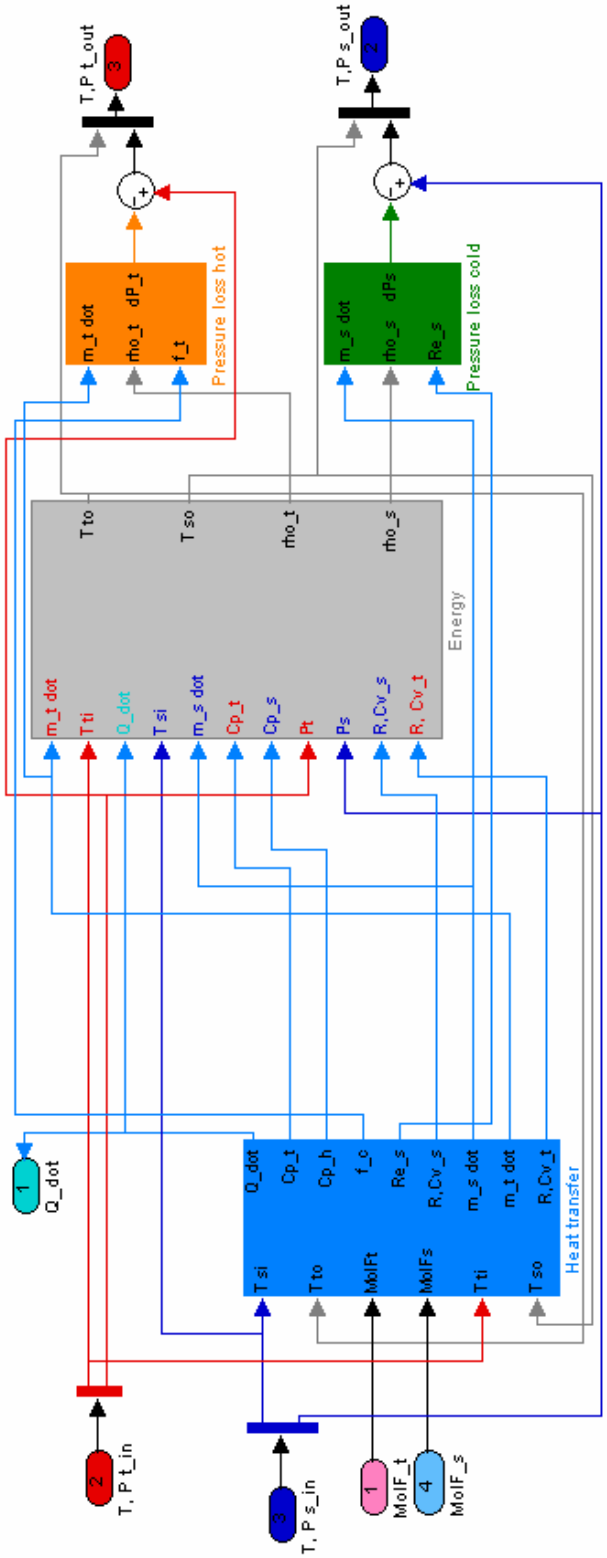

Figure 5.14: 0-D Shell-and-Tube Heat Exchanger Model

5.1.3.2 Tube-Side Pressure Drop

The pressure drop on the tube-side of a shell-and-tube heat exchanger can be found through knowing the number of tube passes and the length, L_{hx} of the heat exchanger. For modeling purposes, the number of tube passes is equal to the number of heat exchanger sections. One pass of the tube bundle would be equivalent to one heat exchanger section, designated by the variable *NS*. The pressure drop in the tube-side is given by Equation 5.55 taken from Kakaç et al [32]

$$\Delta P_t = ff \frac{L_{hx} \cdot NS}{D_i} \frac{G_t^2}{2\rho} \tag{5.55}$$

Where *ff* is the Darcy friction factor, D_i is the inner diameter of a single tube, and G_t is the mass velocity of the fluid on the tube-side. The mass velocity can be calculated by either $G_t = \rho u_m$ where u_m is the mean fluid velocity and ρ is the fluid density, or by $G_t = \frac{\dot{m}_t}{A_i}$ where $\dot{m}$ is the mass flow rate of the fluid on the tube-side and A_i is the inner cross-sectional area of the tube.

5.1.3.3 Shell-Side Pressure Drop

Determining the shell side-pressure drop is a more elaborate process and therefore not as straightforward as calculating the tube-side pressure drop. The shell-side analysis combines cross-flow and baffle window flow as well as baffle-shell and bundle-shell bypass streams [32]. Due to the intricacies of the shell-side flow, the Bell-Delaware method is used and it is considered the most reliable method for the shell-side analysis. In addition to the pressure drop on the main stream of the exchanger, pressure drop is also observed with bypass and leakage streams. The total nozzle-to-nozzle pressure drop

on the shell-side of the heat exchange, determined by the Bell-Delaware method is found to be

$$\Delta P_s = \Delta P_c + \Delta P_w + \Delta P_e \tag{5.56}$$

The first term on the right hand side (RHS) of Equation 5.56 is the combined pressure drop in the entire interior cross-flow section

$$\Delta P_c = \Delta P_{bi}\left(N_b - 1\right)R_l R_b \tag{5.57}$$

Where ΔP_{bi} is the pressure drop of an ideal tube bank in one baffle compartment of the central baffle spacing, N_b is the number of baffles, R_l is the correlation factor for the baffle leakage effects, and R_b is the correlation factor for the bypass flow. The typical range for the correlation factors are R_l = 0.4 to 0.5 and R_b = 0.5 to 0.8, respectfully [32]. The pressure drop in the central baffle compartment can be determined from Equation 5.58,

$$\Delta P_{bi} = ff\left(\frac{\dot{m}_s}{\rho A_{Sm}}\right)^2 \frac{\rho N_c}{2} \tag{5.58}$$

Where A_{Sm} is the flow area at the middle of the central baffle compartment, N_c is the number of tube rows crossed during flow through one cross flow in the exchanger, and $\dot{m}_s$ is the mass flow rate of the fluid in the shell-side. The mass velocity of the fluid in the shell-side $G_s = \frac{\dot{m}_s}{A_{Sm}}$, therefore Equation 5.58 can be reduced to

$$\Delta P_{bi} = ff\,\frac{G_s}{\rho}\frac{N_c}{2} \tag{5.59}$$

The second term on the RHS of Equation 5.56 is the pressure drop for the entire window in the arrangement

$$\Delta P_w = \Delta P_{wi} N_b R_l \tag{5.60}$$

The pressure drop in the window is affected by leakage but not by bypass. The term ΔP_{wi} is the pressure drop of an ideal tube bank in one baffle window section

$$\Delta P_{wi} = \frac{\dot{m}_s^2 \left(2 + 0.6 N_{cw}\right)}{2 \rho A_{Sm} A_{Sw}} \tag{5.61}$$

Where N_{cw} is the number of tube rows crossed in each baffle window, and A_{Sw} is the area for flow through the window.

The final term on the RHS of Equation 5.56 is the combined pressure drop for the entrance and exit sections of the heat exchanger and is determined by

$$\Delta P_e = 2 \Delta P_{bi} \frac{N_c + N_{cw}}{N_c} R_b R_s \tag{5.62}$$

The only new variable in Equation 5.62, is R_s; the correlation factor for the entrance and exit sections. Combining Equations 5.57 through 5.62 yields the total pressure drop over the shell-side of the shell-and-tube heat exchanger

$$\Delta P_s = R_l \left[\left(N_b - 1\right) \Delta P_{bi} R_b + N_b \Delta P_{wi} \right] + 2 \Delta P_{bi} R_b R_s \left(\frac{N_c + N_{cw}}{N_c} \right) \tag{5.63}$$

Table 5.2: Shell-and-Tube Heat Exchanger Values

	Value	Units	Value	Units
R_{fo}	0.0009991	ft^2-R-hr/Btu	0.000176	m^2-K/W
R_{fi}	0.009997	ft^2-R-hr/Btu	0.001761	m^2-K/W
R_w	5.596E-06	ft^2-R-hr/Btu	9.858E-07	m^2-K/W
N_t	305	-	305	-
NS	1	-	1	-
N_{cw}	4	-	4	-
N_b	3	-	3	-
N_c	10	-	10	-
R_s	1	-	1	-
R_b	0.8541	-	0.8541	-
R_l	0.4751	-	0.4751	-
L_{hx}	6.0039	ft	1.8300	m
D_i	0.0515	ft	0.0157	m
D_o	0.0627	ft	0.0191	m
D_s	1.6076	ft	0.4900	m
L_b	1.1483	ft	0.3500	m
t_b	0.0105	ft	0.0032	m
A_i	0.6351	ft^2	0.0590	m^2
A_o	1.0893	ft^2	0.1012	m^2
A_{Sm}	0.4090	ft^2	0.0380	m^2
A_{Sw}	0.2228	ft^2	0.0207	m^2
$\forall$	1.8328	ft^3	0.0519	m^3

5.2 1-Dimensional Zooming of Microturbine Generator

While the molten carbonate fuel cell (MCFC) model and the shell-and-tube heat exchanger model remains 0-Dimensional, the microturbine generator model will demonstrate the 1-D zooming technique. The 1-D zooming simulation is initiated by loading the m-file controller. This will load the thermodynamic property tables and run additional m-files that will provide the individual component parameters required by Simulink into the MATLAB workspace and the Simulink GUI will then execute. The computer flow diagram of this simulation is seen in Figure 5.15.

Each module in the 1-D zooming section represents the set of equations required to solve for the performance parameters of each component. The top level Simulink model is seen in Figure 5.16 and the corresponding variable flow diagram is represented in Figure 5.17. The variable flow diagram shows that the variables are solved in a one-by-one manner and no algebraic loops are present with the calculation of the compressor and turbine variables. The shell-and-tube heat exchanger model is between the compressor and the turbine and remains 0-Dimensional. The zooming takes place in the following manner; 1-D → 0-D → 1-D → 0-D or compressor with inlet → shell-and-tube heat exchanger → turbine with diffuser → oxidizer.

The variables calculated by the heat exchanger model exhibit transient behavior and even though the turbine model portrays steady, 1-D calculations the turbine variables will show the transient behavior. This will be discussed further in Chapter 6. All of the compressor calculations are strictly steady, 1-D behavior. The mathematical modeling of the compressor and turbine will be discussed in Sections 5.2.1 and 5.2.2, respectfully and will reference Sections 4.1.1 and 4.1.2.

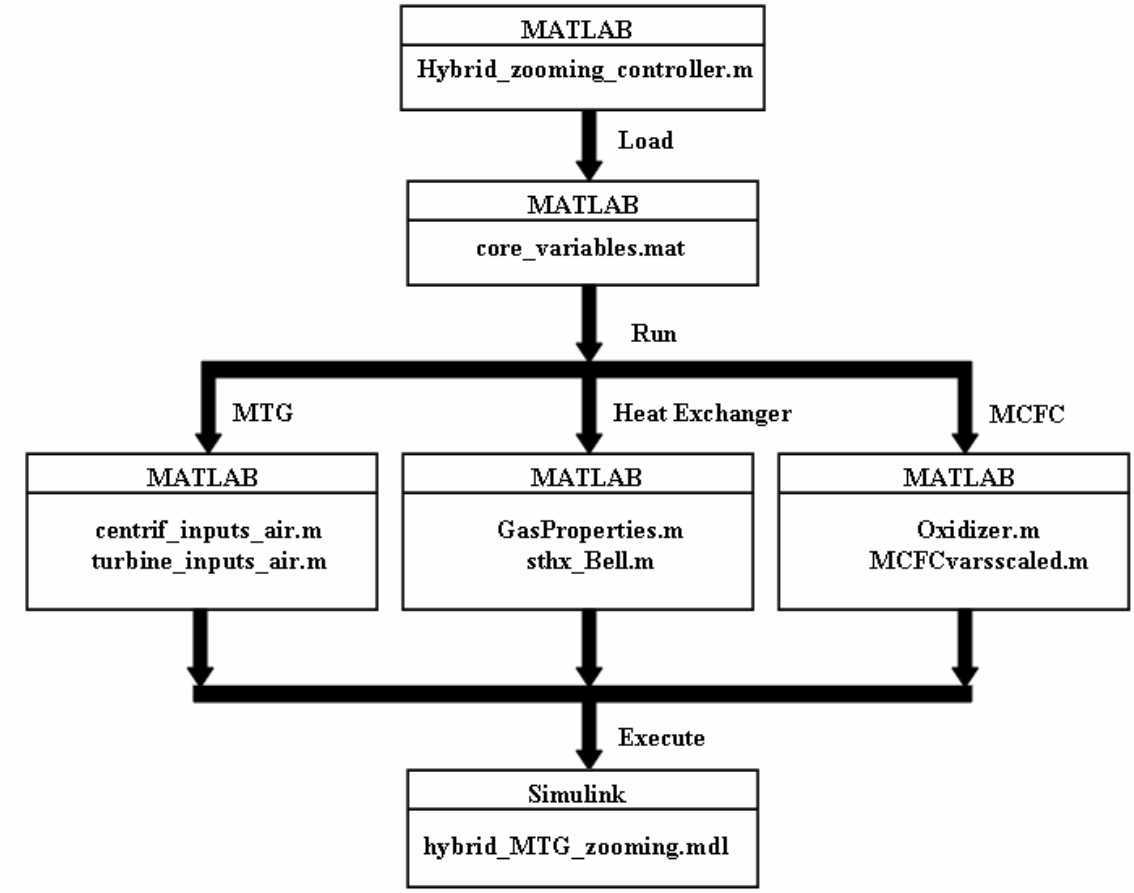

Figure 5.15: Computer Flow Diagram to Execute 1-D Zooming, Modeling and Simulation of MTG in a Hybrid Power Generation System

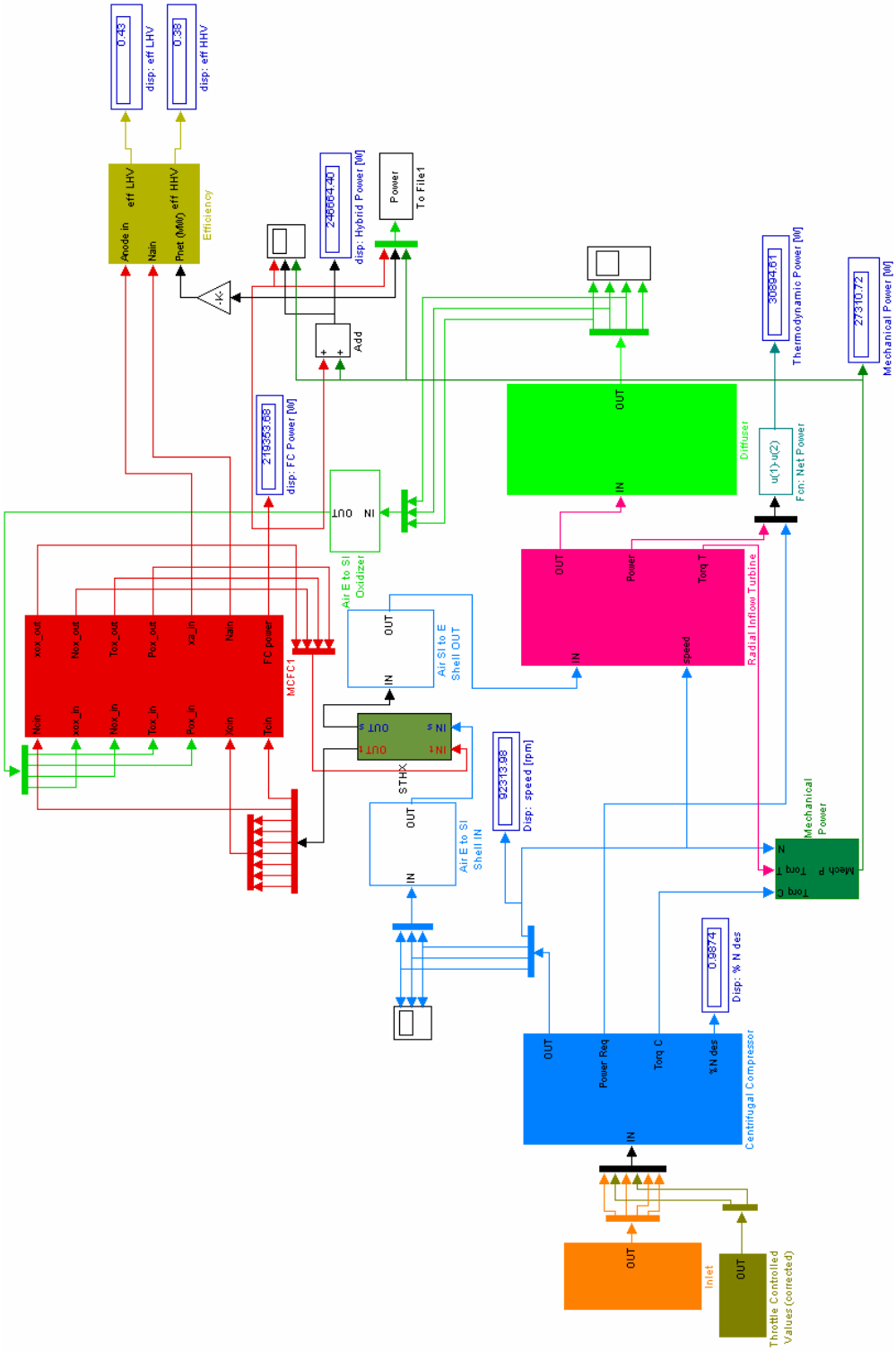

Figure 5.16: Top Level 1-D Zooming of MTG in a Hybrid Power Generation Model

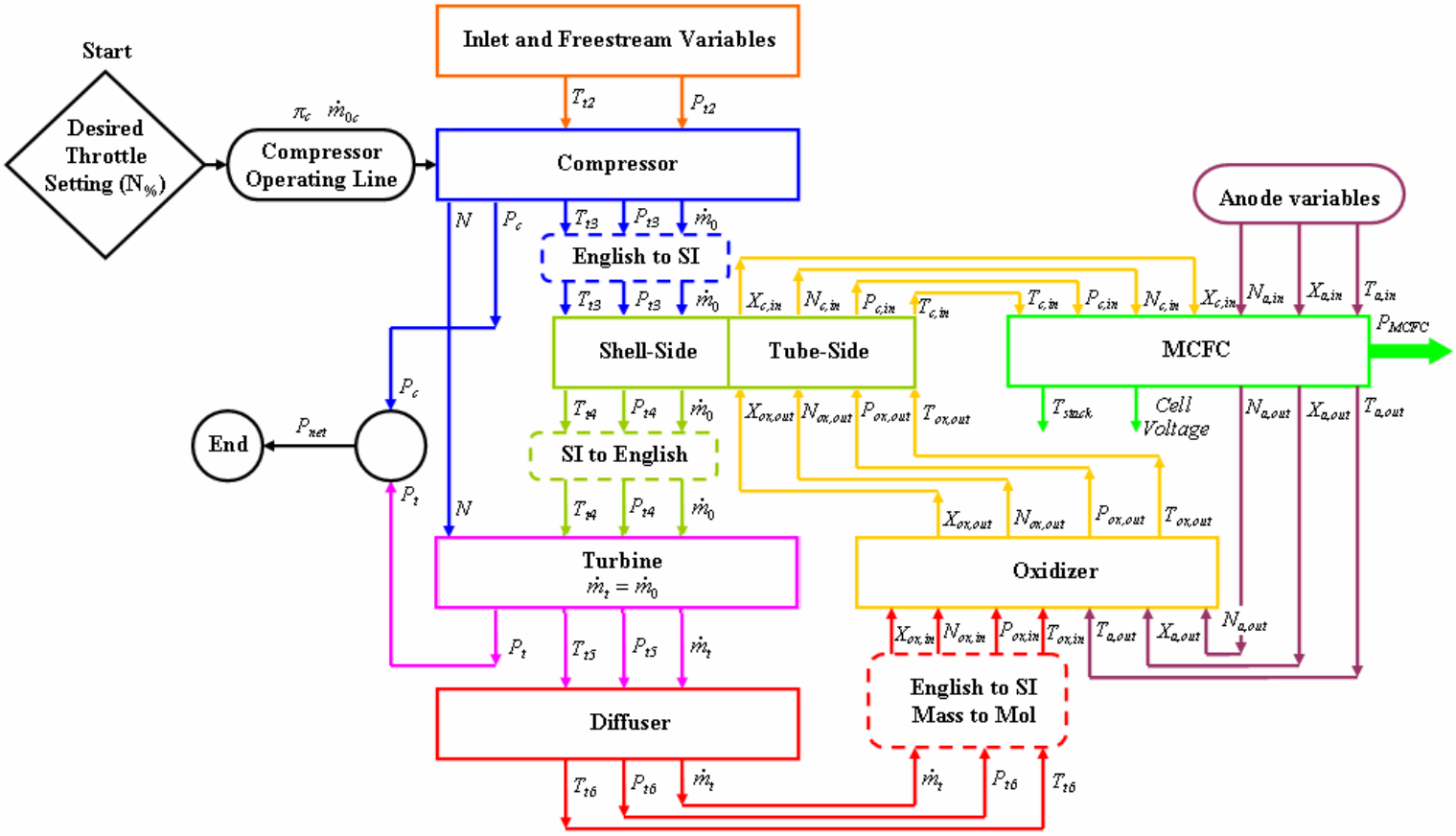

Figure 5.17: Computer Flow Diagram for Top Level 1-D Zooming of MTG in a Hybrid Power Generation System

5.2.1 Centrifugal Compressor

The 1-D zooming model is run on a single operating line with no off-design capabilities. The desired shaft speed or throttle control, in percent of the design speed, is used to determine the corrected mass flow rate of air in the compressor, $\dot{m}_{oc}$ and the total pressure ratio, π_c. The throttle control acts as the controller for the 1-D system model. The isentropic efficiency η_c is calculated from the total pressure ratio and total temperature ratio, Equation 4.14.

The core and mean-line variables calculated for the centrifugal compressor in the 1-D zooming model, are found in the exact same manner portrayed in Section 4.1.1. The assumptions listed for the 1-Dimensional stand alone power generation model can be applied to the 1-D zooming model. These assumptions are listed in tabular form in Table 4.2 of this thesis. The 1-D mean-line calculations are completed station by station through the centrifugal compressor. A visual representation of the mean-line calculations in Station 1 of the centrifugal compressor is given in Figure 5.18.

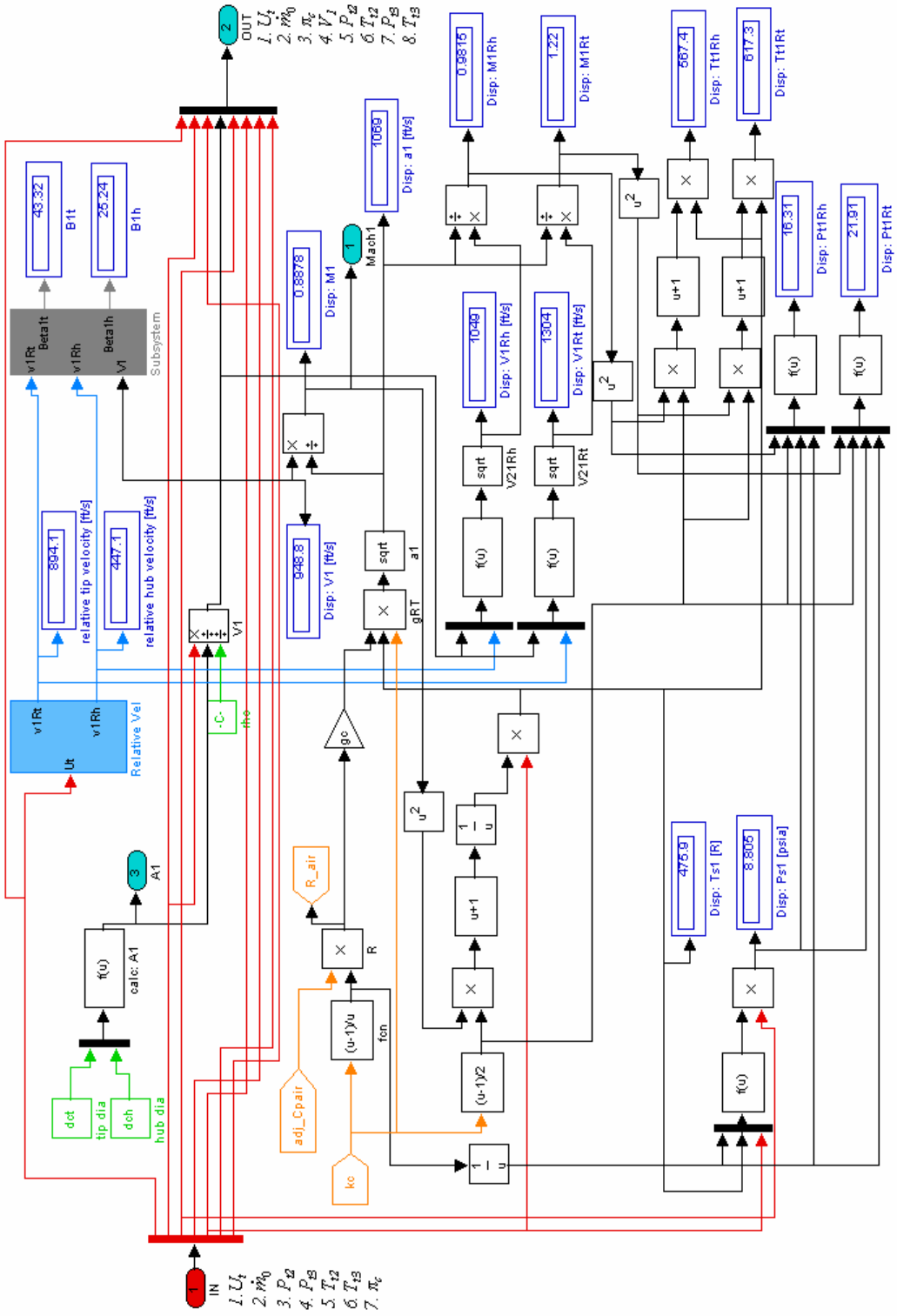

Figure 5.18: 1-D Zooming Centrifugal Compressor Station 1

5.2.2 Radial Inflow Turbine

Component matching is still required for the 1-D zooming of the radial inflow turbine. The shaft speed of the compressor must equal the shaft speed of the turbine, Figure 5.19. The only adjustment to the assumptions made in Section 4.2 is that the total pressure exiting the turbine P_{t4} is not held constant. All other assumptions can be found in Table 4.3 is still valid for the 1-D zooming model.

When the core variable solution path of the 1-D zooming is compared to the 1-D stand alone model, the total temperature entering the turbine T_{t4} is not calculated in the same manner. In the stand alone model, the turbine temperature is calculated directly from the rotor tip speed U_{2t} and the total temperature ratio τ_t, where the total temperature ratio is a function of the known total pressure ratio π_t. With the incorporation of the 0-Dimensional shell-and-tube heat exchanger in the hybrid system, the turbine inlet temperature is provided to the 1-D zooming model. With the steady, algebraic calculations, this can be represented as a known value. The total pressure entering the turbine P_{t4} is also provided by the shell-and-tube heat exchanger.

Instead of calculating T_{t4} in Equation 4.29, with modification this equation is used to calculate T_{t5} and becomes

$$U_{2t}^2 = g_c C_{pt}\left(T_{t4} - T_{t5}\right) \tag{5.64}$$

Once the total temperatures associated with the turbine are calculated the total temperature ratio τ_t is calculated. The total pressure ratio in the zooming hybrid turbine π_t is a function of the total temperature ratio. The temperature and pressure ratios are represented by isentropic relationships and as long as one is know the other can be found. The total pressure exiting the turbine P_{t5} is not held as a constant for the 1-D hybrid

zooming and is calculated from the pre-determined total pressure entering the turbine and the total pressure ratio. The variable solution path can be seen in Figure 5.19. A visual representation of the mean-line calculations in Station 2 of the radial inflow turbine is given in Figure 5.20.

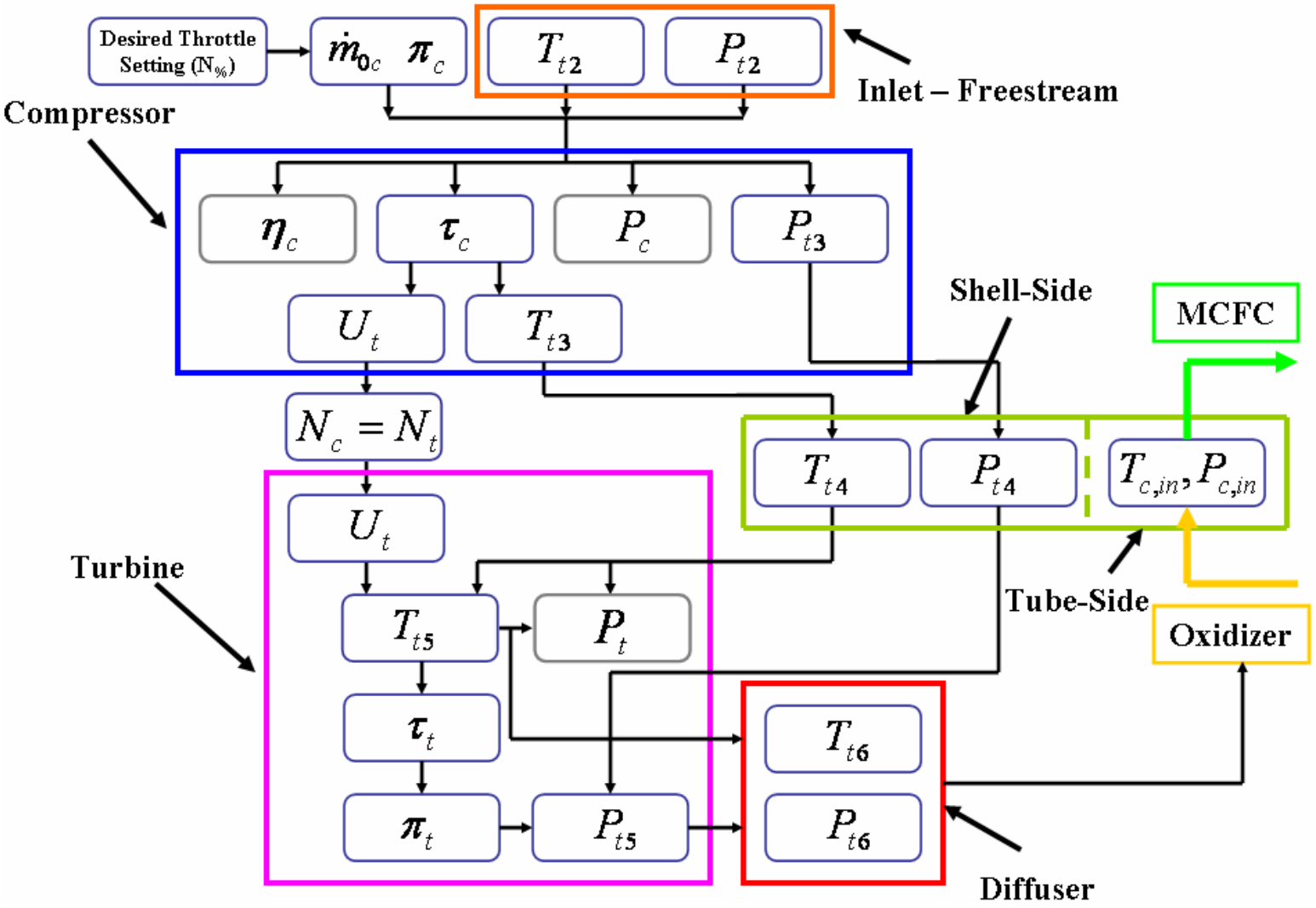

Figure 5.19: 1-D Zooming of MTG Core Variable Solution Path

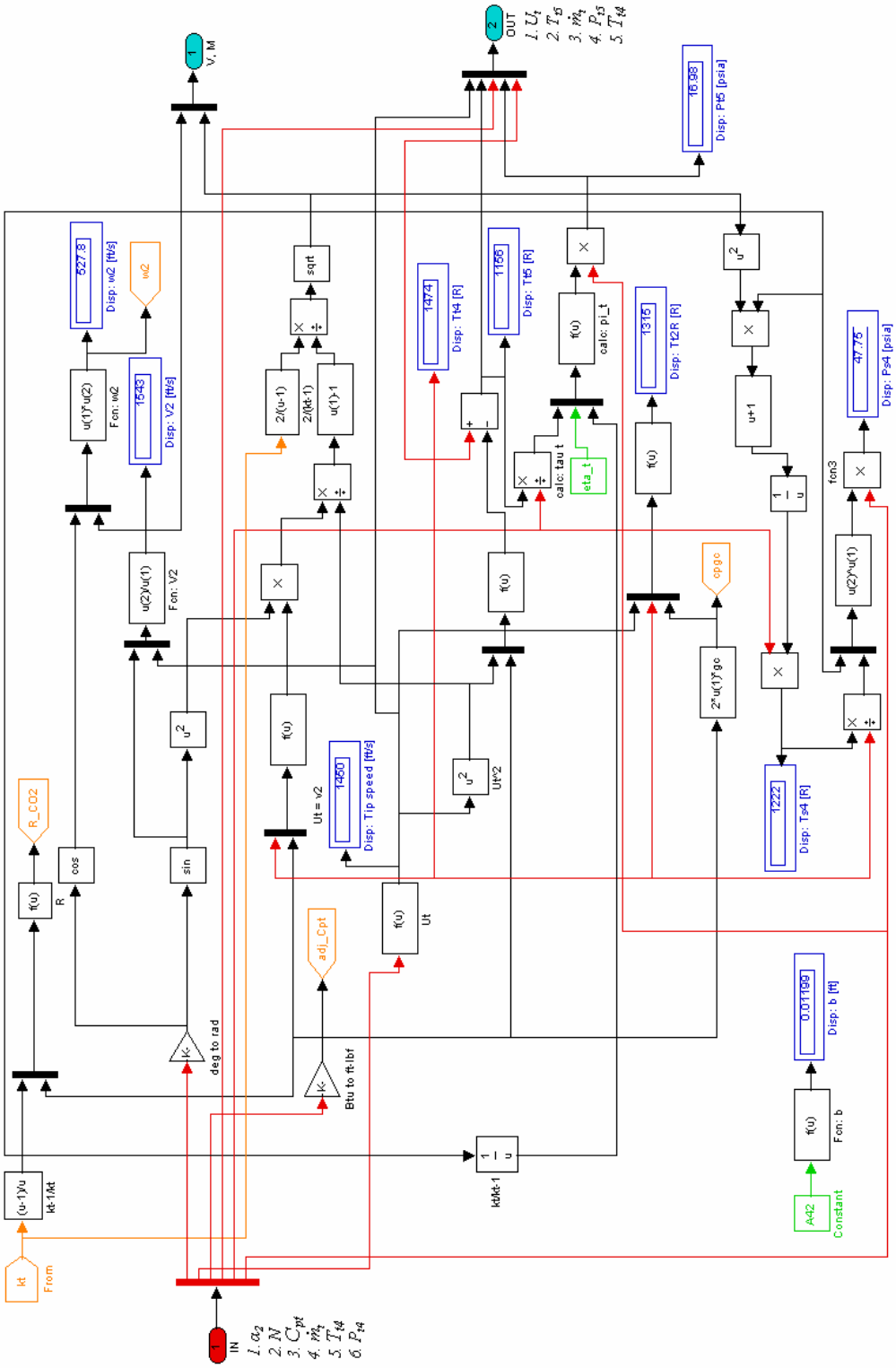

Figure 5.20: 1-D Zooming Radial Inflow Turbine Station 2 Model

CHAPTER 6: ANALYSIS AND RESULTS

6.1 Stand Alone Power Generation Model Development

6.1.1 1-Dimensional with EES Verification

All the tabular data correlating to Figures 6.1 to 6.5 and Figures 6.8 to 6.12 can be found in Appendix A. The tabular data corresponding to the 1-Dimensional zooming of the microturbine generator in the hybrid power generation system can be found in Appendix B. The three 2-D arrays discussed in Section 5.1.1.1 will be portrayed as two figures, total pressure ratio versus corrected mass flow as a function of shaft speed and isentropic efficiency versus corrected mass flow as a function of shaft speed. This will be seen along with the corresponding tabular data in Appendix C. The 2-D array discussed in Section 5.1.1.2 will be seen as a figure of expansion ratio versus corrected mass flow as a function of shaft speed in Appendix D.

The linearity of the 1-Dimensional calculations is defined as the ability of the graphically represented data to enable a curve fit that is linear in nature, i.e. a straight line representation of the data. Figure C.1 in Appendix C has the ideal operating line of the centrifugal compressor represented as a straight line. If the graphical data representing variables along the actual operating line of the microturbine generator has trends that do not allow for a straight line fit, the data analyzed will be determined to be non-linear in nature.

6.1.1.1 Operating Line Calculations

The 1-D MATLAB/Simulink® model calculates the core variables and mean-line variables for the actual MTG operating line based on the ideal compressor operating line. The calculations run from 40 percent to 110 percent of the ideal compressor operating line. The MATLAB/Simulink® model has been validated by using EES (Engineering Equation Solver) software. The EES model calculates all variables based on the ideal compressor operating line independent parameters, $\dot{m}_{oc}$ and π_c. With these two parameters, the actual operating line of the MTG is established. All of the following figures are for the actual operating line of the MTG, and a reference to the ideal compressor operating line will be used for some descriptions. Table 6.1 gives the ideal operating speed at 40-110 percent of the design speed and the actual operating speed that translates into 48-105 percent of the design speed. The design speed is the same for both the ideal and actual operating lines, N_{des} = 92400 rpm.

Figure 6.1 gives the total temperature exiting the compressor T_{t3} and the power required P_c. The error observed between the Simulink model and EES model for the total temperature exiting the compressor was averaged to be 0.04 percent and the error with the compressor power was 0.07 percent.

The total temperature calculated by the turbine model T_{t4} is in Figure 6.2. At the lowest operational speed given in Figure 6.2, the total temperature entering the turbine is phenomenally high, suggesting an error in the calculations of the model. At this speed, 48 percent actual and 40 percent ideal, the Simulink model calculates T_{t4} to be 3667 R and the EES model gives 4036 R, with no cooling effects in the turbine, which is above the melting point of titanium, 3480 R (1933 K) [55].

The Euler equation for turbomachinery states that the rotor blade tip speed squared is directly proportional to the change in enthalpy or temperature through the entire turbine caused by the expansion process and the compressor and turbine are on the same shaft so the shaft rotational speed must be the same. With the engine operating at an actual 48 percent, the shaft rotational speed is quite low resulting in low rotor tip speeds. From Chapter 4, the turbine rotor blade tip speed is determined from the shaft speed and the turbine inlet total temperature T_{t4} is determined from Equation 4.29. Since U_{2t} is small, Equation 4.29 yields a very high T_{t4}.

$$U_{2t}^2 = g_c C_{pt} T_{t4} \left(1 - \tau_t\right) \tag{4.29}$$

The variables in the EES and Simulink models are calculated one at a time with no multi-equation dependencies. At an actual 48 percent of the design speed, the error between the two models observed with the variable T_{t4} is 10 percent. The power provided by the turbine P_t shows errors of less than 1 percent. If T_{t4} at an ideal 40 percent is very high and does not follow the trend established by the subsequent calculations from 45-110 percent of the ideal design speed, then it will be assumed that the microturbine generator is not capable of operating at the ideal 40 percent speed and this point will be dropped from further calculations and comparisons.

With the models calculating each variable with no multi-equation dependencies, then linearity can be assumed. From Figure 6.2, linearity is observed from 74 percent of the actual design shaft speed. This suggests that the microturbine cannot feasible run below this 74 percent of the design speed on the actual operating line.

The mass flow rate of fuel $\dot{m}_f$ is dependent on the turbine inlet temperature T_{t4}, Figure 6.3. The operating line begins with a higher temperature at 56 percent and

linearity is seen from 74 percent to 105 percent on the actual operating line. The higher temperatures seen at slower speeds are again referenced back to Equation 4.29.

The degree of energy conversion from heat to power is the thermal efficiency and can be determined from the *LHV* and from the *HHV* of the fuel. As the power production increases with the shaft speed increase, a corresponding increase in the thermal efficiency of the system is observed. Figure 6.4 has the microturbine generator system efficiency in terms of *LHV* and *HHV* of natural gas. The *LHV* thermal efficiency of the Capstone® Model 330 MTG is around 14 percent [16]. At the design point for the microturbine generator, the *LHV* efficiency is 13.6 percent and the *HHV* efficiency is 12.2 percent. This demonstrates the feasibility of the 1-D stand alone power generation model.

Thermodynamic power is the ideal amount of power that can be produced from the microturbine based on the ideal Brayton cycle. Mechanical power is the actual power produced by the shaft of the microturbine. Figure 6.5 represents the thermodynamic and mechanical power calculated along the actual MTG operating line.

It has already been mentioned that the model does not demonstrate linearity until around 74 percent on the operating line. Looking at Figure 6.5, the actual power of the MTG is greater than the ideal power when the model is run below the 69 percent mark or 63400 rpm. This demonstrates that the ideal cycle does not map the actual cycle accurately below 69 percent of the actual operating line.

Table 6.1: Ideal and Actual MTG Operating Line Shaft Speed

Ideal - EES		Actual - MATLAB		Actual - EES	
Speed	$N_{\%}$	*Speed*	$N_{\%}$	*Speed*	$N_{\%}$
rpm	-	rpm	-	rpm	-
36900	0.400	44200	0.479	44300	0.479
41600	0.450	51900	0.562	51900	0.562
46200	0.500	58100	0.629	59200	0.629
50800	0.550	63400	0.686	63400	0.686
55400	0.600	68000	0.736	68000	0.736
60000	0.650	72000	0.780	72100	0.780
64700	0.700	75700	0.819	75700	0.820
69300	0.750	79000	0.855	79100	0.856
73900	0.800	82100	0.888	82100	0.889
78500	0.850	84900	0.919	85000	0.920
83100	0.900	87500	0.947	87600	0.948
87800	0.950	90000	0.974	90100	0.975
92400	1.000	92300	0.999	92400	1.000
97000	1.050	94500	1.023	94600	1.023
101600	1.100	96600	1.045	96600	1.046

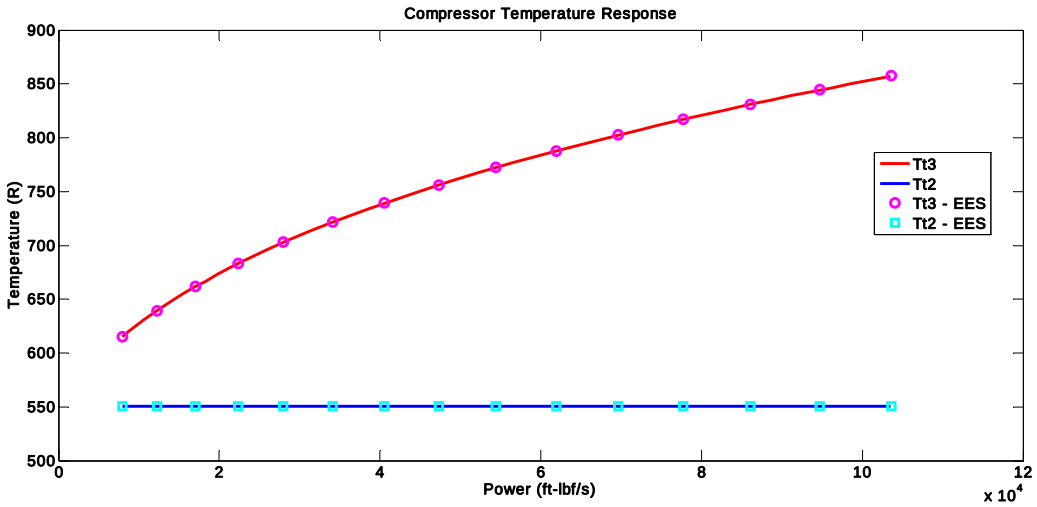

Figure 6.1: Temperature Profile for Centrifugal Compressor

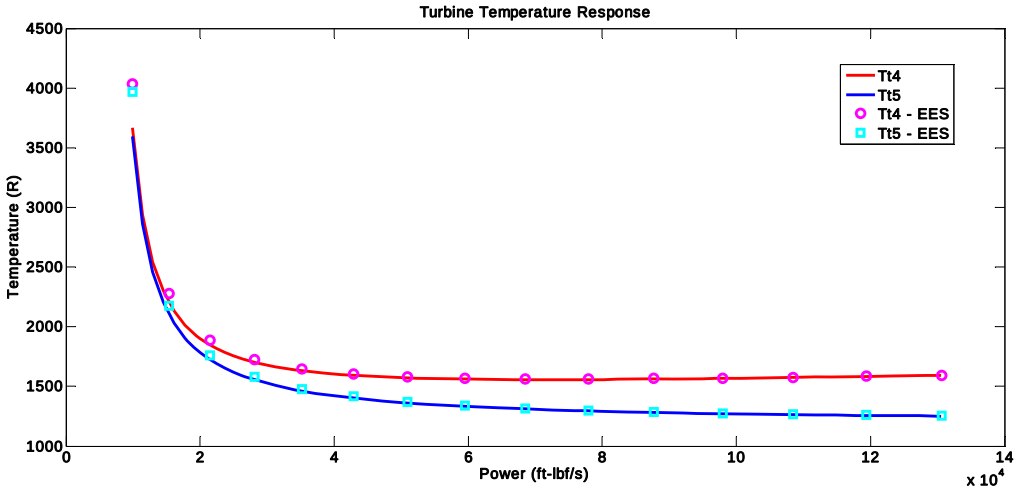

Figure 6.2: Temperature Profile for Radial Inflow Turbine

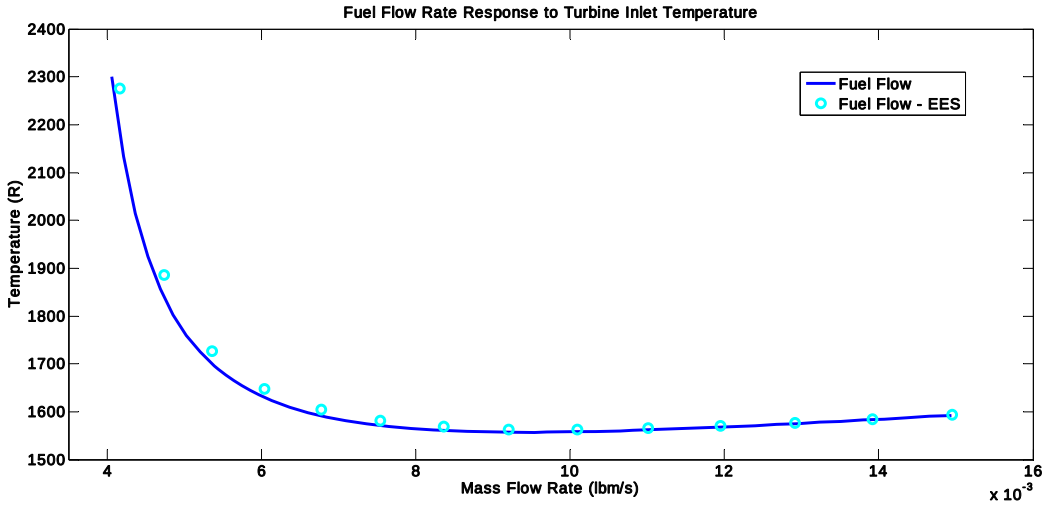

Figure 6.3: Mass Flow of Fuel Required to Attain the Desired Turbine Inlet Temperature

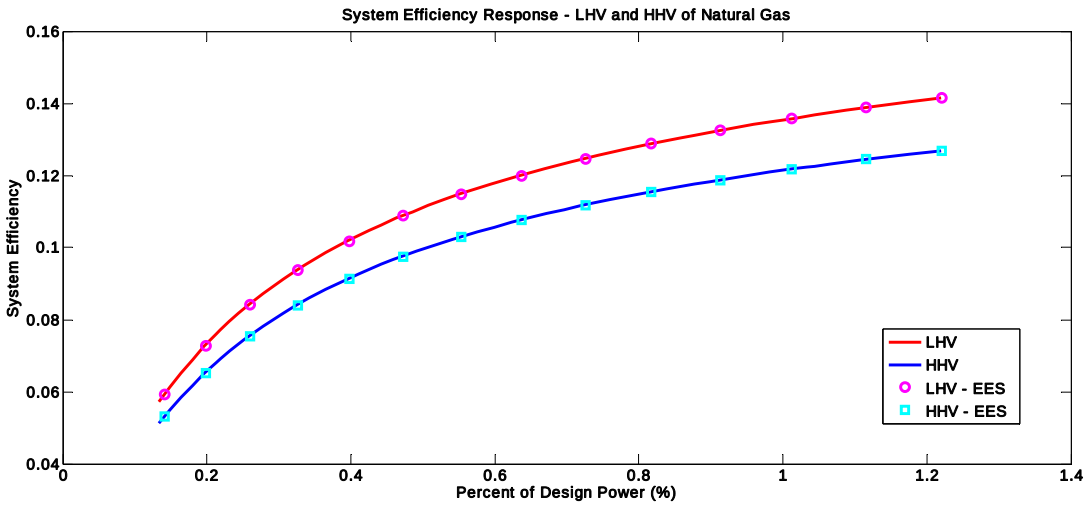

Figure 6.4: Microturbine Generator System Efficiency

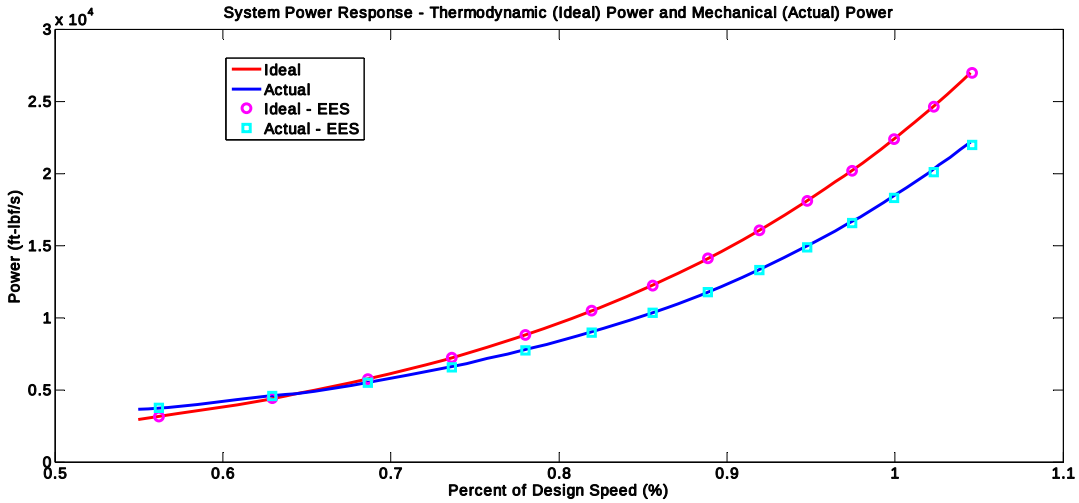

Figure 6.5 Microturbine Generator Power Generation – Thermodynamic and Mechanical

6.1.1.2 Brayton Cycle Thermodynamic Analysis

The *T-s* and *P-v* diagrams shown in Figures 3.1b and 3.1c are for ideal gas turbine cycles. In an ideal cycle, the flow in the inlet is adiabatic and reversible (isentropic) and the same is seen in the turbine and diffuser. The combustion chamber experiences no total pressure loss and 100 percent combustion. The entropy *s* on the *T-s* diagram is the same from Stage 2-3 and Stage 4-5. On the *P-v* diagram, there is no pressure loss from Stage 3-4, combustion, and the cycle from Stage 5-2 is open; this is typical ideal cycle behavior. Real or actual cycle behavior is also adiabatic but it is not reversible and polytropic efficiency is introduced. Total pressure loss is observed in the combustion chamber and combustion is less than 100 percent.

The *T-s* diagram in Figure 6.6 portrays the actual behavior of the Brayton cycle with regeneration. From Stage 2-3 ideal behavior is not observed since the entropy is not constant, and the same is seen from Stage 4-5. For the *P-v* diagram in Figure 6.7, total pressure loss is observed through the combustion stage and total pressure loss is also present in the regeneration stage. The total pressure loss in combustion is around 2 percent and total pressure loss on the cold side of the recuperator is approximately 1 percent. On the hot side of the recuperator, total pressure loss is calculated to be 6.7 percent. This is still within the allowable range set in Chapter 3.

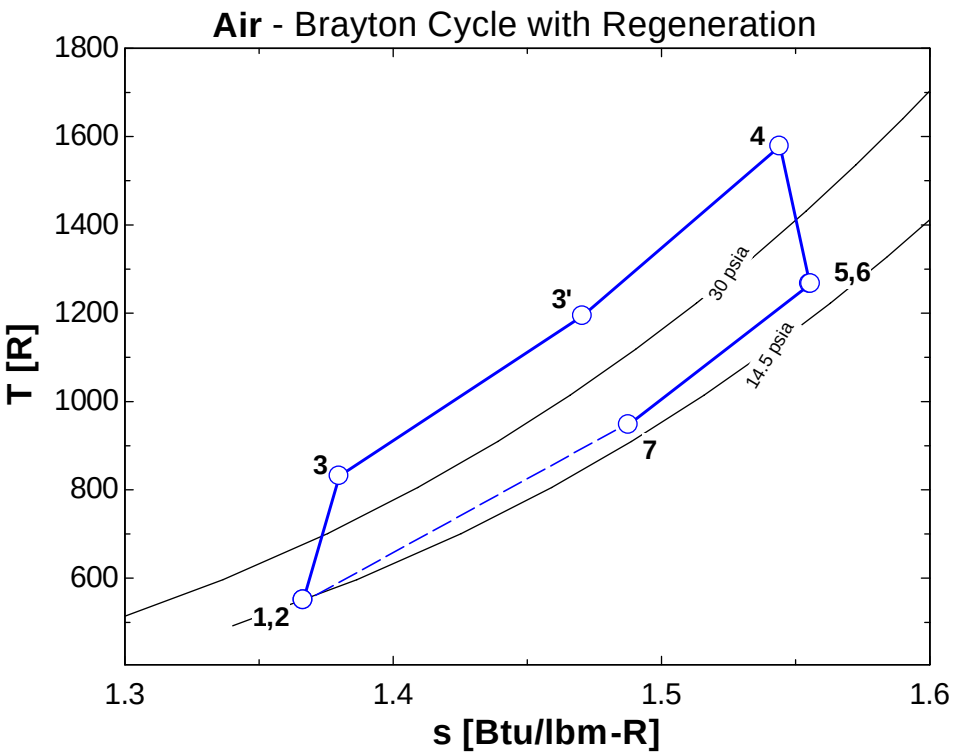

Figure 6.6: *T-s* Diagram of Actual Brayton Cycle with Regeneration

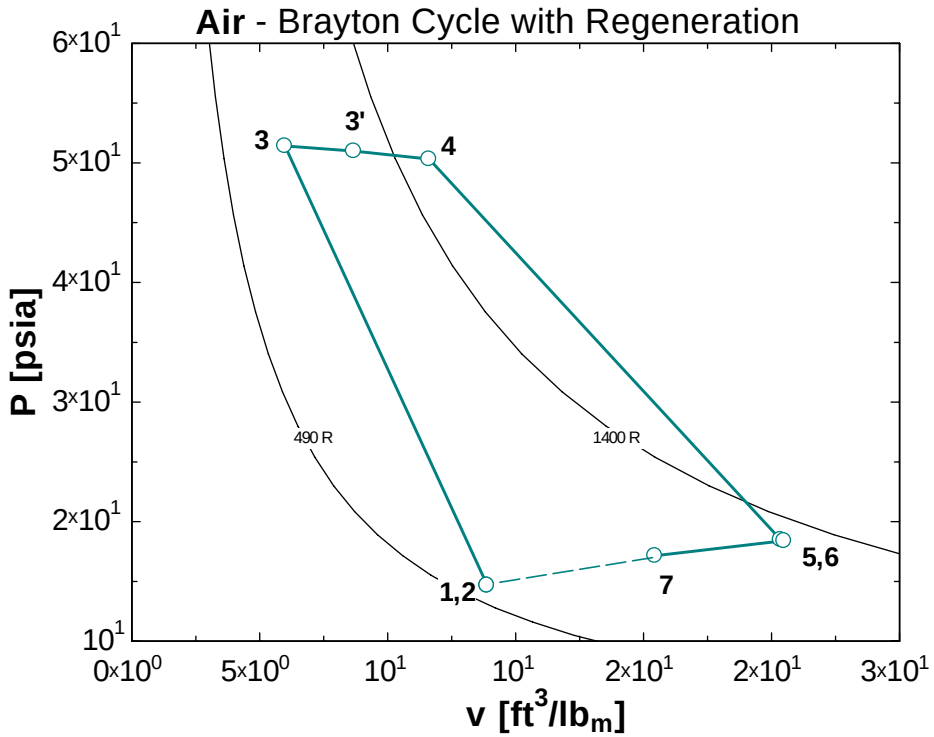

Figure 6.7: *P-v* Diagram of Actual Brayton Cycle with Regeneration

6.1.1.3 Reynolds Number Dependent Recuperator Flow

The pressure drop seen in the recuperator, on both the hot and cold sides, is related to the Reynolds numbers of the hot and cold flows, respectfully. The equation for determining Reynolds number, Equation 4.45 can be used in terms of mass flow rate instead of velocity by substituting $\dot{m}$ for V. Mass flow rate is defined as density ρ times velocity V times area A, or $\dot{m} = \rho VA$, with this substitution the Reynolds number calculation becomes

$$\mathrm{Re} = \frac{\dot{m} D_h}{A\mu} \tag{6.1}$$

Pressure loss on the cold and hot side P_{t3}' and P_{t7}, respectfully, can now be compared with Reynolds number.

As the Reynolds number increases with the increase in the mass flow rate on the cold flow side, the pressure drop also increases in a linear fashion, Figure 6.8. The flow entering the cold side P_{t3} is represented in blue and the flow exiting the cold side P_{t3}' is represented in red. Pressure loss is seen to increase with Reynolds number but the increase is done very slightly, from 0.5 percent total pressure loss to 0.9 percent total pressure loss.

The pressure drop on the hot side of the primary surface recuperator does not portray linearity with Reynolds number increase, Figure 6.9. The pressure entering the hot side P_{t6} does so in a fairly linear manner. The pressure exiting the hot-side of the recuperator does not exhibit linear behavior with the scale size on the y-axis. With pressure entering at an almost consistent 18.5 psia, the exiting pressures stay between 17 and 17.5 psia. The pressure loss calculations give a consistent average of around 6 percent.

The temperature profile on the cold-side of the recuperator is shown in Figure 6.10. The temperatures entering and exiting the recuperator are plotted versus the number of transfer units (*NTU)* to represent the *ε-NTU* method described in Section 4.1.4. For this method, the heat exchanger effectiveness ε is constant for all calculation along the actual operating line. The temperature entering the cold-side is linear throughout the entire operating cycle and the resulting calculations for the exiting temperature do not give linearity until around 4 *NTU* which translates to 69 percent on the actual MTG operating line. For the hot-side temperature profiles, Figure 6.11, non-linearity is seen for the entire operating cycle and linearity can be observed if the *NTU* parameter is less than 4.

The primary surface recuperator operates in a counterflow arrangement. The total temperatures for the hot-side and cold-side flow are represented along the length of the recuperator in Figure 6.12. The counterflow profile does not represent the change in temperatures over the length of the recuperator, but the temperatures entering and exiting the recuperator based on the *ε-NTU* method and the 1-Dimensional calculations.

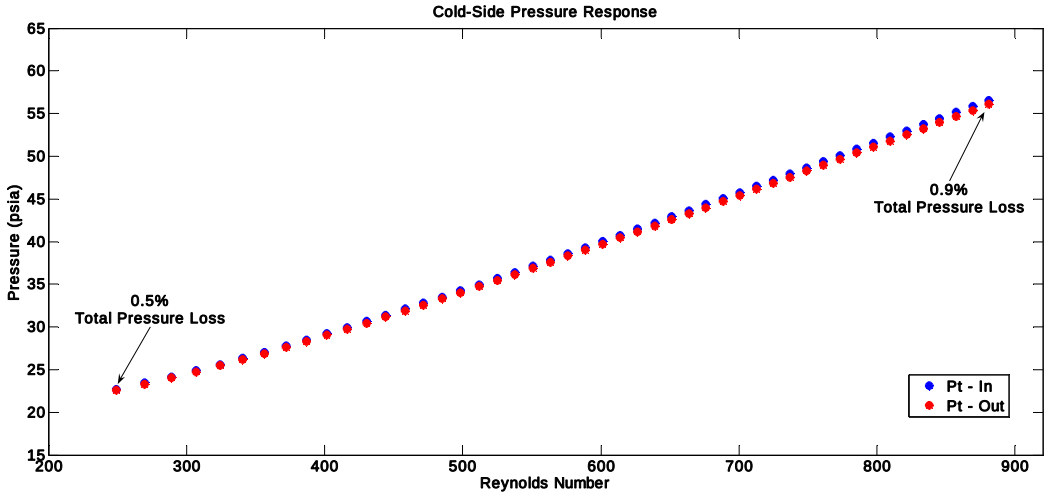

Figure 6.8: Pressure Loss on Cold Side of Primary Surface Recuperator

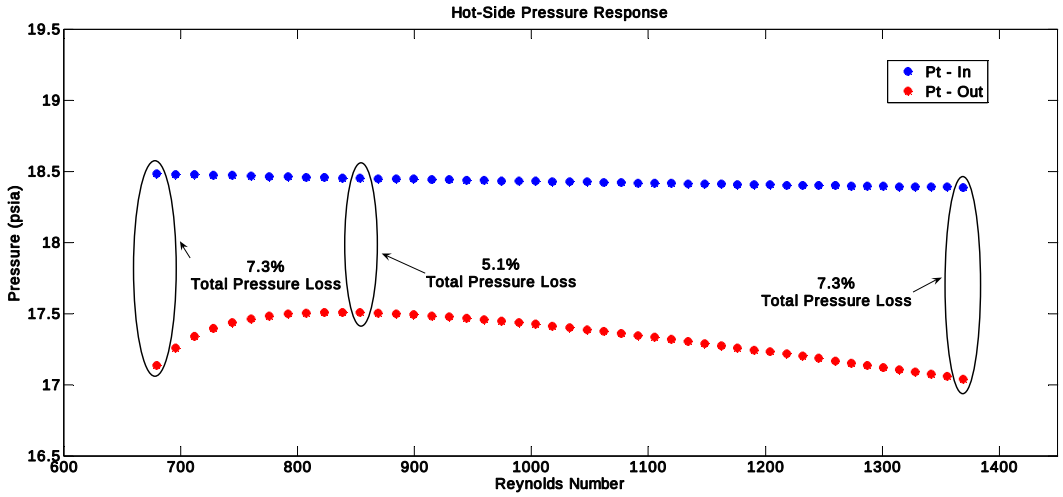

Figure 6.9: Pressure Loss on Hot Side of Primary Surface Recuperator

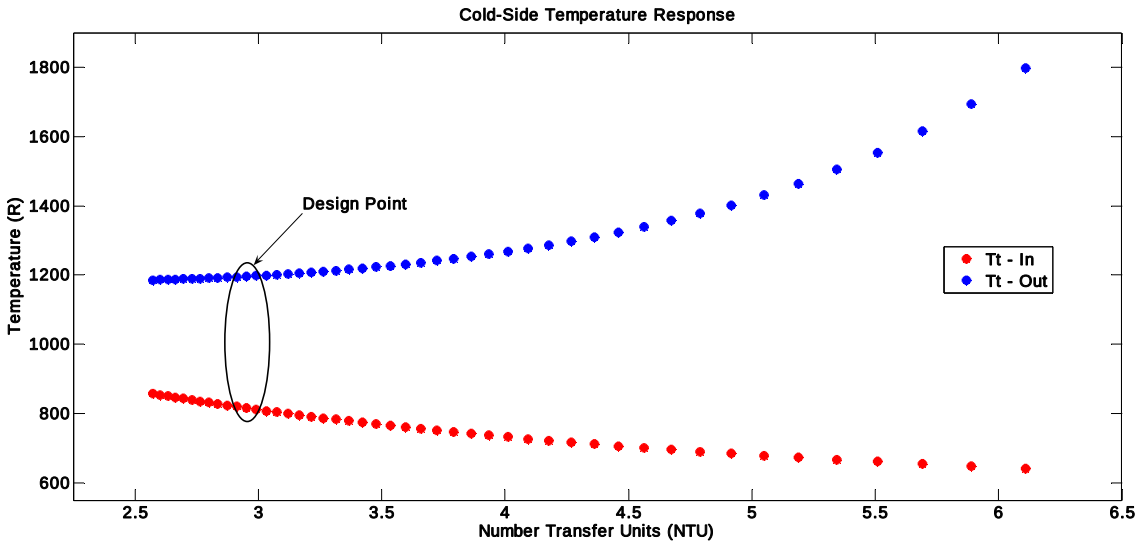

Figure 6.10 Temperature Profile for Cold Side of Primary Surface Recuperator

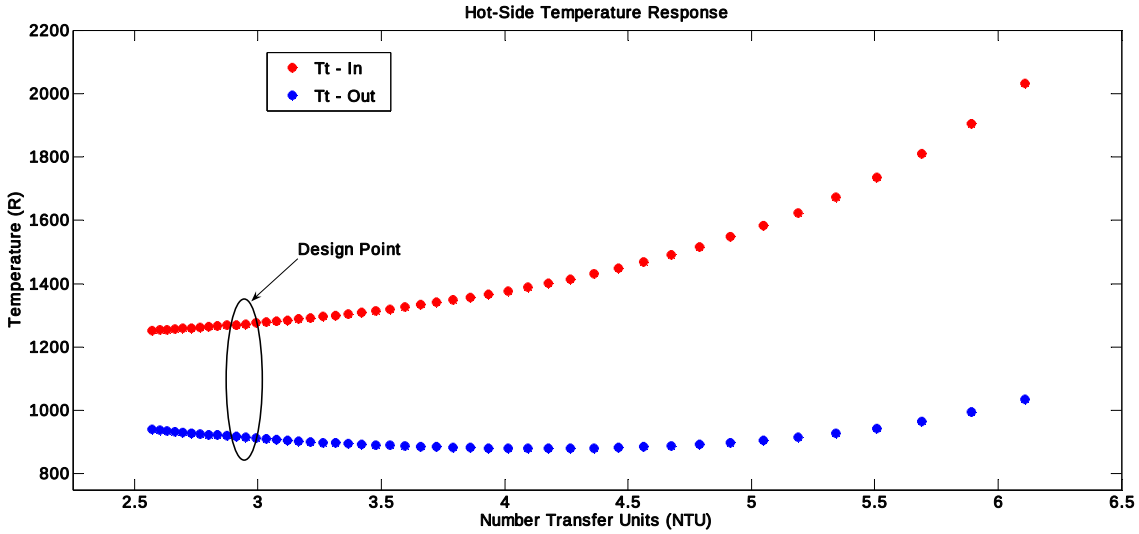

Figure 6.11: Temperature Profile for Hot Side of Primary Surface Recuperator

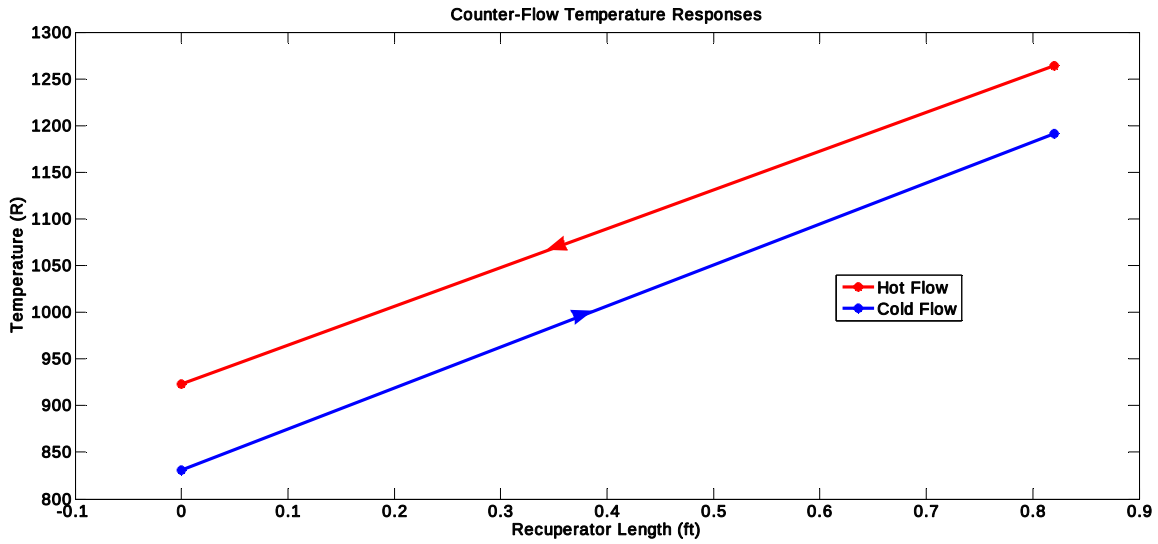

Figure 6.12 Primary Surface Recuperator Counter-Flow Temperature Responses at MTG Design Point

6.1.1.4 Mean-line Calculations

The mean-line calculations for the centrifugal compressor described in Section 4.1.1 are seen in Table 6.2. The 1-D mean-line calculations are completed station by station through the centrifugal compressor and the following parameters are calculated at each station: total and static temperature, total and static pressure, Mach number, absolute and relative velocity and all components of velocity and absolute and relative flow angles at the design point conditions. Calculations are based on trigonometry being applied to the velocity diagram in Figure 3.6, the rotor tip speed established in Equation 4.19, and isentropic relationships. The following limitations are applied to the mean-line calculations for the centrifugal compressor and are described in detail in Section 3.2:

- Rotor tip velocity U_{2t} is limited to 2000-2200 ft/s (610 to 670 m/s)
- relative flow angle at the tip, β_{1t} has swirl angle of 60 – 70 degrees from radial direction
- The tangential or swirl velocity v_2 is roughly 90 percent of rotor tip velocity U_{2t}
- Absolute velocity exiting compressor diffuser V_3 is nominally 300 ft/s (90 m/s)

With these limitations and the before mentioned trigonometry and isentropic relations, the viability of the 1-D mean-line calculations can be determined.

The rotor tip velocity U_{2t} is calculated to be 1376 ft/s. This is below the limited range of 2000-2200 ft/s. The relative flow angle at the tip, β_{1t} is calculated to be 61.36 degrees, within the nominal range. The tangential or swirl velocity v_2 is 1223 ft/s. This calculates to be 89 percent of the rotor tip velocity. The final constraint to match is the absolute velocity exiting the compressor diffuser; V_3 is calculated to be 298.1 ft/s. These variables are represented in bold in Table 6.2.

The mean-line calculations for the radial inflow turbine are given in Table 6.3. As with the centrifugal compressor, the 1-D mean-line calculations are completed station by station through the radial inflow turbine. Since Station 1 is equal to Station 2, the following parameters are calculated at Stations 2, 3m and 3: total and static temperature, total and static pressure, Mach number, absolute and relative velocity and all components of velocity and absolute and relative flow angles from the design point conditions. Calculations are based on trigonometry being applied to the velocity diagram in Figure 3.8, the rotor tip speed established in Equation 4.26, and isentropic relationships. The limitations on the radial inflow turbine are given below and described in detail in Section 3.3:

- The exit flow angle, α_2, is habitually chosen to be 70 degrees relative to the axial direction
- The rotor tip velocity U_{2t} is limited to between 1148 and 1640 ft/s (360 and 500 m/s)
- The tangential velocity v_2 is equal to U_{2t}

The rotor tip velocity U_{2t} for the radial inflow turbine is calculated to be 1450 ft/s and the exit flow angle is set to 70 degrees. These variables are shown in bold in Table 6.3.

Table 6.2: Centrifugal Compressor Mean-Line Calculations at 100 Percent of MTG Design Speed for Stand Alone Power Generation System

Compressor Results – Ideal Throttle at 100%

Station	Units	*1*	1_{Rh}	1_{Rt}	*2*	*3*
T_t	[R]	550.8	567.4	617.3	830.8	830.8
T	[R]	530.9	530.9	530.9	686.4	816.3
P_t	[psia]	14.69	16.31	21.91	56.48	51.44
P	[psia]	12.92	12.92	12.92	28.94	48.37
M	[-]	0.4332	0.587	0.9028	1.026	0.2111
V	[ft/s]	489	662.6	1019	1317	**298.1**
u/w	[ft/s]	489	489	489	489	489
v	[ft/s]	0	447.1	894.1	**1223**	-
radius	[ft]	-	0.0462	0.0925	0.1423	-
α	[deg]	0	-	-	21.81	-
β	[deg]	-	42.46	**61.36**	-	-

Table 6.3: Radial Inflow Turbine Mean-Line Calculations at 100 Percent of MTG Design Speed for Stand Alone Power Generation System

Turbine Results – Ideal and Actual Throttle at 100%

Station	Units	*1*	*2*	3_{Rm}	*3*
T_t	[R]	1575	1575	1316	1264
T	[R]	-	1326	1244	1244
P_t	[psia]	50.34	50.34	27.89	18.5
P	[psia]	-	48.19	20.99	20.99
M	[-]	-	0.8605	0.6636	0.3122
V	[ft/s]	-	1543	1122	527.8
u/w	[ft/s]	-	527.8	527.8	527.8
v	[ft/s]	0	**1450**	990.2	0
radius	[ft]	-	0.15	0.1024	-
α	[deg]	0	**70**	-	0
β	[deg]	-	-	61.94	-

6.2 Hybrid Power Generation Model Development

6.2.1 0-Dimensional

The 0-D hybrid power generation model is manipulated through the PID (Proportional Integral Derivative) controller placed on the microturbine generator portion of the hybrid model. The PID controller allows for the mechanical (actual) power generation from the MTG to be controlled through applying a torque load τ_{LOAD} to the shaft. This loading of the shaft will result in increased power generation and decreased shaft speed. If desired the PID controller will allow for power generation at a consistent 22126 ft-lbf/s (30 kW) which is a design variable for the system. Figure 6.13 shows the torque load being applied and the resulting shaft speed to maintain MTG power generation of 30 kW. The unit system used in the results will be based on the data being portrayed. To analyze the hybrid model, power generation, *LHV* and *HHV* efficiency, temperature, and pressure responses throughout the model will be observed.

6.2.1.1 Power Generation

The hybrid model calculates all transients from initial conditions; the model does not have start up capabilities. The transient behavior is seen from 0-10,000 seconds where steady state operating conditions or numerical convergence is reached. This can be seen Figure 6.14 with the MTG shaft speed response. The power generation for the MTG is at a steady 30 kW to demonstrate the transient response and numerical convergence of the hybrid model.

To evaluate the responses of the hybrid model, the MTG power generation is executed at 0 kW until steady state operation seen at 10,000 seconds is reached and then

the power is ramped to 30 kW. This ramping is accomplished at six different time intervals by varying the slope of the ramp. The ramping is taken from a slope of 0.5, for a very long time constant, to a slope of 3.0 a quick time constant. The power generation ramping can be seen in Figure 6.15. All of the simulations are run to 80,000 seconds for consistency.

Since the molten carbonate fuel cell (MCFC) power generation is dependent on the voltage emitted by the fuel cell, Figure 6.16 shows the transient response of the voltage for the MTG power ramping. The unique behavior in Figure 6.16 is due to the fuel cell model not reaching steady operating conditions as fast as the MTG model. For a ramp slope of 3.0, the power increase begins at 10,000 seconds and is done by 20,000 seconds. The voltage response decreases between this interval and then increases until steady operating conditions are reached approximately 10,000 seconds later. This is observed for all the MTG power ramping conditions of Figure 6.15.

From this voltage response, the corresponding MCFC power generation response and the overall hybrid system power generation response is shown in Figure 6.17. The fuel cell is not excessively responsive to the MTG power ramping since the fuel cell's power calculation is not overly influenced by the MTG or the shell-and-tube heat exchanger. The overall hybrid power generation is increased by the MTG power ramping from 0 – 30 kW.

The hybrid system efficiency response is shown in Figure 6.18. The calculations for the *LHV* and *HHV* of natural gas are dependent on the hybrid power generation. The responses in Figure 6.18 are due to the responsive nature of the PID controller on the MTG power generation. The *LHV* efficiency at steady operating conditions is

approximately 44 percent and the *HHV* efficiency at steady operating conditions is approximately 40 percent. Hybrid power systems are capable of 60 percent *LHV* efficiency, this system's efficiency is low because the power requirement is for 250 kW and the model is capable of producing higher power. Higher power generation would give greater *LHV* and *HHV* efficiencies. Loading the MTG to produce 60 kW gives hybrid power of 290 kW. The *LHV* efficiency becomes 48 percent and *HHV* efficiency becomes 43 percent.

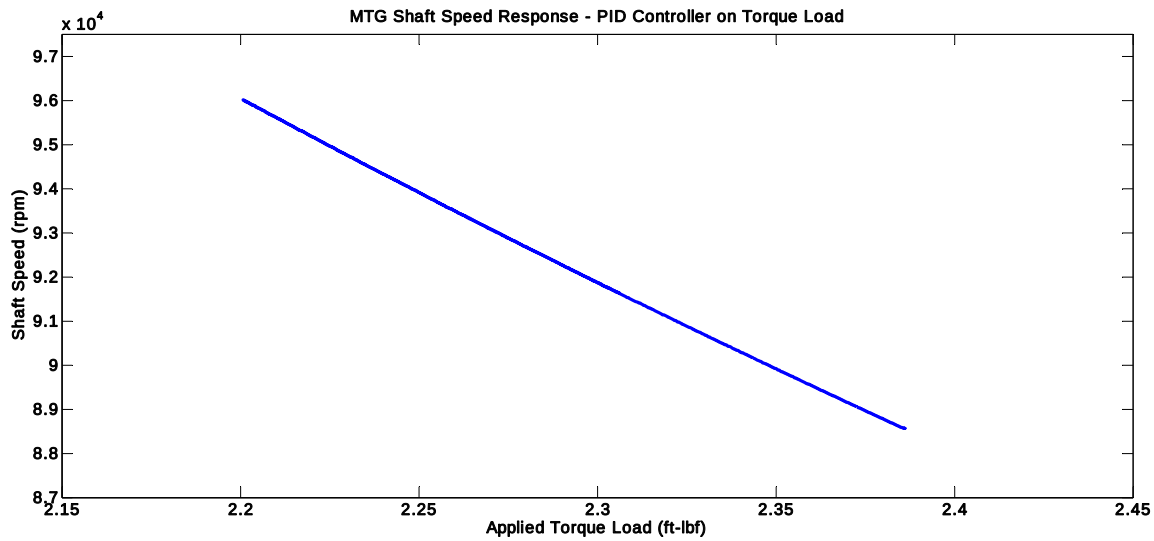

Figure 6.13: Shaft Speed Response to Controlled MTG Power Generation of 30 kW

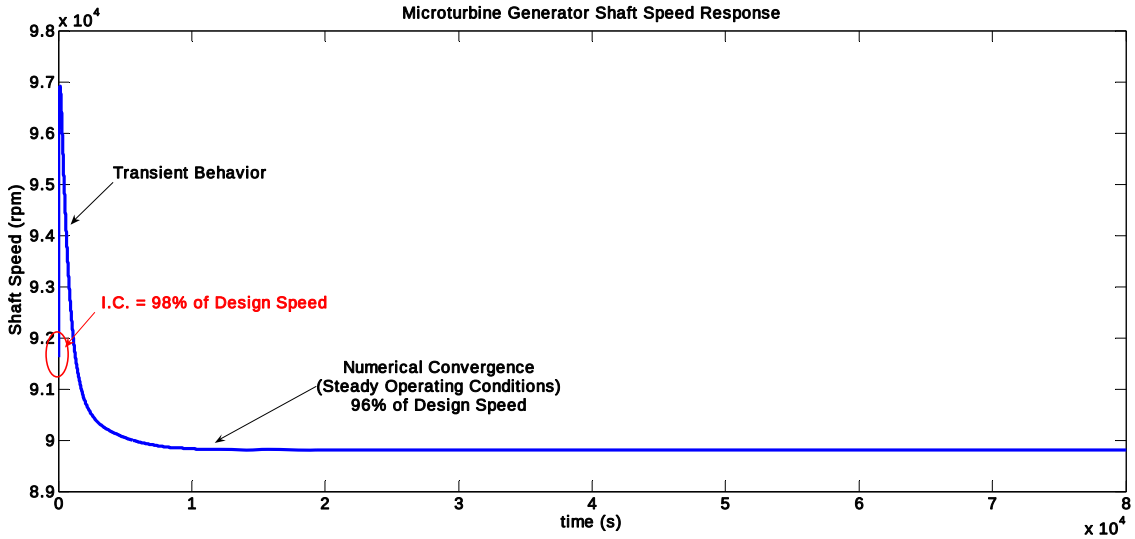

Figure 6.14: Microturbine Generator Shaft Speed Response for Power at 30 kW

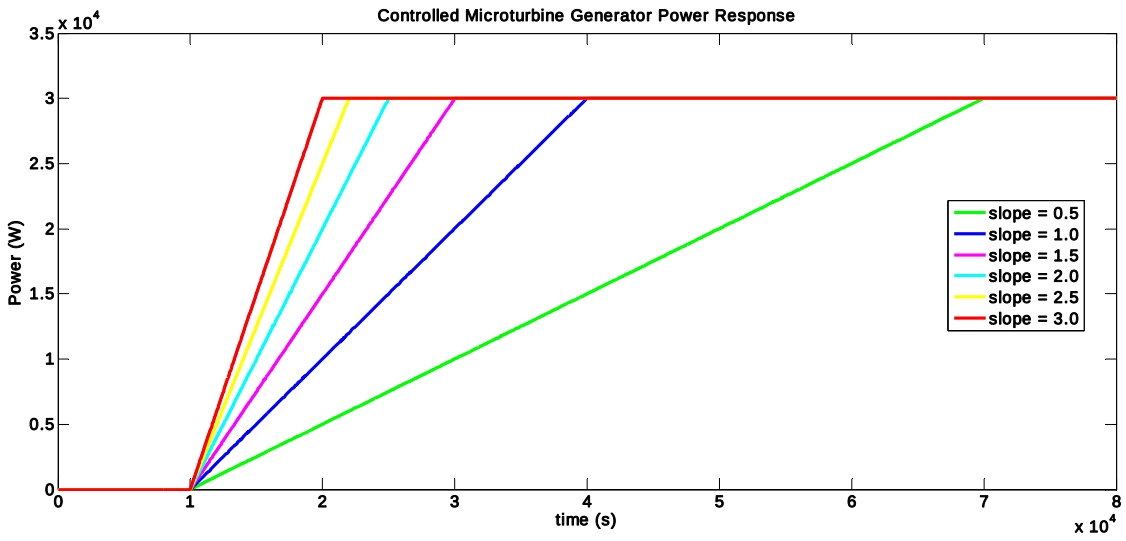

Figure 6.15: Microturbine Generator Forced Ramping Power Response

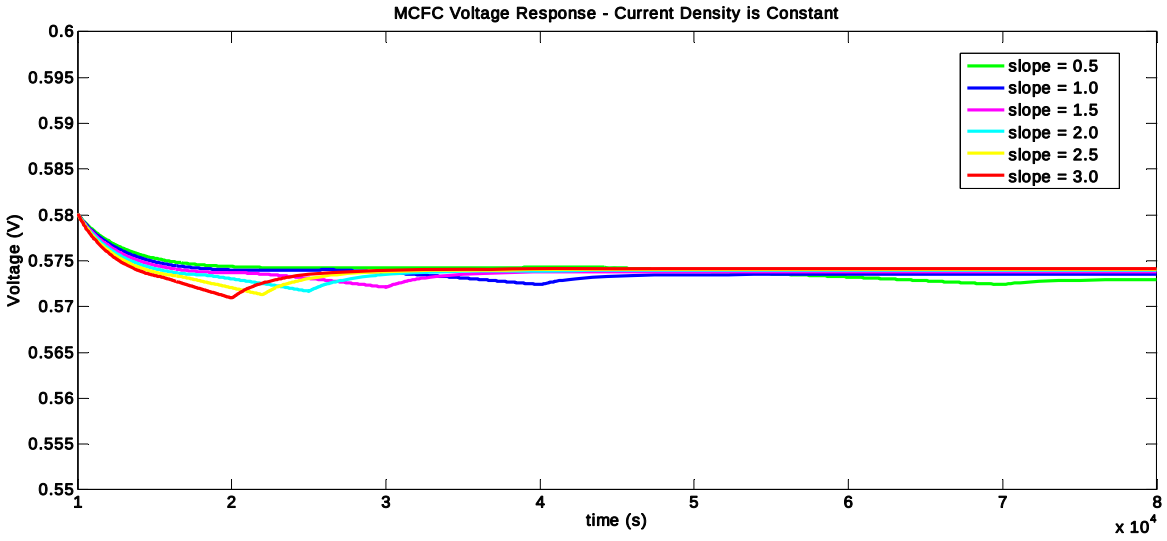

Figure 6.16: Molten Carbonate Fuel Cell Voltage Response

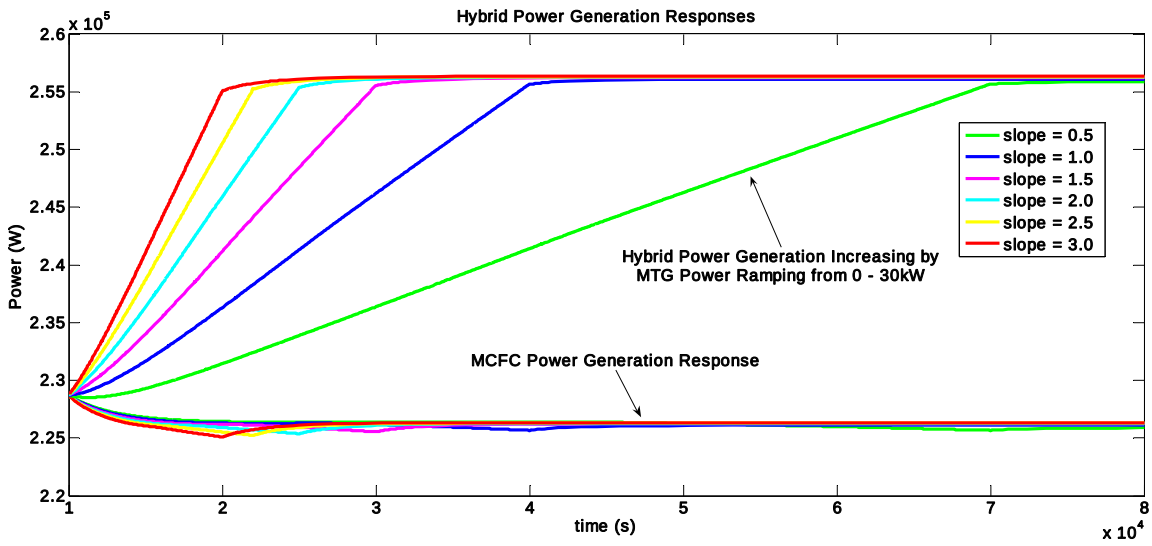

Figure 6.17: Power Response of MCFC and Hybrid Power Generation System

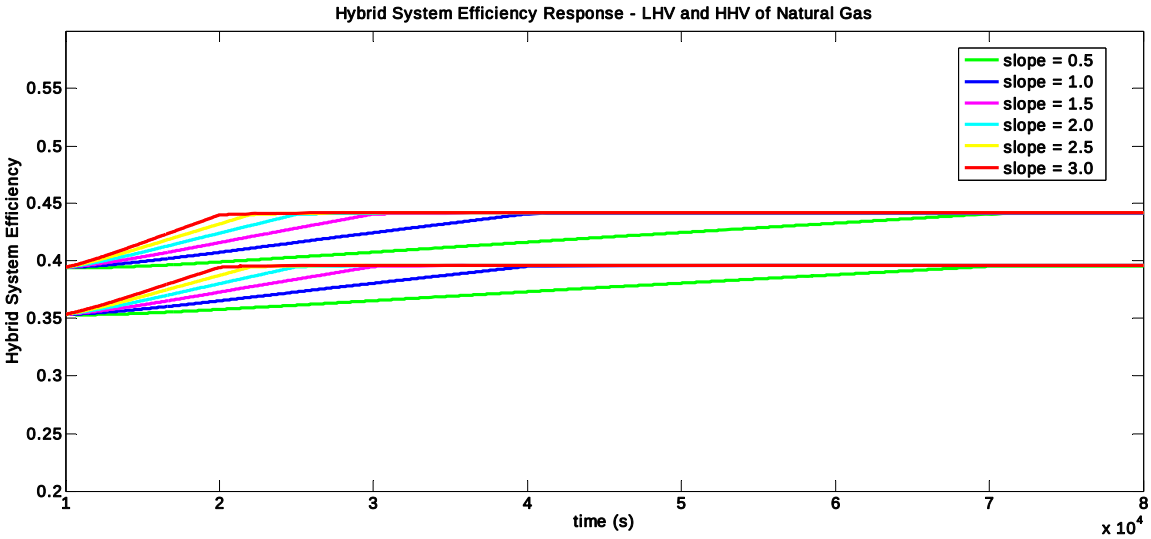

Figure 6.18: Hybrid Power Generation System Efficiency Response

6.2.1.2 Temperature Responses from MTG Power Ramping

Referring to Figure 5.3, the temperature of the flow from the anode, at stack temperature, is sent to the oxidizer along with the temperature of the flow from the turbine diffuser. These two temperatures are combined through enthalpy and then integrated to determine the temperature of the flow exiting the oxidizer. The temperature of the flow exiting the oxidizer is sent to the shell-and-tube heat exchanger where it is used to heat the flow from the compressor, shell-side, before it enters the turbine. Once the oxidizer flow, tube-side, is cooled it is sent to the cathode where combined with the anode temperature, which is constant, the MCFC stack temperature is calculated.

The temperature entering the shell-side of the heat exchanger is directly from the compressor. As the MTG power is increased through applying a ramp to the PID controller a subsequent decrease in shaft speed is seen. The shaft speed is used to determine the total pressure ratio π_c from the compressor mapping and this is used to find the compressor exit temperature. A direct correlation between shaft speed and compressor temperature can be seen in Figure 6.19 (labeled "Temperature In – Shell Side"). As the shell-side temperature is calculated through the heat exchanger at different ramping conditions, the response of the heat exchanger is slow due to the increased time constant and the inability of the temperature calculations on the shell-side to respond quickly. The temperature exiting the shell-side is sent to the turbine where energy is extracted and the flow is cooled before it enters the diffuser, where it is slowed before being fed to the oxidizer.

The temperature into the tube-side of the heat exchanger is from the oxidizer which is calculated from the diffuser temperature and the anode temperature, at stack

temperature. Since the temperature from the diffuser is dependent on the shaft speed and the MTG shaft speed is changing as the load is changing, this phenomenon drives the responses seen in the oxidizer, Figure 6.20 ("Temperature In – Tube Side") and Figure 6.23. As with the temperature calculations on the shell-side, the tube-side temperature responses are slow through the heat exchanger. The temperature exiting the tube-side is sent to the fuel cell cathode.

Determining the fuel cell stack temperature is accomplished through integrating the anode inlet temperature and the cathode inlet temperature. The cathode and anode exit temperatures are at the fuel cell stack temperature. The fuel cell stack temperature response is seen in Figure 6.21. With the anode inlet temperature held constant, the stack temperature response is driven only by the cathode inlet temperature, from the tube-side of the heat exchanger. Since this is the case, the response is slow compared to the compressor or diffuser responses.

The final temperature response for the hybrid system is within the oxidizer. Figure 6.22 portrays the temperatures entering the oxidizer; the MCFC stack temperature and the diffuser temperature. The oxidizer temperature response is quicker than the response through the heat exchanger, both tube- and shell-side. This response is shown in Figure 6.23 and is driven by the diffuser temperature.

All of the temperatures are interwoven except for the anode inlet temperature, which is constant. Model responses can be seen through each of the hybrid components. The slowest responses, which have the longest time constant is with the temperature responses on the hot- and cold-sides of the shell-and-tube heat exchanger. All of the

temperatures are ultimately driven by the shaft speed except for the constant anode inlet temperature.

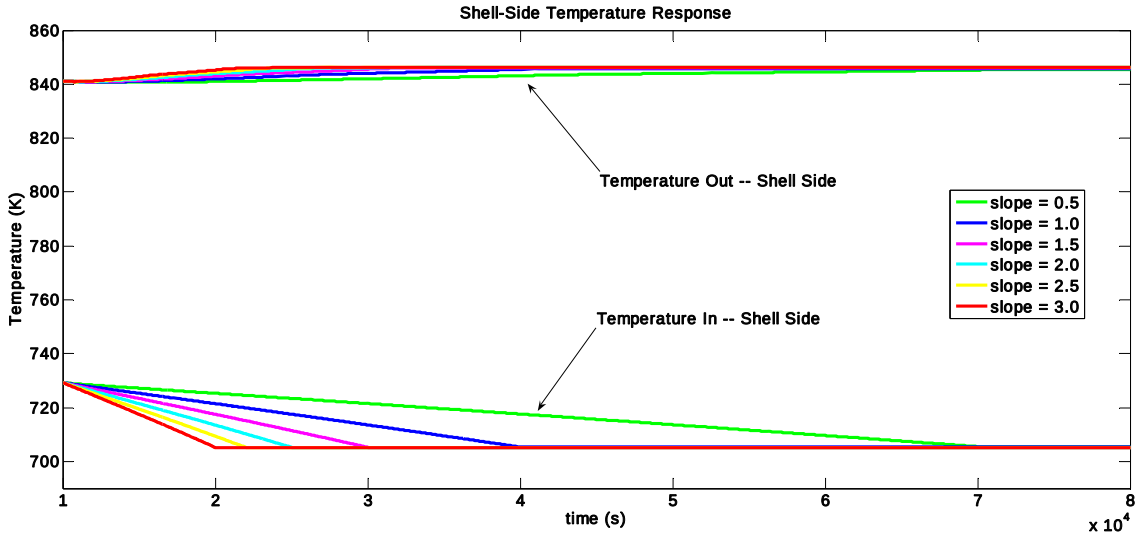

Figure 6.19: Transient Temperature Response Shell – Side of Shell-and-Tube Heat Exchanger

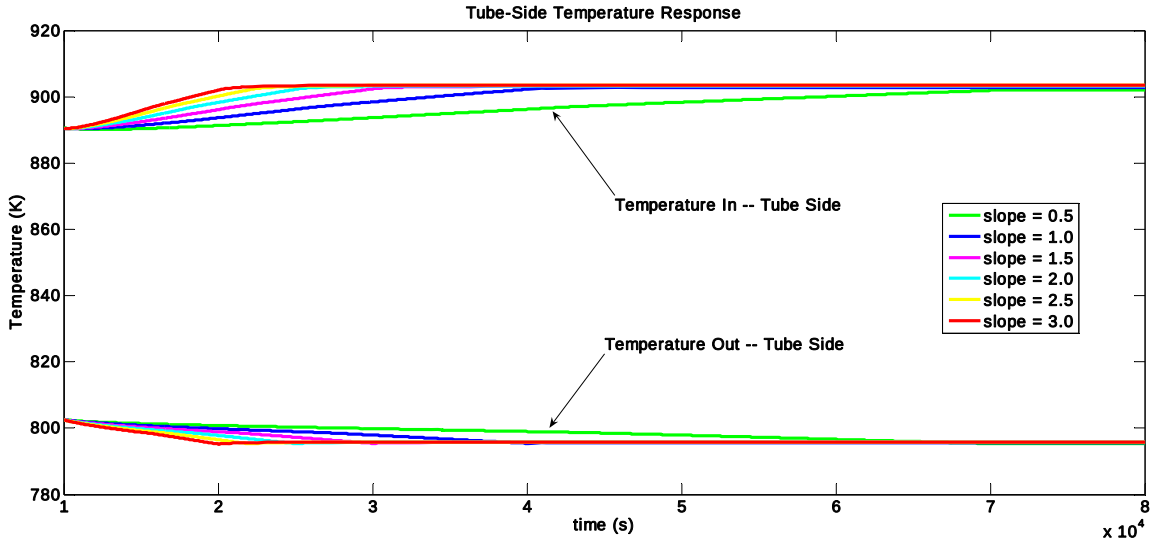

Figure 6.20: Transient Temperature Response Tube – Side of Shell-and-Tube Heat Exchanger

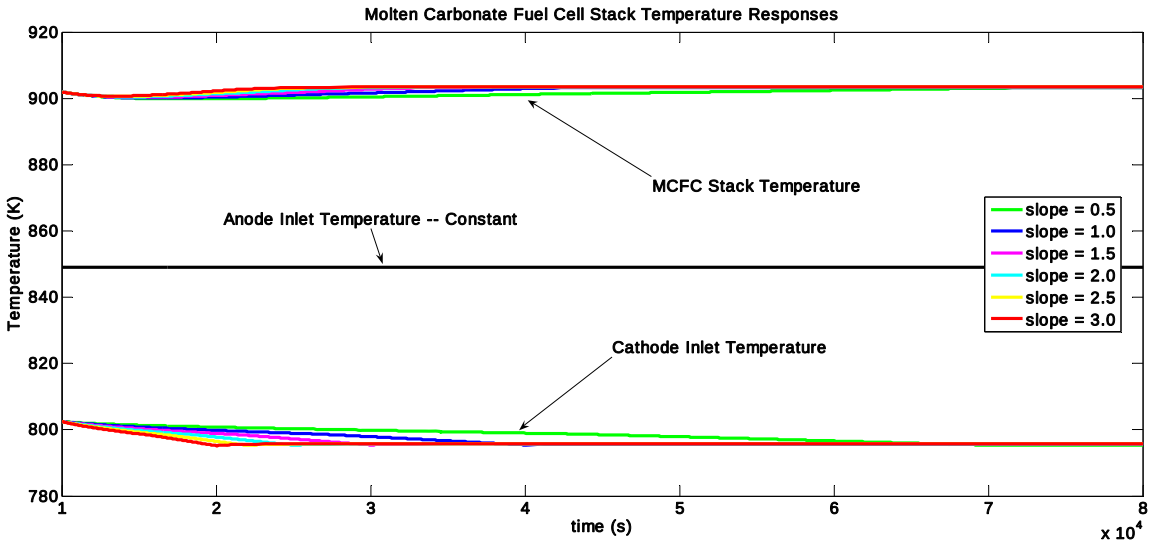

Figure 6.21: Integrated MCFC Stack Temperature Response

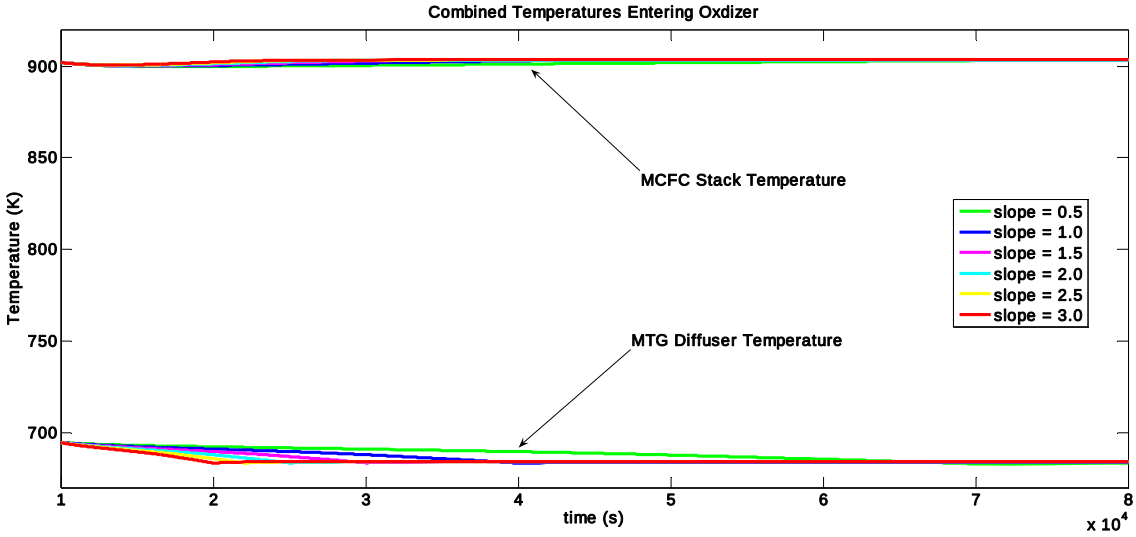

Figure 6.22: Transient Temperature Responses Entering Catalytic Oxidizer

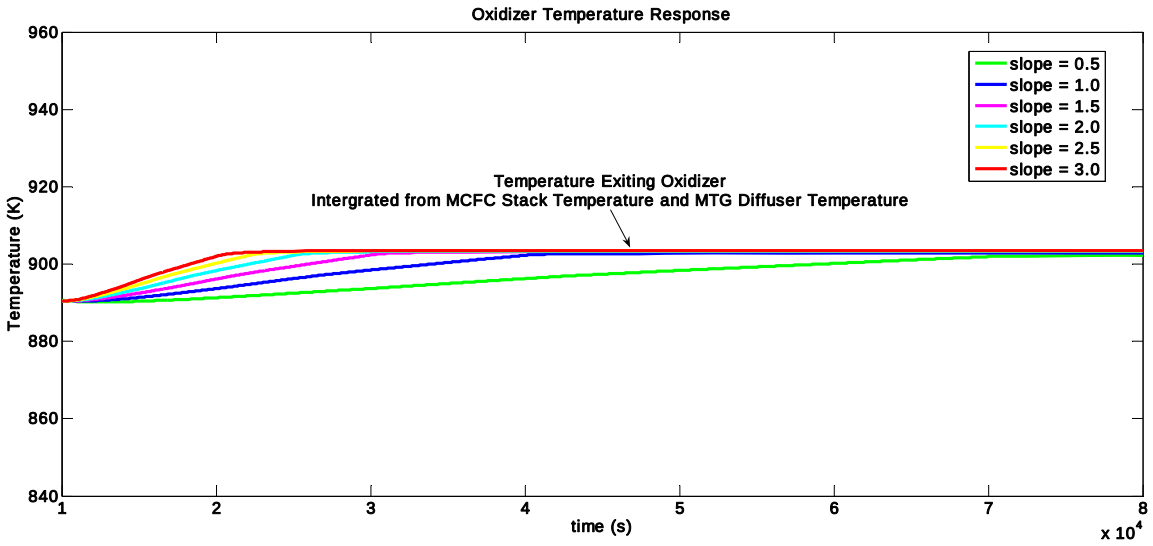

Figure 6.23: Transient Temperature Response of Catalytic Oxidizer

6.2.1.3 Heat Exchanger Pressure Responses from MTG Power Ramping

As the transient hybrid model is run for different MTG power ramping, the pressure loss through the shell-and-tube heat exchanger is shown in Figures 6.24 and 6.25 for the shell-side and tube-side, respectfully. The shell-side pressure loss, in percent, is approximately 2.7 percent before the MTG power ramping is initiated. As the pressure into the shell-side decreases while the load on the shaft is applied, the pressure loss seen in the heat exchanger increases to approximately 2.9 percent at steady operating conditions.

The tube-side pressure loss is at approximately 0.77 percent before the power ramping is initiated. As the MTG shaft is loaded, the pressure loss for the tube-side increases to approximately 1.02 percent when steady operating conditions are reached. The pressure loss response, once ramping is initiated until steady operating conditions, through both sides of the heat exchanger are linear in nature and the pressure integrators react much faster than what was seen with the temperature responses through the heat exchanger.

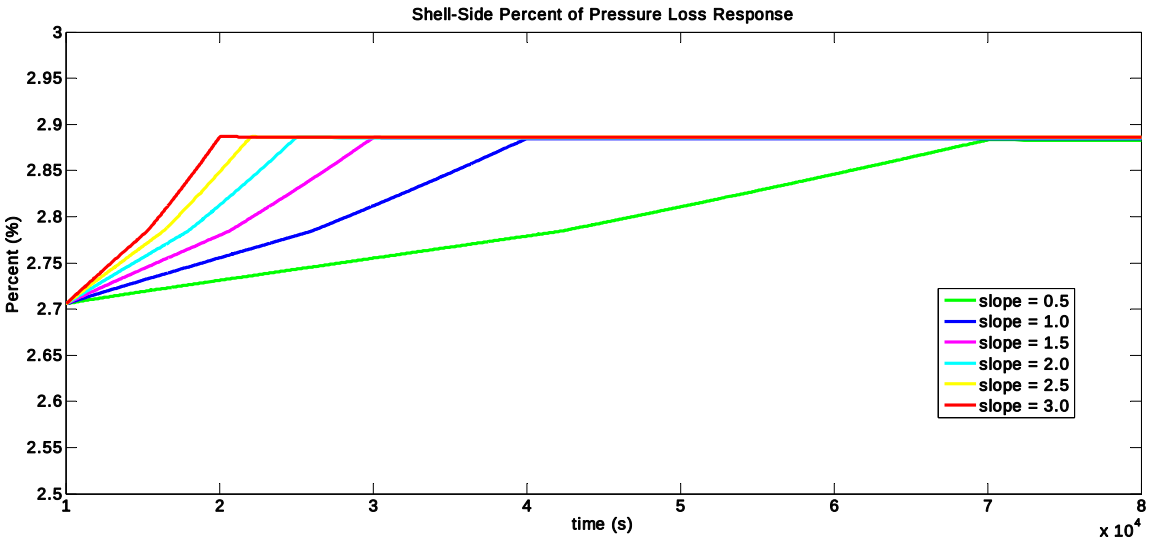

Figure 6.24: Transient Pressure Response Shell – Side of Shell-and-Tube Heat Exchanger

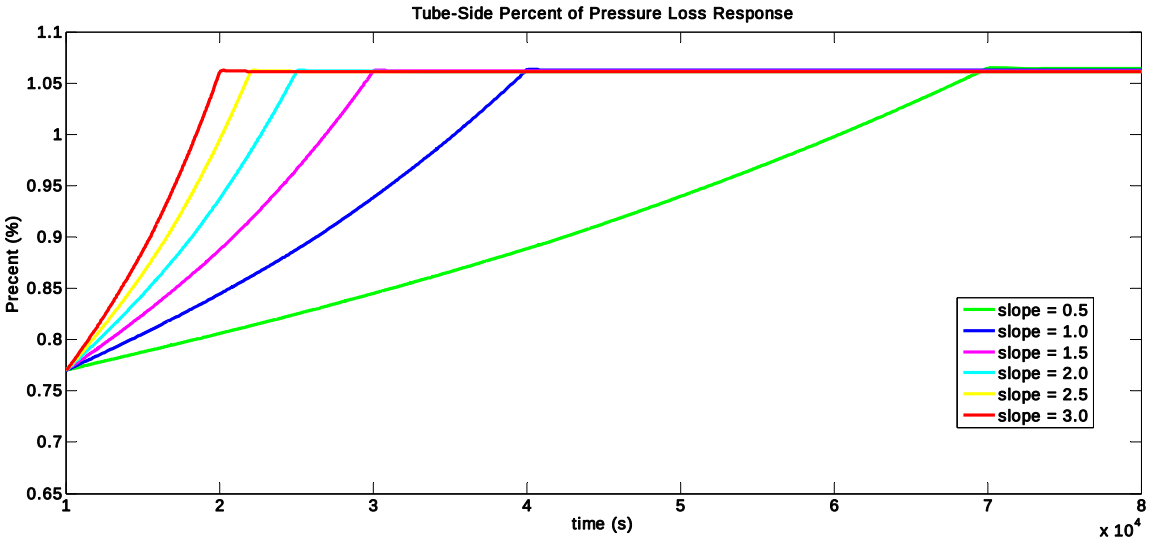

Figure 6.25: Transient Pressure Response Tube – Side of Shell-and-Tube Heat Exchanger

6.2.1.4 Additional PID Controller on MCFC Power Response

To further analyze the controllability of the hybrid power generation system, an additional PID controller was placed on the MCFC power generation response. The two control systems, one with a PID only on the MTG power generation and the other with PID controllers on the MTG power generation and MCFC power generation are compared. The power control for the microturbine generator is the torque load applied to the shaft. For the MCFC it is the current density. Figure 6.26 gives the voltage response to a controlled current density allowing for the MCFC power generation to remain consistent. To compare the MCFC power generation with the two models, the desired MCFC power generation was set to 225 kW. The models are compared at two ramping conditions, slopes of 1.0 and 1.5.

The temperature responses through both the tube- and shell- sides of the heat exchanger were observed. Figure 6.27 has the transient response of the temperature entering the shell-side. The response is seen with only the PID controller on the MTG power generation and with a PID controller on both the MTG power generation and the MCFC power generation. The error once steady state operating conditions are reached is 0.08 percent and the transient behavior before the MTG power ramping is introduced at 10,000 seconds is greater for the system with the two PID controllers in place. Transient temperature responses exiting the shell-side are shown in Figure 6.28. The transient response is greater for the system with the two PID controllers and the steady state error is seen to be 0.7 percent.

For the transient temperature responses entering on the tube-side, the error between the two control systems is seen to be 0.9 percent at steady operating conditions,

Figure 6.29. The transient response for the system with two PID controllers is consistent with the shell-side responses. The temperature responses exiting the tube-side of the heat exchanger is given in Figure 6.30. At steady operating conditions the error between the two systems is 0.5 percent. A large transient response on the two-PID controller system is consistent with the heat exchanger temperature responses shown in this section.

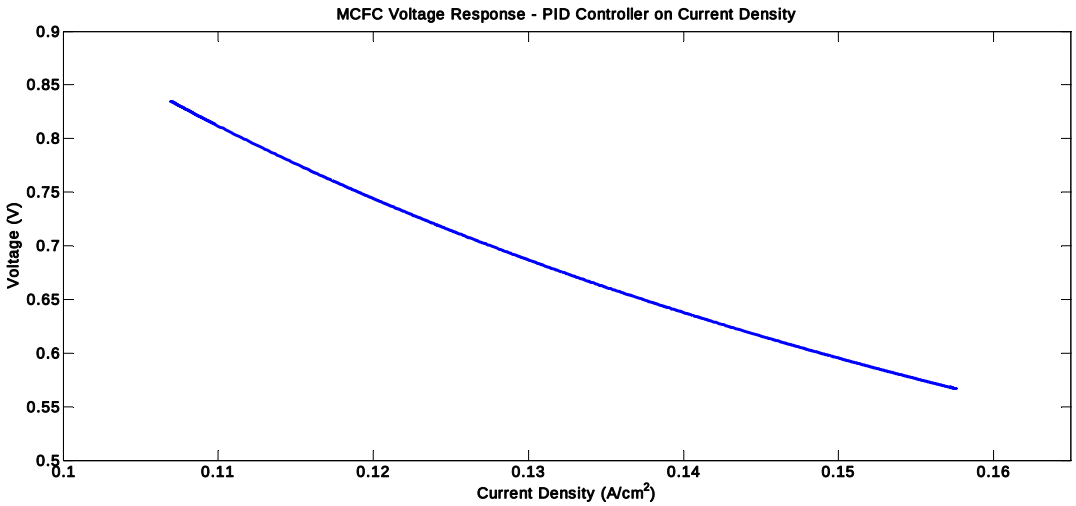

Figure 6.26: MCFC Voltage Response to Controlled MCFC Power Generation of 225 kW

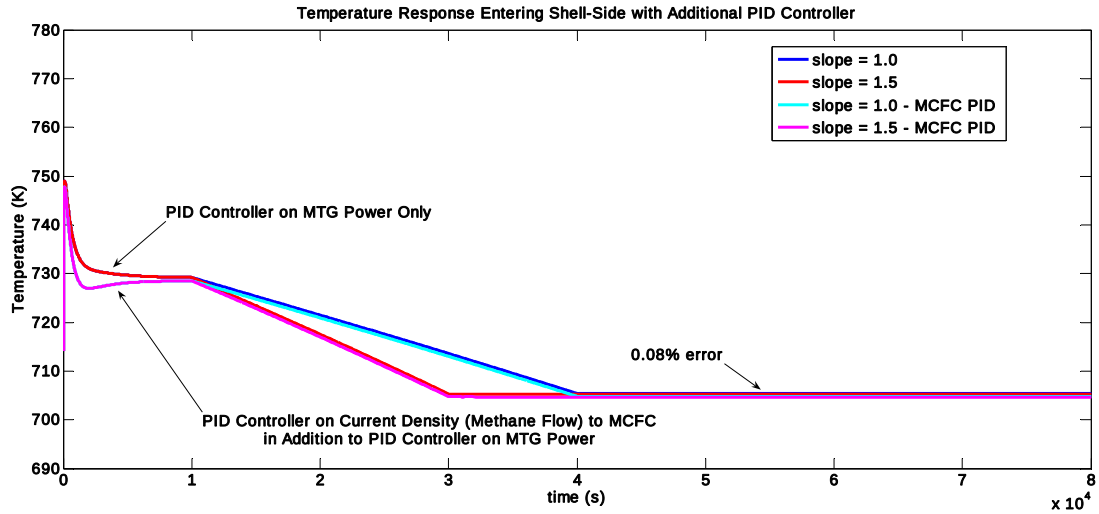

Figure 6.27: Transient Temperature Response (With Error) Entering Shell – Side with Additional PID Controller on MCFC Current Density Input *I*

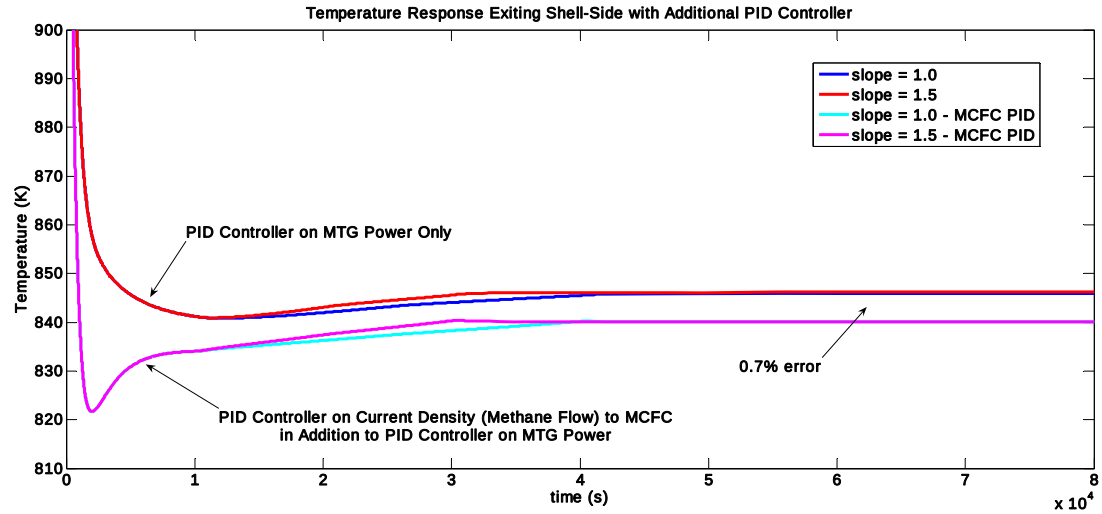

Figure 6.28: Transient Temperature Response (With Error) Exiting Shell – Side with Additional PID Controller on MCFC Current Density Input *I*

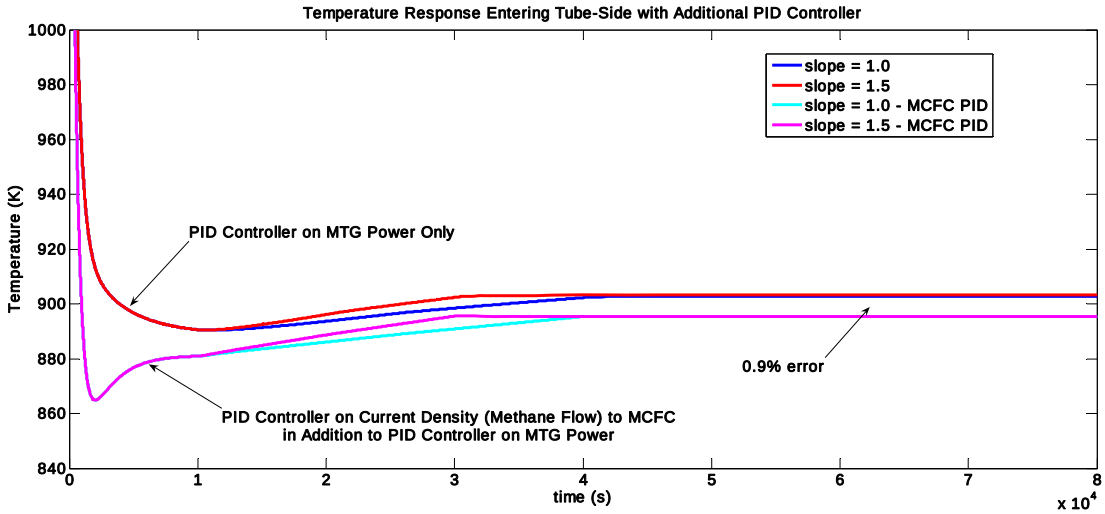

Figure 6.29: Transient Temperature Response (With Error) Entering Tube – Side with Additional PID Controller on MCFC Current Density Input *I*

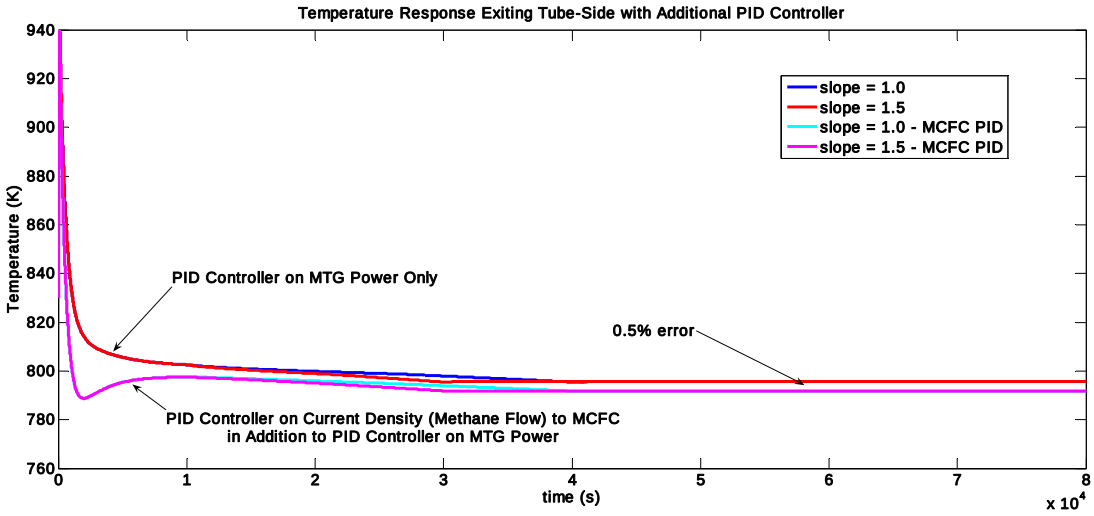

Figure 6.30: Transient Temperature Response (With Error) Exiting Tube – Side with Additional PID Controller on MCFC Current Density Input *I*

6.2.2 1-Dimensional Zooming

All of the data correlating to Figures 6.31 through 6.35 is given in Appendix B. The 1-D zooming of the hybrid microturbine generator portion, consisting of a centrifugal compressor and radial inflow turbine, in the hybrid power generation model has been validated through comparing data with that given in the 1-D stand alone analysis represented in Section 6.1. Linear determination of the data represented in Figures 6.31 though 6.35 will be analyzed in the same manner as in Section 6.1.

6.2.2.1 1-D Zooming Operating Line Calculations

The 1-D zooming MATLAB/Simulink® model calculates the core variables and mean-line variables for the actual hybrid MTG operating line based on the ideal compressor operating line. The calculations are from 40 percent to 110 percent of the ideal compressor operating line. The MATLAB/Simulink® model calculates all variables based on the ideal compressor operating line independent parameters, $\dot{m}_{oc}$ and π_c. With these two parameters, the actual operating line of the MTG is established. All of the following figures are for the actual operating line of the MTG. Table 6.4 gives the ideal operating speed at 40-110 percent of the design speed and the actual operating speed that translates into 47-103 percent of the design speed. The total temperature entering the turbine for the hybrid model is less than that of the stand alone model. Since the shaft speed is a function of temperature, the design shaft speed for the hybrid model is slightly higher than that of the stand alone model. The design speed for the hybrid model is N_{des} = 93500 rpm for the ideal and actual operating cycles.

The shape of the compressor total temperature curve, Figure 6.31 is identical to that for the stand alone model in Figure 6.1. The compressor in the hybrid model does not have transient behavior since calculations through the compressor are analyzed 1-Dimensionally from the compressor operating line. As the flow exits the compressor, it enters the shell-side of the shell-and-tube heat exchanger where 0-Dimensional calculations occur. The flow exiting the shell-side is transported to the turbine where calculations through the turbine are done 1-Dimensionally.

The 1-D hybrid zooming model is allowed to calculate until the transients still present in the model have reached steady operating conditions. The data featured in Figures 6.31 to 6.35 is taken after the transients have been allowed to reach steady conditions. The transient sub-systems in the 1-D hybrid zooming model reach steady operating conditions at 3,000 seconds. This is faster than the 0-D hybrid model which reaches steady conditions at 10,000 seconds. The 0-D hybrid model has additional transients with the microturbine generator shaft speed and power calculations; these are replaced with simple calculations in the 1-D hybrid zooming model.

The turbine temperature calculations in Figure 6.32 do not portray the same curve fit as with the stand alone model in Figure 6.2. This is due to the transient conditions entering the turbine from the 0-D heat exchanger model. The transient entering temperature T_{t4} and the 1-D calculated exiting temperature T_{t5} of the hybrid model does not reach linearity as the design point is approached but the curve of the hybrid model demonstrates better ideal cycle matching to actual cycle than with the purely 1-Dimensional model in Figure 6.2.

The hybrid system efficiency for both *LHV* and *HHV* of natural gas is given in Figure 6.33. These efficiencies are perfectly linear proving the claim that the ideal cycle may in fact accurately map the actual cycle of the microturbine generator. Figure 6.34 has the thermodynamic (ideal) and mechanical (actual) power generation by the microturbine generator. The actual power generated does not cross the ideal power curve, but comes within 99 percent. Since the actual power is not greater than the ideal power, this shows that the ideal cycle does map the actual cycle for the entire actual operating line of the microturbine generator. The general shape of the data in Figures 6.5 and 6.34 are similar in appearance. This strengthens the validation of the 1-D zooming of the hybrid power generation model.

As the flow exits the turbine and diffuser, it combines in the oxidizer with the flow leaving the fuel cell anode, at stack temperature. The fuel cell temperature calculations are completed fully 0-Dimensionally. The flow from the diffuser is created with the 1-D zooming technique. The cathode inlet flow is from the tube-side of the heat exchanger, 0-D calculations. The oxidizer temperature, calculated from diffuser and anode exit temperature, is fed to the tube-side of the heat exchanger. All four of these temperatures are interdependent. In Figure 6.35, the diffuser temperature, represented in yellow, has a more dramatic response to the calculations done along the actual operating line. The stack temperature (anode exit temperature) in red has a more mild reaction. The stack temperature is calculated from the anode inlet temperature which is constant, and the cathode inlet temperature which comes directly from the heat exchanger.

It was established in Section 6.2.1 that the oxidizer temperature is driven by the diffuser temperature. This is seen by the shape of the data in Figure 6.35 represented in

green. The transient temperature responses through the heat exchanger, represented as the cathode inlet temperature in blue in Figure 6.35, drive the responses of the stack temperature. Even though the microturbine generator can function at all points along the operating line, the fuel cell does not operate above 1000 K. From Figure 6.35, the actual cycle for the hybrid model should not operate below 68 percent of the actual microturbine operating line.

Table 6.4: Ideal and Actual Hybrid MTG Operating Line Shaft Speed

Ideal - EES		Actual - MATLAB	
Speed	$N_{\%}$	*Speed*	$N_{\%}$
rpm	-	rpm	-
37400	0.400	44200	0.473
42100	0.450	51900	0.555
46700	0.500	58100	0.622
51400	0.550	63400	0.678
56100	0.600	68000	0.727
60800	0.650	72000	0.770
65400	0.700	75700	0.810
70100	0.750	79000	0.845
74800	0.800	82100	0.878
79500	0.850	84900	0.908
84100	0.900	87500	0.936
88800	0.950	90000	0.963
93500	1.000	92300	0.987
98200	1.050	94500	1.011
102800	1.100	96600	1.033

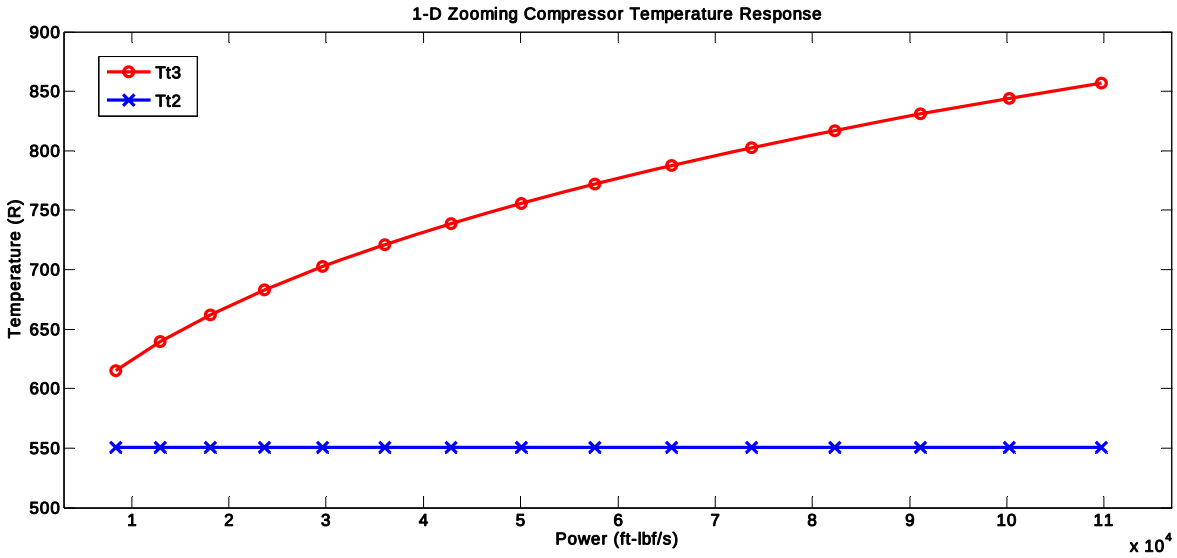

Figure 6.31: Temperature Profile for 1-D Zooming Centrifugal Compressor

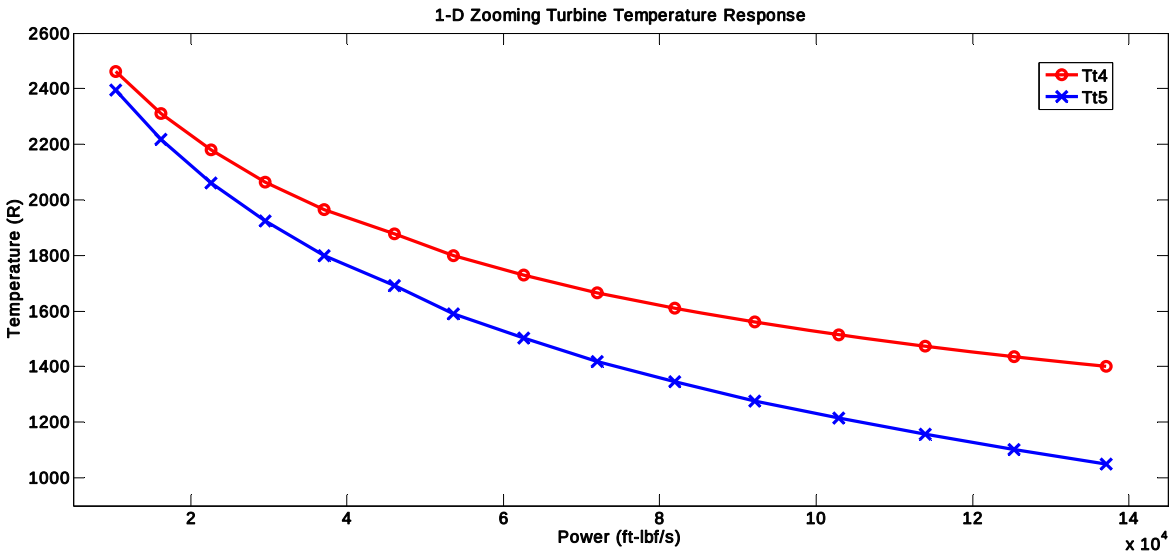

Figure 6.32: Temperature Profile for 1-D Zooming Radial Inflow Turbine

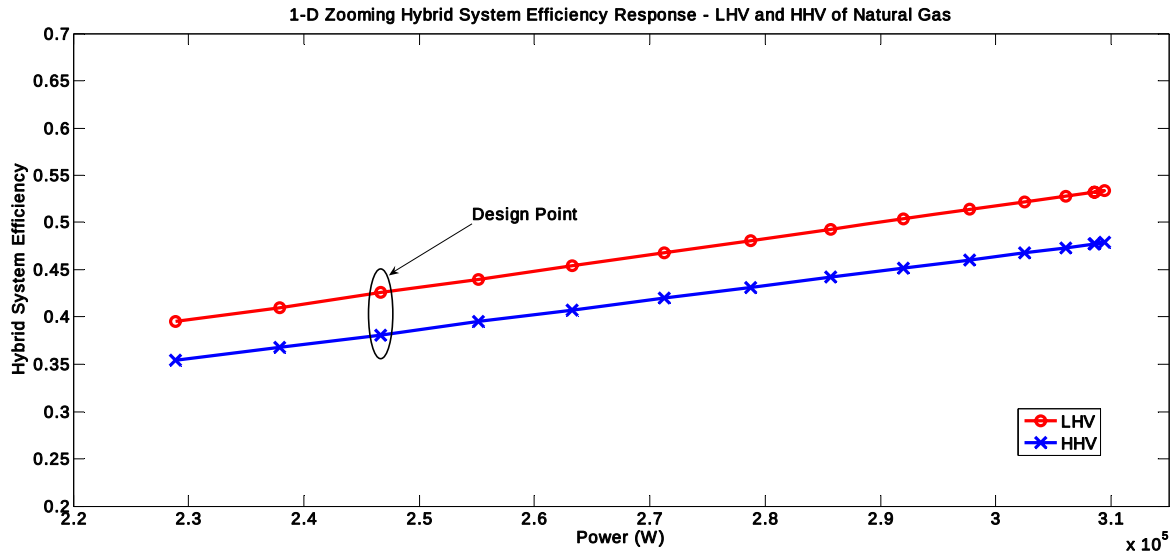

Figure 6.33: 1-D Zooming Hybrid Power Generation System Efficiency

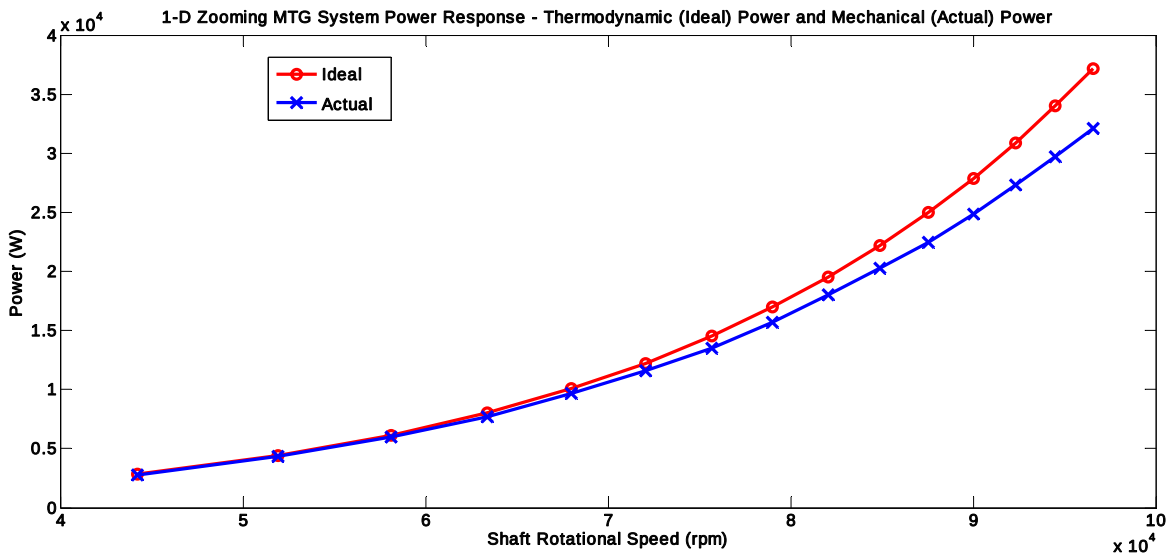

Figure 6.34: 1-D Zooming Microturbine Generator Power Generation for Actual Shaft Speed – Thermodynamic and Mechanical

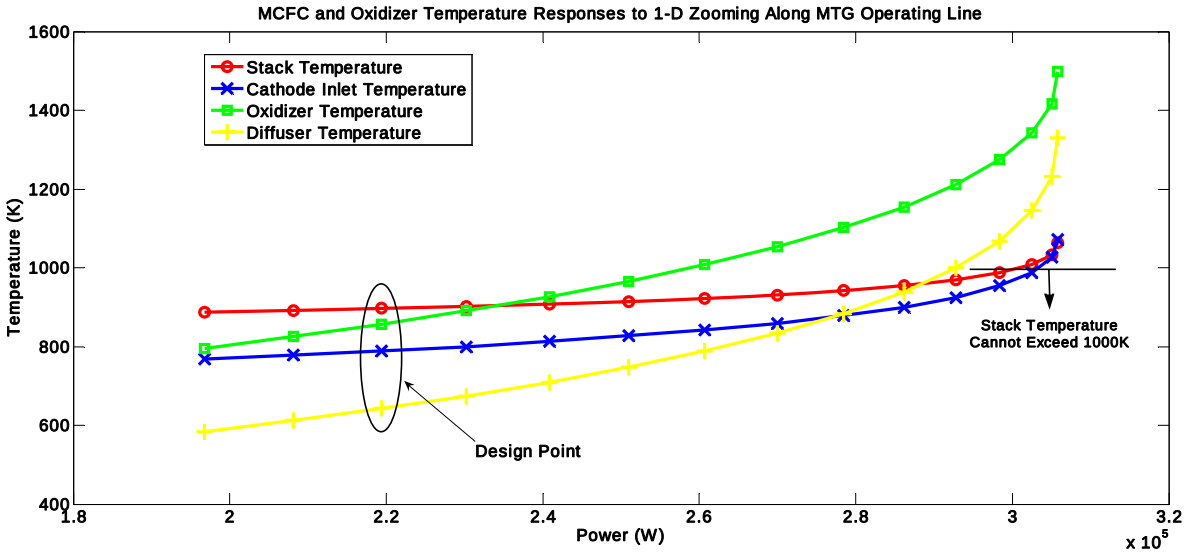

Figure 6.35: Temperature Responses of MCFC and Catalytic Oxidizer for 1-D Analysis Along MTG Operating Line

6.2.2.2 1-D Zooming Brayton Cycle Thermodynamic Analysis

Thermodynamic analysis of the microturbine generator in the hybrid power generation model is represented in Figures 6.36 and 6.37. The *T-s* diagram in Figure 6.36 bears the same shape as that in Figure 6.6. Compression occurs from Stage 2-3, and actual behavior is observed. For the Brayton cycle with regeneration in Figure 6.6, a primary surface recuperator is seen from Stage 3-3' and then combustion occurs from Stage 3'-4. This whole process is replaced by an outside heat source, the shell-and-tube heat exchanger in Figure 6.36. The shell-and-tube heat exchanger is large enough to successfully heat the air entering the turbine such that enough enthalpy is removed from the flow, Stage 4-5, to produce the required power to operate the compressor and have additional power generation of 30 kW. Stage 5-6 is the diffuser and Stage 6-1 represents the open cycle.

The *P-v* diagram in Figure 6.37 is almost an exact representation of the *P-v* diagram in Figure 6.7 representing the Brayton cycle with regeneration. The pressure loss through the shell-side of the shell-and-tube heat exchanger in the hybrid model, Figure 6.37, matches the total pressure loss seen through the primary surface recuperator and the combustion chamber in the stand alone power generation model, Figure 6.7. With the comparisons of the thermodynamic cycle analysis of the two models, the hybrid model has been validated with the stand alone model.

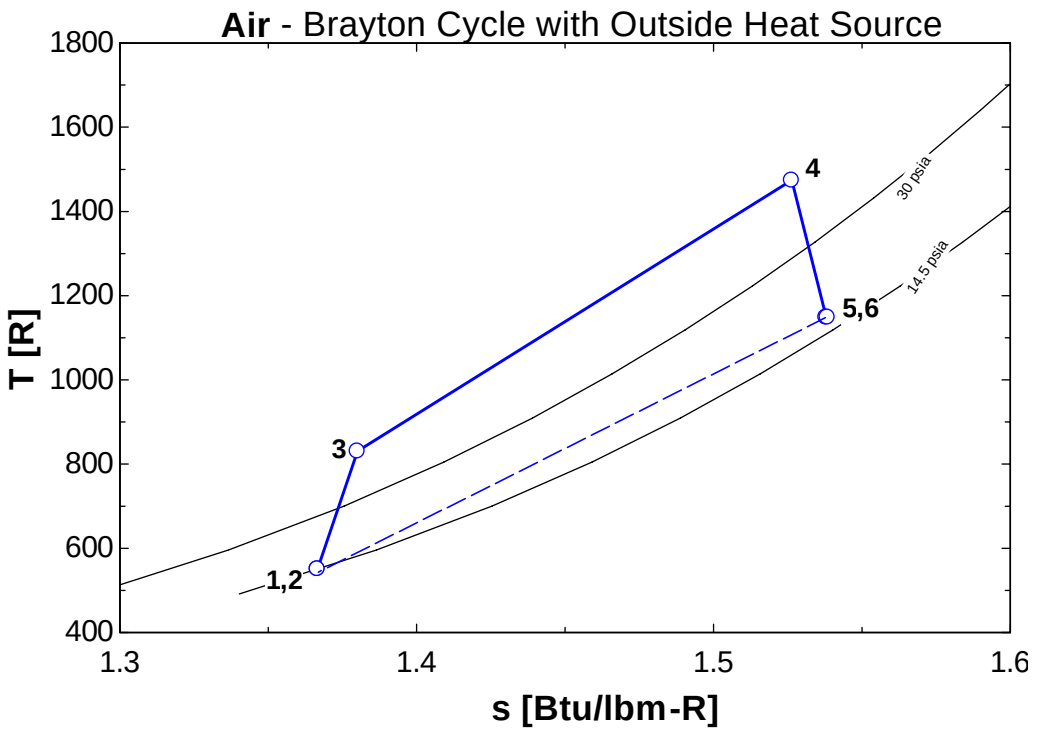

Figure 6.36: *T-s* Diagram of Actual Brayton Cycle with Outside Heat Source

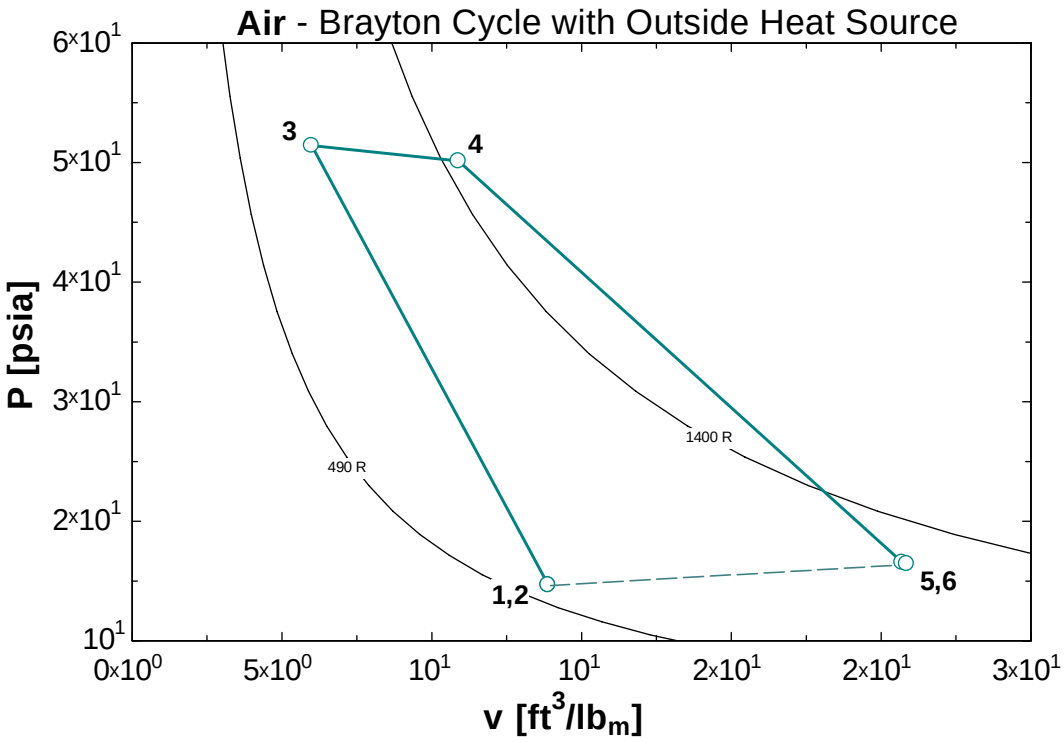

Figure 6.37: *P-v* Diagram of Actual Brayton Cycle with Outside Heat Source

6.2.2.3 1-D Zooming Mean-Line Calculations

The mean-line calculations in the hybrid model are obtained in the same manner as the stand alone model. The limitations given in Section 6.1.4 apply to the hybrid model and the calculations are based on trigonometry applied to the velocity diagrams in Figures 3.6 and 3.8 and isentropic relationships described in Chapter 4. Table 6.5 gives the 1-D mean-line calculations through the centrifugal compressor. To match the limitations placed on centrifugal compressor calculations, the rotor tip velocity U_{2t} in the hybrid model is calculated to be 1376 ft/s. This is below the limited range. The relative flow angle at the tip, β_{1t} is calculated to be 59.94 degrees. The tangential or swirl velocity v_2 is 1223 ft/s. This calculates to be 89 percent of the rotor tip velocity. The final constraint to match is the absolute velocity exiting the compressor diffuser; V_3 is calculated to be 299.5 ft/s. These variables are represented in bold in Table 6.5.

The mean-line calculations for the radial inflow turbine in the hybrid model are seen in Table 6.6. The rotor tip velocity U_{2t} for the radial inflow turbine is calculated to be 1450 ft/s and the exit flow angle is set to 70 degrees. These variables are shown in bold in Table 6.6. Comparing the rest of the variables seen in Tables 6.5 and 6.6 to those in Tables 6.2 an 6.3, the velocity and Mach number calculations at all the stations are higher for the hybrid model than the stand alone model. This is because the mass flow rate for the hybrid model calculated higher than the mass flow rate through the stand alone model.

Table 6.5: Centrifugal Compressor Mean-Line Calculations at 100 Percent of MTG Design Speed for 1-D Zooming of Hybrid Power Generation System

Compressor Results – Ideal and Actual Throttle at 100%

Station	Units	*1*	1_{Rh}	1_{Rt}	*2*	*3*
T_t	[R]	550.8	567.4	617.3	830.8	830.8
T	[R]	528.5	528.5	528.5	684	816.1
P_t	[psia]	14.7	16.31	21.91	56.48	51.44
P	[psia]	12.71	12.71	12.71	28.58	48.32
M	[-]	0.4601	0.6077	0.9176	1.037	0.2121
V	[ft/s]	518.1	684.3	1033	1328	**299.5**
u/w	[ft/s]	518.1	518.1	518.1	518.1	518.1
v	[ft/s]	0	447.1	894.1	**1223**	-
radius	[ft]	-	0.0462	0.0925	0.1423	-
α	[deg]	0	-	-	22.98	-
β	[deg]	-	40.81	**59.94**	-	-

Table 6.6: Radial Inflow Turbine Mean-Line Calculations at 100 Percent of MTG Design Speed for 1-D Zooming of Hybrid Power Generation System

Turbine Results – Ideal and Actual Throttle at 100%

Station	Units	*1*	*2*	3_{Rm}	*3*
T_t	[R]	1474	1474	1209	1156
T	[R]	-	1222	1134	1134
P_t	[psia]	50.14	50.14	25.99	16.98
P	[psia]	-	47.75	19.06	19.06
M	[-]	-	0.8903	0.6914	0.3252
V	[ft/s]	-	1543	1122	527.8
u/w	[ft/s]	-	527.8	527.8	527.8
v	[ft/s]	0	**1450**	990.2	0
radius	[ft]	-	0.15	0.1024	-
α	[deg]	0	**70**	-	0
β	[deg]	-	-	61.94	-

CHAPTER 7: CONCULSIONS AND RECOMMENDATIONS

7.1 Conclusions

The background information on fuel cells and hybrid fuel cell technologies with corresponding power generation has been given. The background and design of a microturbine generator has been discussed in detail. A summary of the different modeling techniques currently in use was provided in Chapter 2. The three MATLAB/Simulink® models presented provide an initial design methodology for modeling and simulation of a hybrid power generation system.

7.1.1 1-Dimensional Stand Alone Power Generation Model

A 1-Dimensional model was created using MATLAB/Simulink® as a possible generic representation of the Capstone® Model 330 microturbine generator for stand alone power generation. The 1-Dimensional model successfully demonstrated the ability to calculate along a mean-line through a centrifugal compressor, radial inflow turbine, primary surface recuperator with limited geometry and a reverse flow annular combustor using the ideal compressor operating line as the input parameters. The model development is for validating the 0-Dimensional and 1-Dimensional hybrid power generation model developed in conjecture with a molten carbonate fuel cell model and the shell-and-tube heat exchanger model.

The ideal operating cycle of the microturbine generator did not map the actual operating cycle below 69 percent of the actual cycle suggesting model inoperability below this point. At the design point the mean-line calculations met all requirements of each component. The desired power generation for the MTG was for 22126 ft-lbf/s (30 kW). The ideal or thermodynamic power generation was found to be 22349 ft-lbf/s (30.3 kW). The actual or mechanical power produced from applying a load on the shaft was calculated to be 18403 ft-lbf/s (24.6 kW). With this power generation the efficiency of the microturbine generator is 81 percent.

7.1.2 0-Dimensional Hybrid Power Generation Model

The 0-Dimensional hybrid power generation model has three complex components modeled individually: a hybrid microturbine generator consisting of a centrifugal compressor and radial inflow turbine, a shell-and-tube heat exchanger and a molten carbonate fuel cell with catalytic oxidizer. The 0-D model was controlled through placing a PID controller on the torque load applied to the shaft of the microturbine generator. As the load was applied, response analysis was done on the temperatures through the complex components of the hybrid model. As the power is ramped from a time constant giving a slope of 0.5 to 3, the temperature responses through the shell- and tube-side of the heat exchanger are slow allowing for the conclusion that the temperature calculations cannot respond quick enough for a corresponding increase of microturbine power.

The fuel cell stack temperature response is driven by the cathode inlet temperature taken directly from the tube-side of the heat exchanger enabling the same response

characteristics as the tube-side temperature response. The catalytic oxidizer is dependent on the fuel cell stack temperature and the diffuser temperature from the microturbine generator. The diffuser temperature has a more robust response, driving the oxidizer temperature response.

The actual power generation of the microturbine generator is equal to the desired power generation. The PID controller on the system assures consistent power generation at the desired amount. With the actual power generation at 30 kW, with the same design conditions the thermodynamic power generation is still higher than the actual at 34.5 kW. The hybrid microturbine generator efficiency is 87 percent. The desired hybrid power generation for the system is 250 kW. The fuel cell has the ability to generate up to 240 kW of power without exceeding the fuel cell stack temperature operating limit of 1000 K. The hybrid power generation is 256 kW at the microturbine design point operating conditions.

The 0-D model can operate with a second PID controller placed on the current density input which drives the natural gas flow and the voltage of the fuel cell. This PID controller is completely separate from the PID controller on the microturbine generator.

7.1.3 1-D Zooming of the Hybrid Power Generation Model

The 1-D hybrid zooming model is verified through comparing calculations with those done in the 1-D stand alone model at design point and along the actual operating line. When the models are compared, the 1-D stand alone model cannot operate below 69 percent of the actual operating line and the zooming model below 68 percent. The compressor temperature responses along the operating line are identical for the two

models. The turbine temperature ranges roughly match after 70 percent on the operating line but the shape of the responses for each model do not match.

Higher turbine inlet temperature at the design point is achieved for the stand alone model then for the zooming model. This is due to the presence of the combustion chamber in the stand alone model. The turbine inlet temperature in the zooming model is calculated from the shell-and-tube heat exchanger still operating with 0-Dimensional calculations. This drives the different shape seen with the turbine temperature responses of the two models. The mean-line calculations match the limitations and requirements set by the 1-D stand alone model thereby verifying the 1-D hybrid zooming model.

7.2 Recommendations for Future Model Development

Develop a 0-Dimensional model of the stand alone power generation system with fuel flow control based on the 1-Dimensional stand alone system. A 0-D stand alone model will enable improved validation of the 0-D hybrid model that is the focus of this study. Initiating start-up capabilities on the 0-D hybrid model to simulate the full operating cycle of start-up, load following and shut-down of the hybrid system. Apply balance-of-plant to the full operating cycle of the hybrid system. Analysis of real-time operation to include climate changes simulating over-night operation. Additional simulation of higher fidelity models applied to the zooming technique on the hybrid system will be essential to improving the validity of the hybrid power generation model.

Appendix A

Actual Microturbine Generator Operating Line Calculations

Table A.1: Compressor Calculations – MATLAB/Simulink

Ideal	$\dot{m}_0$	η_c	T_{t3}	P_{t3}	P_c	P_c	π_c	T_{t2}
[%]	[lbm/s]	[-]	[R]	[psia]	[W]	[ft-lbf/s]	[-]	[R]
40	0.6579	0.86	615.1	20.57	10709	7899	1.400	550.8
45	0.7402	0.86	639.3	23.15	16591	12237	1.580	550.8
50	0.8224	0.86	661.8	25.72	23115	17049	1.750	550.8
55	0.9047	0.86	682.8	28.29	30244	22307	1.925	550.8
60	0.9869	0.85	702.6	30.86	37932	27977	2.100	550.8
65	1.0690	0.85	721.3	33.43	46165	34049	2.275	550.8
70	1.1520	0.85	739.0	36.01	54903	40491	2.450	550.8
75	1.2330	0.85	755.9	38.85	64072	47257	2.625	550.8
80	1.3160	0.85	772.1	41.15	73747	54393	2.800	550.8
85	1.3980	0.85	787.6	43.72	83861	61853	2.975	550.8
90	1.4810	0.85	802.5	46.29	943985	69625	3.150	550.8
95	1.5620	0.85	816.9	48.86	105277	77648	3.325	550.8
100	1.6450	0.85	830.8	51.44	116608	86006	3.500	550.8
105	1.7270	0.84	844.2	54.01	128319	94643	3.675	550.8
110	1.8100	0.84	857.2	56.58	140396	103551	3.850	550.8

Table A.2: Compressor Calculations – EES

Ideal	$\dot{m}_0$	η_c	T_{t3}	P_{t3}	P_c	P_c	π_c	T_{t2}
[%]	[lbm/s]	[-]	[R]	[psia]	[W]	[ft-lbf/s]	[-]	[R]
40	0.6577	0.8637	615.2	20.57	10717	7904	1.400	550.8
45	0.7399	0.8614	639.4	23.14	16602	12245	1.575	550.8
50	0.8221	0.8594	661.9	25.71	23132	17062	1.750	550.8
55	0.9043	0.8575	683.0	28.28	30265	22322	1.925	550.8
60	0.9865	0.8558	702.8	30.85	37962	27999	2.100	550.8
65	1.0690	0.8542	721.5	33.42	46190	34068	2.275	550.8
70	1.1510	0.8528	739.3	35.99	54924	40510	2.450	550.8
75	1.2330	0.8514	756.2	38.56	64137	47305	2.625	550.8
80	1.3150	0.8501	772.4	41.13	73807	54438	2.800	550.8
85	1.3980	0.8489	787.9	43.70	83917	61894	2.975	550.8
90	1.4800	0.8477	802.9	46.27	94448	69661	3.150	550.8
95	1.5620	0.8466	817.2	48.84	105383	77727	3.325	550.8
100	1.6440	0.8456	831.1	51.42	116710	86081	3.500	550.8
105	1.7260	0.8446	844.6	53.99	128414	94713	3.675	550.8
110	1.8090	0.8436	857.6	56.56	140483	103615	3.850	550.8

Table A.3: Turbine Calculations – MATLAB/Simulink

Ideal	T_{t4}	T_{t5}	P_{t5}	P_{t6}	$\dot{m}_t$	P_t	P_t
[%]	[R]	[R]	[psia]	[psia]	[lbm/s]	[W]	[ft-lbf/s]
40	3667	3596	18.5	18.49	0.661	13455	9924
45	2198	2099	18.5	18.48	0.744	20856	15382
50	1848	1725	18.5	18.47	0.827	29061	21434
55	1703	1557	18.5	18.46	0.910	38029	28049
60	1631	1463	18.5	18.45	0.993	47706	35187
65	1592	1403	18.5	18.44	1.076	58072	42832
70	1571	1362	18.5	18.43	1.159	69080	50951
75	1561	1333	18.5	18.43	1.242	80634	59473
80	1557	1312	18.5	18.42	1.325	92831	68468
85	1558	1295	18.5	18.41	1.408	105586	77876
90	1562	1282	18.5	18.41	1.492	118879	87680
95	1568	1272	18.5	18.40	1.574	132606	97805
100	1575	1264	18.5	18.40	1.658	146910	108355
105	1583	1258	18.5	18.39	1.741	161696	119261
110	1592	1252	18.5	18.39	1.825	176950	130512

Table A.4: Turbine Calculations – EES

Ideal	T_{t4}	T_{t5}	P_{t5}	P_{t6}	$\dot{m}_t$	P_t	P_t
[%]	[R]	[R]	[psia]	[psia]	[lbm/s]	[W]	[ft-lbf/s]
40	4036	3965	18.5	18.49	0.661	13469	9935
45	2276	2178	18.5	18.48	0.744	20870	15393
50	1886	1763	18.5	18.47	0.827	29083	21451
55	1727	1581	18.5	18.46	0.910	38057	28069
60	1648	1479	18.5	18.45	0.993	47744	35214
65	1605	1415	18.5	18.44	1.075	58106	42857
70	1581	1372	18.5	18.43	1.158	69107	50971
75	1569	1341	18.5	18.43	1.242	80717	59534
80	1563	1318	18.5	18.42	1.325	92909	68526
85	1563	1300	18.5	18.41	1.408	105657	77929
90	1566	1286	18.5	18.41	1.491	118942	87727
95	1571	1275	18.5	18.40	1.574	132742	97905
100	1577	1266	18.5	18.40	1.657	147039	108450
105	1585	1259	18.5	18.39	1.740	161817	119350
110	1594	1254	18.5	18.39	1.824	177061	130593

Table A.5: Combustion Chamber Calculations – MATLAB/Simulink

Ideal	f	$\dot{m}_f$	P_{t4}	φ
[%]	[-]	[lbm/s]	[psia]	[-]
40	0.003773	0.003309	20.20	0.08631
45	0.004231	0.004148	22.72	0.09615
50	0.004331	0.004710	25.24	0.09827
55	0.004465	0.005339	27.75	0.10130
60	0.004618	0.006023	30.27	0.10470
65	0.004778	0.006751	32.78	0.10830
70	0.004948	0.007529	35.29	0.11210
75	0.005119	0.008340	37.80	0.11600
80	0.005289	0.009193	40.31	0.11990
85	0.005457	0.010080	42.82	0.12370
90	0.005622	0.011000	45.33	0.12740
95	0.005784	0.011940	47.83	0.13110
100	0.005942	0.012910	50.34	0.13470
105	0.006098	0.013910	52.84	0.13820
110	0.006249	0.014940	55.35	0.14170

Table A.6: Combustion Chamber Calculations – EES

Ideal	f	$\dot{m}_f$	P_{t4}	φ
[%]	[-]	[lbm/s]	[psia]	[-]
40	0.004078	0.003581	20.04	0.06474
45	0.004252	0.004169	22.56	0.07259
50	0.004357	0.004738	25.08	0.07431
55	0.004485	0.005361	27.60	0.07662
60	0.004634	0.006041	30.13	0.07924
65	0.004795	0.006771	32.65	0.08199
70	0.004962	0.007545	35.17	0.08490
75	0.005131	0.008359	37.70	0.08783
80	0.005300	0.009209	40.22	0.09075
85	0.005467	0.01009	42.74	0.09363
90	0.005631	0.01101	45.27	0.09646
95	0.005792	0.01195	47.79	0.09924
100	0.005950	0.01292	50.32	0.10200
105	0.006104	0.01392	52.84	0.10460
110	0.006255	0.01495	55.37	0.10720

Table A.7: Primary Surface Recuperator Calculations – MATLAB/Simulink

Ideal	ε	$P_{t3'}$	P_{t7}	$T_{t3'}$	T_{t7}	NTU	$Re_{Dh\text{-}cold}$	$Re_{Dh\text{-}hot}$
[%]	[-]	[psia]	[psia]	[R]	[R]	[-]	[-]	[-]
40	0.832	20.47	15.12	3095	1640	7.400	629.8	167.4
45	0.832	23.02	17.21	1854	1056	6.212	688.9	260.8
50	0.832	25.57	17.44	1546	940	5.485	746.5	326.2
55	0.832	28.12	17.50	1410	899	4.952	803.0	382.3
60	0.832	30.67	17.51	1335	884	4.534	858.1	433.7
65	0.832	33.21	17.49	1288	880	4.191	912.7	482.5
70	0.832	35.76	17.45	1258	881	3.903	966.2	529.6
75	0.832	38.30	17.41	1236	886	3.660	1018	575.0
80	0.832	40.84	17.37	1221	892	3.444	1070	620.0
85	0.832	43.38	17.32	1210	899	3.256	1122	664.3
90	0.832	45.92	17.27	1202	907	3.088	1172	708.2
95	0.832	48.46	17.21	1196	915	2.940	1222	751.1
100	0.832	51.00	17.16	1191	923	2.805	1272	794.1
105	0.832	53.54	17.10	1188	932	2.683	1321	836.9
110	0.832	56.08	17.04	1186	941	2.571	1369	879.3

Table A.8: Primary Surface Recuperator – EES

Ideal	ε	$P_{t3'}$	P_{t7}	$T_{t3'}$	T_{t7}	NTU	$Re_{Dh\text{-}cold}$	$Re_{Dh\text{-}hot}$
[%]	[-]	[psia]	[psia]	[R]	[R]	[-]	[-]	[-]
40	0.832	20.31	15.36	3402	1501	7.476	629.4	162.8
45	0.832	22.86	17.05	1919	1047	6.282	688.3	255.1
50	0.832	25.41	17.33	1578	954	5.545	745.9	321.7
55	0.832	27.97	17.41	1430	921	5.008	802.2	378.5
60	0.832	30.52	17.43	1349	909	4.587	857.5	430.4
65	0.832	33.08	17.43	1299	905	4.244	911.7	479.5
70	0.832	35.64	17.40	1265	907	3.956	965.1	526.8
75	0.832	38.19	17.37	1242	911	3.710	1018	572.8
80	0.832	40.75	17.33	1226	917	3.497	1069	617.9
85	0.832	43.31	17.29	1214	924	3.310	1121	662.4
90	0.832	45.86	17.25	1205	931	3.143	1171	706.2
95	0.832	48.42	17.20	1198	939	2.995	1221	749.7
100	0.832	50.98	17.15	1193	947	2.861	1270	792.8
105	0.832	53.54	17.10	1190	955	2.739	1319	835.6
110	0.832	56.10	17.05	1187	963	2.629	1368	878.1

Table A.9: Stand Alone Power Generation System Calculations – MATLAB/Simulink

Ideal	P_{therm}	P_{therm}	N	η_{LHV}	η_{HHV}	P_m	P_m
[%]	[W]	[ft-lbf/s]	[rpm]	[-]	[-]	[W]	[ft-lbf/s]
40	2745	2025	44233	0.0480	0.0430	3619	2669
45	4265	3145	51906	0.0595	0.0533	5144	3794
50	5945	4385	58126	0.0730	0.0655	6199	4572
55	7785	5742	63391	0.0844	0.0756	7456	5499
60	9774	7209	67972	0.0939	0.0842	8943	6596
65	11908	8783	72036	0.1021	0.0915	10529	7766
70	14177	10456	75694	0.1090	0.0977	12201	8999
75	16562	12216	79022	0.1149	0.1030	13995	10322
80	19084	14076	82078	0.1201	0.1077	15938	11755
85	21725	16023	84906	0.1247	0.1118	18028	13297
90	24480	18056	87537	0.1288	0.1155	20246	14933
95	27329	20157	90000	0.1325	0.1188	22535	16621
100	30301	22349	92314	0.1358	0.1217	24951	18403
105	33378	24618	94498	0.1388	0.1244	27474	20264
110	36554	26961	96566	0.1416	0.1269	30072	22180

Table A.10: Stand Alone Power Generation System Calculations – EES

Ideal	P_{therm}	P_{therm}	N	η_{LHV}	η_{HHV}	P_m	P_m
[%]	[W]	[ft-lbf/s]	[rpm]	[-]	[-]	[W]	[ft-lbf/s]
40	2753	2030	44258	0.0445	0.0399	4275	3153
45	4268	3148	51935	0.0592	0.0531	5114	3772
50	5951	4389	58159	0.0727	0.0652	6187	4563
55	7792	5747	63428	0.0841	0.0754	7454	5498
60	9783	7215	68012	0.0937	0.0840	8886	6554
65	11915	8788	72079	0.1018	0.0913	10461	7716
70	14183	10461	75739	0.1088	0.0975	12168	8975
75	16580	12229	79070	0.1148	0.1029	13996	10323
80	19101	14088	82129	0.1200	0.1076	15940	11757
85	21740	16035	84958	0.1246	0.1117	17993	13271
90	24494	18066	87592	0.1288	0.1154	20153	14864
95	27358	20178	90056	0.1325	0.1187	22414	16532
100	30329	22370	92373	0.1358	0.1217	24775	18273
105	33403	24637	94559	0.1388	0.1245	27232	20085
110	36578	26979	96629	0.1416	0.1269	29782	21966

Appendix B:

1-D Zooming of Actual MTG Operating Line

Table B.1: Compressor Calculations –MATLAB/Simulink

Ideal	$\dot{m}_0$	η_c	T_{t3}	P_{t3}	P_c	P_c	π_c	T_{t2}
[%]	[lbm/s]	[-]	[R]	[psia]	[W]	[ft-lbf/s]	[-]	[R]
40	0.697	0.86	615.1	20.57	11348	8370	1.40	550.8
45	0.784	0.86	639.3	23.15	17578	12965	1.58	550.8
50	0.871	0.86	661.8	25.72	24493	18065	1.75	550.8
55	0.959	0.86	682.8	28.29	32044	23634	1.93	550.8
60	1.046	0.86	702.6	30.86	40208	29656	2.10	550.8
65	1.132	0.85	721.3	33.43	48888	36058	2.27	550.8
70	1.220	0.85	739.0	36.01	58141	42882	2.45	550.8
75	1.307	0.85	755.9	38.58	67903	50083	2.63	550.8
80	1.394	0.85	772.1	41.15	78152	57642	2.80	550.8
85	1.482	0.85	787.6	43.72	88866	65544	2.98	550.8
90	1.568	0.85	802.5	46.29	99966	73731	3.15	550.8
95	1.656	0.85	816.9	48.86	111554	82278	3.33	550.8
100	1.743	0.85	830.8	51.44	123557	91131	3.50	550.8
105	1.830	0.84	844.2	54.01	135960	100279	3.67	550.8
110	1.918	0.84	857.2	56.58	148752	109714	3.85	550.8

Table B.2: Turbine Calculations – MATLAB/Simulink

Ideal	T_{t4}	T_{t5}	P_{t4}	P_{t5}	P_{t6}	$\dot{m}_t$	P_t	P_t
[%]	[R]	[R]	[psia]	[psia]	[psia]	[lbm/s]	[W]	[ft-lbf/s]
40	2461	2394	20.32	17.81	17.8	0.697	14185	10462
45	2311	2217	22.68	18.66	18.65	0.784	21974	16207
50	2180	2062	25.10	19.32	19.3	0.871	30613	22582
55	2065	1923	27.55	19.79	19.76	0.959	40056	29544
60	1965	1800	30.03	20.06	20.01	1.046	50261	37071
65	1877	1691	32.52	20.13	20.08	1.132	61112	46074
70	1799	1591	35.02	20.06	19.99	1.220	72678	53605
75	1729	1502	37.53	19.82	19.75	1.307	84882	62606
80	1667	1420	40.05	19.43	19.35	1.394	97693	72055
85	1611	1345	42.57	18.93	18.85	1.482	111087	81933
90	1561	1277	45.09	18.37	18.28	1.568	124932	92167
95	1516	1214	47.51	17.71	17.61	1.656	139447	102851
100	1474	1156	50.14	16.98	16.87	1.743	154451	113917
105	1437	1101	52.66	16.19	16.08	1.830	169957	125353
110	1402	1051	55.19	15.35	15.24	1.918	185946	137147

Table B.3: Hybrid Power Generation System Calculations – MATLAB/Simulink

Ideal	P_{therm}	P_m	P_{fc}	P_{hybrid}	N	T_{stack}	T_{cin}	T_{oxout}	η_{LHV}	η_{HHV}
[%]	[W]	[W]	[W]	[W]	[rpm]	[K]	[K]	[K]	[-]	[-]
40	2837	2773	305755	308527	44234	1063	1072	1499	0.532	0.477
45	4395	4354	305096	309450	51906	1033	1026	1417	0.534	0.479
50	6124	6011	302545	308556	58126	1008	987	1342	0.532	0.477
55	8012	7723	298369	306092	63391	987	954	1274	0.528	0.473
60	10054	9664	292826	302490	67972	969	925	1211	0.522	0.468
65	12224	11579	286174	297753	72036	954	900	1154	0.514	0.460
70	14538	13531	278478	292009	75694	942	879	1102	0.504	0.452
75	16979	15707	269960	285667	79022	931	859	1053	0.493	0.442
80	19541	18021	260722	278743	82078	922	842	1008	0.481	0.431
85	22220	20293	250976	271269	84906	914	827	966	0.468	0.420
90	24996	22449	240847	263296	87537	907	813	927	0.454	0.407
95	27893	24886	230267	255153	90000	902	800	891	0.440	0.395
100	30895	27311	219354	246665	92314	897	788	857	0.426	0.381
105	33996	29711	208180	237891	94498	892	778	825	0.410	0.368
110	37195	32122	196746	228868	96566	888	768	794	0.395	0.354

Appendix C

Centrifugal Compressor 0-D Performance Mapping

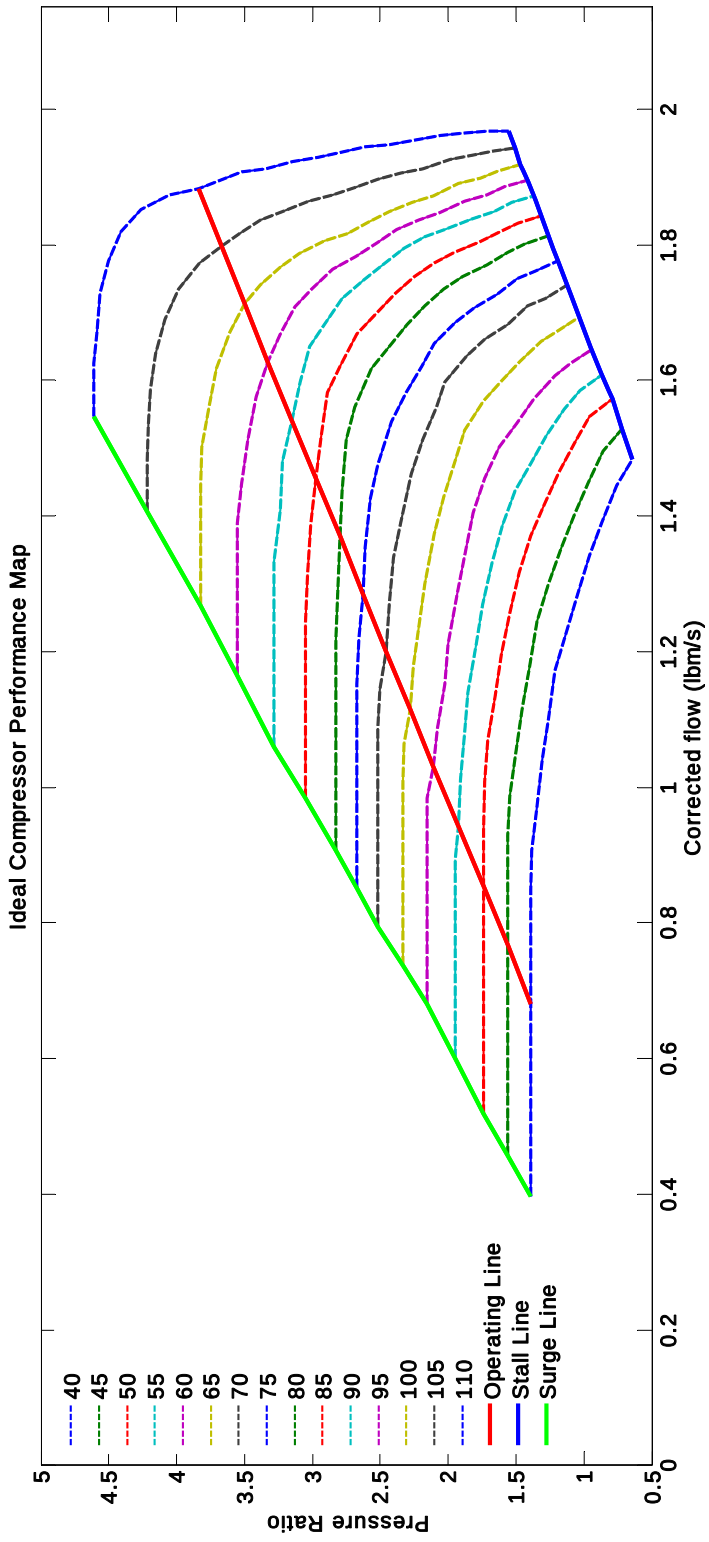

Figure C.1: Ideal Compressor Performance Map – Total Pressure Ratio and Corrected Mass Flow

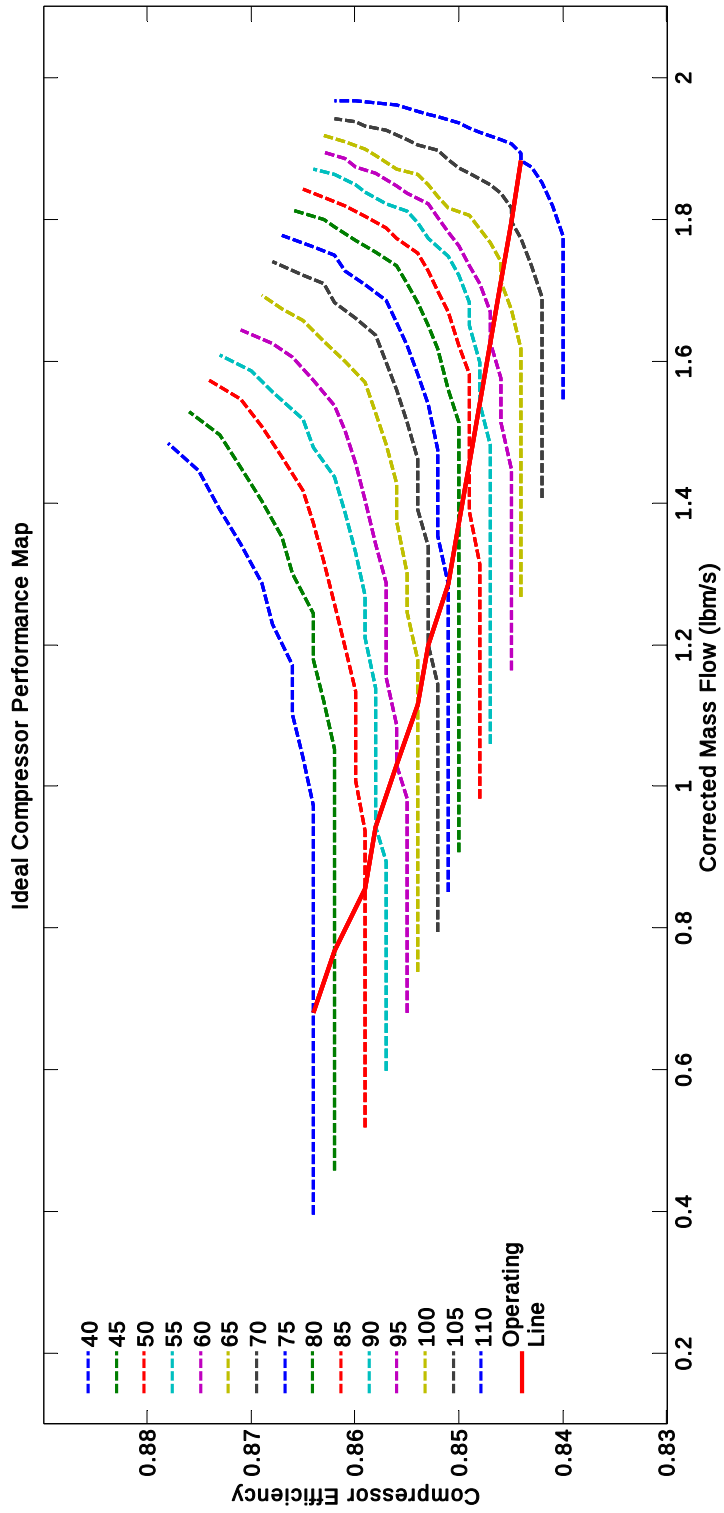

Figure C.2: Ideal Compressor Performance Map – Efficiency and Corrected Mass Flow

Table C.1a: Compressor Performance Map Data

	$N_{\%} = 40$			$N_{\%} = 45$			$N_{\%} = 50$			$N_{\%} = 55$		
R-line	$\dot{m}_{0c}$	π_c	η_c	$\dot{m}_{0c}$	π_c	η_c	$\dot{m}_{0c}$	π_c	η_c	$\dot{m}_{0c}$	π_c	η_c
1	0.396	1.391	0.864	0.458	1.565	0.862	0.519	1.739	0.859	0.600	1.946	0.857
2	0.402	1.391	0.864	0.463	1.565	0.862	0.525	1.739	0.859	0.608	1.946	0.857
3	0.434	1.391	0.864	0.501	1.565	0.862	0.568	1.739	0.859	0.643	1.946	0.857
4	0.464	1.391	0.864	0.537	1.565	0.862	0.609	1.739	0.859	0.683	1.946	0.857
5	0.500	1.391	0.864	0.567	1.565	0.862	0.634	1.739	0.859	0.718	1.946	0.857
6	0.535	1.391	0.864	0.601	1.565	0.862	0.667	1.739	0.859	0.754	1.946	0.857
7	0.568	1.391	0.864	0.639	1.565	0.862	0.710	1.739	0.859	0.795	1.946	0.857
8	0.612	1.391	0.864	0.684	1.565	0.862	0.757	1.739	0.859	0.844	1.946	0.857
9	0.653	1.391	0.864	0.728	1.565	0.862	0.803	1.739	0.859	0.893	1.946	0.857
10	0.680	1.391	0.864	0.768	1.565	0.862	0.855	1.739	0.859	0.942	1.924	0.858
11	0.776	1.391	0.864	0.856	1.565	0.862	0.937	1.739	0.859	1.012	1.908	0.858
12	0.850	1.391	0.864	0.929	1.560	0.862	1.008	1.728	0.860	1.080	1.875	0.858
13	0.907	1.380	0.864	0.988	1.543	0.862	1.068	1.707	0.860	1.139	1.853	0.858
14	0.973	1.348	0.864	1.053	1.500	0.862	1.134	1.652	0.860	1.210	1.793	0.859
15	1.041	1.304	0.865	1.119	1.457	0.863	1.197	1.609	0.861	1.269	1.745	0.859
16	1.101	1.261	0.866	1.179	1.402	0.864	1.257	1.543	0.862	1.330	1.679	0.860
17	1.172	1.217	0.866	1.244	1.348	0.864	1.317	1.478	0.863	1.386	1.603	0.861
18	1.229	1.130	0.868	1.300	1.261	0.866	1.371	1.391	0.864	1.437	1.505	0.862
19	1.287	1.043	0.869	1.352	1.168	0.867	1.418	1.293	0.865	1.478	1.391	0.864
20	1.341	0.957	0.871	1.403	1.071	0.869	1.464	1.185	0.867	1.519	1.277	0.865
21	1.390	0.870	0.873	1.449	0.967	0.871	1.508	1.065	0.869	1.557	1.141	0.868
22	1.445	0.761	0.875	1.496	0.859	0.873	1.546	0.957	0.871	1.586	1.027	0.870
23	1.483	0.641	0.878	1.528	0.717	0.876	1.574	0.793	0.874	1.609	0.870	0.873

Table C.1b: Compressor Performance Map Data

	$N_{\%} = 60$			$N_{\%} = 65$			$N_{\%} = 70$			$N_{\%} = 75$		
R-line	$\dot{m}_{0c}$	π_c	η_c	$\dot{m}_{0c}$	π_c	η_c	$\dot{m}_{0c}$	π_c	η_c	$\dot{m}_{0c}$	π_c	η_c
1	0.680	2.152	0.855	0.738	2.337	0.854	0.795	2.522	0.852	0.851	2.674	0.851
2	0.691	2.152	0.855	0.753	2.337	0.854	0.814	2.522	0.852	0.876	2.674	0.851
3	0.718	2.152	0.855	0.784	2.337	0.854	0.850	2.522	0.852	0.906	2.674	0.851
4	0.757	2.152	0.855	0.822	2.337	0.854	0.888	2.522	0.852	0.945	2.674	0.851
5	0.803	2.152	0.855	0.870	2.337	0.854	0.937	2.522	0.852	0.993	2.674	0.851
6	0.841	2.152	0.855	0.907	2.337	0.854	0.973	2.522	0.852	1.034	2.674	0.851
7	0.880	2.152	0.855	0.958	2.337	0.854	1.035	2.522	0.852	1.094	2.674	0.851
8	0.932	2.152	0.855	1.009	2.337	0.854	1.087	2.522	0.852	1.153	2.674	0.851
9	0.983	2.152	0.855	1.064	2.326	0.854	1.145	2.500	0.852	1.220	2.658	0.851
10	1.030	2.109	0.856	1.115	2.283	0.854	1.199	2.457	0.853	1.285	2.625	0.851
11	1.087	2.076	0.856	1.179	2.255	0.854	1.270	2.435	0.853	1.354	2.609	0.852
12	1.153	2.022	0.857	1.246	2.212	0.855	1.339	2.402	0.853	1.426	2.576	0.852
13	1.210	2.000	0.857	1.300	2.174	0.855	1.390	2.348	0.854	1.475	2.516	0.852
14	1.287	1.935	0.857	1.374	2.103	0.856	1.462	2.272	0.854	1.539	2.418	0.853
15	1.341	1.880	0.858	1.427	2.033	0.856	1.513	2.185	0.855	1.582	2.310	0.854
16	1.404	1.815	0.859	1.482	1.951	0.857	1.560	2.087	0.856	1.621	2.196	0.855
17	1.456	1.728	0.860	1.527	1.875	0.858	1.598	2.022	0.857	1.654	2.098	0.856
18	1.502	1.620	0.861	1.569	1.739	0.859	1.636	1.859	0.858	1.686	1.946	0.857
19	1.538	1.489	0.862	1.599	1.609	0.861	1.661	1.728	0.860	1.707	1.810	0.859
20	1.574	1.370	0.864	1.628	1.467	0.863	1.683	1.565	0.862	1.726	1.641	0.861
21	1.606	1.217	0.866	1.658	1.315	0.865	1.710	1.413	0.863	1.750	1.489	0.862
22	1.625	1.098	0.868	1.673	1.190	0.867	1.721	1.283	0.865	1.761	1.359	0.864
23	1.645	0.946	0.871	1.692	1.033	0.869	1.740	1.120	0.868	1.777	1.190	0.867

Table C.1c: Compressor Performance Map Data

	$N_{\%} = 80$			$N_{\%} = 85$			$N_{\%} = 90$			$N_{\%} = 95$		
R-line	$\dot{m}_{0c}$	π_c	η_c	$\dot{m}_{0c}$	π_c	η_c	$\dot{m}_{0c}$	π_c	η_c	$\dot{m}_{0c}$	π_c	η_c
1	0.907	2.826	0.850	0.983	3.054	0.848	1.060	3.283	0.847	1.164	3.554	0.845
2	0.937	2.826	0.850	1.019	3.054	0.848	1.101	3.283	0.847	1.207	3.554	0.845
3	0.962	2.826	0.850	1.048	3.054	0.848	1.134	3.283	0.847	1.238	3.554	0.845
4	1.003	2.826	0.850	1.087	3.054	0.848	1.172	3.283	0.847	1.284	3.554	0.845
5	1.049	2.826	0.850	1.139	3.054	0.848	1.229	3.283	0.847	1.337	3.554	0.845
6	1.095	2.826	0.850	1.186	3.054	0.848	1.276	3.283	0.847	1.389	3.549	0.845
7	1.153	2.826	0.850	1.243	3.054	0.848	1.333	3.283	0.847	1.446	3.522	0.845
8	1.218	2.826	0.850	1.314	3.033	0.848	1.410	3.239	0.847	1.513	3.473	0.846
9	1.295	2.815	0.850	1.388	3.016	0.849	1.481	3.217	0.847	1.576	3.413	0.846
10	1.371	2.793	0.850	1.456	2.973	0.849	1.541	3.152	0.848	1.627	3.326	0.847
11	1.437	2.783	0.850	1.518	2.935	0.849	1.598	3.087	0.848	1.669	3.234	0.847
12	1.513	2.750	0.850	1.582	2.886	0.849	1.650	3.022	0.849	1.709	3.130	0.848
13	1.560	2.685	0.851	1.621	2.799	0.850	1.683	2.913	0.849	1.735	3.005	0.849
14	1.617	2.565	0.852	1.669	2.674	0.851	1.721	2.783	0.850	1.763	2.848	0.850
15	1.650	2.435	0.853	1.699	2.527	0.852	1.748	2.620	0.851	1.782	2.679	0.851
16	1.683	2.304	0.854	1.728	2.386	0.853	1.773	2.467	0.853	1.803	2.527	0.852
17	1.710	2.174	0.855	1.752	2.250	0.854	1.795	2.326	0.854	1.822	2.380	0.853
18	1.735	2.033	0.856	1.773	2.103	0.856	1.811	2.174	0.855	1.837	2.217	0.855
19	1.754	1.891	0.858	1.788	1.957	0.857	1.822	2.022	0.857	1.847	2.065	0.856
20	1.770	1.717	0.860	1.804	1.772	0.859	1.838	1.826	0.859	1.864	1.875	0.858
21	1.789	1.565	0.862	1.819	1.614	0.861	1.849	1.663	0.860	1.874	1.712	0.860
22	1.800	1.435	0.863	1.832	1.484	0.863	1.863	1.533	0.862	1.886	1.582	0.861
23	1.814	1.261	0.866	1.843	1.315	0.865	1.871	1.370	0.864	1.894	1.418	0.863

Table C.1d: Compressor Performance Map Data

	$N_{\%} = 100$			$N_{\%} = 105$			$N_{\%} = 110$		
R-line	$\dot{m}_{0c}$	π_c	η_c	$\dot{m}_{0c}$	π_c	η_c	$\dot{m}_{0c}$	π_c	η_c
1	1.268	3.826	0.844	1.407	4.217	0.842	1.546	4.609	0.840
2	1.314	3.826	0.844	1.456	4.217	0.842	1.598	4.609	0.840
3	1.341	3.826	0.844	1.483	4.217	0.842	1.625	4.609	0.840
4	1.396	3.826	0.844	1.534	4.207	0.842	1.672	4.587	0.840
5	1.445	3.826	0.844	1.587	4.196	0.842	1.729	4.565	0.840
6	1.502	3.815	0.844	1.639	4.158	0.842	1.776	4.500	0.840
7	1.560	3.761	0.844	1.690	4.087	0.842	1.819	4.413	0.841
8	1.617	3.707	0.844	1.735	3.984	0.843	1.852	4.261	0.842
9	1.672	3.609	0.845	1.773	3.832	0.844	1.874	4.054	0.843
10	1.713	3.500	0.846	1.798	3.668	0.845	1.882	3.837	0.844
11	1.740	3.380	0.846	1.817	3.538	0.845	1.893	3.696	0.844
12	1.767	3.239	0.847	1.837	3.380	0.846	1.907	3.522	0.845
13	1.787	3.098	0.848	1.849	3.223	0.847	1.912	3.348	0.846
14	1.806	2.913	0.849	1.864	3.027	0.849	1.923	3.141	0.848
15	1.817	2.739	0.851	1.873	2.848	0.850	1.929	2.957	0.849
16	1.833	2.587	0.852	1.885	2.685	0.851	1.937	2.783	0.850
17	1.849	2.435	0.853	1.897	2.522	0.852	1.945	2.609	0.852
18	1.863	2.261	0.854	1.905	2.348	0.854	1.948	2.435	0.853
19	1.871	2.109	0.856	1.912	2.185	0.855	1.953	2.261	0.854
20	1.890	1.924	0.858	1.926	1.989	0.857	1.961	2.054	0.856
21	1.899	1.761	0.859	1.931	1.826	0.859	1.964	1.891	0.858
22	1.910	1.630	0.861	1.938	1.668	0.860	1.967	1.707	0.860
23	1.918	1.467	0.863	1.942	1.511	0.862	1.967	1.554	0.862

Appendix D

Radial Inflow Turbine 0-D Performance Mapping

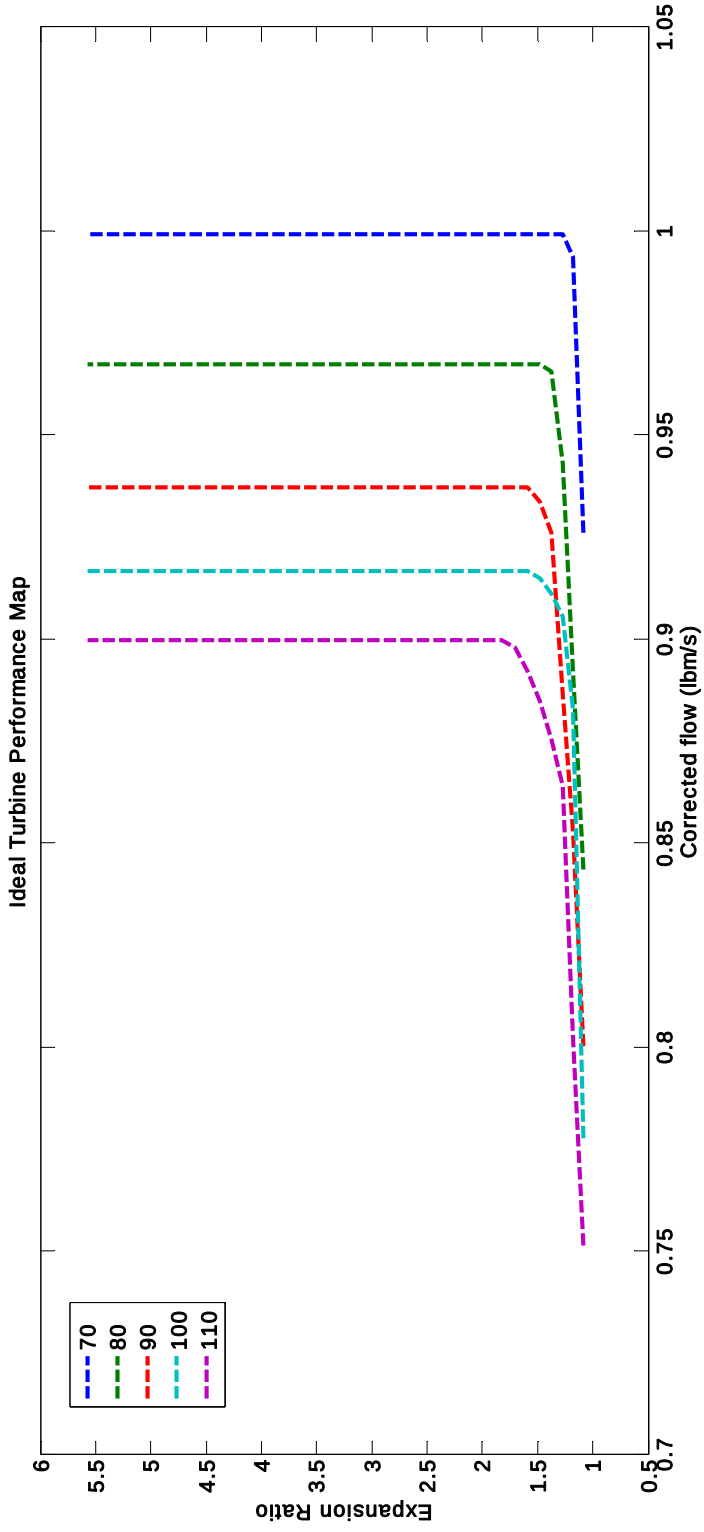

Figure D.1: Ideal Turbine Performance Map

Table D.1: Turbine Performance Map Data

$N_{\%} = 70$		$N_{\%} = 80$		$N_{\%} = 90$		$N_{\%} = 100$		$N_{\%} = 110$	
$\dot{m}_{0c}$	$1/\pi_c$	$\dot{m}_{0c}$	$1/\pi_c$	$\dot{m}_{0c}$	$1/\pi_c$	$\dot{m}_{0c}$	$1/\pi_c$	$\dot{m}_{0c}$	$1/\pi_c$
0.926	1.0879	0.8434	1.0879	0.8002	1.0879	0.7777	1.0879	0.7514	1.0879
0.9937	1.1798	0.8922	1.1798	0.8528	1.1798	0.8828	1.1798	0.8021	1.1798
0.9993	1.2759	0.943	1.2759	0.8866	1.2759	0.9054	1.2759	0.8641	1.2759
0.9993	1.3762	0.9655	1.3762	0.926	1.3762	0.911	1.3762	0.8753	1.3762
0.9993	1.4808	0.9674	1.4808	0.9336	1.4808	0.9149	1.4808	0.8847	1.4808
0.9993	1.5898	0.9674	1.5898	0.9373	1.5898	0.9167	1.5898	0.8922	1.5898
0.9993	1.7033	0.9674	1.7033	0.9373	1.7033	0.9167	1.7033	0.8979	1.7033
0.9993	1.8214	0.9674	1.8214	0.9373	1.8214	0.9167	1.8214	0.8998	1.8214
0.9993	1.9443	0.9674	1.9443	0.9373	1.9443	0.9167	1.9443	0.8998	1.9443
0.9993	2.0719	0.9674	2.0719	0.9373	2.0719	0.9167	2.0719	0.8998	2.0719
0.9993	2.3540	0.9674	2.3540	0.9373	2.3540	0.9167	2.3540	0.8998	2.3540
0.9993	2.6970	0.9674	2.6970	0.9373	2.6907	0.9167	2.6970	0.8998	2.6970
0.9993	3.2802	0.9674	3.2802	0.9373	3.2802	0.9167	3.2802	0.8998	3.2802
0.9993	3.6388	0.9674	3.6388	0.9373	3.6388	0.9167	3.6388	0.8998	3.6388
0.9993	4.2234	0.9674	4.2234	0.9373	4.2234	0.9167	4.2234	0.8998	4.2234
0.9993	4.8677	0.9674	4.8677	0.9373	4.8677	0.9167	4.8677	0.8998	4.8677
0.9993	5.5758	0.9674	5.5758	0.9373	5.5758	0.9167	5.5758	0.8998	5.5758

LIST OF REFERENCES

[1] Willis, H. Lee and Walter G. Scott. Distributed Power Generation: Planning and Evaluation. New York: Marcel Dekker, Inc., 2000.

[2] Shah, R.K. "Compact heat exchangers for microturbines." Paper CHE2005-31. Proceedings of Fifth International Conference on Enhanced, Compact and Ultra-Compact Heat Exchangers: Science, Engineering and Technology. R.K. Shah, M. Ishizuka, T.M. Rudy, and V.V. Wadekar, eds. Hoboken, NJ: Engineering Conferences International: September 2005.

[3] Task 3: Islanding and DG for Enhanced Electric Power Grid Security. Shripad T. Revankar, Nuclear Engineering, Purdue University and Mitch Wolff, Mechanical Engineering, Wright State University (12 November 2005).

[4] Types of fuel cells/How fuel cells work. FuelCellWorks.com, 1999-2003. <http://fuelcellworks.com/Typesoffuelcells.html> (12 Jan 2007).

[5] Roberts, Rory A., Jack Brouwer, Eric Liese and Randall S. Gemmen. "Dynamic simulation of Carbonate fuel cell-gas turbine hybrid systems." Journal of Engineering for Gas Turbines and Power. 128 (April 2006): 294-301.

[6] Moore, M.J., ed. Micro-Turbine Generators. Bury St Edmunds and London, UK: Professional Engineering Publishing, 2002.

[7] Samuelsen, Scott. "Fuel cell/gas turbine hybrid systems." ASME International Gas Turbine Institute. 2004.

[8] Ghosh, S., S. De and S. Saha. "Improved performance and reduced emission from coal and gas fuelled GT-SOFC and GT-MCFC plants: some studies." Paper GT2006-91162. Proceedings of GT2006 ASME Turbo Expo 2006: Power for Land, Sea, and Air. Barcelona, Spain: ASME, May 8-11, 2006.

[9] Ghezel-Ayagh, Hossein, and Hansraj C. Maru. "Direct carbonate fuel cell – gas turbine combined cycle power plant." Paper A10-4. European Fuel Cell Forum. Lucerne, Switzerland: July 5-8, 2005.

[10] Ghezel-Ayagh, Hossein, Principal Investigator. Technical Report Prepared for U.S. Department of Energy DOE Grant No. DE-FC26-00NT40798: Direct Fuel Cell/Turbine Power Plant, Period 11/1/2002 through 12/31/2003. Danbury, CT: FuelCell Energy, Inc., 2004.

[11] Ghezel-Ayagh, Hossein, et al. "High-efficiency fuel cell system." US Patent 6365290 B1. Apr. 2, 2002.

[12] Barchewitz, L., Seume, J., "Conceptual analysis of air supply systems for in-flight PEM-FC." Paper GT2006-90688. Proceedings of GT2006 ASME Turbo Expo 2006: Power for Land, Sea and Air. Barcelona, Spain: ASME, May 2006.

[13] Hussain, M.M, J.J. Baschuk, X. Li and I. Dincer. "Thermodynamic analysis of a PEM fuel cell power system." International Journal of Thermal Sciences. 44 (2005): 903-911.

[14] Jagaduri, Rekha T. and Ghadir Radman. "Modeling/simulation of combined PEM fuel cell and microturbine distributed generation plant." Tennessee Technological University: Department of Electrical and Computer Engineering. 2005.

[15] Juardo, Francisco. "Study of molten carbonate fuel cell – microturbine hybrid power cycles." Journal of Power Sources 111 (2002): 121-129.

[16] Ghezel-Ayagh, Hossein, Joseph M. Daly, and Zhao-Hui Wang. "Advances in Direct fuel cell/gas turbine power plants." Paper GT2003-38941. Proceedings of ASME/IGTI TURBO EXPO 2003. Atlanta, GA: ASME, June 16-19, 2003.

[17] Singh, Prabhakar. "Solid Oxide Fuel Cells." Pacific Northwest National Laboratory. Operated by Battelle for the U.S. Department of Energy. Presented to AVETEC, August 17, 2006.

[18] Baratto, Francesco, Urmila M. Diwekar and Davide Manca. "Impacts assessment and trade-offs of fuel cell-based auxiliary power units Part I: System performance and cost modeling." Journal of Power Sources. 139 (2005): 205-213.

[19] Cocco, Daniele and Vittorio Tola. "Comparative performance analysis of internal and external reforming of methanol in SOFC-MGT hybrid power plants." Paper GT2006-90762. Proceedings of GT2006 ASME Turbo Expo 2006: Power for Land Sea and Air. Barcelona Spain: ASME, May 8-11, 2006.

[20] Costamagna, P., L. Magistri and A.F. Masardo. "Design and part-load performance of a hybrid system based on a solid oxide fuel cell reactor and a micro gas turbine." Journal of Power Sources. 96 (2001): 352-368.

[21] Dicks, A.L. and P.A. Martin. "A fuel cell balance of plant test facility." Journal of Power Sources. 71 (1998): 321-327.

[22] Hartvigsen, J., A. Khandkar, and S. Elangovan. "Development of an SOFC stack performance map for natural gas operation." Paper MTI00-07. Presented at the Sixth International Symposium on Solid Oxide Fuel Cells. Honolulu, Hawaii: McDermott Technology Inc, October 17-22, 1999.

[23] Hack, R.L., et al. "Natural gas combustion: Emission characteristics of a commercial microturbine generator (MTG)." University of California – Irving. Dec. 2005 <http://www.ucicl.uci.edu/RESEARCHPROJECTS/NaturalGasCombustion/Emissions/Index.aspx> (10 Jan 2007)

[24] Kim, Sog-Kyun, Pericles Pilidis and Junfei Yin. "Gas turbine dynamic simulation using Simulink®." Paper 200-013647. Society of Automotive Engineers, Inc. (2000): 231-237.

[25] Al-Hamdan, Qusai Z. and Munzer S.Y. Ebaid. "Modeling and simulation of a gas turbine engine for power generation." Journal of Engineering for Gas Turbines and Power. 128 (April 2006): 302-311.

[26] Shah, Ramesh K. "Advances in science and technology of compact heat exchangers." Heat Transfer Engineering 27.5 (2006): 3-22.

[27] Nagasaki, Takao, Rinzo Tokue, Shoichi Kashima, and Yutaka Ito. "Conceptual design of recuperator for ultramicro gas turbine." Paper IGTC2003Yokyo OS-102. Proceedings of the International Gas Turbine Congress. Tokyo, Japan: GTSJ, November 2003.

[28] Traverso, Alberto and Aristide F. Massardo. "Optimal design of compact recuperators for microturbine application." Applied Thermal Engineering 25 (2005): 2054-2071.

[29] Utriainen, E. and B. Sundén. "Evaluation of the cross corrugated and some other candidate heat transfer surfaces for microturbine recuperators." Journal of Engineering for Gas Turbines and Power. 124 (2002): 550-560.

[30] Manzan, Marco, Diego Micheli, and Stefano Pieri. "Automatic integration in the design of a microturbine compact recuperator." Paper GT2006-90529. Proceedings of GT2006 ASME Turbo Expo Expo: Power for Land, Sea an Air. Barcelona, Spain: ASME, May 2006.

[31] McDonald, Colin F. "Recuperator considerations for future higher efficiency microturbines." Applied Thermal Engineering. 23 (2003): 1463-1487.

[32] Kakaç, Sadik and Hongtan Liu. Heat Exchangers: Selection, Rating, and Thermal Design. 2nd ed. Boca Raton, Florida: CRC Press LLC, 2002.

[33] Aquaro, D., and M. Pieve. "High temperature compact heat exchangers: performance of advanced metallic recuperators for power plants." Paper CHE2005-30. Proceedings of Fifth International Conference on Enhanced, Compact and Ultra-Compact Heat Exchangers: Science, Engineering and Technology. R.K. Shah, M. Ishizuka, T.M. Rudy, and V.V. Wadekar, eds. Hoboken, NJ: Engineering Conferences International: September 2005.

[34] Tochon, Patrice, Christian Mauget and Frank Pra. "The use of compact heat exchangers technologies for the HTRs recuperator application per proper design." Paper E09. 2nd International Topical Meeting on High Temperature Reactor Technology. Beijing, China: September 22-24, 2004.

[35] Technical Data Blue Sheet: Stainless Steel Type 347. ATI Allegheny Ludlum, 2003. <http://www.alleghenyludlum.com> (23 Apr 2006).

[36] Kanaris, Athanasios G., Katerina A. Mouza, and Spiros V. Paras. "Designing novel compact heat exchangers for improved efficiency using a CFD code." 1st International Conference "From Scientific Computing to Computational Engineering." Athens, Greece: IC-SCCE, September 2004.

[37] Matthews, Wendy J. "Additional engine testing of an advanced alloy for microturbine primary surface recuperators." Paper GT2006-90068. Proceedings of GT2006 ASME Turbo Expo 2006: Power for Land, Sea, and Air. Barcelona, Spain: ASME, May 8-11, 2006.

[38] Escola, George, Charles W. Bucey, Preston Montague, and Michael J. Telfer. "Improvement of microturbine recuperators using Taguchi methodology." Paper GT2006-90144. Proceedings of GT2006 ASME Turbo Expo 2006: Power for Land, Sea, and Air. Barcelona, Spain: ASME, May 8-11, 2006.

[39] Utriainen, E. and B. Sundén. "A numerical investigation of primary surface rounded cross wavy ducts." Heat and Mass Transfer. 38 (2002): 537-542.

[40] Morimoto, Kenichi, Yuji Suzuki and Nobuhide Kasagi. "Optimal shape design of counter-flow primary surface recuperators." Paper CHE2005-17. Proceedings of Fifth International Conference on Enhanced, Compact and Ultra-Compact Heat Exchangers: Science, Engineering and Technology. R.K. Shah, M. Ishizuka, T.M. Rudy, and V.V. Wadekar, eds. Hoboken, NJ: Engineering Conferences International: September 2005.

[41] McDonald, Colin F. "Low-cost compact primary surface recuperator concept for microturbines." Applied Thermal Engineering. 20 (2000): 471-497.

[42] Wilson, D.G. and Theodosios Korakianitis. The Design of High-Efficiency Turbomachinery and Gas Turbines. 2nd ed. Upper Saddle River, NJ: Prentice Hall, Inc., 1998.

[43] Module 4A3 – Turbomachinery I Handout 5: Theory of Radial Flow Turbomachines. University of Cambridge, 2005/2006.
<http://www.eng.cam.ac.uk/teaching/courses/y3/3a3.html> (12 May 2006).

[44] Bathie, William W. Fundamentals of Gas Turbines. 2nd ed. New York: John Wiley & Sons, Inc., 1996.

[45] Lewis, R.I. Turbomachinery Performance Analysis. London, NW1 3BH: Arnold a member of the Hodder Headline Group, 1996.

[46] Mattingly, Jack D. Elements of Gas Turbine Propulsion. Reston, Virginia: American Institute of Aeronautics and Astronautics, Inc., 2005.

[47] Rangwala, A.S. Turbo-Machinery Dynamics: Design and Operation. New York: The McGraw-Hill Companies, Inc., 2005.

[48] Boyce, Meherwan P. Gas Turbine Engineering Handbook. Houston, Texas: Gulf Publishing Company, 1982.

[49] Thawley, Scott. "Fundamental chemical kinetic modeling of a Capstone combustor." UTSR Industrtial Fellowship Program. Capstone Turbine Corporation, 2005.

[50] Lefebvre, Arthur H. Gas Turbine Combustion. 2nd ed. Phiadelphia, PA: Taylor & Francis, 1999.

[51] Capstone C30 MicroTurbine™. Capstone Microturbine Corporation (2003). < http://www.microturbine.com/Documents/C30.pdf> (1 Apr 2006).

[52] Buckmaster, J., P. Clavin, A. Liñán, M. Matalon, N. Peters, G. Sivashinsky and F.A. Williams. "Combustion theory and modeling." Proceedings of the Combustion Institute. 30 (2005): 1-19.

[53] Incropera, Frank P. and David P. DeWitt. Fundamentals of Heat and Mass Transfer. 5th ed. Hoboken, NJ: John Wiley & Sons, Inc., 2002.

[54] Roberts, Rory. A dynamic fuel cell-gas turbine hybrid simulation methodology to establish control strategies and an improved balance of plant. Dissertation. University of California, Irvine, 2005.

[55] Bentor, Yinon. Chemical Element.com - Titanium. Yinon Benton (1996-2006). <http://www.chemicalelements.com/elements/ti.html>. (16 Feb 2007).

[56] Fox, Robert W. and Alan T. McDonald. Introduction to Fluid Mechanics. 5th ed. New York: John Wiley & Sons, Inc, 1998.

[57] Bossel, Ulf. "Well-to-wheel studies, heating values, and the energy conservation principle." European Fuel Cell Forum. Morgenacherstrasse 2F CH-5452 Oberrohrdorf, Switzerland: EFCF, October 29, 2003.

[58] Lukas, M.D. and K.Y. Lee. "Model-based analysis for the control of molten carbonate fuel cell systems." Fuel Cells. 5.1 (2005): 115-125.

[59] Lukas, Michael D. and Kwang Y. Lee. “An explicit dynamic model for direct reforming carbonate fuel cell stack.” IEEE Transactions on Energy Conversion. 16.3 (2001): 289-295.